ISSN 1580-2949
UDK 669+666+678+53 MTAEC9, 45(5)379–499(2011)

MATER. TEHNOL.	LETNIK VOLUME 45	ŠTEV. NO. 5	STR. P. 379–499	LJUBLJANA SLOVENIJA	SEP.–OCT. 2011

VSEBINA – CONTENTS

STROKOVNI ČLANKI – PROFESSIONAL ARTICLES

IN MEMORIAM

FRANC VODOPIVEC – OSEMDESETLETNIK

LAUDATION IN HONOUR OF FRANC VODOPIVEC ON THE OCCASION OF HIS 80th BIRTHDAY

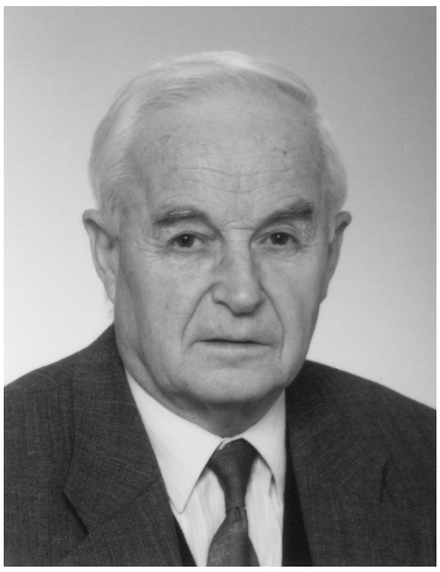

Franc Vodopivec, profesor, doktor metalurških znanosti, znanstveni svetnik, bivši direktor Inštituta za kovinske materiale in tehnologije (1990–1996), bivši član Državnega sveta Republike Slovenije (1992–2002), glavni urednik slovenske znanstvene revije Materiali in tehnologije (od 1996 dalje) praznuje 80. rojstni dan.

Spoštljiva obletnica je priložnost, da osvetlimo ozadje in razvoj tega pomembnega raziskovalca in vpliv njegovega raziskovalnega dela na področju izdelave, predelave in uporabe kovin in zlitin v slovenskem prostoru in v tujini.

Franc Vodopivec je bil rojen v Rakitniku 8. oktobra 1931 leta. Po končani gimnaziji je študiral metalurgijo na Univerzi v Ljubljani. Leta 1956 se je pridružil Metalurškemu inštitutu, sedaj Inštitut za kovinske materiale in tehnologije, kateremu je takrat direktoroval njegov ustanovitelj Ciril Rekar. F. Vodopivec je leta 1959 prejel od mednarodne agencije za atomsko energijo z Dunaja štipendijo francoske vlade, ki mu je omogočila delo na Institute de Recherché de la Siderurgie v St. Germain en Laye v Franciji. V letih od 1960 do 1962 je pripravljal svojo doktorsko nalogo z naslovom *Study of the behavior of arsenic and phosphorous by selective oxidation of iron alloys with low contents of both elements* in jo uspešno zagovarjal leta 1962 na Univerzi v Parizu.

F. Vodopivec se je leta 1962 vrnil na Metalurški inštitut, kjer je ustanovil Laboratorij za metalografijo, 1972 je postal vodja oddelka za tehnologijo, pomočnik direktorja leta 1978 in bil direktor Inštituta za kovinske materiale in tehnologije od 1990 do 1996 leta, ko se je upokojil. Leta 1992 je bil izvoljen za člana Državnega sveta Republike Slovenije za področje znanosti, leta 1997 je bil ponovno izvoljen.

Franc Vodopivec, professor, doctor of metallurgical science, scientific councilor, former director of Institute of Metals and Technology (1990–1996) and former member of the State Council of Republic Slovenia (1992–2002), editor in chief of Slovenian scientific journal Materials and Technology (since 1996) is celebrating his 80th birthday.

The respectful anniversary is the occasion to look at the background and the development of this well known researcher and at the influence which his research work has in the field of elaboration, transformation and use of metals and alloys in Slovenia and abroad.

Franc Vodopivec was born in Rakitnik, on 8th October 1931. After finishing with distinction the secondary school education, he studied Metallurgy at the University of Ljubljana. In 1956 he joined Metallurgical Institute, now Institute of Metals and Technology in Ljubljana directed by founder CirilRekar. In 1959 Franc Vodopivec received through the International Agency of Atomic Energy in Vienna a scholarship from the French Government. Working in the Institute de Recherché de la Siderurgie, in St.Germain en Laye, France from 1960 to 1962 he prepared his doctor thesis and graduated in 1962 at the University of Paris, Paris, France with the thesis *Study of the behavior of arsenic and phosphorous by selective oxidation of iron alloys with low contents of both elements.*

F. Vodopivec returned back in 1962 to the Metallurgical Institute and founded the Laboratory for metallography, 1972 he became head of Technology Department to 1978, assistant director to 1990 and director from 1990 to April 1996 when he retired. In 1992, Professor Vodopivec was elected for the first time in the Council State of Republic

Franc Vodopivec je nenadomestljiv glavni in odgovorni urednik slovenske znanstvene revije Materiali in tehnologije (od leta 1996).

Franc Vodopivec je kljub svojim letom še vedno poln kreativnih idej in razvojnega duha ter aktivno sodeluje tako z mladimi kot starejšimi raziskovalci IMT. Raziskoval je oksidacijo kovin, uvedel je karakterizacijo mikrostrukture na znanstveni ravni in že pred več kot 40 leti uvedel elektronsko mikroanalizo v slovenski in takratni jugoslovanski prostor. Ukvarjal se je tudi z mehanskim preizkušanjem kovin in zlitin, predvsem pa je študiral vedenje kovin pri visokih temperaturah, pri hladni in vroči predelavi, popravi, rekristalizaciji in rasti zrn duktilnih permanentnih magnetnih zlitin, pri neorientirani elektropločevini, rasti zrn, inducirani s selektivno površinsko segregacijo, študiral je tudi topologijo mikrostrukture in vedenje materialov pri uporabi pri visoki temperaturi, termično utrujanje in lezenje materialov.

F. Vodopivec je objavil več kot 300 člankov v mednarodnih revijah in na konferencah ter 320 člankov v slovenskih revijah in na konferencah s področja znanosti, tehnologije in uporabe kovin in zlitin.

F. Vodopivec je bil mentor več doktorandom in magistrandom na univerzah v Ljubljani, Mariboru, Beogradu in Zagrebu. Bil je zelo aktiven na mednarodnem akademskem področju. Bil je predsedujoči na mednarodnih znanstvenih konferencah, recenzent mednarodnih projektov EU in COST.

F. Vodopivec je še vedno predsednik Slovenskega društva za materiale, član Društva za vakuumsko tehniko Slovenije, Slovenskega kemijskega društva, Inženirske akademije Slovenije, Društva zgodovine Ljubljane itd. Bil je predsedujoči letni konferenci o materialih in tehnologijah v Portorožu (1990–1996), bil član znanstvene sekcije Vakuumska metalurgija pri IUVSTA (1992–1995). Leta 1978 je dobil nagrado Kidričevega sklada in 1984 Kidričevo nagrado za znanost.

Mnoge njegove projekte so podprla industrijska podjetja s področja metalurgije v Sloveniji in bivši Jugoslaviji, termoelektrarne in tudi slovenska in jugoslovanska vlada.

Franc Vodopivec je 2003 leta dobil državno Zoisovo nagrado Republike Slovenije za življenjsko delo.

Kolegi in sodelavci upamo, da bo tudi naprej še vedno aktivno sodeloval v razpravah in diskusijah, pri predavanjih in publikacijah.

Francu Vodopivcu želimo še mnogo zdravih let v okviru njegove družine in prijateljev.

Ljubljana, oktober 2011

Monika Jenko

Slovenia by the community of researchers and engineers and in 1997 for the second time.

Franc Vodopivec is indispensable editor in chief of Slovenian scientific journal Materials and Technology since 1996.

F. Vodopivec is still full of development spirit and creative ideas. He has been doing research work on the behaviour of metals in oxidative atmosphere, microstructure characterization of metals by optical and electron microscopy, electron probe analysis, mechanical testing; behavior of material in use at medium and high temperature, hot and cold working of metals, recovery, recrystallization and grain growth, ductile permanent magnet alloys, non oriented electrical steel sheets, grain growth induced by selective surface segregation, topology of microstructure and behavior of metals in use, creep and thermal fatigue.

F. Vodopivec has published over 250 papers in international journals and conferences and 320 papers in Slovenian journals and conferences on topics of science, technology and use of metals and alloys.

Franc Vodopivec has been supervisor to several Ph.D. and Master Degree students at the Universities of Ljubljana, Maribor, Belgrade and Zagreb. He is also very active in the international academic field. He was a chairman of international scientific conferences and project evaluator in EU actions of COST.

He is still president of Slovenian Society of Materials, member of Slovenian Vacuum Society, member of Slovenian Microscopy Society, Slovenian Society of Chemistry, Historical Society of Ljubljana, chairman of the R&D group of the Slovenian Association of Engineers, chairman of annual Conferences on Materials and Technologies (1990 to 1996) and was member of Vacuum Metallurgy scientific division of International Union for Vacuum Science, Technique and Applications – IUVSTA (1992– 1995). He is one of the founders of Slovenian Academy of Engineering Sciences.

He wrote in Slovenian newspapers several tens of articles of industrial and research policy.

In 1978 he received the Boris Kidrič Foundation Award and in 1984 the Boris Kidrič Award for science.

His many projects were supported by 21 industrial societies and associations in Slovenia and the former Yugoslavia from Metallurgy over mechanical energy to power stations as well as the Slovenian and the Yugoslav governments.

Vodopivec prepared forensic analysis of several industrial failures which qualified Slovenian societies to win arbitration for retributions of damages from foreign companies suppliers of industrial equipment.

Franc Vodopivec received in year 2003 state award – ZOIS award for his life work from the Republic of Slovenia.

His colleagues hope very much that he will still take part in discussions, lectures and publications. Most of all we would like to wish him and his family many years to come in good health.

Ljubljana, October 2011

Monika Jenko

UDK 669.14.018.252:539.42
Review article/Pregledni članek

ISSN 1580-2949
MTAEC9, 45(5)383(2011)

Cr-V LEDEBURITIC COLD-WORK TOOL STEELS

LEDEBURITNA JEKLA Cr-V ZA DELO V HLADNEM

Peter Jurči

Czech Technical University in Prague, Faculty of Mechanical Engineering, Karlovo nám. 13, 121 35 Prague 2, Czech Republic
p.jurci@seznam.cz

Prejem rokopisa – received: 2011-01-24; sprejem za objavo – accepted for publication: 2011-03-17

Cold-work tool steels based on Cr-V alloying belong to the most important tool materials for large series manufacturing. To enable high production stability, the tools must withstand various types of degradation processes, concerning firstly plastic deformation and wear. Therefore, the materials should have a high hardness, tensile and/or compressive strength and wear resistance. On the other hand, the materials have to resist brittle fracture, e.g., they must exhibit sufficiently high impact toughness and fracture toughness. This paper deals with an overview of the heat-treatment procedures and surface engineering techniques suitable for Cr-V tool steels. The effect of each of them on the main mechanical properties is also demonstrated and discussed. As a typical example, P/M made from the Cr-V ledeburitic steel Vanadis 6 is presented.

Keywords: P/M cold-work steel Vanadis 6, heat treatment, surface engineering, microstructure, hardness, three-point bending strength, fracture toughness

Orodna jekla za delo v hladnem legirana s Cr-V spadajo med najbolj pomembne materiale za orodja za delo v velikih serijah. Omogočajo veliko stabilnost proizvodnje in prenašajo različne procese degradacije zaradi plastične deformacije in obrabe. Zato morajo imeti visoko trdoto, raztržno in tlačno trdnost ter obrabno obstojnost. Po drugi strani morajo biti jekla dovolj odporna proti krhkemu lomu, kar pomeni, da morajo imeti tudi visoko udarno žilavost in žilavost loma. Članek je pregled postopkov toplotne obdelave in tehnologije površine, primernih za orodna jekla Cr-V, vpliv vsakega postopka pa je opisan in analiziran. Kot tipičen zgled, je obravnavano P/M ledeburitno jeklo Cr-V Vanadis 6.

Ključne besede: P/M hladno orodno jeklo Vanadis 6, toplotna obdelava, inženirstvo površine, mikrostruktura, trdota, tritočkovna upogibna trdnost, lomna žilavost

1 INTRODUCTION

High carbon and chromium ledeburitic steels were developed during World War I as a possible substitution for high-speed steels for cutting operations. However, they have insufficient hot hardness and were too brittle for these purposes. On the other hand, they quickly gained a wide popularity in cold-work applications, due to a high wear resistance and compressive strength. Further development of this group of materials led to two main trends. The first one was characterised by the efforts to get a maximum toughness at an acceptable hardness and wear resistance. A typical representative of this group of materials is the now widely used D2-chromium cold-work tool steel. The second trend was characterized by the development of materials with increased wear resistance. It was found that alloying with vanadium, typically up to the mass-fraction 4 %, combined with an enhanced amount of carbon forms extremely hard MC-carbides. When classically manufactured, unfortunately, the high vanadium containing steels also have important drawbacks. First of all, large segregations take place during slow solidification in industrial ingots, which leads to anisotropy of the physical and mechanical properties. The MC-carbides have a strong tendency to grow during solidification. Large particles of extremely hard phases make the forging and machining of the steels difficult or impossible. In industrial applications, when dynamically loaded, large MC-carbides are responsible for the limitation of toughness. Therefore, the upper limit of the vanadium content for the Cr-V ledeburitic steels manufactured by classical ingot metallurgy was found to be about 4 % V.

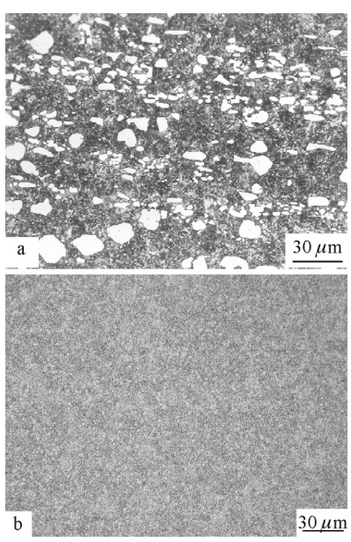

Figure 1: Light micrographs showing the microstructure of ingot metallurgy made Cr-V ledeburitic steel (2 % C, 7,8 % Cr, 6 % V) and PM made steel Vanadis 6 of similar chemical compositions

Slika 1: Optični posnetki mikrostrukture Cr-V-jekla, ki je bilo izdelano z ingotsko tehnologijo (2 % C, 7,8 % Cr, 6 % V) in P/M jekla Vanadis 6 s podobno kemijsko sestavo

For the manufacturing of Cr-V ledeburitic steels with a higher vanadium content, the only possible way to produce them is the powder metallurgy (P/M) of rapidly solidified particles. The technology, based on the rapid solidification of a supercooled melt in small droplets, restricts the segregations in time (due to the rapid solidification itself) and spatially (typical size of powder particles is some tens of micrometers). As a result, materials with an excellent combination of isotropic and fine structure and a high level of mechanical properties can be fabricated (P/M steels). The vanadium content, and proportionally also the amount of carbon, can be increased to more than 10 % without the risks of difficulties in forging and/or machining. Typical examples of conventionally manufactured and P/M steel of similar chemical composition are in **Figure 1**.

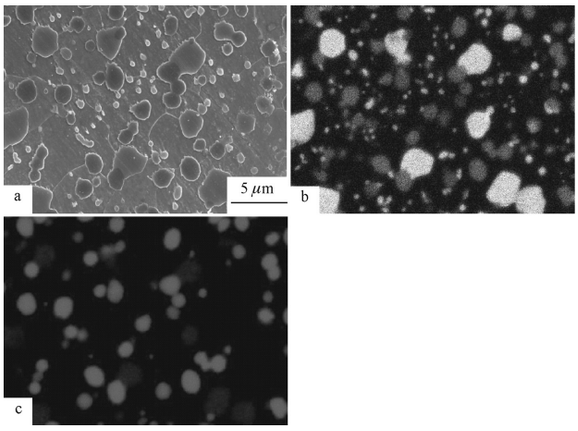

Figure 2: SEM micrograph showing the microstructure of the as-delivered Vanadis 6 steel a – image, b, c – corresponding EDS – maps of Cr and V

Slika 2: SEM-posnetki mikrostrukture dobavljenega jekla Vanadis 6; a – mikrostruktura, b, c – ustrezna EDS-posnetka za Cr in V

2 HEAT TREATMENT

2.1 As-delivered state

Cr-V ledeburitic steels are normally distributed to the end-users in the soft-annealed state. The main reason is to deliver the materials with an acceptable low hardness suitable for machining operations. The microstructure after the soft annealing consists of alloyed pearlite, secondary and eutectic and/or primary carbides, **Figure 2**. As shown in the micrograph, for the P/M made Vanadis 6 steel, the carbides are fine and uniformly distributed throughout the matrix. Previous investigations have shown that the equilibrium of a given alloy is formed by the chromium-based M_7C_3-carbides and vanadium-based MC-carbides [1]. Larger secondary and eutectic particles having a size between 1 μm and 3 μm are of both, e.g., M_7C_3- and MC-type. Ultra-fine carbides with a sub-micron size are the pearlitic ones and they are of M_7C_3-type, **Figures 2a-c**.

2.2 Austenitizing

The tools made from Cr-V ledeburitic steels are used in the heat-treated state only. A proper heat treatment is strictly recommended for the tools, to ensure the appropriate hardness, strength and wear resistance. On the other hand, this procedure should be carried out carefully. Otherwise, there can be a risk of lowering the toughness. The most convenient heat treatment for this type of steels is the so-called vacuum heat treatment.

The first step in heat treatment is austenitizing. Because of the poor thermal conductivity of the materials, the heating up to the final temperature should be slow, with several ramps enabling us to minimize the thermal gradients between the surface and the core, and a subsequent too large distortion of components.

The transformation of pearlite into austenite does not lead to sufficient saturation of the austenite since the amount of alloying elements in pearlite is very low. This is why the Cr-V ledeburitic steels must be heated up to a much higher temperature. During the heating from the A_1 temperature up to the final austenitizing, part of the secondary carbides undergoes a dissolution. Note that the role of the MC- and M_7C_3-phases is clearly different since they differ considerably in terms of thermal stability. As found in our current and previous investigations [2,3], the soft-annealed Cr-V ledeburitic steel Vanadis 6 contains the volume fraction of M_7C_3-carbides 16 % and 13 % of MC-carbides. Even heating up to a temperature of 1000 °C led to a reduction of the M_7C_3-carbides amount to 7 %, while the amount of MC-phase remained almost the same. The M_7C_3-carbides underwent a complete dissolution in the austenite up to 1100 °C, while the MC-phase amount was reduced only slightly, also after austenitizing at 1200 °C, **Figures 3–5** [3]. The dissolution of carbides leads to a saturation of the

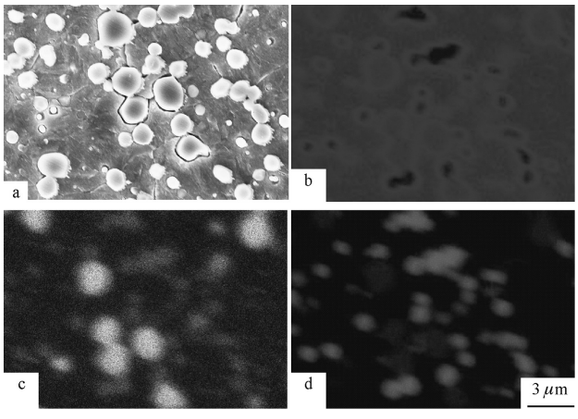

Figure 3: SEM micrograph showing the microstructure of as-quenched Vanadis 6 steel from 1000 °C; a – image, b, c, d – corresponding EDS – maps of Fe, Cr, V

Slika 3: SEM-posnetki mikrostrukture jekla Vanadis 6, kaljenega s 1000 °C; a – mikrostruktura, b, c – ustrezni EDS-posnetki za Fe, Cr in V

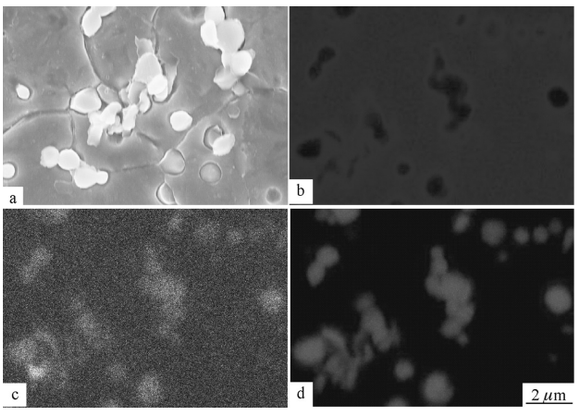

Figure 4: SEM micrograph showing the microstructure of as-quenched Vanadis 6 steel from 1100 °C, a – image, b, c, d – corresponding EDS – maps of Fe, Cr, V

Slika 4: SEM-posnetki mikrostrukture jekla Vanadis 6, kaljenega s 1100 °C; a – mikrostruktura, b, c – ustrezni EDS-posnetki za Fe, Cr in V

matrix with alloying elements. Since the chromium-rich carbides undergo dissolution in a considerably larger extent than the MC-phase, the absolute value of the chromium amount in the matrix increases more rapidly, **Table 1**.

Table 1: Amount of alloying elements dissolved in the matrix
Tabela 1: Vsebnost legirnih elementov, raztopljenih v matici

Austenitizing temperature	1000	1050	1100	1150	1200
Cr	5.66±0.56	5.96±0.22	6.85±0.33	6.96±0.15	7.12±0.09
V	1.72±0.32	1.76±0.48	2.24±0.53	2.18±0.43	2.66±0.37

The upper limit of the austenitizing temperature is determined mainly by the onset of the austenitic grains' coarsening. The second reason why it is essential to keep the recommended austenitizing temperatures is purely

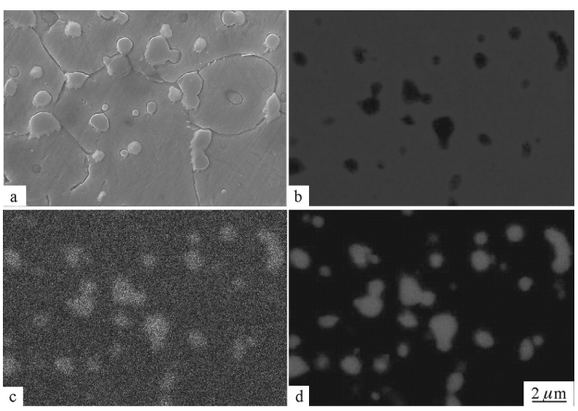

Figure 5: SEM micrograph showing the microstructure of as-quenched Vanadis 6 steel from 1200 °C, a – image, b, c, d – corresponding EDS – maps of Fe, Cr, V

Slika 5: SEM-posnetki mikrostrukture jekla Vanadis 6, kaljenega s 1200 °C; a – mikrostruktura, b, c – ustrezni EDS-posnetki za Fe, Cr in V

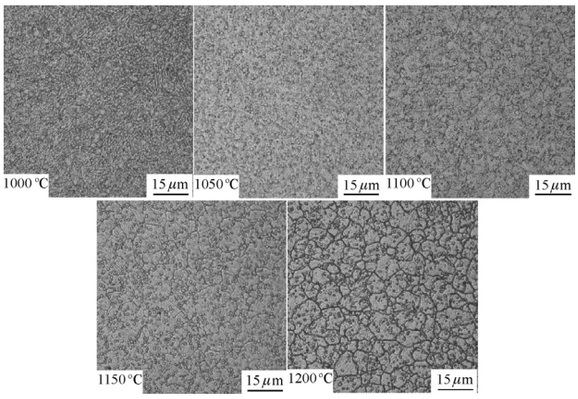

Figure 6: Light micrographs showing the microstructure of the Vanadis 6 ledeburitic steel after quenching from different austenitizing temperatures

Slika 6: Optični posnetki mikrostrukture ledeburitnega jekla Vanadis 6 po kaljenju z različne temperature avstenitizacije

economic – a higher austenitizing temperature increases the costs for realizing of heat-treatment procedure. **Figure 6** gives light micrographs of the as-quenched microstructures of Vanadis 6 steels. A measurement of the austenitic grain size according to the ASTM method revealed that after the quenching from a lower tem-

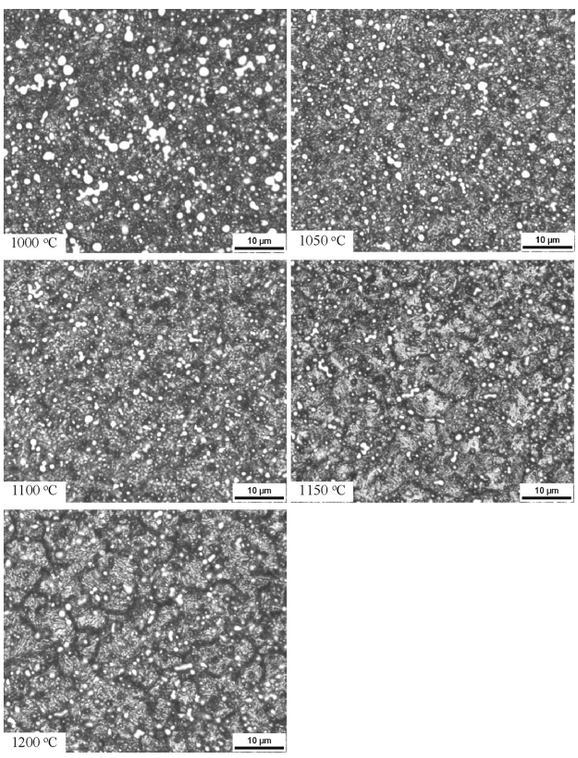

Figure 7: Light micrograph showing the microstructure of the Vanadis 6 ledeburitic steel after quenching from different austenitizing temperatures, colour etching using the Beraha-martensite agent

Slika 7: Optični posnetki mikrostrukture ledeburitnega jekla Vanadis 6 po kaljenju z različne temperature avstenitizacije; barvno jedkanje z Beraha reagentom za martenzit

perature it was 11.5, and it increased slightly to 10 after quenching from a temperature of 1200 °C.

2.3 Quenching

The standard quenching medium used for austenitized Cr-V ledeburitic steels is nitrogen gas under a high pressure – 6 bar as the minimum. Due to the good or excellent through hardenability of these steels there is no risk of hardness loss and, in addition, the method enables us to keep smooth and bright surfaces and to minimize the distortion of tools.

The increased saturation of austenite with carbon and alloying elements, **Table 1**, induces a decrease of the temperatures M_s and M_f, respectively. In classical hardening procedures, the materials are quenched to an ambient temperature. As the M_s temperature is located normally around 100 °C and the M_f well below zero, the retained austenite can be found in as-quenched material. The portion of retained austenite increases with an increasing austenitizing temperature because of the decrease of both the M_s and M_f temperatures. When austenitized at temperatures above 1100 °C, also the M_s of Cr- and Cr-V ledeburitic steels is below 0 °C and lower bainite can be found in the material [4]. This fact is clearly evident from the light micrographs, **Figure 7**. The portion of martensite (blue) slightly decreases and the bainite (red-violet) increases with increased austenitizing temperature. In addition, it seems that also the amount of retained austenite increases.

2.4 Sub-zero processing

The sub-zero processing, followed immediately after quenching, is aimed mainly at a reduction of the retained austenite amount and an increase of the hardness and the associated properties of the materials. However, the opinions on the structure and properties of ledeburitic steels are inconsistent and one would say that the development of this technique is not finished yet. What is clear up to now is that the sub-zero processing reduces the retained austenite amount [5], increases the as-quenched hardness [4] and, in some cases, the wear resistance, also [6]. New results obtained within the industrially oriented project TIP gave similar results regarding the as-quenched hardness, **Table 2** [7]. However, subsequent tempering led to a considerable hardness decrease, as discussed in the next section.

Figure 8 shows TEM bright- and dark-field micrographs from the no-sub-zero processed Vanadis 6 steel. The matrix consists of the martensite with a high dislocation density, and of retained austenite.

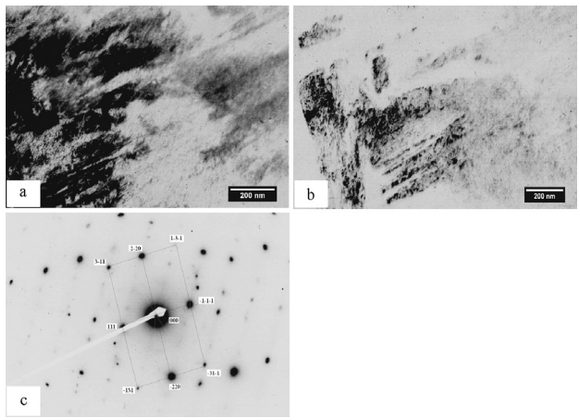

Figure 8: TEM micrographs showing the microstructure of the no-sub-zero processed sample quenched from 1000 °C. a – bright field image, b – dark field image of the same area, c – diffraction patterns from the retained austenite

Slika 8: TEM-posnetki mikrostrukture "sub zero" procesiranega jekla, kaljenega s 1000 °C. a – posnetek v svetlem polju, b – posnetek iste površine v temnem polju, c – difrakcijski odsevi zaostalega avstenita

Table 2: Results of hardness measurements of Vanadis 6 steel after different stages of heat treatment [7]
Tabela 2: Rezultati meritev trdote jekla Vanadis 6 po različnih stopnjah toplotne obdelave [7]

Austenitizing	Sub-zero processing	Tempering	Hardness		
			As-quenched	As-subzero processed	As-tempered
1000	No	2 × 550 °C/2 h	5.5	-	59.5
1000	No	2 × 530 °C/2 h		-	61
1000	– 90 °C/4 h	2 × 550 °C/2 h		66.5	56.5
1000	– 90 °C/4 h	2 × 530 °C/2 h		66.5	58.5
1025	No	2 × 550 °C/2 h	66	-	61
1025	No	2 × 530 °C/2 h		-	61.5
1025	– 90 °C/4 h	2 × 550 °C/2 h		67.5	57.5
1025	– 90 °C/4 h	2 × 530 °C/2 h		67.5	59.5
1050	No	2 × 550 °C/2 h	65.5		61.5
1050	No	2 × 530 °C/2 h			63
1050	– 90 °C/4 h	2 × 550 °C/2 h		68	58
1050	– 90 °C/4 h	2 × 530 °C/2 h		68	60.5
1075	No	2 × 550 °C/2 h	66		62
1075	No	2 × 530 °C/2 h			64
1075	– 90 °C/4 h	2 × 550 °C/2 h		68	58
1075	– 90 °C/4 h	2 × 530 °C/2 h		68	61.5

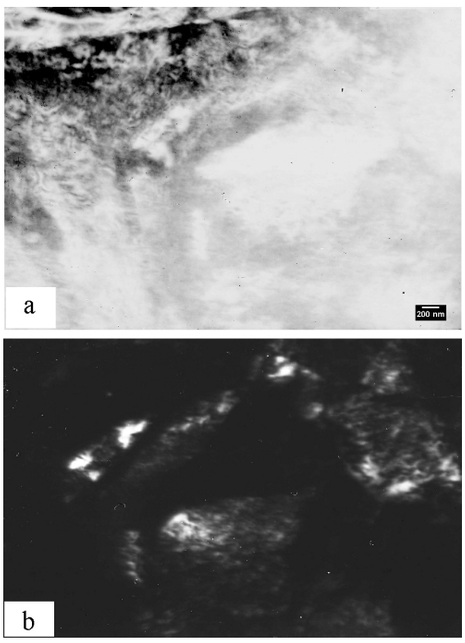

Figure 9: TEM micrographs showing the microstructure of a sample quenched from 1000 °C and sub-zero processed at – 196 °C for 4 h; a – bright field image, b – corresponding dark field image

Slika 9: TEM-posnetki mikrostrukture jekla, kaljenega s 1000 °C, ki je bilo "sub zero" procesirano 4 h pri – 196 °C. a – posnetek v svetlem polju, b – posnetek istega polja v temnem polju

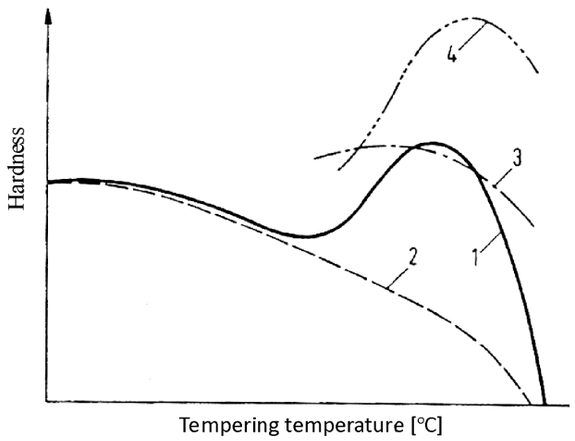

Figure 10: Contribution of main sub-processes to the hardness of ledeburitic steels during tempering [11]. (1 – resulting hardness, 2 – effect of tempering of martensite (softening), 3 – precipitation of carbides, 4 – transformation of retained austenite).

Slika 10: Prispevek glavnih "sub" procesov k trdoti ledeburitnega jekla med popuščanjem [11]. (1 – trdota, 2 – vpliv popuščanja martenzita (mehčanje), 3 – izločanje karbidov, 4 – premena zadržanega avstenita).

The retained austenite amount was significantly lower at first glance in the sub-zero processed steel quenched from the same austenitizing temperature, **Figure 9**.

Table 3 summarizes the results of the X-ray diffraction measurements of no-sub-zero processed and sub-zero processed Vanadis 6 steel. It is important that the retained austenite amount decreases with the sub-zero treatment period included into the heat processing. Also, the tetragonality of martensite increases, which gives a principal explanation of the higher hardness of the as-sub-zero processed steel than that no-sub-zero processed, see **Table 2**.

2.5 Tempering

As-quenched Cr-V ledeburitic steels contain the martensite (or a mixture of martensite and bainite), retained austenite and undissolved carbides. When sub-zero processed, the structure of some constituents can differ from those conventionally heat processed. Firstly, the amount of retained austenite is significantly lower. Collins and Meng [8–10], in addition, presumed that deep cooling leads to an arrangement of the structure that is responsible for the hindering of the dislocation movement and, the martensite originated at very low temperatures can differ from that transformed at higher temperatures in terms of the lattice parameter. Finally, the martensitic transformation may be probably superposed with the precipitation of nano-sized carbides, which are coherent with the matrix. However, these carbides were not detected by any researchers yet.

Tempering should follow the quenching and/or sub-zero treatment as soon as possible. Otherwise, the retained austenite could have been stabilized. For a more complete transformation of the retained austenite to martensite, as well as for tempering of the newly formed martensite, it is necessary to temper at least twice. During the tempering, the alloying elements and carbon diffuse out as from solid solutions forming precipitates, responsible for a secondary hardening effect. Cooling down from the tempering temperature induces the transformation of retained austenite to new martensite.

Table 3: Results of X-ray diffraction measurements of no-sub-zero and sub-zero processed Vanadis 6 steel
Tabela 3: Rezultati difrakcijskih meritev z rentgenskimi žarki za jeklo Vanadis 6, ki ni in je bilo "sub zero" procesirano

Heat treatment	Martensite /%	Retained austenite /%	Lattice parameter of martensite /nm, tetragonality c/a	Carbides
Quenching	49.45	17.76	a = 0.28623, c = 0.29154 c/a = 1.0186	M_4C_3, M_7C_3
112851 Quenching + sub-zero treatment	63.1	6.1	a = 0.28596, c = 0.29234 c/a = 1.0223	M_4C_3, M_7C_3

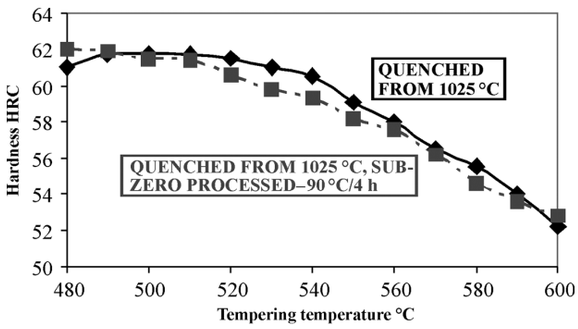

Figure 11: Tempering chart of sub-zero and no-sub-zero processed Vanadis 6 steel

Slika 11: Popuščni diagram za "sub zero" procesirano jeklo Vanadis 6 in za jeklo brez tega procesiranja

Kulmburg et al. schematically divided the total effect of the tempering temperature to the final hardness to the contributions, given by various sub-processes, **Figure 10** [11]. They considered that the final hardness of the material is a result of the competition between the softening of the martensite, due to carbides precipitation, the precipitation of carbides, and the transformation of retained austenite to martensite. For the Cr-V ledeburitic steels there is a hardness decrease up to the tempering temperature of about 350 °C, since the softening of martensite is the dominant process and other sub-processes play only a minor role. At higher temperatures, the sub-processes of the transformation of retained austenite and carbides precipitation become of great importance and if the steel is austenitized and quenched in the right way, the secondary hardness peak occurs at a tempering temperature close 500 °C. Beyond the maximum of the secondary hardness, the Cr-V ledeburitic steels undergo a softening because of the coarsening of precipitates and also due to the fact that during the last tempering cycle, no more austenite can transform to the martensite.

The material tempered after the sub-zero period behaves in a different way, **Figure 11**. In our previous works [7,12], see also **Table 2**, it was established that the tempering at the temperatures of the secondary hardness peak led to a lower hardness of the sub-zero processed material than that of no-sub-zero processed material. The different behaviour (and also rather surprising at first glance) of sub-zero processed material can by indirectly explained using the above-mentioned Kulmburg's consideration: the hardness of as-sub-zero processed material is higher than that of no-sub-zero processed steel due to a more complete martensitic transformation. But, during the tempering, the softening of martensite takes place. On the other hand, a lower retained austenite amount can be transformed into the martensite, thus the contribution of the sub-process 4, **Figure 11**, can be expected to be less significant. And, finally, one would also expect a lower contribution of the sub-process 3 if Meng's assumption [9] on the carbide precipitation at the sub-zero period was confirmed.

2.6 Nitriding

The nitriding of Cr-V ledeburitic steels is mostly carried out in plasma, since the composition of steels can make serious obstacles in gaseous processes. The nitriding temperature should be lower than the tempering temperature. A short processing time is preferred, up to 2h, with a case depth up to 60 μm and with no formation of white compound layers on the surface.

Several beneficial effects on the tool steels can be expected due to the nitriding. The hardness after nitriding can easily reach over 1000 HV, and the wear resistance increased substantially. The nitrogen atoms in the material induces the formation of a high compressive stress, exceeding 1000 MPa for the Vanadis 6 steel [1]. The increased hardness of the plasma-nitrided region has a favourable effect on the adhesion of thin films made with PVD processes. In our previous studies it was found that a properly performed plasma nitriding procedure can enhance the adhesion by two-to-three times [13–15]. Nevertheless, not only the positive effects of plasma nitriding on the material properties were found. Several investigations established that the three-point bending strength decreases with the presence of a nitrided region on the surface [13,16,17]. On the fracture surfaces, some clearly visible transcrystalline cleavages were found, which together with a low fracture toughness makes the material brittle, **Figure 12**.

2.7 Formation of thin ceramic films

For the coating of Cr-V ledeburitic steels, various physical-based low-temperature techniques are used. A variety of thin films can be deposited now onto the

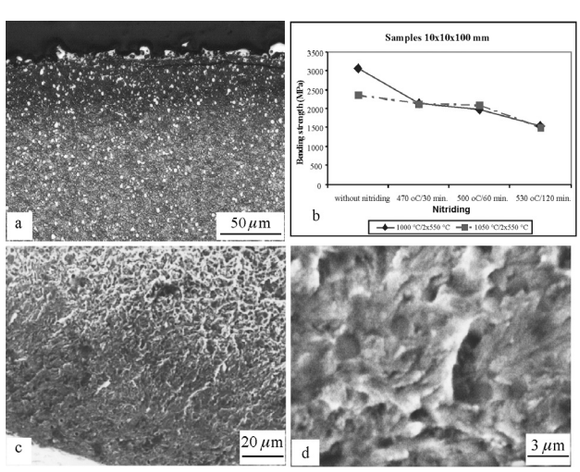

Figure 12: a – light micrograph of plasma-nitrided region formed on the Vanadis 6 steel at 530 °C for 120 min., b – three-point bending strength as a function of processing parameters, c, d – overview and detail SEM micrographs of the fracture surface

Slika 12: a – optični posnetki v plazmi nitrirane površine na jeklu Vanadis 6 po 120 min obdelave pri 530 °C, b – tri točkovna upogibna trdnost v odvisnosti od parametrov procesiranja, c, d – videz in SEM-posnetek površine preloma

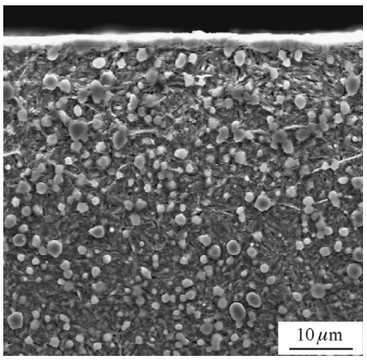

Figure 13: SEM micrograph showing the duplex-layer (plasma nitriding 500 °C/60 min. + CrN 2.5 μm) formed on the Vanadis 6 steel
Slika 13: SEM-posnetek dvojne plasti (plazemsko nitriranje 500 °C/60 min + CrN 2.5 μm), ki je nastala na jeklu Vanadis 6

steels, but the most frequently used are still TiN and CrN and their variations with additions of other elements like Si, Al etc. The main problem in the deposition of thin films is their adhesion to the substrate, since they differ from the metals in many physical and mechanical properties. First of all, they have a much higher hardness and elasticity modulus. Ceramic films generally exhibit very poor fracture toughness and differ from steels also in their thermal expansion coefficient. As a result, they can easily fail when loaded, with heavy normal forces or dynamically.

The current development in PVD coatings is then focused on three main trends. The first one is multilayers with different periodicity of the nano-scaled sub-layers. The effort to develop the multilayers is devoted to the improvement of fracture characteristics of ceramic films based on the assumption that the crack propagation will be hindered by the presence of many interfaces in the film. The second trend in the coatings development is based on the logical consideration that if brittle material contains softer particles of an optimal size and distribution, its resistance to fracture propagation can be improved. Therefore, the addition of small amounts of silver or copper to the CrN (CrAlN, CrSiN) coatings are investigated [18–21]. The last, but not the least, trend in modern coating development is focused on the optimization of the substrate properties before the deposition. For this purpose, plasma nitriding has become of the greatest importance. Nitrided regions have an elevated hardness and a better load-carrying capacity, which led to a several times better coating adhesion in many previous investigations [14,15,22]. **Figure 13** shows an example of a duplex-layer formed on the surface of the PM ledeburitic steel Vanadis 6.

3 MECHANICAL PROPERTIES

3.1 Hardness

Cr-V ledeburitic steels have a heterophaseous composition over their whole lifetime, e.g., from the manufacturing procedure up to the final use of the tools. Therefore, the hardness of the materials is a result of the synergistic effect given by the superposition of the effects of the matrix and the carbides. However, the role of the structural constituents upon the hardness is specific in different stages of the heat treatment of the materials.

In the as-annealed condition, the matrix comprises ferrite and its hardness is low. The hardness of the material is then mainly determined by the quality, size and distribution of carbides. Generally, the hardness increases with increasing amount of carbides. In the group of Cr-V ledeburitic steels, the as-annealed hardness is mainly influenced by the amount of MC-carbides.

In the heat-processed state, the matrix is responsible for the high hardness of the materials. The heat treatment, if properly conducted, leads to the formation of a matrix consisting mainly of martensite and a certain portion of retained austenite. In some cases, bainite can also be formed in as-quenched steels, but, as reported elsewhere, with no risk of a substantial hardness loss [3]. When sub-zero processed, the hardness of steels is increased by several HRC units due to more complete martensitic transformation. Tempering at temperatures up to 450 °C induces a slight hardness decrease. Above that, the hardness increases due to the complex precipitation/transformation process, see section 2.5. Beyond the maximum of the secondary hardness, the coarsening of precipitates proceeds and the hardness decreases.

3.2 Wear resistance

When pure abrasive wear takes place in the use of tools, the resistance of Cr-V ledeburitic steels against it is determined by the amount of large primary and eutectic carbides. But, also the character of the abrasive particles plays an important role. If, for instance, abrasive particles are harder than the hardest structural component of tool steels, no improvement of the wear resistance can be expected [23]. In the case of softer abrasive particles like SiO_2, on the other hand, an enhanced volume fraction of hard MC primary carbides leads to an improvement in the wear resistance by 75–100 %. Nevertheless, also in the case of the SiO_2-abrasive particles the situation is more complex – according to Jacobson [24], better wear resistance of the tool steels can be expected only if the SiO_2-particles are smaller than 100 μm.

However, from various metallurgical aspects it is difficult or impossible to increase the amount of MC-carbides above some limits. A high volume fraction of MC-phase makes serious obstacles in the manufacturing of tool steels, which makes it impossible to obtain a structure and properties, mainly toughness, at an acceptable level [25,26].

If the adhesive wear is the dominant process in the use of ledeburitic tool steels, the presence of hard

carbides itself is not relevant for better wear resistance [27]. According to Fontalvo et al. [28], besides the presence of hard MC-carbides, the interparticle spacing is the dominant factor influencing the adhesive wear resistance. The interparticle spacing has to be as small as possible. Otherwise, the contact area between the relatively softer matrix and counterpart material and the probability of adhesion also increases.

The wear resistance can be improved by various surface-treatment techniques. For instance, it has been reported previously that the plasma nitriding applied for the final processing of Vanadis 6 ledeburitic steel reduces the friction coefficient and makes the weight loss due to wear lower by 50 % [29]. Also, the PVD-coating, if properly made, tends to reduce the friction coefficient and makes the abrasive and adhesive wear lower [14,15,22].

For instance, our first experiments with the incorporation of small silver additions to CrN coatings, developed on the Vanadis 6 steel, have shown that the friction coefficient was reduced considerably when the layers were tested at elevated temperatures using a standard pin-on-disc test.

3.3 Three-point bending strength

The three-point bending strength is a standard measure of the resistance of hard ferrous alloys, including Cr-V ledeburitic steels, against the initiation of brittle fracture. For its determination, standard samples with the dimensions (10 × 10 × 100) mm are used. The standard load rate is 1 mm/min and the samples are loaded in the centre.

There are many parameters of the material manufacturing route and processing that influence the three-point bending strength.

3.3.1 Manufacturing route

There are two main manufacturing routes of the Cr-V ledeburitic steels. The first one is based on the ingot casting and subsequent hot rolling and/or forging of as-cast ingots. It often accompanied by the formation of carbide bands, oriented longitudinally to the dominant deformation direction. As a result, also the three-point bending strength is directionally dependent, while the values measured in various directions to the carbide banding may differ significantly [30].

The second production route for the Cr-V ledeburitic steels is the powder metallurgy of rapidly solidified particles. The manufacturing process involves the powder production (mainly by inert-gas spraying of the melt) and powder consolidation (hot isostatic pressing is normally used). In the powder production, the gas spraying disintegrates the melt stream into small droplets, which freeze rapidly, at typical cooling rates of 10^3–10^5 K s^{-1}. This makes a reduction in scale of segregation because of the spatial (typical size of powder particles is several tens of μm) and time (the droplets freeze in milior microseconds) restrictions. The consolidation via hot isostatic pressing introduces an isotropic deformation into the material. The resulting microstructure of P/M manufactured steels in much finer than that of conventionally produced materials with no preferred orientation of the structural features, see also **Figure 1**. Nevertheless, an improvement of the mechanical properties of materials due to the use of P/M technique for their manufacturing is closely dependent on the quality of stages of the manufacturing. If, for instance, the molten material is insufficiently homogenized before the spraying, clusters of primary carbides can remain in the structure and might easily cause lowering of the three-point bending strength [31].

Unfortunately, a direct comparison of the effect of manufacturing route on the three-point bending strength is missing up to now since there is not a commercially available Cr-V ledeburitic steel that has been produced by both mentioned techniques.

3.3.2 Surface quality

For brittle materials, like Cr-V ledeburitic steels, the surface quality plays an important role in their fracture behaviour. These problems were analysed in various investigations [32] and for the Cr-V ledeburitic steel Vanadis 6 more precisely in [33]. It was found that a worsened surface quality induces a relatively sharp decrease in the three-point bending strength so the plastic component of the total work of fracture, **Figure 14**. As a consequence, a higher topography of the fracture surfaces of samples with a higher surface quality has been established, **Figure 15**.

3.3.3 Heat treatment

It is well known that the austenitizing and subsequent quenching increases the hardness of Cr-V ledeburitic steels, but, simultaneously, the three-point bending strength drop is lowered. The lowering of the three-point bending strength is more significant with increasing austenitizing temperature because of the grains' coarsening, **Figure 16** [7].

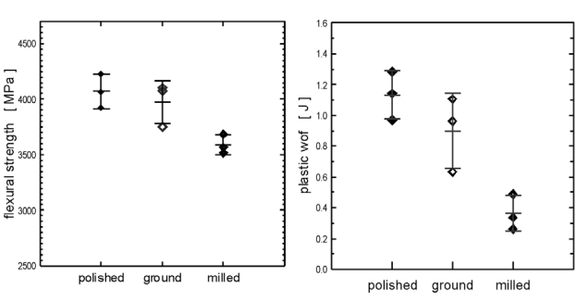

Figure 14: Flexural strength and plastic component of work of the fracture for heat-processed samples from the Vanadis 6 ledeburitic steel with various surface quality: polished – up to mirror finish, ground (R_a = 0.1) and milled (R_a = 6.3).

Slika 14: Upogibna trdnost in plastična komponenta energije preloma za toplotno obdelane vzorce ledeburitnega jekla Vanadis 6 z različno kakovostjo površine: zrcalno polirana, brušena (R_a = 0.1) in rezkana (R_a = 6.3).

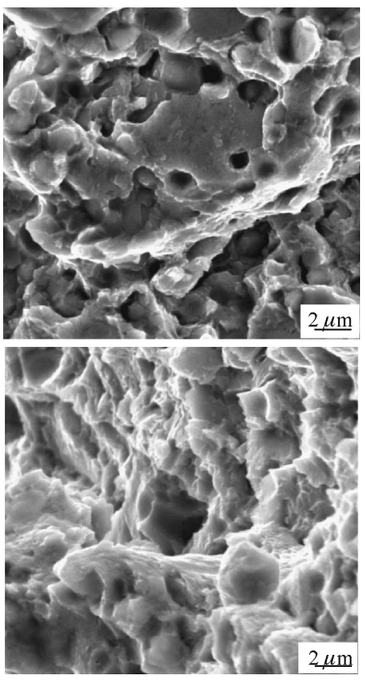

Figure 15: SEM micrographs of fracture surfaces of milled (left) and polished sample (right)

Slika 15: SEM-posnetki površine preloma rezkanega (levo) in poliranega (desno) vzorca.

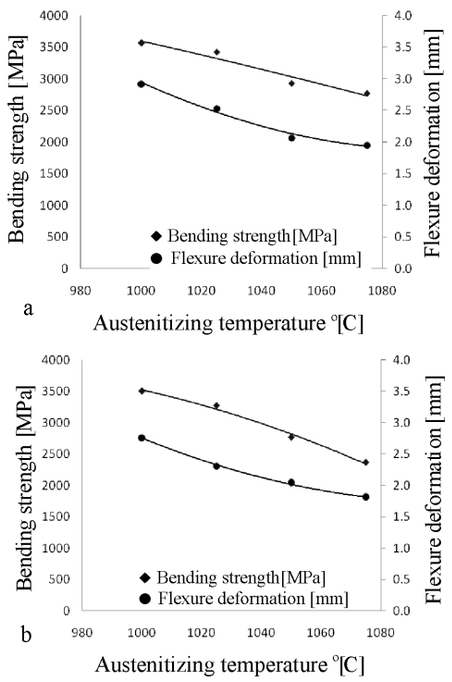

Figure 16: Effect of austenitizing temperature on bending strength after heat treatment. a – austenitizing, tempering 2 × 530 °C/2 h, b – austenitizing, sub-zero period –90 °C/4 h, tempering 2 × 530 °C/2 h

Slika 16: Vpliv temperature avstenitizacije na upogibno trdnost po toplotni obdelavi: a – avstenitizacija, popuščanje 2 × 530 °C/2 h, b – avstenitizacije, "sub zero" obdelava –90 °C/4 h, popuščanje 2 × 530 °C/2 h

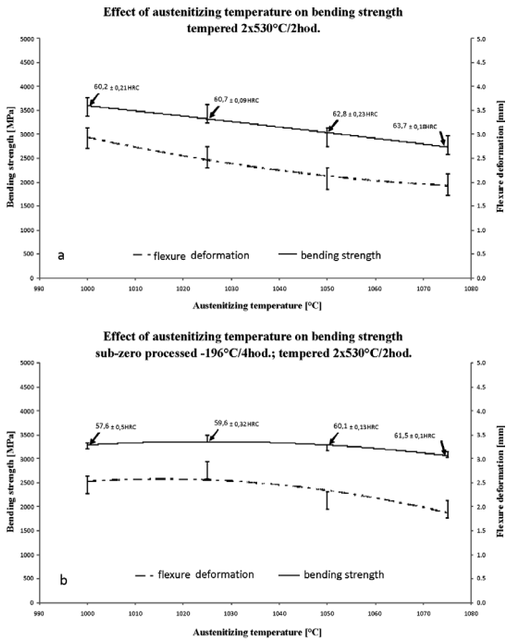

Figure 17: Three-point bending strength and flexure deformation for no-sub-zero and sub-zero processed Vanadis 6 steel

Slika 17: Tri točkovna upogibna trdnost in upogibna deformacija za ne sub zelo in sub zero procesirano jeklo Vanadis 6

Tempering at low temperatures, typically below 400 °C, results in a slight increase of the three-point bending strength because of the martensite softening. The increase of the tempering temperature to the range typical for the secondary hardness peak leads to a lowering of the three-point bending strength. The first

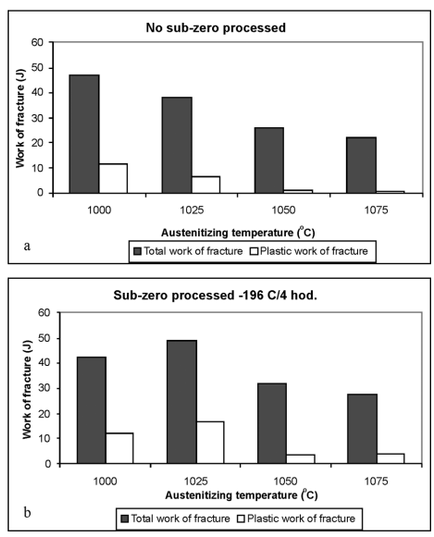

Figure 18: Work of fracture and its plastic component of no-sub-zero (a) and sub-zero (b) processed Vanadis 6 steel as a function of austenitizing temperature

Slika 18: Energija preloma in njena plastična komponenta za ne "sub zero" (a) in "sub zero" (b) procesirano jeklo Vanadis 6 v odvisnosti od temperature avstenitizacije

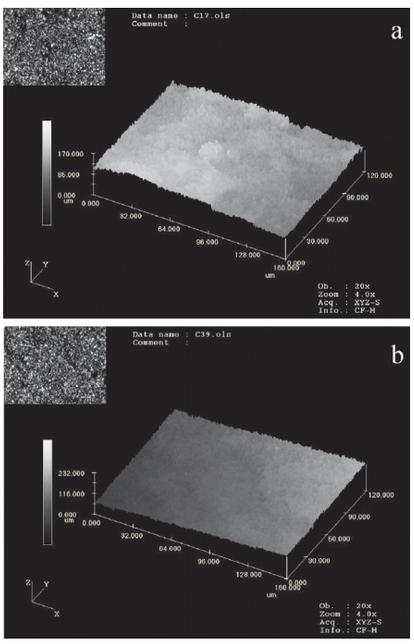

Figure 19: Fracture surfaces of the three-point bending test samples. a – sub-zero processed, b – no-sub-zero processed steel Vanadis 6
Slika 19: Površina preloma vzorcev po tritočkovnem upogibnem preizkusu; a – "sub zero" procesirano, b – ne "sub zero" procesirano jeklo Vadadis 6

process responsible for that is the transformation of the softer retained austenite to the harder martensite. Simultaneously, the precipitation of carbides from martensite and retained austenite contributes to the embrittlement of the materials.

If the sub-zero period is inserted into the heat processing, then the three-point bending strength can slightly increase, in particular when a higher austenitizing temperature was used, **Figure 17**. But some results of the investigations published previously also indicate a slightly opposite tendency, **Figure 21** [12]. The plastic component of the work of fracture increases with the sub-zero treatment, **Figure 18**. This is reflected in the topography of the fracture surfaces, as shown in **Figure 19**. From these two micrographs it can be derived that the sub-zero processing could have a positive effect on the plasticity of the material. This finding is also consistent with the fracture toughness investigations in previous work [12], which is discussed in one of the next paragraphs.

3.3.4 Surface treatment

The effect of the plasma nitriding on the three-point bending strength has been described in Section 2.6.

One would say that the PVD layering cannot influence the three-point bending strength in a negative way since the diffusion bonding of thin ceramic films onto the steel surfaces is poor due to a very low deposition temperature. However, our last investigations have fixed a weak tendency of the material to become more brittle when layered, **Figures 20** [34].

3.4 Fracture toughness

Fracture toughness is a measure that characterizes the resistance of the Cr-V ledeburitic steels against the crack propagation. In these materials, the fractures are typical formed by a "dimple morphology". It is a result of the mechanism of the fracture propagation, where two main mechanisms take place. The first is the carbide cracking. The carbides undergoing fragmentation are mostly the M_7C_3-particles. The second propagation mechanism is decohesion at the carbide/matrix interfaces, which is connected with plastic deformation of the matrix. It is logical that for the second mechanism, much more energy is spent, and also that the capability of the matrix to be deformed is the most important parameter describing the resistance of the materials against crack propagation.

Therefore, in real materials, the hardness of the matrix is the main parameter influencing the fracture toughness. Berns et al. [35,36] have reported that for the steel X210Cr12, the fracture toughness decreases from 31–50 MPa $m^{1/2}$ in the soft-annealed state to 14–22 MPa $m^{1/2}$ after austenitizing and quenching. Subsequent tempering led to a slight increase in K_{IC}, but the level of the K_{IC} increase was proportional to the as-tempered hardness. In addition, the authors of the above-mentioned papers have found that the effect of the morphology of carbides (as-cast networks, as-wrought banding) has an importance only in the soft-annealed state of the material and it becomes much less significant with the increasing hardness of the steels.

For Cr-V ledeburitic steels made via PM, there are practically no relevant data on their fracture toughness. Only in our recent work [12] we attempted to evaluate the fracture toughness of the Vanadis 6 steel after the application of various heat-treatment regimes. Two austenitizing temperatures (1000 °C and 1050 °C) were applied for a standard tempering temperature of 550 °C. Some specimens were also sub-zero processed in liquid nitrogen at –196 °C for 24 h.

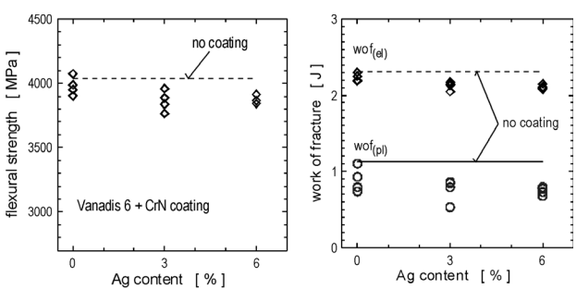

Figure 20: Flexural strength and plastic component of work of fracture for the CrN and CrAgN layered samples made from the Vanadis 6.
Slika 20: Upogibna trdnost in plastična komponenta prelomnega dela za vzorce s pokritjem CrN in CrAgNi iz jekla Vanadis 6

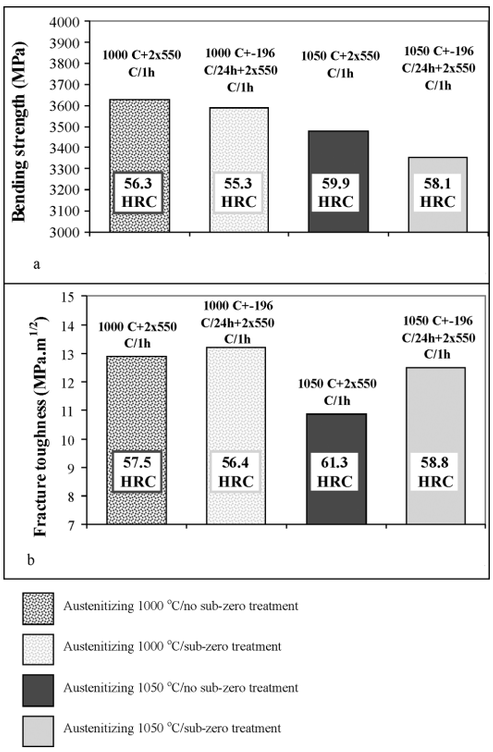

Figure 21: Graphical presentation of the obtained experimental results for a) three-point bending strength and b) average fracture toughness vs. processing route

Slika 21: Grafičen prikaz doseženih eksperimentalnih rezultatov za a) tritočkovno upogibno trdnost in b) povprečno žilavost loma za različne načina procesiranja

The results of the investigations are in **Figure 21**. The fact that a higher austenitizing temperature led to a lower fracture toughness has been expected, since it is logical that the matrix hardness was higher in this case. Nevertheless, the average fracture toughness after the performed heat processing of Vanadis 6 steel was found to be slightly higher for sub-zero processed material. At a first glance, this was rather surprising, since normally it is assumed that as the three-point bending strength so the resistance against crack propagation should be lowered. However, it was found in various investigations [7,12] that the hardness after the tempering was lower for the sub-zero processed material, see also Section 2.5. The observations, that the sub-zero processed Vanadis 6 steel had higher fracture toughness, seems to be consistent with other investigations [35,36].

There is no comparison between the fracture toughness for the Cr-V ledeburitic steels made via classical ingot metallurgy and the PM of rapidly solidified particles, since the only material produced using both manufacturing routes does not exist. The only paper describing the fracture toughness of the ledeburitic steels of the same chemical composition, but manufactured as by ingot metallurgy so via the PM is the pioneer work of Olsson and Fischmeister [37]. They reported that the fracture toughness of the PM made M2-type high-speed steel seems to be slightly better than the conventionally produced material.

4 CONCLUSIONS

As-delivered Cr-V ledeburitic steels should be in the soft-annealed state. When the soft annealing is properly done, they contain primary, eutectic and secondary carbides and spheroidized pearlite. The hardness of the materials should be as low as possible.

During austenitizing, the chromium-based carbides dissolve in the austenite while the vanadium-based particles remain stable up to high temperatures.

The dissolution of carbides induces the enrichment of a solid solution with carbon and alloying elements. As result, the through-hardenability of the materials increases, but also the portion of the retained austenite after quenching tends to increase.

If the optimal austenitizing temperature is exceeded, grain coarsening takes place and the retained austenite amount increases rapidly up to more than 50 %.

Properly quenched materials have a hardness easily exceeding 60 HRC. A too high austenitizing temperature lowers the hardness, due to an increased amount of retained austenite. When sub-zero treated, the materials have slightly elevated hardness due to a more complete martensitic transformation.

Tempering of Cr-V ledeburitic steels is a complex process, which involves the softening of martensite, the formation of new martensite from the retained austenite during cooling down from the tempering temperature and the precipitation of carbides during holding at the tempering temperature. When properly done, the maximum secondary-hardness peak occurs at a temperature of slightly above 500 °C.

It seems that sub-zero processed materials exhibit a tendency to have a slightly lower as-tempered hardness than those no-sub-zero treated. An exact interpretation of the lower as-tempered hardness is not available yet, but its nature should be probably considered in a different structure of deep-cooled material compared to classically heat-processed steels.

Plasma-nitriding possesses an increased hardness, lowered friction coefficient, improved wear resistance and adhesion of thin ceramic films, but, on the other hand, also embrittlement of the materials.

Physical vapour deposition processes are mainly used for the layering of Cr-V ledeburitic steels. Current development trends in the PVD-layering are focused on the development of nano-structured and duplex layers with customer-tailored properties.

The abrasive wear resistance of Cr-V ledeburitic steels is determined mainly by the volume fraction of primary and/or eutectic MC-carbides. However, if the abrasive particles are harder than the MC-phase, the effect of these carbides becomes negligible. In adhesive

wear, the interparticle spacing of carbides is important. Surface layering, when properly chosen and made, can lead to a significant increase in the abrasive/adhesive wear resistance.

The toughness of the Cr-V ledeburitic steels is influenced by many parameters. The presence of carbide bands or clusters decreases the toughness. This is why the PM-made steels are tougher than those manufactured via ingot metallurgy. Further, the increased roughness, presence of brittle structures on the surface but also increased matrix hardness, due to heat treatment, make the toughness lower.

The fracture toughness of the discussed materials is mainly dependent on the matrix hardness and it decreases with the increasing matrix hardness. At a constant and low matrix hardness, the fracture toughness depends on the carbide size and distribution also. However, the effect of carbides on the fracture toughness diminishes at a high matrix hardness.

5 REFERENCES

[1] Jurči, P., Hnilica, F.: Powder Metallurgy Progress, 3 (**2003**) 1, 10

[2] Bílek, P., Sobotová, J., Jurči, P.: Evaluation of structural changes in Cr-V ledeburitic tool steels depending on temperature austenitization, lecture given at the 18th Conf. on Mater. Techn., November 2010, Portorož, Slovenia

[3] Jurči, P.: Materials Engineering, 17 (**2010**), 1

[4] Berns, H.: Härterei – Tech. Mitt., 29 (**1974**), 236

[5] Kulmburg, A. et al.: Härterei – Tech. Mitt., 47 (**1992**), 318

[6] Stratton, P. F.: In.: Proc. of the 1st Int. Conf. on Heat Treatment and Surf. Eng. of Tools and Dies, Pula, Croatia, 8.–11. 6. 2005, 11–19

[7] Jurči, P. et al.: Proc. of the 19th Int. Conf. METAL 2010, Rožnov pod Radhoštem, May, 18–20, 2010, Tanger s.r.o., 512

[8] Collins, D. N.: Heat Treatment of Metals, 23 (**1996**), 2

[9] Meng, F. et al.: ISIJ International, 34 (**1994**) 2, 205–210

[10] Collins, D. N., Dormer, J.: Heat Treatment of Metals, 24 (**1997**) 3, 71

[11] Kulmburg, A. et al.: Härterei – Tech.Mitt., 47 (**1992**), 318

[12] Jurči, P., Šuštaršič, B., Leskovšek, V.: Mater. Tehnol., 44 (**2010**) 77

[13] Jurči, P., Panjan, P.: Metal Powder Report, 61 (**2006**), 28

[14] Jurči, P., Hudáková, M.: Mater. Tehnol., 42 (**2008**), 197

[15] Jurči, P. et al.: In: Proc. of Int. Conf. Nordtrib 2008, Tampere, Finland, June 10–13, 2008, CD – rom + Book of abstracts

[16] Jurči, P. et al.: Mater. Tehnol., 38 (**2004**), 13

[17] Hnilica, F., Čmakal, J., Jurči, P.: Mater. Tehnol., 38 (**2004**), 263

[18] Mulligan, C. P., Gall, D.: Surf. Coat. Techn., 200 (**2005**), 1495

[19] Basnyat, P. et al.: Surf. Coat. Techn., 202 (**2007**), 1011

[20] Mulligan, C. P., Blanchet, T.A., Gall, D.: Surf. Coat. Techn., 204 (**2010**), 1388

[21] Yao, S.H. et al.: Surf. Coat. Techn. 201 (**2006**), 2520

[22] Jurči, P., Hudáková, M., Maixner, J.: In: Proc. of the 17th Int. Conf. METAL 2008, Hradec nad Moravicí, May 2008, Tanger s.r.o., CD-ROM

[23] Bergman, F., Hedenqvist, P., Hogmark, S.: Tribology Int., 30 (**1997**), 183

[24] Jacobson, W., Wallén, P., Hogmark, S.: Wear, 123 (**1988**), 207

[25] Wei, S. et al.: Tribology Int., 39 (**2006**), 641

[26] Wei, S., Zhu, J., Xu, L.: Mater. Sci. Engng., A404 (**2005**), 138

[27] El-Rakayby, A. M., Mills, M.: Wear, 112 (**1986**), 327

[28] Fontalvo, G. A. et al.: Wear, 260 (**2006**), 1028

[29] Jurči, P., Stolař, P., Hnilica, F.: Proceedings of the 9th International Seminar of the IFHTSE, Warsaw, Poland, September 22–25, 2003, 333

[30] Grgač, P.: Neue Hütte, 12 (**1989**), 459

[31] Jurči, P., Cejp, J., Suchánek, J.: In: Proc. of the Int. Conf. on Powder Metallurgy, Piešťany, Slovak Republic, September 19–22, 1999, 206

[32] Geller, J. A.: Tool Steels, (Instrumentalnyje stali), 5th issue, Moscow, Metallurgija, 1983

[33] Jurči, P., Dlouhý, I.: In: Proc. of Int. Conf. "Heat treatment of metallic surfaces", Jihlava, November 24–25, 2009, 31

[34] Jurči, P., Dlouhý, I., Chlup, Z.: Effect of CrN-based thin films on bending strength of Cr-V ledeburitic tool steel, lecture given at 23rd Int. Conf. on Heat Treatment, Jihlava, November 2010

[35] Berns, H., Fischer, A., Hönsch, W.: Härterei-Tech. Mitt., 45 (**1990**), 217

[36] Berns, H., Bröckmann, C., Weichert, D.: Engineering Fracture Mechanics, 58 (**1997**) 311

[37] Olsson, L. R., Fischmeister, H. F. Powder Metallurgy, 1 (**1978**), 13

UDK 621.791:669.715
Original scientific article/Izvirni znanstveni članek

ISSN 1580-2949
MTAEC9, 45(5)395(2011)

EXPERIMENTAL COMPARISON OF RESISTANCE SPOT WELDING AND FRICTION-STIR SPOT WELDING PROCESSES FOR THE EN AW 5005 ALUMINUM ALLOY

EKSPERIMENTALNA PRIMERJAVA ODPORNOSTI PROCESOV TOČKOVNEGA VARJENJA IN TOČKOVNEGA TORNEGA VARJENJA PRI ALUMINIJEVI ZLITINI EN AW 5005

Mustafa Kemal Kulekci[1], Ugur Esme[1*], Onur Er[2]

[1]Mersin University Tarsus Technical Education Faculty, Department of Mechanical Education, 33480, Tarsus-Mersin, Turkey
[2]Kocaeli University, Department of Mechanical Engineering, 41380, Umuttepe/Kocaeli, Turkey
uguresme@gmail.com

Prejem rokopisa – received: 2011-05-11; sprejem za objavo – accepted for publication: 2011-07-13

Friction-stir spot welding (FSSW) is a solid-state welding process suitable for the spot joining of lightweight low-melting-point materials. The process is performed by plunging a rotating pin that creates a connection between sheets in an overlap configuration by means of frictional heat and mechanical work. In this study the tensile-shear-strength and hardness variations in the weld regions are discussed. The results obtained are compared with those derived from the application of traditional resistance spot welding (RSW). The experimental results of the study show that FSSW can be an efficient alternate process to electrical resistance spot welding.

Keywords: aluminium alloys, friction stir welding, friction stir spot welding, resistance spot welding, tensile shear strength

Torno mešano točkovno varjenje (FSSW) je proces, ki se odvija v trdnem in je primeren za točkovno spajanje lahkih kovin z nizkim tališčem. Pri tem postopku se z vrtečim se trnom, s toploto trenja in z mehanskim delom ustvari povezava med pločevino in konfiguracijo prekritja. Študija obravnava variacije natezne strižne trdnosti in trdote v območjih zvara. Dosežene rezultate smo primerjali s tistimi, ki so bili doseženi s tradicionalnim uporovnim točkovnim varjenjem (RSW). Rezultati preizkusov kažejo, da je lahko FSSW učinkovit altrenativen proces za električno točkovno uporovno varjenje.

Ključne besede: aluminijeve zlitine, torno mešalno varjenje, torno mešalno točkovno varjenje, uporovno točkovno varjenje, natezna strižna trdnost

1 INTRODUCTION

Friction-Stir Spot Welding (FSSW) is a derivative of Friction-Stir Welding (FSW), and has been gaining momentum since the beginning of this decade. Unlike FSW, FSSW can be considered as a transient process due to its short cycle time (usually a few seconds). Friction-Stir Spot Welding (FSSW) is a novel variant of the "linear" FSW process; it creates a spot, lap-weld without any bulk melting[1]. As indicated in **Figure 1**, during FSSW, the tool penetration and the dwell period essentially determine the heat generation, the material plasticization around the pin, the weld geometry and therefore the mechanical properties of the welded joint[1].

This technique has the same advantages as FSW. The advantages of FSW over fusion welding processes are the ease of handling, the joining of dissimilar materials and materials that are difficult to fusion weld, the low distortion, the excellent mechanical properties and the little waste or pollution. Hence, we envisage applying the technique the for joining of lightweight materials in order to achieve high performance and the energy and cost savings of machines and structures[3].

The rapid development of applications of lightweight materials in the automotive industry is reflected in the increasing use of aluminum alloys[4]. Many components produced from these alloys, by stamping, casting, extrusion and forging, have to be joined as a part of the manufacturing processes.

Resistance welding is one of the oldest of the electrical welding processes in use by industry today. The weld is made by a combination of heat, pressure and time. Mild or low-carbon steel comprises the largest percentage of material welded with the resistance spot welding process. All low-carbon steels are readily weldable with the process if the proper equipment and procedures are used[5]. The resistance welding of aluminium is more difficult than steel because of the characteristics of aluminium. The electrical conductivity of

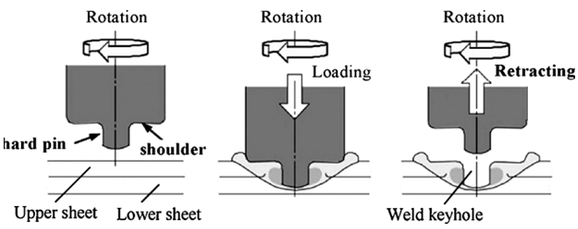

Figure 1: Schematic representation of FSSW process[2]
Slika 1: Shematičen prikaz procesa FSSW[2]

Table 1: Chemical and mechanical properties of the EN AW 5005 aluminum alloy[7]
Tabela 1: Kemična sestava v masnih deležih (*w*/%) in mehanske lastnosti aluminijeve zlitine EN AW 5005[7]

Chemical composition *w*/%	Fe	Si	Cu	Mn	Mg	Zn	Cr	Al
	0.45	0.3	0.05	0.15	0.5–1.1	0.2	0.1	Balance
Mechanical properties	Yield Strength (MPa)		Tensile strength (MPa)		Elongation (%)		Hardness (HV)	
	45		110		15		32	

aluminium is high, and welding machines must provide high currents and exact pressures in order to provide the heat necessary to melt the aluminium and produce a sound weld. A FSW of aluminium has several advantages over fusion-welding processes. Problems arising from the fusion welding of aluminium alloys, such as solidification cracking, liquation cracking and porosity, are eliminated with FSW, due to the solid-state nature of the process[6]. In this study, the hardness distribution and the tensile shear strength of RSW and FSSW welds in the EN AW 5005 aluminum alloy has been investigated based on our experimental results.

2 EXPERIMENTAL DETAILS

2.1 Workpiece material

The EN AW 5005 aluminum alloy was used as a workpiece material with a thickness of 1.5 mm. The specimens were machined out in 100-mm lengths and 25-mm widths. The specimens were overlapped with an area of 25 mm × 25 mm. The composition and mechanical properties of the workpiece material are listed in **Table 1**. **Figure 2** (a) and (b) schematically shows the resistance spot and FSSW welding processes.

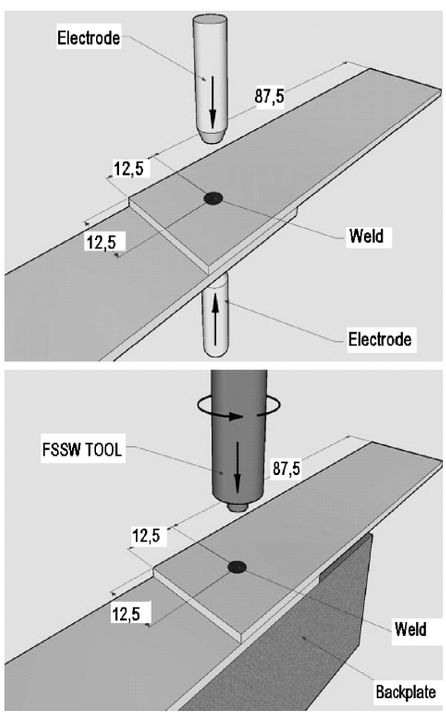

Figure2: Schematic representations of: (a) RSW process and (b) FSSW process
Slika 2: Shematičen prikaz: (a) proces RSW, (b) proces FSSW

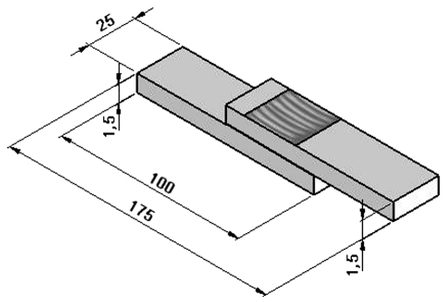

Figure 3: Dimensions of tensile shear test specimens
Slika 3: Dimenzije nateznih strižnih preizkušancev

The welded samples were loaded on an *INSTRON 8801* tensile testing machine with a load of 100 kN capacity. **Figure 3** shows the dimensions of the lap-shear specimen used to investigate the shear strength of the friction-stir spot weld and the resistance spot welds under shear loading conditions.

2.2 Tool Geometries and Welding Equipment

a) Resistance Spot Welding

Water-cooled copper is used as the electrode material. The electrode shape is flat-ended with a contact diameter of 4 mm. The experiments were performed on a resistance spot welding machine, which is a pneumatically operated, electronically current-and-timing controlled welding machine. The current values of the spot welding machine range from 5 kA to 50 kA. The pressure, applied through the pneumatic cylinder, can be controlled and adjusted according to the required value during the welding period. The applied pressure is measured and controlled with the help of a manometer, which is mounted on the valve section of the machine. The selected RSW parameters were taken as recommended in literature[8]. The parameters of the RSW were 2.5-kN electrode force, 30-kA welding current, holding time 10 periods, and welding time 7 periods. The experiments were performed by maintaining the type of

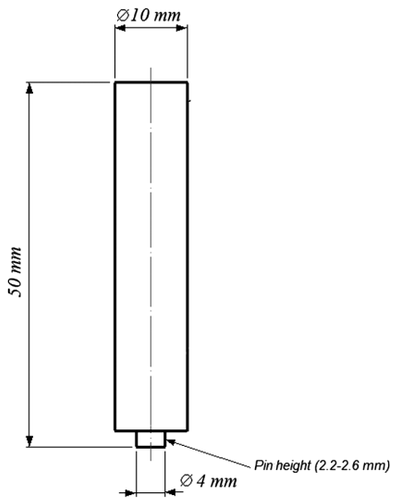

Figure 4: Tool geometry used in the FSSW process
Slika 4: Geometrija orodja, uporabljenega pri procesu FSSW

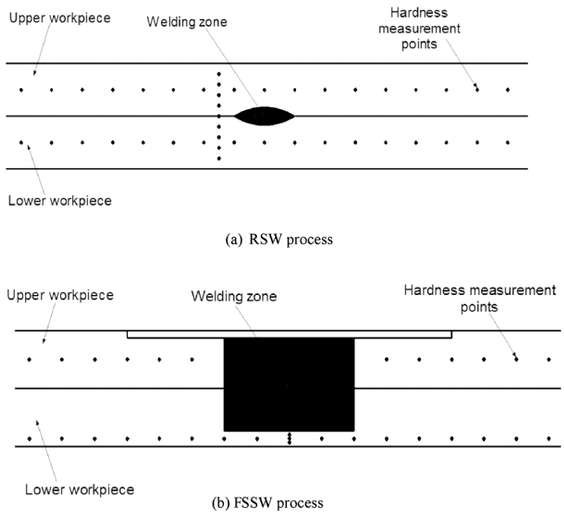

Figure 5: Hardness-measurement distribution
Slika 5: Porazdelitev izmerjenih trdot

electrode and tool materials, the water flow rate, the electrode nose geometry (flat ended) and the contact diameter constant, and then changing the other parameters.

b) Friction-Stir Spot Welding

AISI 1050 steel was used as the FSSW tool material. The tool was manufactured with the dimensions shown in Figure 4. The tool was hardened to 52 HRC before the welding applications. The pin height (h) was varied as 2.2 mm and 2.6 mm. The contact diameter of the tool was manufactured as 4 mm. The FSSW welding was performed on a CNC vertical milling machine.

In the FSSW process, parameter identification is still being investigated. In this study, the FSSW parameters were selected as given in **Table 2**.

Table 2: Welding parameters for the FSSW processes
Tabela 2: Varilni parametri za procese FSSW

Experiment No	Pin height (mm)	Tool rotation (r/min)	Welding time (s)	Tensile shear strength (MPa)
1	2.2	1500	5	70.27
2	2.2	1500	10	58.92
3	2.2	2000	5	70.86
4	2.2	2000	10	60.66
5	2.6	1500	5	68.21
6	2.6	1500	10	122.16
7	2.6	2000	5	102.70
8	2.6	2000	10	100.71

2.4 Microhardness

The hardness measurements were performed on a Vickers Microhardness Tester (HV_{50}). The measurements were taken at various points along the cross-section of the welded specimens. As shown in **Figure 5**, in order to eliminate the indentation effect, the readings were taken with 1-mm increments.

3 RESULTS AND DISCUSSION

3.1 Tensile Shear Strength

The maximum average tensile shear strength of the RSW and FSSW welded joints were 41.38 MPa and 122.16 MPa, respectively. The maximum tensile shear strength of the FSSW joint is 295 % higher than the RSW joint.

When experiments 3 and 7 were compared, it is clear that the tensile shear strength increased from 70.86 MPa to 102.70 MPa, as seen in **Figure 6**. The FSSW joints that were obtained with higher pin heights resulted in a higher tensile shear strength. These results can be explained by the larger volume of bonded materials as the pin height increases. Increasing the pin height has a positive effect on the tensile shear strength. These results

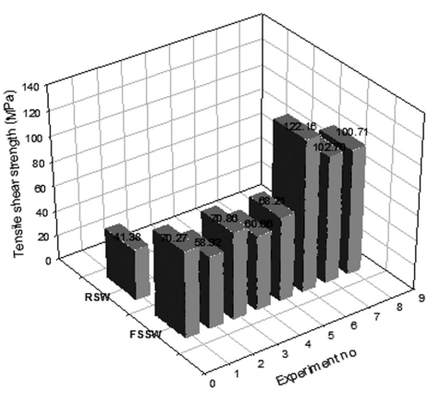

Figure 6: Comparison of the tensile shear strength of the RSW and FSSW welded joints
Slika 6: Primerjava natezne strižne trdnosti zvarov RSW in FSSW

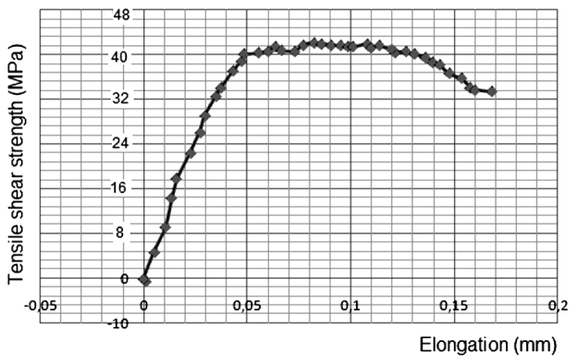

Figure 7: Tensile shear strength of RSW joints (Electrode force, 2.5 kN; welding current, 30 kA; holding time, 10 cycles; welding time, 7 cycles)

Slika 7: Natezna strižna trdnost zvarov RSW (sila elektrode 2,5 kN, varilni tok 30 kA, čas držanja 10 ciklov, čas varjenja 7 ciklov)

show that the stirring effect and the refined structure improve the mechanical properties of the FSSW joints. The tensile shear strengths of the FSSW joints reduced when the welding time increased from 5 s to 10 s. The experiments 1–2, 3–4, 7–8 verify this result. This situation can be explained by the statement of Kalpakjian et al.[9], i.e., there is a relation between the temperature, the time and the strength.

The graphical results of the tensile shear strength of the RSW and FSSW welded joints are given in **Figure 7** and **Figure 8**, respectively. The results of the tensile shear tests show that a 304 % improvement can be obtained with the FSSW process when compared with the RSW. The tensile strength of the FSSW joint is stronger than that of the RSW This strength improvement can be explained by the structure obtained with the FSSW process. The studies in the literature report that the microstructure of the FSSW is a refined structure, while the RSW welds have a cast structure[1,3]. The stirring effect and the refined structure improve the mechanical properties of the FSSW joint.

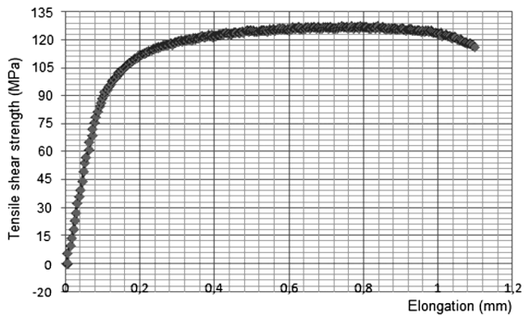

Figure 8: Tensile shear strength of FSSW joints (pin height, 2.6 mm; tool rotation, 1500 r/min; welding time, 10 s)

Slika 8: Natezna strižna trdnost zvarov FSSW (višina trna 2,6 mm, hitrost vrtenja trna 1500 r/min, čas varjenja 10 s)

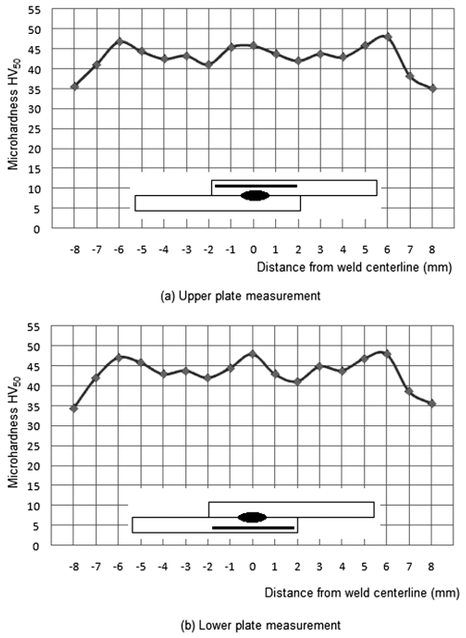

Figure 9: Microhardness distribution of RSW welded joints

Slika 9: Porazdelitev mikrotrdote v zvarih RSW

3.2 Microhardness

The microhardness of the base plates was measured to be 32 HV_{50}. The microhardnesses of the RSW and FSSW welded joints are given in **Figure 9** (a. upper

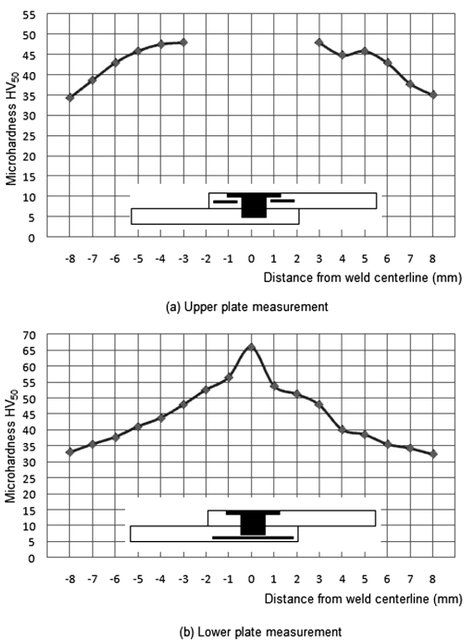

Figure 10: Microhardness distribution of FSSW welded joint (sample 6)

Slika 10: Porazdelitev trdote v zvaru FSSW (vzorec 6)

plate, b. bottom plate) and **10** (a. upper plate, b. bottom plate). The hardness of both of the RSW and FSSW were higher than the un-welded material. Plastic deformation during the joining processes increased the hardness of the welds, as seen in **Figure 9 and 10**. The average microhardnesses of the RSW and FSSW were 42 HV_{50} and 45 HV_{50}.

The hardness of the weld nugget was measured as 47 HV_{50} for the RSW. The hardness value of the upper and lower plates of the FSSW were measured as 48 HV_{50} and 65 HV_{50}, as seen in **Figure 9**. The reason for obtaining higher hardness value on the lower plate of the FSSW welded joints can be explained by the higher plastic deformation due to the higher pin-plunge distance. The increase in the hardness of the plates can be explained by the plastic deformation during the welding process. From the **Figure 10**, it is clear that there is more plastic deformation in the FSSW process than in the RSW process. The plastic deformation of the materials results in an increase in the strength and hardness[9].

4 CONCLUSIONS

In this work the mechanical properties of the friction-stir spot-welded overlap connections of the EN AW 5005 aluminum alloy material were investigated and compared with resistance spot welding. It can be concluded from this study that:

- Pin-height, tool-rotation and welding-time parameters affect the tensile shear strength of the FSSW joints,
- Pin height is the major factor that affects the tensile shear strength in the FSSW process. The welding time and tool rotation are the second and third, respectively, in the FSSW process,
- The tensile shear strengths of the FSSW welded joints are higher than those of the RSW welded joints,
- Tool rotation and welding time give better results when larger pin heights are used.
- Higher plastic deformation is obtained in the welding zone of the FSSW process than the RSW process,
- The hardness increase in the FSSW process is higher than in the RSW process,
- FSSW can be a more efficient alternate process the electrical RSW process.

5 REFERENCES

[1] H. Badarinarayan, Q. Yang, S. Zhu: Effect of tool geometry on static strength of friction stir spot-welded aluminum alloy, International Journal of Machine Tools & Manufacture, 54 (**2009**), 142–148

[2] Q. Yang, S. Mironov, Y. S. Sato, K. Okamoto: Material flow during friction stir spot welding, Mater. Sci. Eng. A., 2010, doi:10.1016/j.msea.2010.03.082

[3] Y. Tozakia, Y. Uematsub, K. Tokaji: Effect of tool geometry on microstructure and static strength in friction stir spot welded aluminium alloys, International Journal of Machine Tools & Manufacture, 47 (**2007**), 2230–2236

[4] D. A. Wang, S. C. Lee: Microstructures and failure mechanisms of friction stir spot welds of aluminum 6061-T6 sheets, Journal of Materials Processing Technology, 186 (**2007**), 291–297

[5] Handbook for resistance spot welding, Miller Electric Mfg. Co. Appleton, 2010

[6] Çam G., Güçlüer, S., Çakan, A., Serindağ, H. T., Mechanical properties of friction stir butt-welded Al-5086 H32 plate, Mat.-wiss. u. Werkstofftech, 40 (**2009**), 638–642

[7] T. Y. Pan, A. Joaquin, D. E. Wilkosz, L. Reatherford, J. M. Nicholson: Spot friction welding for sheet aluminum joining, in: Proceedings of the 5th International Symposium on Friction Stir Welding, Metz, France, 2004

[8] M. K. Kulekci, E. Kaluç, A. Şık, O. Basturk: Experimental comparison of mig and friction stir welding processes for en AW-6061- T6 (AlMg1SiCu) aluminum alloy, The Arabian Journal for Science and Engineering, 35 (**2010**), 321–330

[9] S. Kalpakjian, S. Schmid: Manufacturing, Engineering & Technology, fifth edition, 2009

UDK 669.018.9:539.3
Original scientific article/Izvirni znanstveni članek

ISSN 1580-2949
MTAEC9, 45(5)401(2011)

THE FRICTION AND WEAR BEHAVIOR OF Cu-Ni_3Al COMPOSITES BY DRY SLIDING

TRENJE IN OBRABA Cu-Ni_3Al KOMPOZITOV PRI SUHEM DRSENJU

Mehtap Demirel[1], *Mehtap Muratoglu[2]

[1]Vocational High School, Adiyaman University, 02040 Adiyaman, Turkey
[2*]Department of Metallurgy and Material Engineering, Engineering Faculty, Firat University, 23119 Elazig, Turkey
mehtug@firat.edu.tr

Prejem rokopisa – received: 2011-03-14; sprejem za objavo – accepted for publication: 2011-08-10

The suitability of Ni_3Al intermetallics as reinforcements for Cu-base materials in tribological applications has been studied. For this purpose, Cu/Ni_3Al (5 wt %, 10 wt % and 15 wt %) composites were prepared by powder-metallurgy techniques and tested on a pin-on-ring apparatus. The effects of the applied load (83–150 N) at a constant sliding velocity of 0.4 m/s on the wear behaviour of Cu-Ni_3Al composites and wear mechanisms during dry sliding were investigated. The worn surfaces were examined by scanning electron microscopy (SEM) and energy-dispersive spectrometry (EDS). It was found that with increasing applied load, the weight loss of the composites increased to levels comparable to those of an unreinforced Cu matrix. In addition, the weight loss increased with the weight percentage of Ni_3Al particles. The coefficients of friction for the composites increased with the increasing of the applied load and increased with increasing the weight percentage of the Ni_3Al particulates. For a Cu-15wt % Ni_3Al composite the weight fraction of reinforcement was critical, as it showed the highest wear rate for all the applied loads.

Key words: metal-matrix composites; Ni_3Al; copper; wear; coefficient of friction

Raziskana je bila primernost za tribološko uporabnost kompozitov Cu-Ni_3Al. Pripravljeni so bili kompoziti (s 5 mas %, 10 mas % in 15 mas %) s tehnologijo metalurgije prahov in preizkušeni na konica – na-obroč napravi.

Raziskani so bili učinki obremenitev (83-150 N) pri konstantni hitrosti drsenja 0,4m/s na obrabo Cu-Ni_3Al in mehanizmi obrabe pri suhem drsenju. Obrabljene površine so bile pregledane v vrstičnem elektronskem mikroskopu (SEM) in analizirane v energijskem spektrometru (EDS). Ugotovljeno je bilo, da se je s postopnim povečanjem obremenitev izguba teže kompozitov povečala na raven primerljivo z neojačano Cu-matico. Izguba teže se je povečala s povečanjem vsebnosti Ni_3Al delcev. Pri Cu-15mas% Al_2O_3 kompozitu se je pokazala kot kritična vsebnost ojačitve z največjo obrabo pri vseh obremenitvah. Koeficient trenja kompozitov se je večal pri večanju obremenitve in še posebej pri večanju vsebnosti Ni_3Al.

Ključne besede: kovinski kompoziti, Ni_3Al, baker, obraba, koeficient trenja

1 INTRODUCTION

The development of metal-matrix composite (MMC) materials in recent years has been one of the most important in the field of materials. Among them, particulate composites are widely used due to the simplicity of their manufacturing. Specifically, MMCs are among the most promising materials for wear-resistant and structural applications, and the use of different possible reinforcement particles was proposed [1].

Metal-matrix composites show a combination of superior mechanical properties, such as a better elastic modulus, tensile strength, and high-temperature stability in comparison with an unreinforced matrix, yet they suffer from poor tensile ductility, fatigue-crack growth resistance and fracture toughness. The sliding wear of the composites is a complex process involving not only mechanical but also thermal and chemical interactions between the surfaces in contact [2]. Particle-reinforced metal-matrix composites are recognized as having a better wear resistance due to the presence of hard particles. These materials can be used as a reinforced part in pistons and in several wear-resistance applications [3,4]. In addition, the wear resistances of these materials are applied in internal combustion engines, as brake rotors, or in the study of the problem of die wear during the extrusion of the metal matrix composites [2]. The tribological behaviour of MMCs depends on the type of MMCs, the counter-face materials and the contact situation.

Cu-matrix composites have demonstrated a superior combination of thermal/electrical conductivity and strength, and exhibit a significant increase in the mechanical properties and an improvement in the tribological properties [5–7]. These attractive properties make such composites promising for sliding electrical contact applications where high electrical and thermal conductivity and good wear resistance are required. More recent studies have considered the possibility of adding intermetallics as a reinforcement, which seems to be a highly interesting option in terms of wear [8]. Ni_3Al is probably one of the best known and characterized intermetallics [9]. Its processing using powder metallurgy provides structural materials with high strength and reliability [10]. Nickel aluminide-based intermetallic compounds have low density, good oxidation resistance and metal-like

properties, which makes them attractive materials for a wide range of applications [11,12]. The information presented in the previous paragraphs indicates that the wear behaviour and wear mechanisms of Ni_3Al-reinforced metal matrix composites, especially Ni_3Al/Al matrix composites, are starting to be understood. However, the friction and wear behaviour of Cu matrix composites reinforced with Ni_3Al have not received the attention they deserve. A better understanding of these composites will open the door to the design of new materials that are promising for sliding electrical contact applications where high electrical and thermal conductivities and a good wear resistance are required. So, the present work aims to investigate systematically the influence of load on the dry sliding wear behaviour of Cu-Ni_3Al powder metallurgical composites.

2 MATERIAL AND EXPERIMENTAL PROCEDURE

2.1. Materials

Commercial Cu powder supplied by Merck with an average size of <63 μm was used as matrix and Ni_3Al particles supplied by Alfa (USA) with a mean size of <149 μm were used as the reinforcement. The particle-reinforced composites contained 5, 10 and 15 wt. % Ni_3Al and were fabricated by powder metallurgy (PM) techniques. The powders were mixed for 30 min. and after mixing, the powder mixtures were uniaxially cold pressed at 350 MPa and sintered at 900 °C for 30 min in an Ar atmosphere. The dimensions of the cylindrical specimens were a diameter of 12 mm and a height of 7.5 mm. The SEM in **Figure 1** illustrates a typical microstructure of the Cu-Ni_3Al composite prepared by the powder metallurgy route. This Cu-Ni_3Al composite exhibits a well-dispersed distribution of Ni_3Al particles. The bulk hardness measurements were made using a Brinell hardness tester, with a contact pressure of 15 g. The results of the hardness test on the composites are listed in **Table 1**. The hardness of the composites is much higher than that of the unreinforced Cu-matrix and it clearly increases with an increasing Ni_3Al weight percentage.

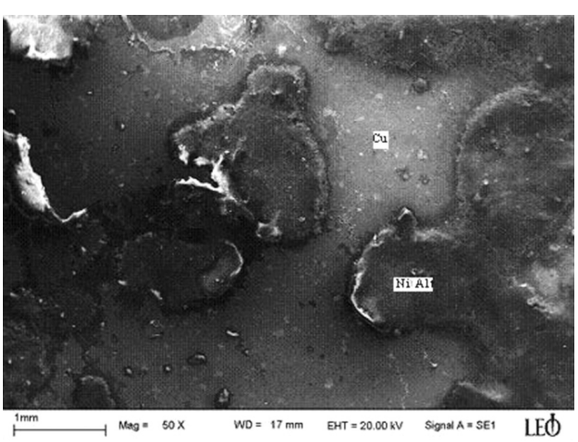

Figure 1: SEM images of a metallographic section of the Cu-10 wt % Ni_3Al composite.
Slika 1: SEM slika Cu-10 wt % Ni_3Al kompozita

Table 1: The macrohardness of the unreinforced Cu and Cu-Ni_3Al composite specimens
Tabela 1: Makrotrdota neojačanega Cu in Cu-Ni3Al kompozitov pri dolžini drsenja 1500 m in hitrosti drsenja 0,4 m/s.

Specimen	Average macrohardness (HB)
Unreinforced Cu	70
Cu-5 wt. %Ni_3Al	75
Cu-10 wt. %Ni_3Al	77
Cu-15 wt. %Ni_3Al	80

2.2 Friction and wear tests

Sliding-wear and friction tests were performed using a pin-on-ring apparatus with the composite specimen serving as the pin under dry conditions. A schematic diagram of the experimental arrangement is shown in **Figure 2**. The dry-sliding wear tests were carried out at a constant sliding velocity of 0.4 m/s and a constant temperature of 25 °C within an applied normal load in range of 83–150 N. Steel rings with a diameter of 35 mm were used as the counter-face. The counterparts in the experiments were fabricated from AISI 1050 steel as a ring which was hardened to a value of HRC 55. Prior to the tests, the contact surfaces of the composite specimens were polished using 600-, 800-, 1000- and 1200-grit SiC emery paper in running water. The specimens and rings, ultrasonically cleaned and washed in acetone, were weighed to the nearest 0.1 mg using an electronic analytical balance before and after each wear test. The coefficients of friction were obtained periodically by measuring the force on the specimen using a strain-gauge bridge. The microstructures of the specimens were examined by scanning electron microscopy (SEM) and energy-dispersive microanalyses (EDS).

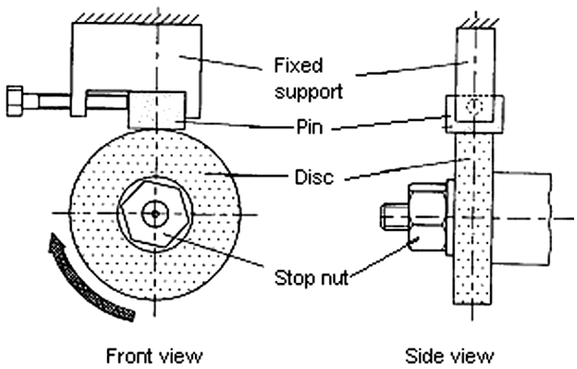

Figure 2: Schematic diagram of pin-on-ring apparatus.
Slika 2: Shematični prikaz trn-na-obroču

3 RESULTS AND DISCUSSION

The relationship between weight loss and load for various reinforcement (Ni_3Al) amounts within the sliding distance of 1500 m is given in **Figure 3**. and shows that the weight loss of all the composite specimens increased with the increasing weight percentage of intermetallics. All types of specimens suffered small weight losses after testing for the lower loads, with the exception of the Cu-15 wt. % Ni_3Al specimen. For loads of 83 and 100 N, Cu- %5 and -%10 wt. The Ni_3Al composite specimens exhibited superior wear resistance to the unreinforced Cu specimens. However, at 150 N, the reverse was true. The weight losses of the Cu-15 wt. % Ni_3Al specimen was close to that of the unreinforced Cu at 100 N. It increased with increasing load and showed the highest weight loss among all the specimens. The wear behaviour could lead to the conclusion that the Ni_3Al particles do not improve the wear resistance of pure Cu at the highest load (150 N). This reveals that Ni_3Al-particle-reinforced Cu matrix composites have the ability to increase the wear resistance for the lower loads (83 and 100 N). The hardness of the Ni_3Al particle is larger than that of the Cu, and the particle can keep the structural integrity of the composite at low loads. When the load is increased to reach the fracture strength of the particles, the particles began to fracture[3] and to increase the intensity of wear. For particle-reinforced composites, the particles near the contact surface may more readily induce the nucleation of cracks due to the interface debonding between the particles and the matrix in comparison to the unreinforced Cu. In the sliding wear process, these cracks may propagate and connect to form subsurface cracks. In this way, the subsurface damage process is increased by the presence of particles [3]and for all applied loads, the weight loss of the Cu-15 wt. % Ni_3Al composite is higher than that for other tested materials. Thus, the wear behaviour leads to the conclusion that Ni_3Al particles do not improve the wear resistance of the Cu matrix with the highest load (150 N).

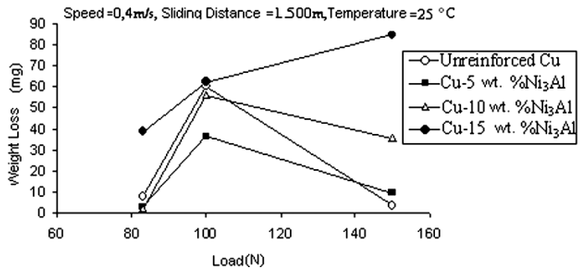

Figure 3: Variation of weight loss with load for all the specimens tested for a sliding distance of 1500 m and a sliding speed of 0.4 m/s.
Slika 3: Variacija izgube teže z obremenitvijo za vse preizkuse pri razdalji drsenja 1500 m in hitrosti 0,4m/s

Figure 4a and b show SEM images of the worn unreinforced specimen surfaces at loads of 83 and 150 N. At low load the surface exhibited a plastic flow occurring because of the adhesion in the wear surface of

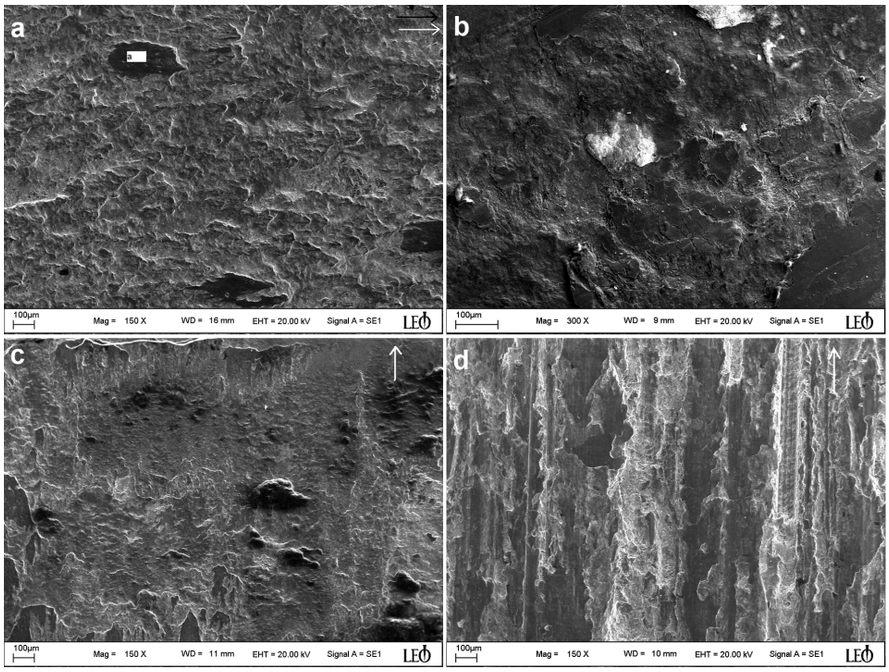

Figure 4: SEM images of the worn surfaces: (a) unreinforced Cu matrix tested at 83 N; (b) unreinforced Cu matrix tested at 150 N; (c) Cu-10 wt % Ni_3Al composite tested at 83 N; and (d) Cu-10 wt % Ni_3Al composite tested at 150 N. The arrow indicates the sliding direction.
Slika 4: SEM slike obrabljene površine: (a) neojačana Cu matica testirana pri 83 N, (b) neojačana Cu matica pri 150 N, (c) Cu-10 wt % Ni_3Al kompozita pri 83N, (d) Cu-10 wt % Ni_3Al kompozit pri 150 N. Puščica prikazuje smer drsenja.

the unreinforced Cu. The delamination, which is a common wear mechanism, was progressive. In addition, adhesive wear predominates because of the tear areas with large ripples were mostly present. As the load was increased, the occurrence of tear areas with large ripples at the highest load was not observed and large areas with large smooth grooves appeared. This explains why the weight loss of the specimen worn at 83 N was higher than that of the specimen worn at 150 N (the reason is explained with EDS results in a later paragraph). The SEM micrographs of the worn surface of Cu-10 wt. % Ni_3Al composite are presented in **Figure 4c and d**. The wear mechanisms involving plastic deformation, ripple layers and the pulling out of particles at applied loads is observed and the delamination also progressed, and at 150 N the composite surface exhibited extensive grooving, most probably produced by ploughing with the harder asperities, which pulled out the composite on the counter surface, and also showed abrasive wear characterization. On the other hand, compared with the unreinforced Cu matrix, the local plastic deformation on the worn composite surface was reduced at 83 N (nearly the same as 83N with the Cu-5wt. % Ni_3Al composite specimen). The surface was smoother than the unreinforced Cu matrix, but was still covered with grooves. The composite worn surface at 150N was generally rougher than that of the surface at 83 N.

For the composites investigated, the most important feature is the presence of Ni_3Al particles, whose hardness (HV 381) is much greater than the Cu matrix and lower than that of the steel counterpart. During the sliding wear process, the Cu-matrix surrounding them was rapidly worn away and all the contact was essential between the Ni_3Al particles and the steel counterpart [16]. The sliding wear imposed a substantial tangential force on the Ni_3Al particles in contact with the counterpart and the resulting shear stress at the particle-matrix interface. Generally, increasing the contact pressure tends to increase the shear stress. At low loads, the shear stress was too small to debond or pull out the Ni_3Al particles from the Cu-matrix or deform the matrix plastically causing cracks. So, the wear rate of composites was controlled by the wear rate of the more wear-resistant Ni_3Al phase. Thus, the wear losses of the composites were mainly dependent on the level of the applied load and the weight percentage of Ni_3Al particles. Compared with the unreinforced Cu matrix, the local plastic deformation on the worn surface (**Figure 4c, d**) was greatly reduced. This suggests that the extent of the wear was reduced by the presence of Ni_3Al, presumably because of the reduced driving force for the reaction between this phase and the counter surface. For the investigated specimens the wear surface showed a predominantly adhesive wear at the lower load (small ripples with craters) and changes to a predominantly abrasive-adhesive wear at the higher loads (large smooth areas with long grooves).

In **Figure 5** the EDS results of the worn surface of the unreinforced Cu specimen tested at 83–150 N and that of the worn surface of Cu-10 wt. % Ni_3Al composite specimen tested at 83–150 N are shown. For both loads, the EDS spectra indicated that the specimens also contained Fe and O. The higher intensity of the Fe indicates the transfer of counter-face materials to the surface of the specimens (see also **Figure 4a**). Fe and O was present in both materials, but in much greater quantities at the highest load for composite specimens, while at 150N the reverse was true for the unreinforced Cu specimen. The concentration of Ni for the composite specimen also showed some increase, reflecting the fact that worn Ni_3Al fragments spread onto the surface. The wear products coming either from the counter-face (Fe-rich oxides) or the worn surface itself penetrate into the Cu matrix. This leads to the formation of a mechanically mixed tribolayer (MML) that is basically made up of oxide particles and Cu [13,14]. Further work, including a detailed examination of the MML layer with TEM, is underway to identify the wear mechanisms and the wear results, and this will be reported at a later date. In addition, by the transfer of Fe from the counter-face to

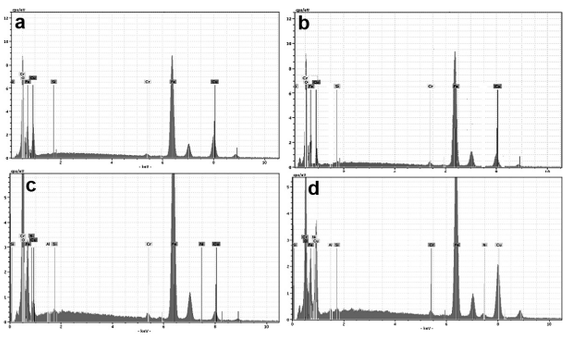

Figure 5: (a) EDS spectra of areas (labelled by "a ") of the worn surface of the unreinforced Cu specimen tested at 83 N, (b) EDS

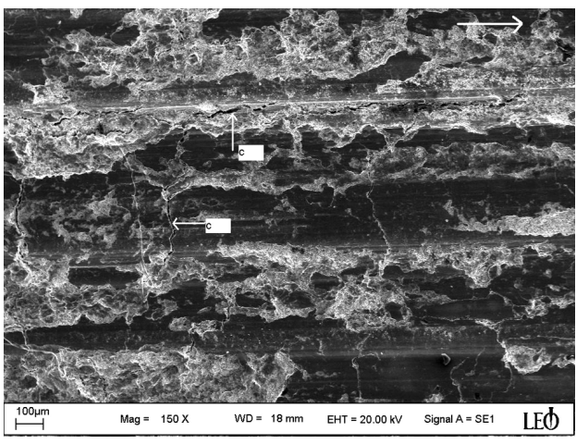

Figure 6: SEM images of the worn surfaces of Cu-15 wt. % Ni_3Al composite at 150 N ("c " showed cracks). The arrow indicates the sliding direction.

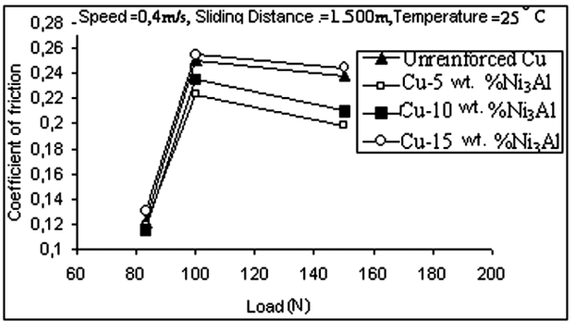

Figure 7: The coefficient of friction of unreinforced Cu and the composites for a sliding distance of 1500 m and a sliding speed of 0.4 m/s.
Slika 7: Koficient trenja neojačanega Cu in kompozitov z obremenitvijo pri drseči razdalji 1500 m in pri hitrosti drsenja 0.4 m/s.

the matrix severe plastic deformation was observed in the matrix around these particles (Fe-rich regions labelled as "a" in **Figure 4a**).

On the other hand, at a high applied load (150 N), it showed that increasing the weight percentage of the Ni_3Al particulates tends to cause an increasing weight loss of the composite (see **Figure 3**). Increasing the weight percentage of the Ni_3Al particulate causes a reduction in the extent of the plastic deformation of the matrix, and increasing the load tends to cause extensive plastic deformation of the matrix, and an increase in the number of cracks formed at the particulate-matrix interface due to poor cohesion that can cause particle decohesion. Due to the occurrence of work-hardening of the plastic deformation in the subsurface materials, cracks nucleated around the reinforcement particulate. Under repeated loading and deformation, these cracks propagated in the matrix (see **Figure 6**). This situation then occurred in the Cu-15 wt % Ni_3Al composite specimen. Eventually, the propagating cracks joined, causing the particles to pull out. The detached particles would also cause severe abrasive wear against the composite. **Figure 6** clearly revealed grooves (as "g") and to some extent cracks, which are parallel and perpendicular to the sliding direction (indicated by arrow as "c") and severely damaged regions on the worn surface of the Cu-15 wt.% Ni_3Al composite at 150 N. The wear rate of the composites containing a high volume fraction of particulate increased considerably under the high-contact-pressure conditions when applying a high load (150N). In the present tests, the results show that all the applied test loads are high for the Cu-15 wt. % Ni_3Al composite specimens.

The results of the coefficient of friction for unreinforced Al and the composites with different applied loads are shown in **Figure 7**. The coefficients of friction for the composites, with the exception of the Cu-15 wt. % Ni_3Al composite, were lower than those for the unreinforced Cu matrix. With an increasing volume fraction of Ni_3Al particulate, the coefficient of friction for the composite increased, especially at high loads (100 N and 150 N). The coefficient of friction for all the materials increased with increasing load. This result is in good agreement with the results in references [15,16]. In fact, the friction coefficient is in general determined by two contributions: the first due to the adhesive interaction between the contacting asperities and the second related to the ploughing contribution due to abrasion [16]. At high loads the contribution of the adhesion increased in importance because the greater hardness reduced the contribution of the abrasion, and the friction coefficient is increased with the load because of the increase in the real area of contact. In reality, the sliding wear will impose a substantial tangential force on the particles in contact with the steel counter surface and the resulting shear stress at the particle-matrix interface can cause particle decohesion. Thus, the wear rate will be largely controlled by the rate at which particles decohere. The effect of the shear stress is related to the friction coefficient: if the friction coefficient is low, the effect of the shear stress is low [17]. However, if the particle decohesion is easy, the contact will be between the copper matrix and the steel counter surface, and the wear rate of the composite will be comparable or even greater. Since loose hard particles can cause third-body abrasion, the friction coefficient will be high. This situation, in the present experiments, was progressive for the Cu-15 wt. % Ni_3Al composite specimens. The friction coefficient of those specimens was higher than that of the unreinforced Cu matrix for all the loads.

4 CONCLUSION

Based on the friction and wear studies for dry sliding between unreinforced Cu/Ni_3Al composites and a GCr15 steel counterpart, the following conclusions were drawn.

1. At all loads the weight loss of the composites increased with an increasing weight percentage of Ni_3Al particulate. At low loads, the wear resistance of the Cu-5% and -10 wt. % Ni_3Al composites are about an order of magnitude better than that of unreinforced Cu, which is attributed to the wear of the copper matrix directly with the steel. On the other hand, due to the poor interfacial bonding between the particles and the matrix, the Cu-15 wt. % Ni_3Al composite showed a critical weight fraction of reinforcement, and the wear results indicate that the highest wear rate was observed for the Cu-15 wt. % Ni_3Al composite specimens for all the applied loads.

2. For composite materials, a significant amount of Fe (from the counter-faces), Ni, O particles is incorporated into the Cu matrix, forming a wear surface, with its Fe, Ni, O content increasing with load.

3. The coefficients of friction for the composites were increased with increasing the applied load from 83 N to 100 N, and continued nearly with same rate to 150 N. In this relation, the coefficient of friction for the composites

also increased with increasing the weight percentage of the Ni_3Al particulate. The highest friction coefficient was observed for the Cu-15 wt. % Ni_3Al composite specimens in all the test specimens.

The overall wear tests and results presented in this manuscript for the Cu-Ni_3Al composite was made of studies of the wear of the MMC up to this time. So, an explanation of wear mechanisms mentioned in the paper matched with other studies made on other metal matrix composites labelled as references in the paper. But the results may not be matched with the other results related to MMCs.

Acknowledgements

The authors would like to acknowledge the Firat University Research Fund (FUBAP- 1209) for financial support throughout this study.

5 REFERENCES

[1] Da Costa, C. E., Torralba, J. M., Velasco, F., Mechanical, intergranular corrosion,and wear behavior of aluminum-matrix composite materials reinforced with nickel aluminides, Metallurgical and Materials Transactions A 33A (**2002**), 3541–3553

[2] A. T. Alpas, J. Zhang, Effect of microstructure (particulate size and volume fraction) and counterface material on the sliding wear resistance of particulate-reinforced aluminum matrix composites, Metallurgical and Materials Transactions A 25A , (**1994**), 969–982

[3] R. Chen, A. Iwabuchi, T. Shimizu, H. S. Shin, H. Mifune, The sliding wear resistance behavior of NiAl and SiC particles reinforced aluminum alloy matrix composites, Wear 213 (**1997**), 175–184

[4] M. Muratoglu, M. Aksoy, the effects of temperature on wear behaviours of Al- Cu alloy and Al-Cu-SiC composite, Materials Science and Engineering A, 282 (**2000**) 1–2, 91–99

[5] J. D. Verhoeven, F. A. Schmidt, E. D. Gibson, W. A. Spitzig, Copper-refractory metal alloys, J. Metals, (**1986**), Sept., 20–24

[6] H. L. Downing, J. D. Verhoeven, E. D. Gibson, The emissivity of etched Cu-Nb in situ alloys, J. Appl. Phys. 61 (**1987**) 7, 2621–2625

[7] P. D. Funkenbusch, T. H. Courtney, D. G. Kubisch, Fabricability of and microstructural development in cold worked metal matrix composites, Scripta Metall. 18 (**1984**), 1099–1104

[8] Z. Chen, P. Liu, J. D. Verhoeven, E. D. Gibson, Sliding wear behavior of deformation-processed Cu-15 vol.% Cr in situ composites, Wear 195 (**1996**) 1–2, 214–222

[9] J. L. Gonza´lez-Carrasco, F. Garci´a-Cano, G. Caruana, M. Lieblich, Aluminum / Ni_3Al composites processed by powder metallurgy, Materials Science and Engineering: A 183, (**1994**), L5–L8

[10] P. Pérez, J. L. González-Carrasco, G. Caruana, M. Lieblich, P. Adeva, Microstructural characterization of P/M Ni_3Al consolidated by HIP, Materials Characterization, 33 (**1994**), 349–356

[11] P. Pérez, J. L. González-Carrasco, P. Adeva, Influence of the powder particle size on tensile properties of Ni_3Al processed by rapid solidification and hot isostatic pressing, Materials Science and Engineering A, 199 (**1995**), 211–218

[12] D. B. Miracle, Overview No. 104 The physical and mechanical properties of NiAl, Acta Metallurgica et Materialia, 41 (**1993**), 649–684

[13] A. E. Anderson, Friction and wear of automobile brakes, ASM Handbook, 18 (**1992**), 569–577

[14] G. Strafellini, M. Pellizzari, A. Molinari, Influence of load and temperature on the dry sliding behaviour of Al-based metal-matrix-composites against friction material, Wear 256 (**2004**), 754–763

[15] R.D. Neobe, R.R. Bowman, M.V. Nathal, Int. Mater. Rev. 38 (**1993**), 193

[16] J. P. Tu, L. Meng, M. S. Liu, Friction and wear behavior of Cu-Fe_3Al powder metallurgical composites in dry sliding, Wear, 220 (**1998**), 72–79

[17] Y. Wang, W.M. Rainforty, H. Jones, M. Lieblich, Dry wear behaviour and its relation to microstructure of novel 6092 aluminium alloy-Ni_3Al powder metallurgy composite, Wear 251 (**2001**), 1421–1432

UDK 621.791:669.715
Original scientific article/Izvirni znanstveni članek

ISSN 1580-2949
MTAEC9, 45(5)407(2011)

WELDABILITY OF METAL MATRIX COMPOSITE PLATES BY FRICTION STIR WELDING AT LOW WELDING PARAMETERS

VARIVOST PLOŠČ KOMPOZITA S KOVINSKO OSNOVO PO VRTILNO TORNEM POSTOPKU PRI NIZKIH VARILNIH PARAMETRIH

Yahya Bozkurt

Marmara University, Technical Education Faculty, Department of Materials Technology, 34722, Göztepe - Istanbul / Turkey
ybozkurt@marmara.edu.tr

Prejem rokopisa – received: 2011-09-15; sprejem za objavo – accepted for publication: 2011-09-21

Metal matrix composites (MMCs) are engineering materials that their increasingly replacing of a number of conventional materials in automotive, aerospace, and sports industries is driven by the demand for lightweight, high specific strength and stiffness. Their wide application as structural materials needs proper development of suited joining processes. Friction stir welding (FSW) is a fairly new solid state welding process for joining metals using thermal energy produced from localized friction forces.

In this study, the weldability of AA2124 containing (volume fractions) 25 % of SiC particles with T4 heat treated aluminum MMC plates was investigated at low welding parameters by FSW process. Microstructure, ultimate tensile strength, surface roughness and microhardness determination have been carried out to evaluate the weld zone characteristics of friction stir welded MMC plates. The FSW specimens were tested without post-weld heat treatment or surface modification. The temperature dissipation at the distance of 15 mm from the weld center was also measured using K-type thermocouples to demonstrate the FSWed joining without melting. Because of microstructural modification, improvement of microhardness of the stir zone was observed in comparison to the base composite. Ultimate tensile tests indicated a joint efficiency of approximately 73 %.

Keywords: metal matrix composites, friction stir welding, welding parameters, microstructure

Kompoziti s kovinsko osnovo (MMCs) so inženirski material, ki vse bolj nadomešča številne konvencionalne materiale v avtomobilski, letalski in v športnih industrijah, pri tem pa se pojavlja veliko povpraševanje po manjši specifični masi ter visoki trdnosti in togosti. Za široko uporabo je potreben pravilen razvoj ustreznih postopkov varjenja. Vrtilno torno varjenje (FSW) je dokaj nov način za spajanje kovin v trdnem stanju s toplotno energijo, ki jo ustvarja trenje.

Raziskana je bila varivost kompozita AA2124 z volumenskim deležem 25 % SiC-delcev s T4 toplotno obdelano MMC-ploščo aluminija pri nizkih parametrih FSW-varjenja. Mikrostruktura, natezna trdnost, hrapavost površine in mikrotrdota so bile določene za ovrednotenje značilnosti območja zvara. Preiskani FSW-vzorci niso bili toplotno ali površinsko obdelani. Temperatura je bila izmerjena na oddaljenosti 15 mm od centra vara s K-termoelementom, da bi dokazali FSW-spoj brez taljenja. Zaradi spremembe mikrostrukture so bile izboljšane mikrotrdota v mešanem v primerjavi s tisto pri osnovnem kompozitu. Natezna trdnosti vara je dosegala približno 73 % trdnosti plošče.

Ključne besede: kompoziti s kovinsko osnovo, vrtilno torno varjenje, parametri, mikrostruktura

1 INTRODUCTION

Aluminium and its alloys are used commonly in aerospace and transportation industries because of their low density and high strength to weight ratio. Especially Al-based Metal Matrix Composites (MMC) exhibit high strength, high elastic modulus, and improved resistance to fatigue, creep and wear; which make them promising structural materials for many industries.[1] The high cost of current MMCs compared to aluminum alloys has inhibited production on a large industrial scale.[2] Aluminium 2124 alloy is a high strength wrought alloy generally used in aerospace industry for making structural components. Addition of high wear resistant ceramic particles, such as SiC, Al_2O_3, AlN, B_4C, TiC to the alloy is expected to increase the mechanical properties considerably. These MMCs suffer from the disadvantage of low ductility which is due to different reasons, like brittle interfacial reaction products, poor wettability, particle-matrix debonding or presence of porosity or particle clusters.[3, 4] The welding of aluminum and its alloys has always represented a great challenge for designers and technologists.[5] One of the main limitations for the industrial applications of these alloys are the difficulty in using conventional welding methods for joining. The disadvantages associated with the fusion welding of these composites include: (a) incompatible mixing of the base and filler materials, (b) presence of porosity in the fusion zone, (c) excess eutectic formation and (d) formation of undesirable deleterious phases.[6] With the aim to obtain high quality welds, MMC has recently been widened by employing solid state welding process, in which joining is obtained at temperatures substantially below the melting point of the base material.[7] In the FSW process, a special tool mounted on a rotating probe travels down through the length of the

base metal plates in face-to-face contact; the interference between the welding tool and the metal to be welded generates the plastically deformed zone through the associated stirring action. At the same time, a thermo-mechanical plasticized zone is produced by friction between the tool shoulder and the top plate surface and by contact of the neighboring material with the tool edges, inducing plastic deformation. No melting takes place in the weld zone during FSW.[8] As result, the joint is produced in solid state. Due to this feature, FSW has emerged as a promising technique for joining of MMCs.[9]

FSW has attracted considerable attention in the industrial world due to its many advantages and has been successfully applied to the joining of various types of Al[10, 11], Cu[12,13], Ti[14], Mg[15], Fe[16] and different alloys[17,18] The applicability of friction stir welding to join aluminium MMCs reinforced with ceramic particles has been investigated by several authors.[8,19,20]

In this study, Friction stir welded joints on a AA2124 with 25 % (volume fractions) of SiC particles MMC plates were obtained using low welding parameters. The microstructure, microhardness profile, surface roughness, and tensile properties of the welds were examined. The objective of the present study was to clarify how the welding parameters are related to the mechanical properties of AA2124/SiC/25p-T4 MMC joints.

2 EXPERIMENTAL PROCEDURE

The plates used in this study are AA2124-T4 alloy matrix MMC strengthened with 25 % SiC particles (AA2124/SiC/25p-T4). This material was supplied by Aerospace Metal Composite Limited (UK) in form of billet with size of 400 mm × 260 mm × 50 mm. The MMC material was produced by powder metallurgy and mechanical alloying techniques followed by hot forging and tempering to T4 condition (solution heating at about 505 °C for 1 h, quenching in 25 % polymer glycol solution and room temperature aging for >100 h). The ultimate tensile strength of the base AA2124/SiC/25p-T4 MMC is of 454 MPa. The chemical composition of the AA2124/SiC/25p-T4 MMC was in mass fractions: Al-3.86 Cu-1.52 Mg-0.65 Mn-0.17 Si (%).

MMC plates of 130 mm × 50 mm × 3 mm size were cut from this billet by electro-discharge machining (EDM) technique with a feeding rate of 2 mm/min. The AA2124/SiC/25p-T4 MMC plates were friction stir butt welded using an FSW adapted numeric controlled milling machine. The FSW tool was of high speed steel with shoulder and probe diameter 22 mm and 6 mm, respectively. The tool was tilted by 2° with respect to *Z*-axis of milling machine and rotated in clockwise direction chosen according to the optimum results obtained at high welding parameters of AA2124/SiC/25p-T4 MMC joints.[8] FSW process was carried out at the tool rotation speed of 450 rpm and tool traverse speed of 40 mm/min. This welding parameters were optimized after preliminary welding tests for weldability of metal matrix composite plates at low welding parameters. Scanning electron microscopy (SEM) and energy dispersive spectroscopy (EDS) observations were conducted on JEOL JSM-5910LV.

Temperature measurements were made during the butt welding with eight gage K-type thermocouples with a diameter of 3 mm. Holes of 3 mm diameter and 2 mm depth were drilled 15 mm away from the centerline of the weld. Four of the thermocouples embedded on the advancing side and the others embedded on the retreating side with (10, 45, 85, and 120) mm intervals as in Ref. [8].

The specimens were polished using conventional polishing methods and chemically etched. Numerous Vickers microhardness measurements ($HV_{0,5}$) were performed on the transverse cross-sections of welded joints at the centerline with a 1 mm interval using a 500 g load for a dwell time of 20 s to determine the hardness variations across the joints.

The modification of surface roughness induced by the FSW process was evaluated by means of Mitutoyo Suftest-211 for the side in contact with the shoulder. The tensile tests were carried out at room temperature according to ISO/TTA2 standard[21] by an universal type tensile test machine to determine the tensile properties of the joints. At least three specimens were tested under the same conditions to guarantee the reliability of the results.

3 RESULTS AND DISCUSSION

3.1 Microstructure

As shown in **Figure 1**, AA2124/SiC/25p-T4 MMC plates with a thickness of 3 mm were successfully joined by FSW technique. Top view of the friction stir welded composite is shown in **Figure 1**. Surface roughness measurements were performed in the FSW zone on the side in contact with the shoulder, both on longitudinal

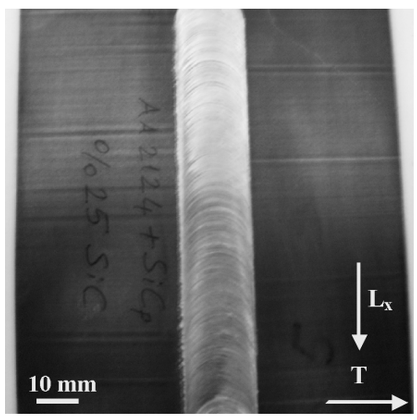

Figure 1: Top view of friction stir welded AA2124/SiC/25p-T4 MMC plates

Slika 1: Pogled od zgoraj na plošče AA2124/SiC/25p-T4 MMC zvarjene po vrtilno tornem postopku

(L) and transverse (T) directions. As revealed in **Table 1**, it should be stated that the surface in contact with the shoulder showed high values of the roughness parameters (Ra, Ry and Rz), typical of a milled surface. Similar results have also been obtained by L. Ceschini et. al.[22]

Table 1: Surface roughness measurements on FSW zone
Tabela 1: Površina hrapavosti meritve na FSW območje

Direction of material	Ra (μm)	Ry (μm)	Rz (μm)
T	2.89	20.1	20.4
	2.28	28.8	21.5
	3.69	36.1	21.1
Average values	2.95	28.3	21
L_x	6.68	23.6	19
	4	36.4	29.1
	6.6	29.1	26.3
Average values	5.76	29.7	24.76
L_y	6.26	34.5	28.4
	3.69	23	34.4
	6.58	27.8	24.6
Average values	4.51	28.43	29.13

T: transverse, L: longitudinal, ($_x$): perpendicular, ($_y$): opposite side of perpendicular

Figure2 shows the SEM and EDS results of the FSWed of AA2124/SiC/25p–T4 composite. The macrostructure of the friction stir welded AA2124/SiC/25p–T4 MMC is shown in **Figure 2a**, where the MMC material from shoulder zone moved across the joint from the retreating side (RS) against the advancing side (AS).[23] This puzzle macrostructure of FSW joint is formally divided into four zones: (1) base material (BM); (2) heat affected zone (HAZ); (3) thermo-mechanically affected zone (TMAZ); and (4) stir zone (SZ).[8,24] No visible superficial porosity or macroscopic defects have been observed in AA2124/SiC/25p-T4 MMC joints. The AA2124/SiC/25p-T4 MMC plates contain SiC particles with two different particle sizes, of 0.1–0.5 μm and of 1–5 μm, as shown in **Figure 2b**. The SEM microstructure examination revealed a non uniform distribution of SiC particles in the matrix (**Figure 2b**). The grain size changes from base MMC to stir zone can be seen clearly in **Figure 2c**. The microstructure of stir zone is greatly refined due to dynamic recrystallization.[24,25,26] According to base MMC recrystallized fine equiaxed SiC particulates structure were homogeneously distributed in stir zone due to the high deformation and stirring action.[27] Exposure to high stresses and the heat produced by stirring tool is responsible for the plastic

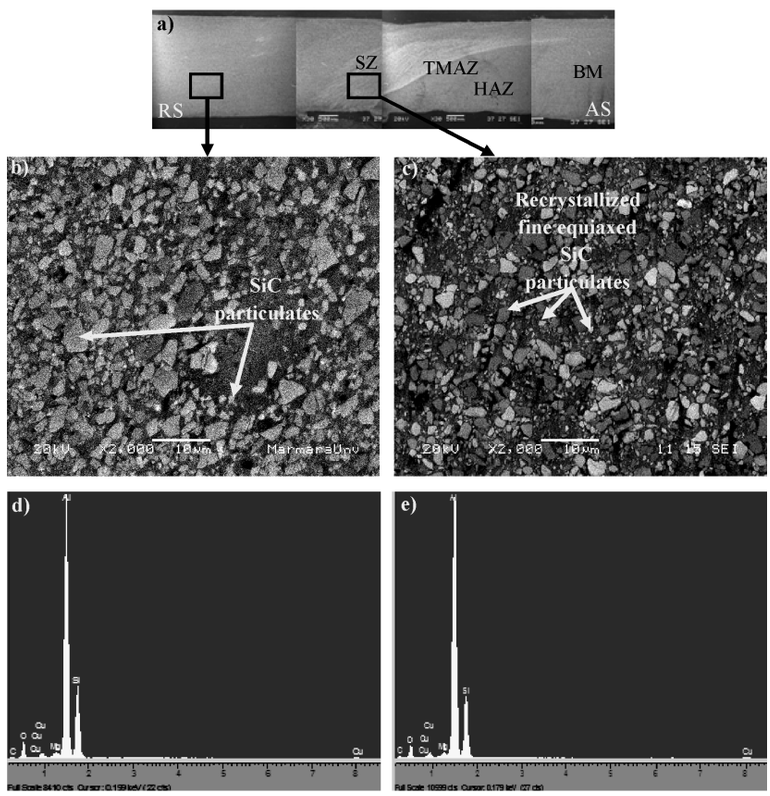

Figure 2: SEM and EDS analysis of the AA2124/SiC/25p-T4 MMC showing: (a) macrostructure of the FSW of MMC, (b) base MMC, (c) stir zone, (d) EDS analysis of base MMC, (e) EDS analysis of stir zone
Slika 2: SEM in EDS analiza AA2124/SiC/25p-T4 MMC prikazuje: (a) makro strukturo od FSW MMC compozita, (b) osnovno mikrostrukturo MMC, (c) mešamo področje, (d) EDS analizo osnovne MMC, (e) EDS analizo mešanega področja

deformation which results in the rearrangement of particles.[8] **Figure 2d** and **Figure 2e** show EDS analysis results of base MMC and stir zone, respectively. The variation of elements in these zones detected by EDS analysis is given in **Table 2**. As mentioned in previous studies,[8, 28] the stir zone contains SiO_2 phase because of entrapment of O_2 from air and frictional heating at the shoulder/composite interface.

No evidence of particle cracking was found in the stir zone, as bright point in the SEM micrographs in **Figure 2c** and **Figure 2e** and by EDS analysis (**Table 2**). A few studies in the literature reported that tool wear occurs during FSW of Al matrix ceramic particulate-reinforced composites.[26,28,29] However, in this study, no tool wear was established in spite of the presence of hard SiC particulates in the stir zone.[8]

Table 2: EDS analysis of base composite and the stir zone
Tabela 2: EDS analiza z osnovna kompozitne in mešamo

Micrography	Element (%)					
	C	O	Mg	Al	Si	Cu
Base composite	13.75	12.49	0.86	47.90	22.50	2.17
Stir zone	15.23	15.69	0.62	46.19	20.50	1.77

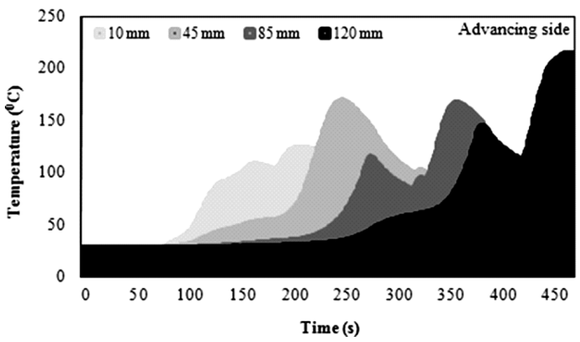

Figure 3: Temperature measurements at 15, 45, 85 and 120 mm intervals at the advancing side of the weld line
Slika 3: Temperature izmerjene na 15, 45, 85 in 120 mm na prednji strani z varilne linije

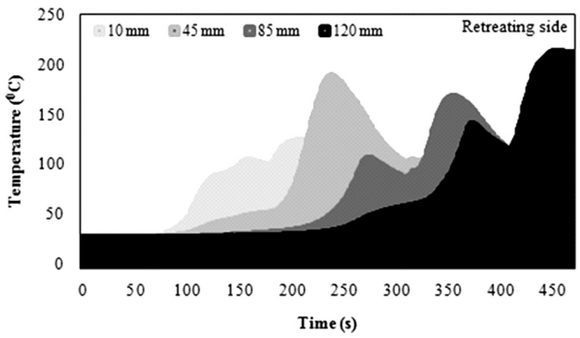

Figure 4: Temperature measurements at 15, 45, 85 and 120 mm intervals at the retreating side of the weld line
Slika 4: Temperature izmerjene na 15, 45, 85 in 120 mm na zadnji strani varilne linije

3.2 Temperature measurements

The temperature measurements at the distance of 15 mm from the weld center were carried out on four points at both advancing and retreating side to determine the peak temperature reached during welding. In **Figure 3** and **Figure 4** are shown the temperature measurements at (15, 45, 85 and 120) mm intervals at the advancing and retreating side of the weld line. The result show that the temperature is very similar on both sides of the weld bead, as shown in **Figures 3 and 4**. The temperature of 215–220 °C was determined at 15 mm from the weld center. The temperature in this zone depends on the tool rotation speed during FSW. High tool rotation speed gives rise to higher heat input into the material.[4] However, higher heat dissipation (255–270 °C) at high tool rotation speed at 15 mm from the weld center was observed.[8] As mentioned in the previous study,[30] the peak temperature during FSW was below the melting point of BM. Computer simulation of FSW has suggested that the maximum temperature in the workpiece, at the probe/workpiece interface, can reach the lower bound of the melting temperature range of the workpiece during FSW of aluminum alloys, including Alloys 6061, 7030, and 7075.[31]

3.3 Hardness

Figure 5 shows the hardness profile on the cross section of the FSWed of MMC. In the previous studies, the hardness in the stir zone was reduced at high tool rotation speed because the heat generated by rotating probe causes a reduction of cooling rate.[8,32] In this study the opposite was established, because of increased effect of dynamic recrystallization, homogeneous distribution of SiC particles and reduced dimension. A similar trend was observed by Nami et. al.[6] during FSWed of Al/Mg_2Si composites. The microhardness values were in the range of 185–190 $HV_{0.5}$ for AA2124/SiC/25p-T4 base MMC. The microhardness was decreased from base

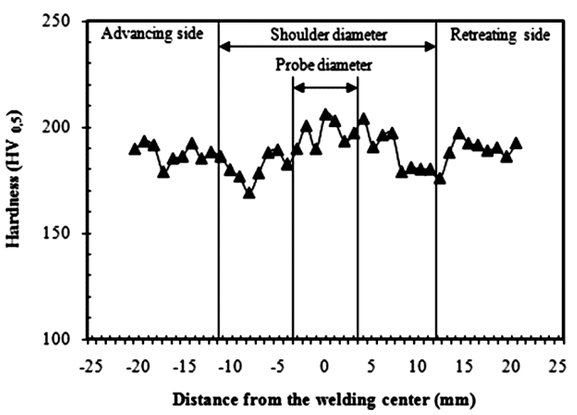

Figure 5: Hardness profiles on the cross section of the FSWed of MMC
Slika 5: Profil trdote na prerezu FSW MMC

MMC to the stir zone. The average microhardness values decreased slowly from stir zone (205 $HV_{0.5}$) to HAZ (approximately 180 $HV_{0.5}$) due to the annealing process[26] or because the shoulder supplied sufficient heat and force action.[1] As shown in **Figure 5**, the hardness from both advancing and retreating side of the HAZ to TMAZ zone was increased because of age hardening mechanism.[7]

3.4 Tensile tests

The MMCs tensile test samples were cut by EDM and tested at room temperature with the weld traverse to the welding direction without any post-weld heat treatment or surface modification. During the tensile tests, failure locations of the joints were observed in the TMAZ as shown in **Figure 6**. In this figure, can be seen clearly surface in contact with the shoulder and opposite side of the joint. As already known, the reinforcement particles have a significant impact on the strength of the MMCs.[33] For BM, an increased concentration of SiC particles increases the strength and reduces the elongation to failure of the MMC.[9] It is significant to improve the reproducibility of the weld tensile test results. The results of tensile test, carried out on the base and FSWed

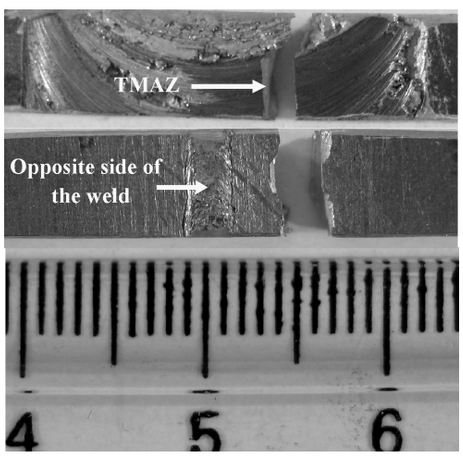

Figure 6: Surface in contact with the shoulder and opposite side of the joint
Slika 6: Površina na stiku z ramenom in z nasprotno stranjo varjenja

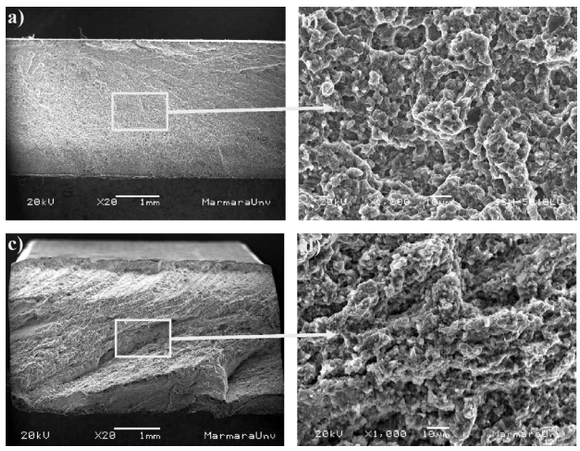

Figure 7: SEM micrographs of the tensile fracture surfaces; (a) Low magnification of BM, (b) High magnification of BM, (c) Low magnification of the stir zone, (d) High magnification of the stir zone
Slika 7: SEM posnetki nateznega peloma; (a) Majhna povečava z BM, (b) Velika povečava z BM, (c) Majhna povečava mešanega področja, (d) Velika poečaba mešanega področja

of MMCs plates are shown in **Table 3**. It is seen from this table that the maximum UTS value was 326 MPa which show a 73 % joint efficiency (i.e., $UTS_{FSW}/UTS_{BM} \times 100$). Because of SiC particulates probably non-uniform distributed at the TMAZ, in this region UTS and elongation was reduced. Similar results (72 %) were also obtained by some researcher[20,34] for the FSWed AA2219-T87 age hardenable aluminium-copper alloys and AA6061/20 % Al_2O_{3p} MMC plates.

A better comprehension and understanding of the mechanical fracture and defect nucleation properties are strongly dependent on purposed analyses of the rupture surfaces, since the influence of microstructural morphology of the joined interfaces on the endurance time results to be fundamental.[35] **Figure 7** shows SEM micrographs of the tensile fracture surfaces. Different magnifications of fracture surfaces in BM and stir zone are shown in **Figure7 a, b and c, d**, respectively. The fracture surfaces revealed a mixed brittle-ductile fracture mode and showed also the superiority of bonding

Table 3: Tensile test results of the base and the FSWed composite
Tabela 3: Natezne rezultati testov z osnovna in FSWed kompozitne

Material	Test (N)	Tool rotation speed (rpm)	Tool traverse speed (mm/min)	Ultimate tensile strength (MPa)	Elongation (%)	Joint efficiency (%)
AA2124/SiC/25p-T4 (Base Composite)	1	–	–	450	2.5	–
	2			461	2.5	
	3			450	2.3	
Average values				± 454	± 2.4	
FSW-AA2124/SiC/25p-T4	1	450	40	337	2.4	75
	2			330	2.7	74
	3			312	2.6	70
Average values				± 326	± 2.6	± 73

between the SiC particles and the Al matrix. A similar fracture morphology was observed in other studies.[8,33]

4 CONCLUSIONS

In this research, weldability of 25 % of SiC particles MMC plates by friction stir welding at low tool rotation and traverse speed were investigated. The obtained results can be summarized as follows:

- The AA2124/SiC/25p-T4 MMC plates were successfully joined by friction stir welding at low welding parameters.
- Surface roughness measurements showed on the surface in contact with the shoulder high values of roughness parameters.
- In microstructural examination no visible superficial porosity or macroscopic defects have been observed in AA2124/SiC/25p-T4 MMC joints. Grain size changes from base MMC to stir zone have been observed.
- The temperature measurement was determined as 215–220 °C at 15 mm away from the weld center.
- The hardness from both advancing and retreating side of the HAZ to TMAZ zone was increased because of age hardening mechanism.
- The maximum tensile strength of 326 MPa was obtained which shows a 73 % joint efficiency.
- After tensile testing the specimen fracture surfaces have revealed a mixed brittle-ductile fracture mode.

ACKNOWLEDGEMENTS

The authors are deeply grateful for the financial support of Marmara University Scientific Research Fund (BAPKO), Grant No: FEN-C-YLP-280110-0012.

5 REFERENCES

[1] A. Kurt, I. Uygur, E. Cete, J Mater Process Technol., 211 (**2011**), 313–317
[2] V. M. Kevorkijan, B. Šuštaršič, M. Torkar, G. Chiarmetta, Kovine Zlit. Tehnol., 32 (**1998**) 6, 539–543
[3] K. Sukumaran, K. K. Ravikumar, S. G. K. Pillai, T. P. D. Rajan, M. Ravi, R. M. Pillai, B. C. Pai, Mater Sci Eng A, 490 (**2008**), 235–241
[4] D. Yadav, R. Bauri, Mater Sci Eng A, 528 (**2011**), 1326–1333
[5] H. Aydin, A. Bayram, U. Esme, Y. Kazancoglu, O. Guven, Mater. Tehnol., 44 (**2010**) 4, 205–211
[6] H. Nami, H. Adgi, M. Sharifitabar, H. Shamabadi, Mater Des., 32 (**2011**), 976–983
[7] F. Rotundo, L. Ceschini, A. Morri, T. S. Jun, A. M. Korsunsky, Compos A, 41 (**2010**), 1028–1037
[8] Y. Bozkurt, H. Uzun, S. Salman, J Compos Mater, 45 (**2011**), 21, 2237–2245
[9] X. G Chen, M. Da–Silva, P. Gougeon, L. St-Georges, Mater Sci Eng A, 518 (**2009**), 174–184
[10] I. Charit, R. S. Mishra, M. W. Mahoney, Scripta Materialia, 47 (**2002**), 631–636
[11] L. Cederqvist, A. P. Reynolds, Weld Res Supp., (**2001**), 281–287
[12] W. B. Lee, S. B. Jung, Mater Lett., 58 (**2004**), 1041–1046
[13] C. Meran, Mater Des., 27 (**2005**), 719–726
[14] W. B. Lee, C. Y. Lee, W. S. Chang, Y. M. Yeon, S. B. Jung, Mater Lett., 59 (**2005**), 3315–3318
[15] W. Xunhong, W. Kuaishe, Mater Sci Eng A, 431 (**2006**), 114–117
[16] H. Fujii, L. Cui, N. Tsuji, M. Maeda, K. Nakata, K. Nogi, Mater Sci Eng A, 429 (**2006**), 50–57
[17] Y. J. Chao, Y. Wang, W. Miller, Weld Res Supp., (**2001**), 196–200
[18] H. Uzun, C. D. Done, A. Argagnotto, T. Ghidini, C. Gambaro, Mater Des., 26 (**2005**), 41–46
[19] M. Amirizad, A. H. Kokabi, M. A. Gharacheh, R. Sarrafi, B. Shalchi, M. Azizieh, Mater Lett., 60 (**2006**), 565–568
[20] L. Ceschini, I. Boromei, G. Minak, A. Morri, F. Tarterini, Compos A, 38 (**2007**), 1200–1210
[21] ISO/TTA2, Tensile tests for discontinuously reinforced metal matrix composites at ambiant temperatures. First edition. Technology trends assess, (**1997**), 4–15
[22] L. Ceschini, I. Boromei, G. Minak, A. Morri, F. Tarterini, Compos Sci Technol., 67 (**2007**), 605–615
[23] R. S. Mishra, Z. Y. Ma, Mater Sci Eng R., 50 (**2005**), 1–78
[24] S. Di, X. Yang, G. Luan, B. Jian, Mater Sci Eng A, 435–436 (**2006**), 389–395
[25] W. Xunhong, W. Kuaishe, Mater Sci Eng A, 431 (**2006**), 114–117
[26] H. Uzun, Mater Des., 28 (**2007**), 1440–1446
[27] Y. Bozkurt, R. Artýr, H. Uzun, S. Salman, Adv Compos Lett., 18 (**2009**) 5, 151–155
[28] G. J. Fernandez, L. E. Murr, Mater Charac, 52 (**2004**), 65–75
[29] R.A. Prado, L. E. Murr, D. J. Shindo, K. F. Soto, Scripta Materialia, 45 (**2001**), 75–80
[30] S. Mandal, K. Williamson, J Mater Process Technol., 174 (**2006**), 190–194
[31] G. Cao, S. Kou, Weld J Res Supp (January **2005**), 1–8
[32] K. Elangovan, V. Balasubramanian, Mater Sci Eng A, 459 (**2007**), 7–18
[33] Y. Bozkurt, S. Duman, Sci Res Essays, 6 (**2011**) 17, 3702–3716
[34] P. B. Srinivasana, K. S. Arora, W. Dietzel, S. Pandey, M. K. Schaper, J Alloys Comp., 492 (**2010**), 631–637
[35] P. Cavaliere, R. Nobile, F.W. Panellaa, A. Squillace, Int J Mach Tool Manuf., 46 (**2006**), 588–594

UDK 621.791.05:669.14.018.8
Original scientific article/Izvirni znanstveni članek

ISSN 1580-2949
MTAEC9, 45(5)413(2011)

INFLUENCE OF THE GAS COMPOSITION ON THE GEOMETRY OF LASER-WELDED JOINTS IN DUPLEX STAINLESS STEEL

VPLIV VRSTE ZAŠČITNEGA PLINA NA GEOMETRIJO ZVARA PRI LASERSKEM VARJENJU NERJAVNEGA DUPLEKSNEGA JEKLA

Branko Bauer[1], Angela Topić[2], Slobodan Kralj[1], Zoran Kožuh[1]

[1]Faculty of Mechanical Engineering and Naval Architecture, University of Zagreb, I. Lucica 1, 10000 Zagreb, Croatia
[2]Faculty of Mechanical Engineering and Computing, University of Mostar, Matice Hrvatske bb, 88000 Mostar, Bosnia and Herzegovina
angela.mustapic@tel.net.ba

Prejem rokopisa – received: 2010-10-27; sprejem za objavo – accepted for publication: 2011-03-03

Shielding gases, i.e., argon or an argon-nitrogen mixture, are normally used during the laser-beam welding of duplex stainless steel. Helium is also often added to the argon. The effect of the type of shielding gas – argon, nitrogen, helium and their mixtures – on the geometrical characteristics of laser-welded joints of the duplex steel W.Nr. 1.4462 was studied. The welding was carried out according to the experimental model with mixtures. The effect of the welding speed and the gas flow rate were additionally explored using a factorial experiment. The obtained data were statistically processed and mathematical modeling, applying the method of response surfaces, was carried out. The analysis revealed that the impact of the shielding gas mixtures on the geometrical characteristics of the joint is significant. The effect of the gas flow rate on the geometrical characteristics was registered, while the effect of the heat input is the most significant. Special cubic, quadratic and reduced quadratic models, depicting the effects of the shielding gases on the geometrical characteristics of the welded joint, were obtained.

Key words: laser, welding, duplex steel, shielding gas, weld geometry

Pri laserskem varjenju dupleksnega jekla se kot zaščitna plina večinoma uporabljata čisti argon in mešanica argona z dušikom, pogosto pa se k argonu dodaja tudi helij. Pri laserskem varjenju dupleksnega jekla W.Nr. 1.4462 se je preučeval vpliv vrste zaščitnega plina: argona, dušika, helija in njihovih mešanic, na geometrijske značilnosti zvarov. Varjenje je bilo izvedeno po eksperimentalnem modelu z mešanicami. Na osnovi faktorskega eksperimenta je bil preučen tudi vpliv hitrosti varjenja in pretoka zaščitnega plina. Dobljeni rezultati so bili statistično ovrednoteni in ustvarjen je bil matematični model po metodi odzivnih površin. Rezultati tako dobljene analize razkrivajo, da je vpliv zaščitnega plina na geometrijske značilnosti zvarov signifikanten. Ob opaznem vplivu pretoka zaščitnega plina na geometrijske značilnosti zvara je očitno dejstvo, da je najbolj signifikanten vnos toplote. Dobljeni so bili posebni kubični, kvadratični in reducirani kvadratični modeli geometrijskih značilnosti zvarov.

Ključne besede: laser, varjenje, dupleksno jeklo, zaščitni plin, geometrija zvara

1 INTRODUCTION

Duplex and super-duplex steels are materials that have been increasingly used and applied in the past ten years. The petrochemical, food processing, chemical, paper and cellulose, oil and gas, transport and tanker production industries are just some of the areas where duplex steels have found many applications. In many steel constructions, duplex steels are replacing the standard carbon steels and austenite stainless steels very effectively.

Duplex stainless steels are optimised with respect to mechanical properties and corrosion stability so that their structures contain equal proportions of austenite and ferrite. However, the weldability of duplex steel when the laser-welding process is applied is still under investigation and is particularly related to an increased rate of ferrite formation after welding, induced by the high cooling rates. A large ferrite content tends to produce a deterioration of the mechanical properties and in particular a reduction of the corrosion resistance. The ferrite content may be higher than 90 % in the microstructure of the weld metal and HAZ, while the target is to achieve at least 35 % of austenite. One of approaches to realize such a goal is to apply filler material that may increase the costs and the technical difficulties. Another approach includes heat treatment, applying a defocused laser beam, induction heating or treatment in a furnace. Such methods also involve increased production costs. Heat treatment in a furnace additionally impedes the main advantage of laser welding, i.e., the production rate. Welding without filler material tends to produce a strong formation of ferrite and a large grain growth in the weld metal, but there is an advantage in the case of laser welding, for it much simplifies the actual execution of the welding [1–5].

The shielding gas has an important role in laser welding, fulfilling the following tasks: protection of molten pool and heat-affected zone from the effect of the surrounding atmosphere, affecting the shape of the weld and protection of the optics of the device against metal vapors and spatter droplets. According to the reference

data, argon as a shielding gas is the best selection in Nd:YAG laser welding. An acceptable shape of welded joint may be achieved with all shielding gases [6,7]. Argon and helium are inert gases, having no effects on the metallurgical processes during welding. Nitrogen is a reactive gas, affecting the metallurgical processes occurring in the welded joint [6]. When nitrogen shielding is used, a significant amount of nitrogen is absorbed into the welded joint. Doping the welded joint with nitrogen is particularly important in the welding of duplex steel, since nitrogen stimulates the formation of austenite [6,8]. The most frequently used shielding gases for the laser welding of duplex steels are pure argon and argon/nitrogen mixtures. Also, there is a widespread use of argon/helium mixtures.

The application of argon-based gas mixtures with the addition of nitrogen and/or helium for the Nd:YAG laser welding may reduce the ferritization rate. Current investigations indicated that the application of the mentioned mixtures ensures an acceptable appearance and quality of the welded joints [2,3]. In such investigations, testing with specific gas mixtures has been made without detecting the interaction between the components of gas mixtures and mathematical modeling. An experimental model for the mixtures appears to be suitable for the investigation and mathematical modeling of the effects of shielding-gas mixtures on the welding [9–13]. The mixture contains two or more constituents. The target of mixing certains components into the mixture is to investigate whether such a mixture has a more favorable effect upon the specific properties than a single component. The application of the planned experiment is of utmost importance in such investigation, since this approach provides rational determination of the response functions. The next aim was to describe quantitatively the effect of the mixture composition on the geometrical characteristics of the welded joint, applying a mathematical model, developed on the basis of the experimental data measured for a three-component mixture.

It is important to achieve the optimum weld shape and geometry to fullfil the quality requierments according to the standard EN ISO 131919-1. It is important to optimize the root width, which could compensate for the inaccuracy of the positioning and the clamping of the sheets, and also the inaccuracy of the laser-beam guidance, to eliminate the lack of fusion defects. In this way, the costs of the equipment for positioning and clamping in th eindustrial production of laser-beam welded structures could be reduced.

These concepts indicate that investigations of the effects of input energy, type and flow rate of the shielding gas on achieving a two-phase microstructure with approximately equal portions of austenite and ferrite are justified. Welding with maximum speed, without the use of filler material and with the use of the appropriate gas mixture that contains nitrogen would considerably increase the economy and productivity of laser welding.

The final objective of this research was to determine the influence of the shielding gas – argon, nitrogen, helium and their mixtures – on the geometrical characteristics of the welded joint on a 2-mm-sheet of duplex stainless steel W.Nr. 1.4462 and additionally explore the influence of the welding speed and the gas flow rate for every shielding-gas and mixture.

2 EXPERIMENTAL WORK

2.1 Equipment

The welding was performed using a Nd:YAG laser "ROFIN CW 020" with a continuous power of 2 kW. An optical fiber with a 600-µm core diameter was used for the beam transfer. Focusing optics of 120/120 mm were used. The beam diameter in the focus was equal to 0.6 mm. The focusing optics were attached to the robot arm, and the robot "IGM Limat RT 280" features 6 degrees of movement freedom.

2.2 Experimental

The welding was performed on 2-mm-thick sheets of duplex steel W.Nr. 1.4462. The sample dimensions were (250 × 130) mm and (230 × 130) mm. The longer welded sides were machined. Prior to welding, the samples were cleaned by applying emery paper and ethanol. The samples were fixed in the jigging tool and argon was used for the root shielding.

The tests were conducted according to a "simplex grid" planned experiment [9]. The simplex grid for a three-component mixture is represented by a triangle, within which the states of the experiments are distributed uniformly in a "grid" pattern. A uniform distribution of

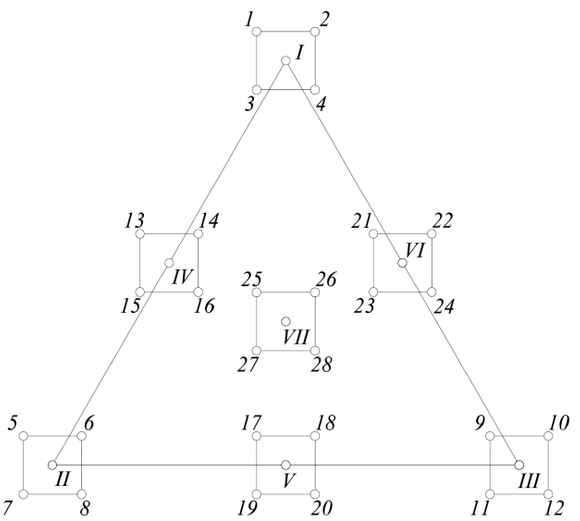

Figure 1: Plan of experiment with 28 states
Slika 1: Načrt eksperimenta z 28 stanji

the states of the experiment in equal intervals of all the component portions in mixture is required to attain an acceptable definition of the response surface. Each response function can be associated with a polynomial and the appropriate coefficients for the equation can be calculated. Seven types for three-component mixtures for the simplex-grid model were selected. For every shielding gas – argon, nitrogen, helium and their mixtures – in the simplex grid, a factorial plan on two levels 2^n, with two factors for the welding speed and gas flow rate were additionaly conducted. A complete plan of the experiment is shown in **Figure 1**.

In **Table 1**, the percentage of components for all 7 points of the experiment and their combinations with the welding parameters are listed. The intervals of the welding parameters providing quality weldments with full penetration were determined through preliminary testing.

Constant welding parameters

The constant parameters in all states of the experiment:

Power: P = 1800 W

Optic focal length: f = 120 mm

Tip diameter of the coaxial gas nozzle: 5 mm

Distance of gas nozzle tip from the workpiece: 8 mm

2.3 Inspection and testing

The welded specimens were inspected visually and with radiographic control, followed by destructive testing methods. In order to determine the weld geometry, macro-etches of the joint cross-sections were prepared. The weld geometry measurement on the macro-etches was performed under 50-times magnificaction.

With the aim of determining the quality of the laser welded joint according to the standard EN ISO 13 919-1, the weld and root reinforcement/underfill, linear misalignment of the sheets and the size of the undercut were measured. Measurements were also performed on the width of the weld b_zav, the width of the HAZ b_zut, the width of the weld root b_kor and the area of the weld cross-section A, in order to determine the influence of the parameters on the geometrical characteristics of the welded joint.

The results of the measurements of local mechanical properties of the welded joint were processed by applying the software package "Design Expert 6.0.6". A statistical analysis of measured data for all 7 states of the experiment revealed the appropriate model. The model

Table 1: States of experiment. (v – welding speed, Q – gas flow rate, z – focus position relative to the workpiece surface)
Tabela 1: Stanja eksperimenta (v – hitrost varjenja, Q – pretok plina, z – položaj žarišča glede na površino varjenca)

Shielding gas/mixture	State of experiment	Mixture components (%)			Process parameters		
		Ar	N_2	He	v (cm/min)	Q (l/min)	z (mm)
I	1	100	0	0	110	18	–1,0
	2				140	18	
	3				110	9	
	4				140	9	
II	5	0	100	0	110	18	–0,8
	6				140	18	
	7				110	9	
	8				140	9	
III	9	0	0	100	110	33	–1,2
	10				140	33	
	11				110	21	
	12				140	21	
IV	13	50	50	0	110	18	–0,9
	14				140	18	
	15				110	9	
	16				140	9	
V	17	0	50	50	110	25	–1,0
	18				140	25	
	19				110	15	
	20				140	15	
VI	21	50	0	50	110	25	–1,1
	22				140	25	
	23				110	15	
	24				140	15	
VII	25	33,33	33,33	33,33	110	23	–1,0
	26				140	23	
	27				110	13	
	28				140	13	

could be linear, quadratic, special cubic, interactional or mean value if there are no significant effects of the tested factors. Subsequently, the significance of the model and the members of the response polynomial was tested by applying the variance analysis. For the linear model, only the members Ar, N_2 and He appear. In the square model, members of second order, i.e., Ar*N_2, Ar*He and N_2*He appear, and in special cubic model, the member Ar*N_2*He.

R-squared is a determination coefficient that represents the estimation of the total variation of the data described by the model. The adjusted "R-Squared" is R-squared adjusted to the number of members in the model in relation to the number of experiment states. The predicted "R-Squared" is a measure for the variation of the values within a new set of data described by the model. The values of both R-squares should be close to 1, and if they are equal to 1, then 100 % of the variations of the tested values are explained by the model. If the adjusted R-squared is higher than 75 %, the model can be considered as significant.

A mathematical model established through such an approach provides very a distinctive graphic interpretation and the optimization of tested parameters [10,11].

3 RESULTS AND DISCUSSION

3.1 Geometrical characteristics of welded joints

Good welding results were achieved. The welds feature a slight reinforcement of the face and the root without undercuts. Cracks, open pores and other surface defects did not occur and welds without porosity were obtained. According to the standard EN ISO 13919-1 for 2-mm-thick sheets, for high-quality B, the reinforcement of the weld root and the face have to be less than 0.5 mm, whereas the incompletely filled groove, linear misalignment of sheets and root undercuts have to be less than 0.2 mm. All the laser welds are classified into group B, i.e., they are of high quality.

The appearance of the weld face is acceptable for all the experimental conditions, while increased spattering occurred on the root side on certain samples. Increased spattering is noted in all the samples welded in an argon shield. Increased spattering while applying a nitrogen shield is registered in the experimental conditions No. 5 and 7, where a lower welding speed was used. In samples No. 6 and 8, which were welded applying the same shielding gas, but a higher speed, spattering was not registered.

A uniform root shape along the full weld length and full penetration were obtained for all the experimental conditions. All the applied shield gasses and mixtures produced faultless welds without defects and of acceptable geometric shape, this being the first target of the testing. **Figure 2** shows good results when nitrogen was used as the shielding gas. This is an important finding, because of its favorable effect upon ferritization [2,3].

Relationship between the geometric characteristics of welded joint and the welding parameters

For all shielding gasses and mixtures, samples welded with a lower speed have larger geometric characteristics, due to the higher energy input. With a lower welding speed the weld root is wider and therefore this compensates for the beam-guidance accuracy. A higher welding speed is economical but requires better

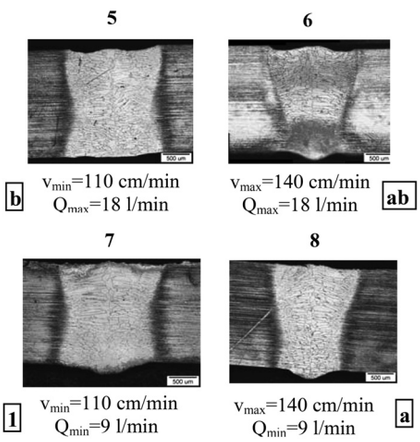

Figure 2: Cross-sections of welded joints in a N_2 shield according to the factorial plan of the experiment – condition 1 (v_{min}, Q_{min}), a (v_{max}, Q_{min}), b (v_{min}, Q_{max}) and ab (v_{max}, Q_{max})

Slika 2: Prečni prerezi zvarov v zaščiti N_2 v skladu s faktorskim načrtom eksperimenta pri pogojih 1: (v_{min}, Q_{min}), a (v_{max}, Q_{min}), b (v_{min}, Q_{max}) in (v_{max}, Q_{max})

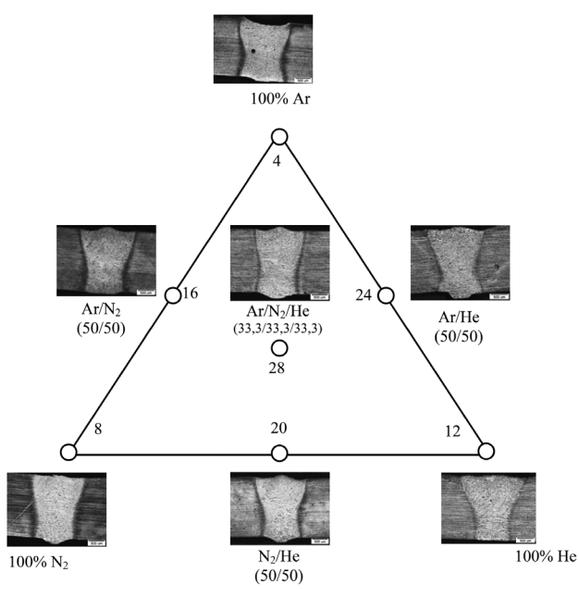

Figure 3: Cross-sections of welded joints for all shielding gases and mixtures at maximum welding speed and minimum flow rate of the shielding gas – experimental condition a (v_{max}, Q_{min})

Slika 3: Prečni prerezi zvarov za vse zaščitne pline in mešanice pri največji hitrosti varjenja in minimalnem pretoku zaščitnega plina pri pogoju eksperimenta a (v_{max}, Q_{min})

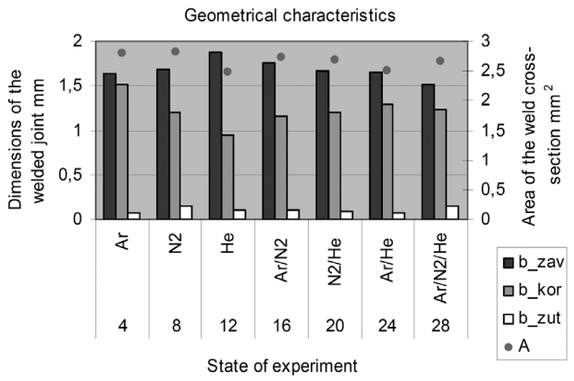

Figure 4: Geometrical characteristics of the welded joint – conditions a(v_{max}, Q_{min}), (b_zav – weld width, b_kor – root width, b_zut – HAZ width, A – area of the weld cross-section)
Slika 4: Geometrijske značilnosti zvara pri pogojih a(v_{max}, Q_{min}), (b_zav – širina temena zvara, b_kor – širina korena, b_zut – širina toplotno vplivanega področja, *A* – ploščina prečnega prereza zvara)

edge preparation, while without any beam-guidance sensor a risk of a lack of fusion defects is higher. For welded samples, by applying a higher welding speed the root is significantly narrower than the joint face, except for the samples made in an argon shield. Thus, with respect to the root width, an argon shield is the best choice. The geometrical characteristics of the welds made applying the same welding speed and different shield flows do not differ significantly.

Relationship between geometric characteristics of the welded joint and the composition of the shielding gas

From the economic point of view, i.e., a reduction of costs, the best solution is to apply the highest welding speed and the lowest flow rate of the shielding gas, thus v_{max}, Q_{min}. **Figure 3**. shows cross-sections of the welded joint for experimental conditions applying all the shielding gases and mixtures at maximum welding speed and minimum flow rate of the shielding gas, i.e., condition a. **Figure 4**. shows a graphical representation of the geometric characteristics of the weld for the experimental condition a. The mixture Ar/N_2 and pure nitrogen, no matter which welding parameters were used, produced welded joints with the largest cross-section and root width within the experiment. This fact may provide a higher content of austenite in the microstructure of the welded joint, thus improving the mechanical properties and the corrosion resistance of the joint.

The use of helium contributes to a reduction of the geometric characteristics of the welded joint. Since the price of helium is significantly higher than that of argon, and particularly nitrogen, its application is not justified.

3.2 Mathematical models depicting the relationship between the composition of the shielding gases and the geometrical characteristics of the welded joint

Mathematical models obtained for mixtures in states 1 (v_{min}, Q_{min}), a (v_{max}, Q_{min}), b (v_{min}, Q_{max}) and ab (v_{max}, Q_{max}) are listed in **Table 2**. "Outliers" did not occur in any model, indicating that none of the measured data has a significant deviation.

An adjusted R-squared value for the weld joint width b_zav, **Table 2**, close to the value of one, and variance analysis of the model indicate that special cubic models are significant for all four combinations of parameters. From the graphic plot for state a (v_{max}, Q_{min}), **Table 3**, it could be noted that the widest face of the weld is obtained for pure He and that additions of N_2 and Ar to helium cause a width reduction. The smallest width of the welded joint is obtained in the centre applying a (Ar/N_2/He) mixture. It can be concluded that the type of shielding gas/mixture affects the weld width that can be easily predicted by applying a special cubic mathematic model.

The square model in state a and the special cubic model in state ab have been yielded for the root width b_kor, **Table 2**. For states 1 and b a negative Predicted R-squared was obtained, meaning that the mean value predicts the response better than the special cubic model. For low welding speeds, no significant model was obtained, while for high welding speeds different significant models are revealed. Different models may be explained by the effects of some other factors, unaccounted effects combined with the effects of mixtures. Such factors may be, for example, no uniform gap between the plates clamped in the jig or plates' misalignment. It can be concluded that the selection of the gas mixture has a significant effect on the root width in the case of high welding speeds, while in the case of low welding speeds it is not important which mixture is used. From the graphic plot for state a (v_{max}, Q_{min}, **Table 3**) it can be seen that the root width is the widest in the case

Table 2: Mathematical models of weld width b_zav, root width b_kor, HAZ width b_zut, area of the weld cross-section A
Tabela 2: Matematični modeli širine temena zvara b_zav, širine korena b_kor, širine toplotno vplivanega področja b_zut, ploščine prečnega prereza zvara A

Measured value	State			
	1 – v_{min}, Q_{min}	a – v_{max}, Q_{min}	b – v_{min}, Q_{max}	ab – v_{max}, Q_{max}
b_zav mm	Special cubic	Special cubic	Special cubic	Special cubic
b_kor mm	–	Quadratic	–	Special cubic
b_zut mm	–	–	–	–
A mm^2	Reduced quadratic	Reduced quadratic	Reduced quadratic	Special cubic

Table 3: Mathematical models and graphical plots for condition a (v_{max}, Q_{min})
Tabela 3: Matematični modeli in grafični prikaz za pogoje a (v_{max}, Q_{min})

No	Model	2D plot	3D plot X1=A=Ar; X2=B=N_2; X3=C=He
1	Special cubic "Prob>F"<0,0001 Adjusted R-squared=0,94 b_zav = +1.615 * Ar +1.670 * N2 +1.855 * He +0.430 * Ar * N2 -0.300 * Ar * He -0.450 * N2 * He -4.395*Ar*N2*He	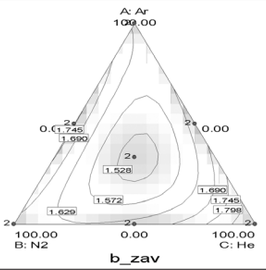	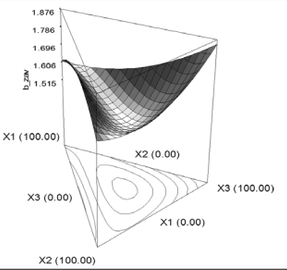
2	Quadratic "Prob>F"<0,0001 Adjusted R-squared=0,9920 b_kor = +1.49894 * Ar +1.21394 * N2 +0.94894 * He -0.76879 * Ar * N2 +0.32121 * Ar * He +0.49121 * N2 * He	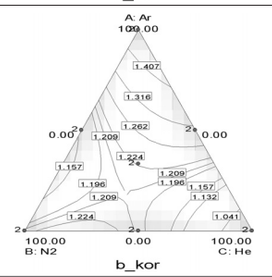	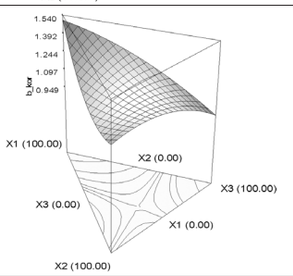
3	Reduced quadratic "Prob>F"<0,0001 Adjusted R-squared=0,9140 A = +2.750 * Ar +2.760 * N2 +2.437 * He -0.355 * Ar * He +0.385 * N2 * He	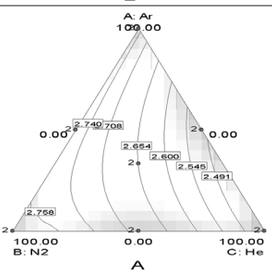	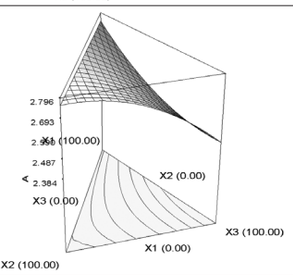

of the application of pure Ar. Additions of N_2 and He to argon reduce the root width.

An adjusted R-squared for the HAZ width for states 1 and ab has a value less than 0.75, while the predicted R-squared has a negative sign, indicating that no one model is significant. Thus, it can be concluded that the mean value predicts the response of model more adequately. Also, it may be concluded that the type of gas mixture has no significant effect on the width of the joint HAZ.

Significant reduced square models for states 1, a and b for the cross-section area of welded joint A were obtained, **Table 2**. A significant special cubic model for state ab has been developed. From graphic plots, relationships between the models produced for different conditions cannot be detected. For state 1 the largest area is for pure argon and it is reduced with additions of nitrogen and helium. In state a (v_{max}, Q_{min}, **Table 3**), argon and nitrogen produce the largest area, which is reduced with additions of helium, attaining its minimum for pure helium. In state b, the largest area is obtained for pure nitrogen and it is reduced with additions of argon and helium. In state ab, the largest surface is obtained for mixtures Ar/N_2 and Ar/He and it is reduced for the center (Ar/N_2/He) and pure gases. It can be concluded that the type of shielding gas/mixture affects the cross-section area of welded joint and it can be well predicted by the model. Also, it can be concluded that the model depends on a combination of welding speed and gas flow rate.

Mixtures have a significant effect on the geometric characteristics of the welded joint. Special cubic, quadratic and reduced quadratic models were obtained. In state a (v_{max}, Q_{min}) the helium content increases the weld width and reduces the root width and the area of the cross-section. Nitrogen content reduces the root width.

4 CONCLUSION

Metal sheets of duplex steel W. Nr. 1.4462, some 2-mm thick, were welded with a Nd:YAG laser. The shielding gases – argon, nitrogen, helium and their mixtures – were used and for root shielding argon was

used. A coaxial shielding-gas nozzle was used. The welding was carried out according to the experimental model with mixtures.

For the tested shielding gases and mixtures, high-quality welds were produced, meeting the requirements of the group B in EN ISO 13919-1 standard. No cracks occurred.

Statistical processing of the results and the developed mathematical models indicate that there is a significant effect of welding speed on the geometrical characteristics of the welded joint for the tested range of parameters. An increase of the welding speed reduces the geometrical characteristics, while the effect of the shielding-gas flow rate is not significant.

Special cubic, quadratic and reduced quadratic mathematical models were obtained, which can accurately predict the effects of the shielding gases (argon, nitrogen, helium) and their mixtures on the weld width, root width and the area of cross-section. The shielding gas/mixture has an effect on the geometric characteristics, while the model type depends on a combination of the welding speed and the flow rate of the shielding gas. No model is significant for the width of the HAZ, i.e., the mean value can better predict the response than the model. The type of mixture has no significant effect upon width of the HAZ. Using the obtained mathematical models it is possible to optimize the composition of the gas mixture with regard to the geometrical characteristics of the laser-beam welded joints.

As the application of helium shielding for Nd:YAG welding of duplex steels does not offer advantages over the argon shielding, it may be concluded that the application of much more expensive helium is not justified, particularly because of the higher shielding-gas flow rates. An analysis of the weld appearance quality and the geometrical characteristics of the welded joint, points towards the mixture (Ar/N_2) as being optimal. Considering the root width, the best choice is argon. The best choice to prevent ferritization would be pure nitrogen, provided that an acceptable microstructure and mechanical properties are attained. The Ar/N_2 mixture produces a wider root width and is a better choice if geometric characteristics are considered. Nitrogen is also cheaper than argon and helium, which means that its use contributes to making welding more economical. Additions of nitrogen to argon have no effect on the area of the weld cross-section, while additions of helium cause a reduction.

Duplex stainless steel W.Nr.1.4462 can be successfully welded by applying a laser using the shielding gases argon, nitrogen, helium and their mixtures.

The choice of shielding gas can affect the microstructure of the welded joint. An evaluation of the effects of the tested gas mixtures on the microstructure, mechanical properties and corrosion resistance of duplex grade steels will be the topic of future research.

Acknowledgement

The materials and shielding gases were sponsored by Messer Croatia Plin d.o.o. We express our thanks to the Messer Croatia Plin and ROFIN-SINAR Laser, Hamburg for their technical and financial support.

5 REFERENCES

[1] V. Šimunović, Zavarivanje, Zagreb, 43 (**2000**) 3/4, 75

[2] H.-D. Steffens, E. Honekamp, J. Wilden, DVS Berichte Band 194, Düsseldorf, (**1999**), 199

[3] E. Marquardt, G. Sitte, Plasma- und Laserstrahlschweißen von Feinblechen aus Duplexstahl 1.4462, Abschlußbericht, SLV Halle, 1996

[4] U. Dilthey, A. Wieschemann, DVS Berichte Band 205, Düsseldorf, (**1999**), 41

[5] K. Borggreen, J. Klaestrup Kristensen, L. E. Hansen, M. Koçak, J.F. dos Santos, Laser welding of heavy section duplex stainless steel grade 2205, Proc. Of Stainless Steel World 99 Conference, (**1999**), 267–274

[6] M. Faerber, Process gases for laser welding, Proc. of CISFFEL 6, Toulon, (**1998**), 837–841

[7] W. Danzer, T. Ammann, B. Bauer, Zavarivanje, Zagreb, 49 (**2006**), 1–2, 5

[8] B. Bauer, S. Kralj, M. Miculinić, Welding in the world, 51 (**2007**), 835

[9] J. A. Cornell, Experiments with mixtures, John Wiley & Sons, New York, 1981

[10] V. Panić, Master Thesis, Faculty of mechanical engineering and naval architecture, Zagreb, Croatia, 2001

[11] N. Šakić, V. Panić, Experimental design for investigating the influence of process variables and mixture components, Proc. of 3rd International Conference Welding in Maritime Engineering, Hvar, (**2004**), 495–500

[12] B. Bauer, Ph.D. Thesis, Faculty of mechanical engineering and naval architecture, Zagreb, Croatia, 2006

[13] A. Topić, Ph.D. Thesis, Faculty of mechanical engineering and computing, Mostar, Bosnia and Herzegovina, 2008

UDK 620.175:620.168:669
Original scientific article/Izvirni znanstveni članek

ISSN 1580-2949
MTAEC9, 45(5)421(2011)

MULTISCALE MODELLING OF HETEROGENEOUS MATERIALS

MIKRO IN MAKRO MODELIRANJE HETEROGENIH MATERIALOV

Martin Lamut[1], Jože Korelc[2], Tomaž Rodič[3]

[1]Institute of metals and technology, Lepi pot 11, 1000 Ljubljana, Slovenia
[2]Faculty of Civil and Geodetic Engineering, University of Ljubljana, Jamova 2, 1000 Ljubljana, Slovenia
[3]Faculty of Natural Sciences and Engineering, University of Ljubljana, Aškerčeva 12, 1000 Ljubljana, Slovenia
martin.lamut@space.si

Prejem rokopisa – received: 2011-01-08 sprejem za objavo – accepted for publication: 2011-06-27

In this work an approach to solving coupled micro-macro problems was developed that enables efficient analyses of modern heterogeneous materials. It provides an efficient problem-solving tool for problems with complex microstructures, which are used in demanding structural components. An effective way of transferring the microscale information to the macroscale analysis is to use a multilevel finite-element approach-FE2. Within the FE2 framework one conducts an embedded micro-scale computation in order to extract the quantities required at a point of the macroscale finite-element mesh. The aplication of FE2 circumvents the need to construct an explicit macroscale constitution formulation, though at an increased computational cost. Here, a general method for the calculation of the consistent macroscopic stiffness matrix via a sensitivity analysis at the micro level was developed. The performance of the proposed method was studied for different microstructures with porosities and stiff inclusions.

Keywords: heterogeneous materials, multiscale analysis, macroscopic tangent computation, sensitivity analysis

V tem delu je bila razvita metoda za učinkovito reševanje vezanih mikro-makro sodobnih heterogenih materialov. Nova metoda je inovativno orodje pri reševanju problemov s kompleksno mikrostrukturo, uporabljeno pri zahtevnih inženirskih komponentah. Za prenos informacij med mikroskopskim in makroskopskim nivojem smo izbrali večnivojsko metodo končnih elementov (FE^2). V FE^2-shemi reševanja je v vsaki Gaussovi točki makroskopskega končnega elementa izvedena mikroskopska analiza, ki prispeva potrebne neznane vrednosti. Pri FE^2-metodi reševanja ne potrebujemo več makroskopske konstitutivne zveze, saj je le-ta na račun povečanega računskega časa pridobljena z natančno mikroskopsko analizo v posamezni točki makroskopskega končnega elementa. Metoda je splošen način reševanja makroskopske togostne matrike z občutljivostno analizo mikroskopskega nivoja. Lastnosti metode so bile preizkušene za različni mikrostrukturi: za porozno mikrostrukturo in mikrostrukturo s togimi vključki.

Ključne besede: heterogeni materiali, mikro-makro analize, makroskopska togost, občutljivostna analiza

1 INTRODUCTION

Materials used in engineering sciences and industrial applications prove to be heterogeneous at some scale. This heterogeneous nature, such as inclusions, pores, fibers and grain boundaries, has a significant impact on the observed macroscopic behaviour of multi-phase materials. Typical examples are metal alloy systems, various composites, porous and cracked structures, polymeric blends and polycrystalline materials. Processing and advanced forming operations force a material to undergo complex loading paths. This results in varying microstructural responses and easily provokes the evolution of the microstructure. Because of time and cost requirements, straightforward experimental measurements on a number of material samples including various phase properties, volume fractions and loading histories are highly unlikely. On the other hand, it is still impossible to discretize the macrostructure so that it accurately represents the microstructure and at the same time allows a numerical solution within a reasonable amount of time. To determine the overall macroscopic characteristics of heterogeneous structures, the effective numerical models have to be developed. Conventionally, in structural mechanics the hierarchical approach is used, especially when the scales are significantly separated. By employing micromechanical models, the material behavior at the microscale is efficiently transferred to the macroscale analysis and used for all the structural calculations. The most straightforward way is to use the multilevel finite-element method ML-FEM,[1–5] whereby the behavior of each volume element results from a finite-element computation of the microscopic structure. When analyses at both levels are made in the context of the FEM, it can be referred to as the FE^2 method.[6, 7] This new type of model falls within the general category of multiscale models. The aplication of the FE^2 method removes the need to construct an explicit macroscale constitution formulation, though at an increased computational cost. The constitutive equations are written only on microscopic scale and homogenisation and localisation equations are used to compute the macroscopic strains and stresses knowing the mechanical state at the microscopic level.

The aim of this work stems from the need for a general and effective way of computing the macroscopic tangent, since this represents the main part of the FE^2

method. A conventional way of computing the macroscopic tangent in a condensation procedure necessitates the computation of a Shur complement. It inflicts for increasingly complex microstructure higher memory-allocation demands that may not be met by today's computers. Therefore, as an alternative, a tangent-computation technique based on a sensitivity analysis at the microscopic level will be presented.

2 MULTISCALE MODELING

2.1 Basic hypotheses

The material under consideration is assumed to be macroscopically homogeneous, so that continuum mechanics can be used to describe the macroscopic behavior. However, at the microlevel the material configuration is heterogeneous, consisting of many distinguishable components, e.g., grains, cavities, and hard inclusions.

In order to estimate the effective properties of a heterogeneous material, most of the micro-macro methods assume the existence of a micromechanical sample that is statistically representative of the microstructural features. The identification of such a representative volume element (RVE) is a somewhat delicate task and is outside the scope of this work. The RVE is considered both smaller enough than the macroscale media and larger enough than the heterogeneities on the micro scale, without introducing non-existing properties (e.g., anisotropy). For further issues associated with the identification procedure the reader is referred to.[8–12]

Here, the existence of an appropriate RVE is supposed. Then the problem on the RVE level can be formulated as a standard problem in quasi-static continuum solid mechanics, where kinematic, equilibrium and constitutive equations are needed.

In the computational homogenization technique, a macroscopic deformation gradient tensor (F_M) is calculated for every integration point of the macrostructure. From the macroscopic deformation tensor the appropriate boundary conditions are derived to be imposed on the RVE that is assigned to this point. After the solution of the boundary-value problem for the RVE, the macroscopic stress tensor (P_M) is obtained by averaging the resulting RVE stress field over the volume of the RVE. Additionally, the local macroscopic consistent tangent is derived from the sensitivity analysis of the RVE. This framework is schematically illustrated in **Figure 1**. In the subsequent sections these issues are discussed in more detail.

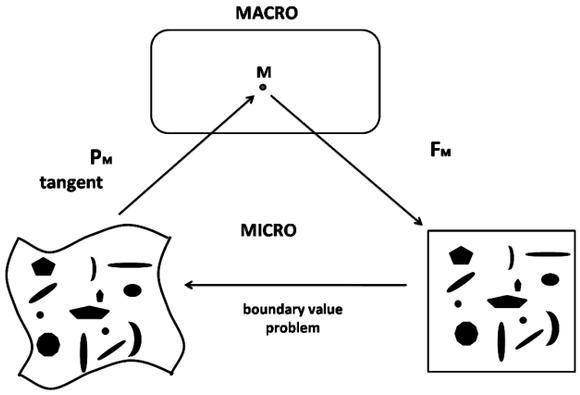

Figure 1: Shematic diagram of the FE^2 model
Slika 1: Shema FE^2-modela

2.2 Coupling of the macroscopic and microscopic levels

The actual coupling between the macroscopic and microscopic scales is based on averaging theorems. The energy averaging theorem, known in the literature as the Hill condition or macrohomogeneity condition,[12,13] requires that the macroscopic volume average of the variation of the work performed on the RVE is equal to the local variation of the work on the macroscale. Formulated in terms of a deformation gradient tensor and the first Piola-Kirchhoff stress tensor, the work criterion in differential form is written:

$$\left\langle P_{\mathrm{m}} \cdot \mathrm{d}F_{\mathrm{m}} \right\rangle = \left\langle P_{\mathrm{M}} \right\rangle \cdot \left\langle \mathrm{d}F_{\mathrm{M}} \right\rangle \tag{2.1}$$

It is well known that this criterion is not satisfied for arbitrary boundary conditions (BCs) applied to the RVE. Classically, three types of RVE boundary conditions are used, i.e., prescribed displacements, prescribed tractions and prescribed periodicity. Periodicity here is referring to an assumption of the global periodicity of the microstructure, suggesting that the whole macroscopic specimen consists of spatially repeated unit cells. Among them the periodic BCs show a more reasonable estimation of the effective properties. This was supported and justified by a number of authors.[8–11] The periodicity conditions for the microstructural RVE are written in a general format as:

$$\begin{aligned} \vec{x}^{+} - \vec{x}^{-} &= F_{\mathrm{M}} \cdot \left(\vec{X}^{+} - \vec{X}^{-}\right) \\ \vec{p}^{+} &= \vec{p}^{-} \end{aligned} \tag{2.2}$$

where $\vec{x}$ and $\vec{X}$ represent the actual and initial position vectors and $\vec{p}$ is the boundary traction of the RVE. In equation (2.1) the macroscopic first Piola-Kirchhoff stress tensor (PM) and the macroscopic deformation gradient tensor (FM) are the fundamental kinetical and kinematical measures, which are defined in terms of the volume average of their microscopic counterparts. Every time that the work criterion is satisfied, the volume average of the above-mentioned macroscopic measures can be obtained through a knowledge of the boundary information only.

$$F_{\mathrm{M}} = \left\langle F_{\mathrm{m}} \right\rangle_{\mathrm{RVE}} = \frac{1}{V_{\mathrm{RVE}}} \int_{\mathrm{RVE}} F_{\mathrm{m}} \mathrm{d}V = \frac{1}{V_{\mathrm{RVE}}} \int_{\Gamma} \vec{x} \vec{N} \mathrm{d}\Gamma \tag{2.3}$$

$$P_{\mathrm{M}} = \left\langle P_{\mathrm{m}} \right\rangle_{\mathrm{RVE}} = \frac{1}{V_{\mathrm{RVE}}} \int_{\mathrm{RVE}} P_{\mathrm{m}} \mathrm{d}V = \frac{1}{V_{\mathrm{RVE}}} \int_{\Gamma} \bar{p}\bar{X} \mathrm{d}\Gamma \tag{2.4}$$

Here, V_{RVE} is the undeformed RVE, and P_{m} and F_{m} are the microscopic stress tensor and deformation gradient tensor, respectively, Γ represents the boundary of the RVE, while $\bar{N}$ represents the normal vector to the surface of the RVE.

2.3 Macroscopic tangent computation (consistent stiffness)

In the realization of the multilevel FEM approach, the macroscopic constitutive formulation is not explicitly obtained from the experimental data. Instead, the needed stiffness matrix at every macroscopic integration point has to be determined directly from the numerical relation of the macroscopic stress (P_{M}) and macroscopic deformation gradient (F_{M}) at that point.[11,14,15] The weak form of the macroscale problem in the absence of body forces and acceleration can be written in the variational form as:

$$\delta\pi = \int_{V_0} \delta F_{\mathrm{M}} \cdot P_{\mathrm{M}} \mathrm{d}V \tag{2.5}$$

To solve the macroscopic primal problem within the FE^2 setting, at the i-th iteration step of a standard Newton-Raphson solution scheme, the following linearization needs to be computed.

$$\begin{aligned} &\int_{V_0} \delta F_{\mathrm{M}} \cdot P_{\mathrm{M}}^{\mathrm{i}+1} \mathrm{d}V \approx \\ &\approx \int_{V_0} \delta F_{\mathrm{M}} \cdot P_{\mathrm{M}}^{\mathrm{i}} \mathrm{d}V + \int_{V_0} \delta F_{\mathrm{M}} \frac{DP_{\mathrm{M}}^{\mathrm{i}}}{DP_{\mathrm{M}}} \Delta F_{\mathrm{M}} \mathrm{d}V \end{aligned} \tag{2.6}$$

The macrolevel element tangent stiffness matrix and the residual force vector can be obtained with the knowledge of the stress (P_{M}) and macroscopic tangent ($\partial P_{\mathrm{M}} / \partial F_{\mathrm{M}}$) obtained from the RVE analysis, since F_{M} is an explicit function of the node displacements. The (P_{M}) can be obtained directly from the RVE analysis by using averaging theorem equation (2.4), while for the determination of the macroscopic tangent a RVE sensitivity analysis is performed. For the sensitivity problem[16] the residuals and the vector of unknowns are defined as a function of the sensitivity parameters, which are in this case the elements of the tensor (F_{M}). The sensitivity problem can then be obtained from the primal problem by differentiating the response functional and the residuals with respect to the macroscopic deformation gradient (F_{M}), and the following system on the microlevel has to be solved:

$$\frac{\partial \psi_{\mathrm{m}}}{\partial a} \frac{Da}{D\phi} = \frac{\partial \psi_{\mathrm{m}}}{\partial \phi} \tag{2.7}$$

where, ψ_{m} represents the response functional on the microlevel, a is a set of unknowns (displacements), while ϕ represents an arbitrary sensitivity parameter, in our case F_{M}.

With the assembling of the macroscopic stiffness matrix, the problem on the macro level is fully described and can be solved to produce an update of the macroscopic displacement field.

Remark 1: for consistency the particular type of BC employed for the computation of K must match the type of BC employed in the computation of P.

2.4 Finite-element implementation

The multiscale algorithm has been implemented into the computer program AceFEM,[17] where a special macroscopic element can be readily defined in open-source code. The mechanical characterizations of the microstructural components are modeled as Neo-Hook isotropic hyperelastic material for which the strain-energy function takes the form:

$$W = \frac{1}{2} \lambda_{\mathrm{g}} (J-1)^2 + \mu_{\mathrm{g}} \left(\frac{1}{2} (Tr[C]-3) - Ln[J] \right) \tag{2.8}$$

where $J = \det F$, C is the right Couchy-Green deformation tensor, with λ_{g} and μ_{g} as the first Lame constant and shear modulus.

The efficiency of the FE^2 method was enhanced by developing a framework that allows the micro-macro approach to be applied only at critical regions of the macrostructure, while for the other domains, the effective macroscopic properties are derived by the numerical homogenization of the micromechanical model. In order to evaluate the presented method a tree-point bending test, **Figure 2**, with a height-to-length ratio of 0.25 and unit thickness, load displacements Δ = 1 unit, under plain strain condition, has been examined. In the example two heterogeneous microstructures of a homogeneous matrix material with 6 % volume fraction of randomly distributed voids or stiff inclusions are studied. The tests were made in 2D and 3D geometry. The material parameters for the calculations are as follows: shear modulus of the matrix material and stiff inclusions are G_{m} = 77 GPa and G_{i} = 307 GPa, respectively, and the bulk modulus of the matrix material and stiff inclusions are K_{m} = 167 GPa and K_{i} = 667GPa, respectively. For the homogenized part the effective material constants are as follows: voided microstructure G = 72 GPa and K = 156 GPa, microstructure with stiff inclusions G = 90 GPa and K = 194 GPa.

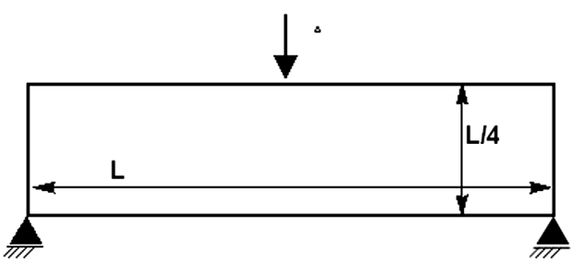

Figure 2: Three-point bending test
Slika 2: Tritočkovni upogibni preizkus

3 RESULTS – EXAMPLE OF MICRO-MACRO MODELING

Micro-macro calculations for a heterogeneous structure with voids and homogenized structure for the three-point bending test were carried out. In **Figure 3** the undeformed and deformed states of the two cases are presented. The contour plots of the equivalent Misses stress are compared. It is shown that in the case of micro-macro analysis, higher effective stresses occur than in the homogenized macrostructure.

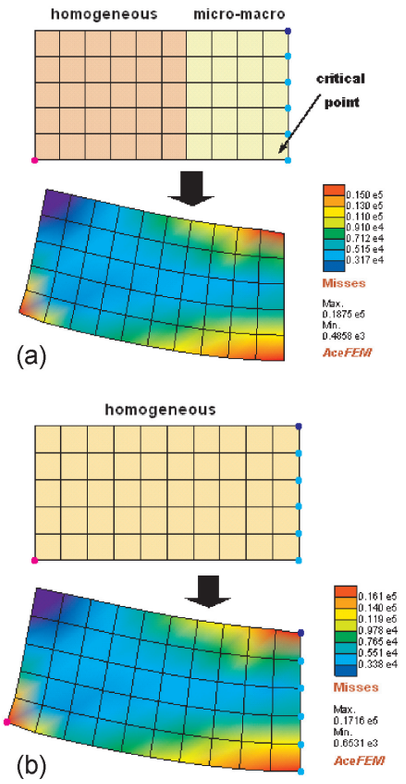

Figure 3: Macroscopic effective stress in micro-macro and homogenized problem, voided microstructure

Slika 3: Makroskopska efektivna primerjalna napetost za homogeniziran in mikro-makro problem, mikrostruktura s porami

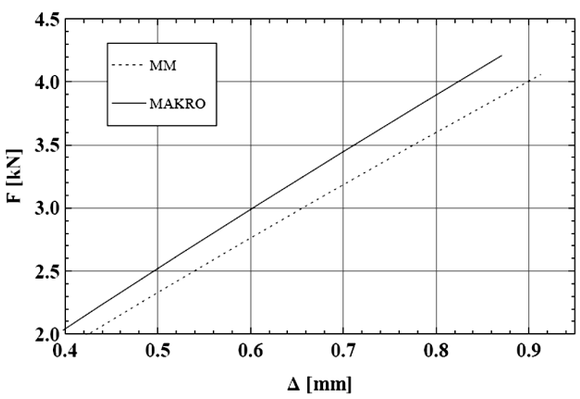

Figure 4: Loading force vs. displacement of a critical point from the micro-macro and homogenized problem, voided microstructure.

Slika 4: Sila obremenjevanja glede na pomik kritične točke za homogeniziran in mikro-makro problem, mikrostruktura s porami

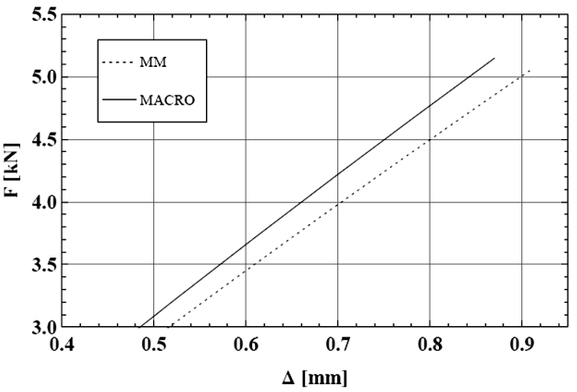

Figure 5: Loading force vs. displacement of a critical point from the micro-macro and homogenized problem, microstructure with stiff inclusions

Slika 5: Sila obremenjevanja glede na pomik kritične točke za homogeniziran in mikro-makro problem, mikrostruktura s togimi vključki

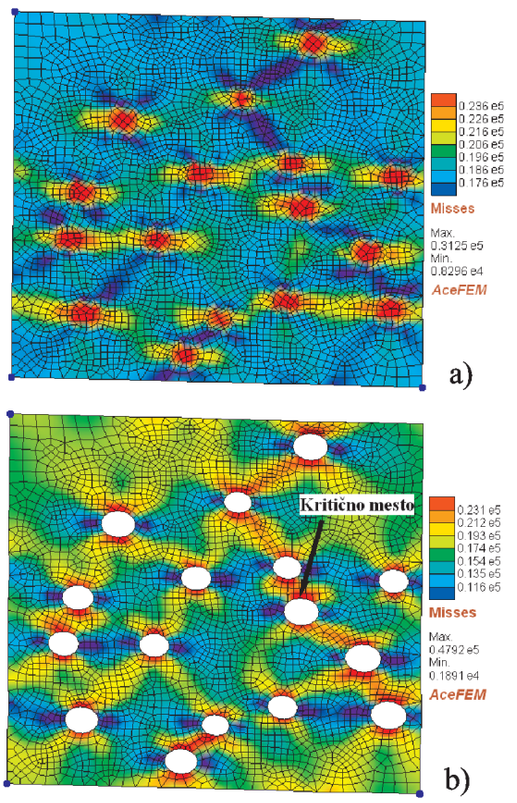

Figure 6: Effective stress in the RVE from the critical point of the macrostructure 2D a) stiff inclusions, b) voided microstructure.

Slika 6: Primerjalna napetost v RVE, vzet iz kritične točke makro strukture, a) mikrostruktura s togimi vključki, b) mikrostruktura s porami

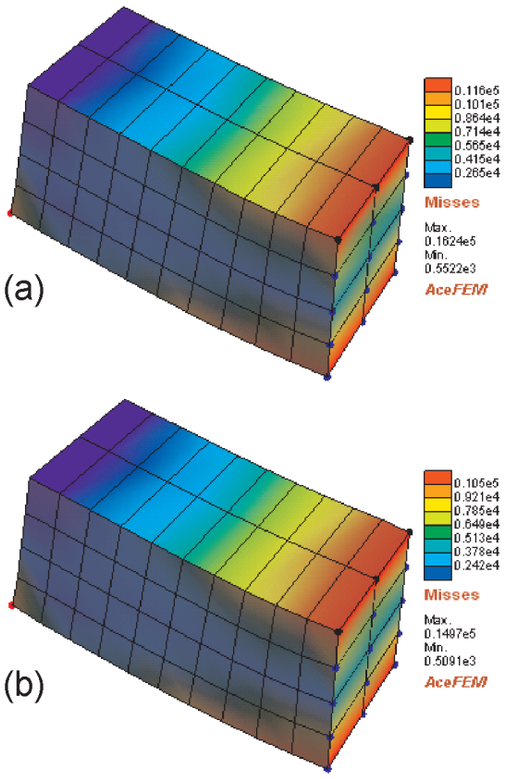

Figure 7: Macroscopic effective stress in the micro-macro and homogenized problems, voided microstructure
Slika 7: Makroskopska efektivna primerjalna napetost za homogeniziran in mikro-makro problem, mikrostruktura s porami

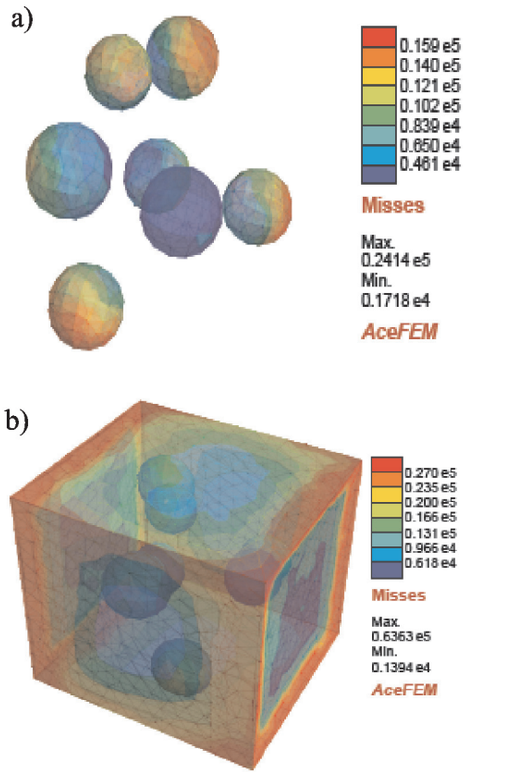

Figure 8: Effective stress in the RVE from the critical point of the macrostructure 3D a) stiff inclusions, b) voided microstructure
Slika 8: Primerjalna napetost v RVE, pripadajoč kritični točki makro strukture, a) mikrostruktura s togimi vključki, b) mikrostruktura s porami

Figure 4 shows a comparison of the load-displacement curve for micro-macro and homogenized analyses with a voided microstructure. The same situation for a microstructure with stiff inclusions is presented in **Figure 5**. The results imply that for the correct calculations, needed in precision-forming operations, the use of the micro-macro approach could provide a better estimation of the real situation. Namely, the results obtained with the micro-macro approach showed a softer response than the homogenized macrostructure.

The detailed analysis of the RVE in the critical point, the lower point in the middle of the three-point bending test, for both microstructures in 2D geometry are shown in **Figure 6**. It can be seen that the voids act as a stress concentrator and that some stress-concentration regions can be seen between the neighboring voids, **Figure 6b**. By comparing the stress field with the one in **Figure 3**, substantially higher stresses are observed. So by simultaneously examining the RVE at critical macro points, while deforming the macrostructure, a deeper understanding of the real deformation mechanisms is gained. In the case of stiff inclusions a detailed RVE analysis revealed the stress peaks in the inclusions, which can be very helpful in studying the damage mechanisms.

In addition to the 2D tests, some 3D tests were made. In **Figure 7** an effective Misses stress is shown for the two considered microstructures. By comparing the macroscopic stress field with the RVE stress field, **Figure 8**, again much higher stresses are observed.

4 CONCLUSIONS

In this work numerical models of heterogeneous materials were adapted to a multilevel finite-element framework called the FE^2 method. The key importance of this method is the efficient calculation of the macroscopic stiffness matrix, which can be done in various ways. Here, a general method for a calculation of the consistent macroscopic stiffness matrix via a sensitivity analysis of the micro level was developed. It enables a problem-solving tool for a wide variety of different micro-macro problems. Furthermore, the FE^2 method makes it possible to study easily the complex microstructural morphology and with a detailed RVE analysis it provides useful information for investigating damage mechanism at the micro level. Microstructures with stiff inclusions and voids were tested. The results showed that by using the

FE^2 method more accuracy and a deeper understanding of deformation mechanisms can be obtained.

5 REFERENCES

[1] Kouznetsova, V., Brekelmans, W. A. M., Baaijens, F. P. T.: An approach to micro-macro modeling of heterogeneous materials, Comp. Mech., 27 (**2001**), 37–48

[2] Temizer, I., Wriggers, P.: On the computation of the macroscopic tangent for multiscale volumetric homogenization problems, Comput. Methods Appl. Mech. Engrg., 198 (**2008**), 495–510

[3] Smit, R. J. M., Brekelmans, W. A. M., Meijer, H. E. H.: Prediction of the mechanical behavior of nonlinear heterogeneous systems by multi-level finite element modeling, Comput. Methods Appl. Mech. Engrg., 155 (1998), 181–192

[4] Miehe, C., Koch, A.: Computational micro-to-macro transitions of discretized microstructures undergoing small strains, Archive of Applied Mechanics, 72 (**2002**), 300–317

[5] Miehe, C.: Computational micro-to-macro transitions for discretized micro-structures of heterogeneous materials at finite strains based on the minimization of averaged incremental energy, Comput. Meth. Appl. Mech. Eng., 192 (**2003**), 559–591

[6] Feyel, F., Chaboche J. L.: FE2 multiscale approach for modelling the elastoviscoplastic behaviour of long fibre SiC/Ti composite materials, Comput. Methods Appl. Mech. Engrg., 183 (**2000**), 309–330

[7] Feyel, F.: Multiscale FE2 elastoviscoplastic analysis of composite structures, Comput. Mat. Sci., 16 (**1999**), 344–354

[8] Terada, K., Hori, M., Kyoya T., Kikuchi, N.: Simulation of the multi-scale convergence in computational homogenization approaches, International Journal of Solids and Structures, 37 (**2000**), 2285–2311

[9] Khisaeva, Z. F., Ostoja-Starzewski, M.: On the size of RVE in finite elasticity of random composites, J. Elasticity., 85 (**2006**),153–173

[10] Sluis, O., Schreurs, P. J. G., Brekelmans, W. A. M., Meijer H. E. H.: Overall behaviour of heterogeneous elastoviscoplastic materials: effect of microstructural modelling, Mechanics of Materials, 32 (**2000**), 449–462

[11] Temizer, I., Wriggers, P.: On the computation of the macroscopic tangent for multiscale volumetric homogenization problems, Comput. Methods Appl. Mech. Engrg., 198 (**2008**), 495–510

[12] Hill, R.: Elastic properties of reinforced solids : some theoretical principles, J. Mech. Phys. Solids., 2 (**1963**), 357–372

[13] Hill, R.: On constitutive macro-variables for heterogeneous solids at finite strain, Proc. R. Soc. Lond. A., 326 (**1972**),131–147

[14] Temizer, I., Zohdi, T. I.: A numerical method for homogenization in non-linear elasticity, Comput. Mech., 40 (**2007**), 281–298

[15] Miehe, C.: Numerical computation of algorithmic (consistent) tangent moduli in large-strain computational inelasticity, Comput. Methods Appl. Mech. Engrg., 134 (**1996**), 223–240

[16] Korelc, J. Automation of primal and sensitivity analysis of transient coupled problems, Comput. Mech., 44 (**2009**), 631–649

[17] Korelc, J.: AceGen & AceFEM user manual, FGG-UL, 2007

Martin Lamut[1] – Avtor ni več zaposlen na IMT.
(The Author is no longer with the Institute of Metals and Technology.)

UDK 669.1:621.785.33
Original scientific article/Izvirni znanstveni članek

ISSN 1580-2949
MTAEC9, 45(5)427(2011)

GENETIC PROGRAMMING AND SOFT-ANNEALING PRODUCTIVITY

GENETSKO PROGRAMIRANJE IN PRODUKTIVNOST MEHKEGA ŽARJENJA

Miha Kovačič[1], Božidar Šarler[2]

[1]ŠTORE STEEL d.o.o., Železarska cesta 3, SI-3220 Štore, Slovenia
[2]Laboratory for Multiphase Processes, University of Nova Gorica, Vipavska 13, SI-5000, Nova Gorica, Slovenia
miha.kovacic@store-steel.si

Prejem rokopisa – received: 2011-02-02; sprejem za objavo – accepted for publication: 2011-05-20

An optimal thermo-mechanical processing in the steel industry is difficult because of the multi-constituent and multiphase character of commercial steels, the variety of the possible processing paths and the plant-specific equipment characteristics. This paper shows a successful implementation of the genetic programming approach for increasing the furnace conveyor speed and consequently the higher productivity of the heat-treatment furnace in the soft-annealing process. The data (222 samples covering 24 different steel grades) on a furnace conveyor's speed, the chemical composition of the steel (weight percent of C, Cr, Mo, Ni and V) and the Brinell hardness before and after the soft annealing were collected during daily production. On the basis of the measured data a mathematical model for the hardness after the soft annealing was developed by genetic programming. According to the modelled influences on the hardness, a higher furnace conveyor speed was attempted in practice. The experimental results of the hardness after the soft annealing with the increased conveyor speed and the predictions of the mathematical model were compared with an agreement of 3.24 % (2.68 % at testing data set). The genetic model was also compared and verified with a linear regression model. As a consequence of the used computational intelligence approach, the productivity of the soft-annealing process increased (from the furnace conveyor speed 3.2 m/h to 7 m/h).

Keywords: steel, soft annealing, furnace productivity, hardness, modeling, genetic programming

Zaradi raznolikosti tehnoloških poti je v jeklarski industriji težko izbrati primerne parametre toplotne obdelave. V članku je predstavljen način, kako smo z metodo genetskega programiranja povečali produktivnost žarilne peči. Na podlagi podatkov o trdoti materiala pred mehkim žarjenjem in po njem (222 vzorcev, 24 različnih kvalitet jekla), o hitrosti žarjenja in kemični sestavi (C, Cr, Mo, Ni in V) smo z genetskim programiranjem dobili matematični model trdote materiala po mehkem žarjenju. Model smo preizkusili s testnimi podatki. Na podlagi modela, ki se odmika od eksperimentalnih podatkov za 3,24 % (2,68 % pri testnih podatkih), nam je uspelo hitrost žarjenja povečati s 3,2 m/h na 7 m/h.

Ključne besede: jeklo, mehko žarjenje, produktivnost peči, trdota, modeliranje, genetsko programiranje

1 INTRODUCTION

There is a strong demand in the steel industry for enhanced productivity, safety, and the environmental friendliness of the involved processes in parallel with the enhanced product variability and quality. In the past two decades, thermo-mechanical physical models have been increasingly developed for casting, rolling, and heat-treatment operations.[1] However, the current state of the art in physical modeling does not permit us to quantitatively model the whole range of steel behavior, neither from the microscopic materials science point of view, nor from the macroscopic process level. This is probably due to the multi-constituent and multi-phase character of the steel as well as due to the fact that the important physical processes took place over a huge range of length scales from the nanoscale up to 100 m. Physical modeling is thus increasingly connected with intelligent algorithms (such as, for example, artificial neural networks, evolutionary computation, swarm intelligence, artificial immune systems, and fuzzy systems)[2,3] which are to complement or replace the physical models in solving realistic industrial problems. An example of such symbiosis[4] is the continuous casting physical modeling with the evolutionary algorithm for searching the optimum casting conditions. The purpose of the heat treatment of steels is to obtain the desired changes in the metallurgical structure and thus material properties.[5] Soft annealing represents a heat treatment wherein a material is altered, causing changes in its ductility and hardness. Several attempts have been made to attain the control of the above-mentioned material properties during the soft-annealing treatment.[6–11] The aim of the present work is to determine the possibilities of increasing the furnace productivity (speed of the furnace conveyor) during the soft-annealing process. The genetic programming method is used in the present work to establish the relations between the chemical composition of the principal alloying elements (carbon, chromium, molybdenum, nickel and vanadium), the principal process parameters (such as the speed of the furnace conveyor), and the principal material property (hardness after soft annealing). Having the set of relations, more optimal conveyor speed could be easily determined with respect to the process-parameter constraints, i.e., the maximum possible speed of the conveyor, and product properties constraints, i.e., the maximum hardness.

Genetic programming is one of the methods of evolutionary computation.[12,13] In genetic programming, organisms which are more or less complicated computer programs, are subject to adaptation. In the present study the computer programs are in fact models for the prediction of hardness after soft annealing. Many different prediction models, differing in the quality of prediction and the complexity of the structure, were obtained during the simulated evolution. Only one model out of many is discussed in the paper.

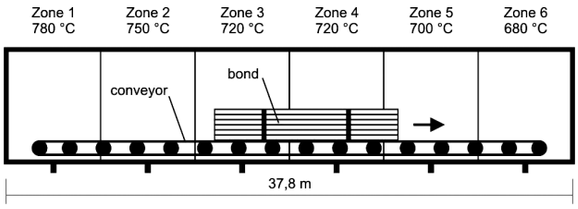

Figure 1: Heat-treatment furnace with its six equidistant soft-annealing temperature zones

Slika 1: Peč za toplotno obdelavo s šestimi ekvidistančnimi komorami z različnimi temperaturami

2 HEAT-TREATMENT FURNACE DESIGN AND EXPERIMENTAL DATA

All the experimental data used in the present paper were obtained from the pusher-type furnace of the Štore Steel steelworks, Slovenia, one of the major spring-steel producers in Europe. The scheme of the furnace is depicted in **Figure 1**. The hardness after the annealing process depends on the chemical composition of the steel and the furnace process parameters. The main difficulty with the research was that, according to the pace of production, the production lining parameters could only be monitored and not varied. The principal seven adjustable furnace process parameters are the six different temperatures of the heat-treatment zones and the time of the annealing (inversely proportional to the speed of the furnace conveyor). The principal two fixed construction parameters of the furnace are the maximum bond-specific weight of 2.5 t/m and the maximum conveyor speed of 7 m/h. The cross-sections of the round and flat bars in the bond varied from 43.28 mm^2 to 5676.40 mm^2. The temperature of the six heat-treatment zones was kept constant in all cases (see data in **Figure 1**). The only influential heat-treatment productivity process parameter was the speed of the furnace conveyor. The speed of the furnace conveyor was kept steady during the heat treatment of the individual bond. The required hardness of the annealed steel must be below 260 HB before the bond steel bars are subsequently saw-cut.

The number of each steel grade specimens and the average chemical composition (wt% of C, Cr, Mo, N and V) is shown in **Table 1**.

In the actual production technology only two furnace conveyor speeds of 2.5 m/h and 3.2 m/h were used for

Table 1: The number of steel grade specimens and the average chemical composition

Tabela 1: Število različnih kvalitet jekla in povprečna kemična sestava

			Composition				
#	Steel grade	Number of specimens	C [wt%]	Cr [wt%]	Mo [wt%]	Ni [wt%]	V [wt%]
1	15CrNi6	1	0.14	1.56	0.04	1.53	0
2	16MnCr5	1	0.19	1.03	0.02	0.09	0
3	17CrNiMo6	2	0.18	1.65	0.28	1.50	0
4	18 CrNi 8	1	0.19	1.95	0.02	2.01	0
5	18CrNiMo7-6	15	0.17	1.64	0.29	1.53	0.001
6	18CrNiMo7-6 HH	2	0.19	1.69	0.29	1.53	0
7	23MnNiCrMo5-2-A	12	0.22	0.49	0.21	0.47	0
8	25CrMo4	4	0.24	1.01	0.20	0.10	0
9	34CrNiMo6	28	0.36	1.61	0.22	1.60	0.003
10	41Cr4	7	0.42	1.08	0.03	0.11	0
11	42CrMo4	33	0.42	1.07	0.22	0.11	0
12	42CrMoS4	8	0.43	1.03	0.21	0.11	0
13	50CrMoS4	14	0.51	1.04	0.22	0.13	0
14	50CrV4	34	0.50	1.05	0.04	0.11	0.156
15	51CrMoV4	1	0.54	1.06	0.18	0.09	0.11
16	51CrV4	11	0.51	1.08	0.04	0.11	0.1555
17	51CrV4 HH	3	0.51	1.08	0.04	0.12	0.170
18	52CrMoV4	6	0.54	1.05	0.18	0.10	0.113
19	55Si7	16	0.57	0.29	0.04	0.12	0
20	70MnVS4	20	0.70	0.15	0.03	0.08	0.113
21	25CrMo4	1	0.24	1.05	0.21	0.14	0
22	42CrMo4	2	0.43	1.03	0.21	0.11	0
	SUM	222					

Table 2: Part of the monitored data set
Tabela 2: Del zbranih podatkov

#	Conveyor speed [m/h]	Hardness before the soft annealing [HB]	C [wt%]	Cr [wt%]	Mo [wt%]	Ni [wt%]	V [wt%]	Hardness after the soft annealing [HB]
1	3.2	298	0.51	1.09	0.22	0.19	0	219
2	3.2	248	0.43	1.08	0.02	0.1	0	191
13	3.2	313	0.69	0.14	0.02	0.08	0.11	229
4	3.2	309	0.70	0.13	0.02	0.08	0.12	215
5	3.2	290	0.55	0.28	0.04	0.12	0	229
6	3.2	290	0.59	0.36	0.05	0.12	0	229
…	…	…	…	…	…	…	…	…
220	3.2	298	0.17	1.64	0.29	1.53	0	198
221	3.2	290	0.40	1.04	0.22	0.08	0	207
222	3.2	333	0.52	1.14	0.05	0.11	0.15	229

soft annealing. The Brinell hardness for each data set before and after the soft annealing was measured at the bar centre at the three positions per bond: once from the bar taken from the bond surface and twice from the bar taken from the middle of the bond. Then the average hardness per bond was calculated and used for modeling. Only a part of the respective monitored data set is shown in **Table 2**.

3 GENETIC PROGRAMMING MODELING OF THE HARDNESS AFTER THE SOFT ANNEALING

Genetic programming is probably the most general evolutionary optimization method.[12,13] The organisms that undergo adaptation are in fact mathematical expressions (models) for the hardness after the soft annealing in the present work. The prediction consists of the available function genes (i.e., the basic arithmetical functions) and the terminal genes (i.e., the independent input parameters and the random floating-point constants). In the present case the models consist of the following function genes: addition (+), subtraction (–), multiplication (*) and division (/), and the following terminal genes: furnace conveyor speed (speed) in m/h, hardness before soft annealing (HB), in Brinell units, and the chemical composition of the principal alloying elements: carbon (C), chromium (Cr), molybdenum (Mo), nickel (Ni) and vanadium (V), in mass fractions (*w*/%). One of the randomly generated mathematical models (Mo/speed + V)·C/5.1 is schematically represented in **Figure 2** as a program tree with included function genes (*, + , /) and terminal genes (Mo, speed, V, C, and randomly generated real number constant 5.1).

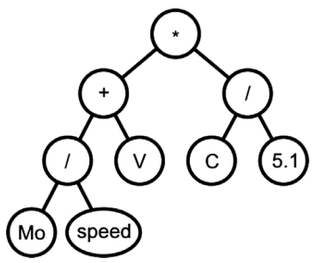

Figure 2: Randomly generated mathematical model for the hardness after the soft annealing, represented in the form of a program tree
Slika 2: Naključno ustvarjen matematični model za napovedovanje trdote po mehkem žarjenju, predstavljen kot programsko drevo

Random computer programs of various forms and lengths are generated by means of the selected genes at the beginning of the simulated evolution. The varying of the computer programs is performed by means of genetic operations during several iterations, known as generations. After the completion of the variation of the computer programs, a new generation is obtained. Each generation is compared with the experimental data. The process of changing and evaluating the organisms is repeated until the termination criterion of the process is fulfilled. The maximum number of generations is chosen as a termination criterion in the present algorithm.

The following evolutionary parameters were selected for the process of simulated evolutions: 500 for the size of the population of organisms, 100 for the maximum number of generations, 0.4 for the reproduction probability, 0.6 for the crossover probability, 6 for the maximum permissible depth in the creation of the population, 10 for the maximum permissible depth after the operation of the crossover of two organisms, and 2 for the smallest permissible depth of organisms in generating new organisms. The genetic operations of reproduction and crossover were used. For the selection of the organisms the tournament method with a tournament size of 7 was used. A total of 100 independent civilizations of the mathematical models for the prediction of the hardness after the soft annealing have been developed. Each evolution of the 100 generations has been computed for an average of 1 h on a 2.39 GHz processor and 2 GB of RAM using an AutoLISP in-house coded program.

The model fitness has been expressed in the L_2 norm as:

$$f = \frac{\sum_{i=1}^{n} (E_i - G_i)^2}{n} \quad (1)$$

where n is the size of the monitored data (in the present case 222), E_i and G_i are the values of the actual measured hardness after soft annealing and the model-predicted hardness after soft annealing, respectively.

In order to make the presentation more clear, let us have a closer look at the development of one of the independent civilizations with the previously mentioned genes. The result of the blind random searching for mathematical models in the initial generation is not, as expected, accurate enough. The best mathematical model (out of 100) for the prediction of the hardness after the soft annealing in the initial generation is:

$$\text{HB} - 9.44639\ (-\text{Mo} + 4.24533\ \text{speed}) \quad (2)$$

with a fitness of 4153.45 and an average percentage deviation of 21.36 %.

A better model develops (evolves) in generation 10:

$$2638.58 + \text{HB} + \text{Mo} - 0.105861\ \text{HB}\ (4.24533 - \text{Mo speed}) \quad (3)$$

with a fitness of 1082.28 and an average percentage deviation of 12.40 %. Increasingly better adopted and more complex mathematical models are created through further subsequent generations of the simulated evolution.

The best model of the civilization, also without the terminal gene Mo, occurred in the last, i.e., the 100th generation:

$$\begin{aligned}
&127.132 + 19.309\,\text{Cr} + \frac{\text{V}\left(3.436 + \text{Mo} + 4.117\,\text{Ni} - \frac{\text{V}}{\text{Mo}}\right)}{-2.234\,\text{Mo} + 2\,\text{Ni} + \frac{1}{\text{speed}} + \text{V}} + \frac{\left(\text{C} + \frac{1+\text{Cr}}{\text{V}}\right)\text{V}}{\text{Ni}\left(-1.234\,\text{Mo} - 1.234\,\text{Ni} + 2.845\,\text{speed} - \frac{\text{V}}{\text{Mo}}\right)} + \\
&\text{C}\left(136.993 + 6.298\,\text{Mo} + 38.664\,\text{Ni} + 6.117\,\text{V} - \frac{6\,\text{V}}{\text{Mo}} - \frac{\text{V}}{\text{Ni}} + \frac{-2.234\,\text{Mo} + \text{Ni} + \text{V}}{\text{Ni}} - \frac{-2.234\,\text{Mo} + \text{Ni} + 2\,\text{V}}{\text{Mo}}\right) + \\
&\text{Mo}\left(-2.234 - 2.234\,\text{Mo}\left(4.117 + \text{C} + \frac{\text{Cr}}{\text{Mo}} - 2\,\text{V}\right) + \text{V} + \frac{\left(\text{C} + \frac{1}{\text{V}}\right)\text{V}}{\text{Ni speed}}\left(\left(\frac{\text{Cr}}{\text{Mo}} - \frac{(0.2429 + \text{C})(-2.234\,\text{Mo} + \text{Ni} + 2\,\text{V})}{\text{speed}}\right) + \right.\right. \\
&\qquad 0.021\left(\text{HB} + \text{Mo} + \frac{2 + 2\,\text{Mo} + 5.117\,\text{Ni} + \frac{\text{speed}\left(2\text{C} + \frac{1}{\text{Cr}\text{V}}\right)}{\text{Cr}} + \text{V} - \frac{\text{V}}{\text{Ni}}}{-1 + 19.075\,\text{Mo} + 6.117\,\text{Ni} - \frac{4.117\text{V}}{\text{Mo}} - \frac{\left(\text{C} + \frac{\text{Cr}}{\text{Mo}}\right)\text{V}}{\text{speed}} - \frac{\text{V}}{\text{Ni}+\text{V}}}\right) + \\
&2.845\left(\text{speed} + \text{V}\left(19.309\,\text{Cr} - 1.234\,\text{Mo} + \frac{\frac{\text{C}+\text{Cr}}{\text{speed}} + \frac{\text{C}+\text{Cr}}{\text{speed}}}{19.309\,\text{Mo} + 5.117\,\text{Ni} + 4.117\,\text{V} - \frac{\text{V}}{\text{Mo}}} - \frac{4.117\,\text{Ni} + \frac{\text{Cr}+\text{C}\,(4.117+4.117\text{V})}{\text{speed}}}{-2.234 + 20.309\,\text{Mo} + 2\,\text{Ni} + \text{V} - \frac{2\,\text{V}}{\text{Mo}}}\right)\right)
\end{aligned} \quad (4)$$

with a fitness of 90.79 and an average percentage deviation of 3.24 %.

The development of the best organism – the best mathematical model for hardness after soft annealing can be easily represented with the fitness curve in **Figure 3**.

The randomly driven process builds the fittest and complex models from generation to generation and uses

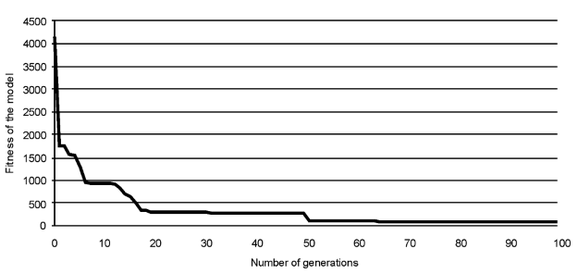

Figure 3: Fitness curve from generation 0 to 100
Slika 3: Uspešnost generacij od 0 do 100

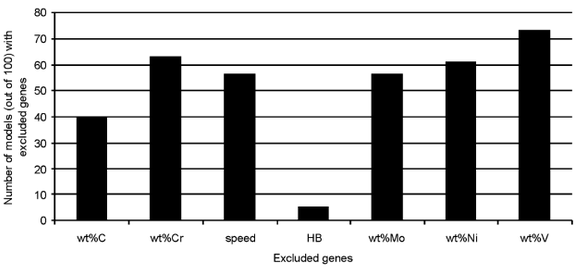

Figure 4: Frequency of the excluded genes from the best 100 mathematical models for hardness after soft annealing
Slika 4: Število genov, ki so bili izločeni v najboljših 100 matematičnih modelih za napovedovanje trdote po mehkem žarjenju

ingredients that are most suitable for the experimental environment adaptation. The analysis of the excluded genes (parameters) from the model is presented in **Figure 4**.

According to the number of excluded genes in 100 obtained mathematical models, we may assume the influence of the parameters on the hardness after soft annealing. It is clear from **Figure 4** that out of 100 genetically obtained mathematical models only 5 models exclude the parameter hardness before soft annealing. So we can speculate that this parameter is probably one of the most important parameters influencing the hardness after soft annealing. It also seems that the conveyer speed does not influence the material hardness after soft annealing.

4 MODEL COMPARISON AND VERIFICATION

For a comparison and verification of the usefulness of the genetic programming approach the linear-regression method for modeling the hardness after soft annealing was also used. The same monitored data set (**Table 2**) give us the results collected in **Table 3** and the idea how the classical modeling approach can deal with temperature-treating furnace-productivity problems.

The linear-regression model according to results is:

$$\begin{aligned}
&-0.624 \cdot \text{speed} + 0.018 \cdot \text{HB} + 128.076 \cdot \text{C} + 17.942 \cdot \\
&\cdot \text{Cr} - 14.613 \cdot \text{Mo} + 5.717 \cdot \text{Ni} - 12.123 \cdot \text{V} + \\
&+ 141.409
\end{aligned} \quad (6)$$

with a selected genetic programming fitness (the average squares of deviation from the monitored data) of 173.79 and an average percentage deviation 4.50 %. The linear regression results show that the conveyor speed, the hardness before soft annealing, and the w(Mo)/% and w(V)/% (significance is above 0.05) do not significantly influence the hardness after soft annealing.

The genetic programming results of the fitness of 90.79 and the average percentage deviation of 3.24 % are favorable, compared to the results obtained by the classical statistical analysis.

Table 3: Linear regression results
Tabela 3: Rezultati linearne regresije

Coefficients					
Model	Unstandardized Coefficients		Standardized Coefficients	T	Sig.
	B	Std. Error	Beta		
(Constant)	141.409	12.017		11.767	0.000
Conveyor speed [m/h]	-0.624	3.028	-0.010	-0.206	0.837
Hardness before soft annealing	0.018	0.023	0.057	0.781	0.436
wt%C	128.076	12.501	0.955	10.245	0.000
wt%Cr	17.942	3.634	0.420	4.937	0.000
wt%Mo	-14.613	17.045	-0.073	-0.857	0.392
wt%Ni	5.717	2.484	0.183	2.302	0.022
wt%V	-12.123	21.483	-0.044	-0.564	0.573

5 PRACTICAL IMPLEMENTATION

The maximum furnace conveyor speed, declared by the furnace producer, is 7 m/h. As previously mentioned, the required hardness of the cutting material should be below 260 HB in order to satisfy the product's quality requirement.

Both approaches – genetic programming and linear regression – show that the conveyer speed is not one of the influencing parameters.

The previously mentioned results and behavior regarding the sensitivity of the furnace conveyor speed in the soft-annealing process allow us to carefully (in several steps) increase the conveyor speed up to 5 m/h and finally for 7 m/h in industrial practice. The experimental results of the hardness for 13 specimens are shown in **Table 4**, compared with the calculated values from the computational intelligence model and the linear regression model.

The hardness of all 13 measured specimens was below the required 260 HB. The average percentage deviation was as low as 2.68 % and 4.44 % for the genetic programming model and the linear regression model, respectively.

6 CONCLUSIONS

The possibility of a productivity enhancement for the heat-treatment furnace with the soft annealing of round and flat steel bars in the Štore Steel company was studied. The Brinell hardness after the process was measured for 24 different steel grades as a function of the furnace process parameters and steel composition. This established an experimental database for the deve-

Table 4: Measured and calculated hardness after soft annealing
Tabela 4: Izmerjene in izračunane trdote po mehkem žarjenju

#	Conveyor Speed [m/h]	Hardness before soft-annealing	C [wt%]	Cr [wt%]	Mo [wt%]	Ni [wt%]	V [wt%]	Hardness after the soft annealing (monitored) [HB]	Hardness after the soft annealing (genetic programming model) [HB]	Hardness after the soft annealing (linear regression model) [HB]	Percentage deviation (genetic programming)	Percentage deviation (linear regression)
	5.0	298.0	0.59	0.28	0.05	0.13	0.00	229	237.089	227.062	3.53%	0.85%
	5.0	464.0	0.34	1.51	0.20	1.50	0.01	229	235.528	225.618	2.85%	1.48%
3	5.0	335.0	0.53	1.13	0.05	0.19	0.14	229	236.332	233.940	3.20%	2.16%
4	5.0	438.0	0.36	1.64	0.23	1.64	0.01	229	241.571	230.406	5.49%	0.61%
5	5.0	438.0	0.34	1.51	0.20	1.50	0.01	229	234.982	225.150	2.61%	1.68%
6	5.0	339.0	0.43	1.18	0.22	0.15	0.00	215	224.551	221.085	4.44%	2.83%
7	5.0	339.0	0.43	1.18	0.22	0.15	0.00	215	224.551	221.0859	4.44%	2.83%
8	5.0	309.0	0.7	0.12	0.02	0.07	0.11	215	216.467	237.2396	0.68%	10.34%
9	5.0	309.0	0.7	0.12	0.02	0.07	0.11	215	216.467	237.2396	0.68%	10.34%
10	5.0	309.0	0.7	0.13	0.02	0.08	0.12	215	214.519	237.355	0.22%	10.40%
11	7.0	335.0	0.55	1.14	0.03	0.12	0.15	249	237.717	236.3271	4.53%	5.09%
12	7.0	313.0	0.53	1.13	0.03	0.10	0.15	239	235.34	233.0758	1.53%	2.48%
13	7.0	361.0	0.54	1.08	0.17	0.09	0.12	249	250.438	232.5842	0.58%	6.59%
Average percentage deviation										2.68%	4.44%	

lopment of 100 models deduced through genetic programming methodology. Genetic programming predicts the hardness after the soft annealing with an average percentage deviation of only 3.24 %. Also, the linear regression method was used for modeling and gave us similar results of an average percentage deviation of 4.50 %. The best models (genetic programming and linear regression) were closely analyzed and it was established that the furnace conveyer speed is not a sensitive parameter for influencing the hardness after the soft annealing. A statistically significant influence, according to linear regression, comes from the w(C)/%, w(Cr)/% and w(Ni)/%.

These findings lead to changes of the maximum furnace conveyor speed from 3.2 m/h up to 7 m/h in production practice. The substantially higher conveyor speed did not influence the hardness of the steel after soft annealing, as expected from the model prediction. The hardness after the soft annealing was below the required hardness of 260 HB also in the case of the enhanced conveyor speed in all 13 tested cases. The agreement between the tested and the calculated data is 2.68 % and 4.44 % for the genetic programming model and the linear regression model, respectively. Our future research, coming straight from the present paper, is aimed to continue towards the possibility of optimizing other material properties, for instance tensile strength. In this case also the variation of the annealing temperature in the six control zones of the heat-treatment furnace probably has to be taken into account. There are many important topics connected with the relations of the steel composition and the material properties of the steel (including the hardness) that require the additional attention of the computational intelligence and materials science community. The present paper shows the relevance and success of using the genetic programming for straightforward analyses and the optimization of an industrial problem.

Acknowledgement

The authors acknowledge the Štore Steel company for its permission to publish the present research. The project was funded by Štore Steel company and the Slovenian Research Agency under grant L2-7204.

7 REFERENCES

[1] B. Verlinden, J. Driver, I. Samajdar, R. D. Doherty, Thermo-mechanical processing of metallic materials, Elsevier, Amsterdam, 2007, 1–5

[2] A. P. Engelbrecht, Computational intelligence – An introduction, Second Edition, J. Willey & Sons, Chichester, 2007, 11–13

[3] B. Igor, Neural networks and modelling in vacuum science. Vacuum, (**2006**) 80, 1107–1122

[4] B. Šarler, B. Filipič, M. Raudensky, J. Horsky. An interdisciplinary approach towards optimum continuous casting of steel, Materials Processing in the Computer Age III, TMS, Warrendale, 2000, 27–36

[5] G. E. Totten, M. A. H. Howes, Steel treatment handbook, Marcel Dekker, New York, 1997, 1–44

[6] Zeytin, H. K., Aydin, C. K. H. Investigation of dual phase transformation of commercial low alloy steels: Effect of holding time at low inter-critical annealing temperatures. Materials Letters, 62 (**2008**) 17–18, 2651–2653

[7] Kain, V., Gupta, V., Pranab K. Embrittlement cracking of a stabilized stainless steel wire mesh in an ammonia converter. Environment-induced cracking of materials, 2008, 411-420

[8] J. S. Broughton, M. Mahfouf, D. A. Linkens, Paradigm for the scheduling of a continuous walking beam reheat furnace using a modified genetic algorithm, Materials and Manufacturing Processes, 22 (**2007**), 607–614

[9] S. S. Sahay, R. Mehta, K. Krishnan, Genetic-algorithm-based optimization of an industrial age-hardening operation for packed bundles of aluminum rods, Materials and Manufacturing Processes, 22 (**2007**), 615–622

[10] R. Mehta, S. S. Sahay, A. Datta, A. Chodha, Neural network models for industrial batch annealing operation, Materials and Manufacturing Processes, 23 (**2008**), 204–209

[11] N. Chakraborti, K. J. A. Deb, A genetic algorithm based heat transfer analysis of a bloom re-heating furnace, Steel Research, 71 (**2000**), 396–402

[12] J. R. Koza, Genetic Programming III. Morgan Kaufmann, San Francisco, 1999, 3–16

[13] M. Kovačič, P. Uratnik, M. Brezočnik, R. Turk, Prediction of the bending capability of rolled metal sheet by genetic programming, Materials and Manufacturing Processes, 22 (**2007**), 634–640

UDK 54:66
Original scientific article/Izvirni znanstveni članek

ISSN 1580-2949
MTAEC9, 45(5)433(2011)

SEMI-SOLID GEL ELECTROLYTES FOR ELECTROCHROMIC DEVICES

POLTRDNI GELSKI ELEKTROLITI ZA ELEKTROKROMNE NAPRAVE

Metka Hajzeri[1], Marija Čolović[1], Angela Šurca Vuk[1,*], Uwe Posset[2], Boris Orel[1]

[1]National Institute of Chemistry, Hajdrihova 19, SI-1000 Ljubljana, Slovenia
[2]Fraunhofer Institut Silicatforschung ISC, Neunerplatz 2, D-9782 Wuerzburg, Germany
angela.surca.vuk@ki.si

Prejem rokopisa – received: 2010-10-20; sprejem za objavo – accepted for publication: 2011-07-12

The di-urethanesil organic-inorganic hybrid bis N-triethoxysilyl propylcarbamoil poly(ethylene oxide) 400 (PEOCS) was used for the preparation of electrolytes appropriate for applications in electrochromic devices. The obtained PEOCS-based sol-gel network was able to accommodate the co-solvent γ-butyrolactone up to a molar ratio of PEOCS : γ-butyrolactone = 1 : 20. Lithium bis(trifluoromethanesulfonyl)imide was used as a guest salt. The initial conductivities were of the order 10^{-4} S/cm to 10^{-3} S/cm, but diminished during the course of the condensation reactions. This decrease was less obvious when a larger amount of co-solvent was present. The time-dependent stability of the conductivity was achieved with the addition of 3-chloropropylmethyldimethoxysilane. The best response was achieved for electrochromic devices with the electrolyte PEOCS : γ-butyrolactone : Li^+ salt = 1 : 15 : 0.5, with or without a dialkoxysilane additive.

Keywords: di-uretanesils, ormolytes, organic-inorganic hybrids, EC devices

Di-uretanesilni organsko-anorganski hibrid bis N-trietoksisilil propilkarbamatoil poli(etilen oksid) 400 (PEOCS) smo uporabili za pripravo elektrolitov za elektrokromne naprave. V nastale sol-gel mreže PEOCS smo lahko vključili sotopilo γ-butirolakton celo do molskega razmerja PEOCS : γ-butirolakton = 1 : 20. Litijev bis(trifluorometansulfonil)imid smo uporabili kot litijevo sol. Začetne prevodnosti gelov so se bile v območju od 10^{-4} S/cm do 10^{-3} S/cm, vendar so se nekoliko zmanjšale kot posledica reakcij kondenzacije. To zmanjšanje je bilo manjše v primeru večje vsebnosti so topila v elektrolitu. Časovno stabilnost prevodnosti pa smo dosegli z dodatkom 3-kloropropilmetildimetoksisilana. Najboljše lastnosti smo dosegli z elektrokromnima sklopoma z elektrolitoma PEOCS : γ-butirolakton : Li^+ sol = 1 : 15 : 0,5, brez dodatka dialkoksisilana ali z njim.

Ključne besede: di-uretanesili, ormoliti, organsko-anorganski hibridi, EC-sklopi

1 INTRODUCTION

Conventional battery-type electrochromic (EC) devices consisting of two films with intercalation properties are well established as smart windows, enabling the control of heat-loads and illumination levels inside buildings simply by the application of a potential pulse at the occupant's will[1]. Electrolytes play an important role in electrochromic devices, enabling their functioning and ensuring long exploitation times but, despite numerous investigations, they have remained the weakest part of the whole system. Since liquid electrolytes present long-term sealing problems, various polymeric electrolytes have been tested to date[2], such as proton-conducting electrolytes on the basis of either poly(vinyl alcohol) [3] or poly(vinyl acetate) [4], and lithium salts incorporated into various polymers, such as poly(methyl methacrylate) (PMMA) [5], poly(ethylene oxide) (PEO) [6] and organic-inorganic hybrids[2,7–8]. The latter materials belong to a special class of advanced polymeric materials[9–10] that combine the flexibility of the organic phase like PEO, poly(propylene oxide) (PPO) and poly(propylene glycol) (PPG) with the hardness of the inorganic phase. The latter is introduced as a simple tetraalkoxysilane compound (Class I) or is linked to the organic part via a covalent bond (Class II) [9]. From the materials processing perspective, organic-inorganic hybrids provide the possibility of making a variety of products with multifunctional properties, especially through the use of various trialkoxysilanes (Class II) characterised by hydrolysable reactive trialkoxy groups, which can undergo the sol-gel reactions of hydrolysis (solvolysis) and condensation, leading to the formation of tridimensional networks. Such hybrid electrolytes are called ormolytes (organically modified silicate electrolytes) and are characterised by good transparencies and ionic conductivities of 10^{-6} S/cm to 10^{-4} S/cm, while the mechanical properties surpass those of organic conducting polymers[11–13].

In previous years, we have investigated in our laboratory a di-ureasil organic-inorganic hybrid bis[(N′-(3-triethoxysilylpropyl)ureido]-terminated poly(propylene glycol) 4000 (PPGU, for short), in which the PPG segments and a siloxane backbone are covalently bonded through urea (-NH-C(=O)-NH-) groups, as an electrolyte for proton-conducting membranes in fuel cells[13] and also as a redox electrolyte for dye-sensitised photoelectrochemical cells (DSPEC) [14]. The results have shown a promissing efficiency of 4.1 % for DSPEC, while the conductivity values of membranes were of the order of magnitude of 10^{-4} S/cm to 10^{-3} S/cm at room tem-

perature. Similar di-ureasils, but with PEO chains, have also been studied as ormolytes doped with lithium triflate[15–16], perchlorate[17–18] and bis(trifluoromethanesulfonyl)imide (LiTFSI) [19–21]. The reason for using PEO chains in these ureasil hybrids is their remarkable ability to solvate cations; however, plain salt-PEO mixtures possess rather poor conductivities as a result of the fact that salts increase the tendency of PEO to crystallise and also shift the glass-transition temperature T_g to higher values[22]. On the other hand, organic-inorganic hybrids are often completely amorphous, which improves the ion transport, possess good thermal stability, mechanical resistance and can be easily prepared in the form of thin films. An extensive ATR IR study of ormolytes with lithium triflate[16] have shown that Li^+ ions bond to carbonyl oxygens, leading to the disruption of the PEO/urea and urea/urea hydrogen bonds and to the formation of new and more ordered hydrogen bonded associations. Moreover, at higher Li^+ uploads ($n \leq 20$; $n = OCH_2CH_2/Li^+$), the cation also bonded to the ether oxygen atoms of the PEO chains[16]. The conductivity of the electrolytes with lithium triflate was from 10^{-6} S/cm to 10^{-5} S/cm at room temperature, depending on the amount of salt[15]. However, when lithium perchlorate or LiTFSI was used, the ionic transport became almost independent of the salt concentration and the conductivity increased to an order of magnitude of 10^{-6} S/cm to 10^{-4} S/cm[17,19]. The application of these electrolytes in semi-solid-state EC devices is proposed[20,23–24].

A similar organic-inorganic hybrid on the basis of PEO chains and ethoxysilyl groups, which can be classified as single end-capped urethanesil (urethane -NH-C(=O)-O- bond instead of urea one), was also investigated as an electrolyte with lithium triflate salt[25]. The results showed moderate conductivity values (approximately 10^{-6} S/cm) but the electrochemical window was quite large, the mechanical properties were good and the electrolyte films were highly transparent. The described properties therefore encouraged us to re-examine the properties of urethanesils as possible precursors for the preparation of electrolytes for EC devices (**Figure 1**).

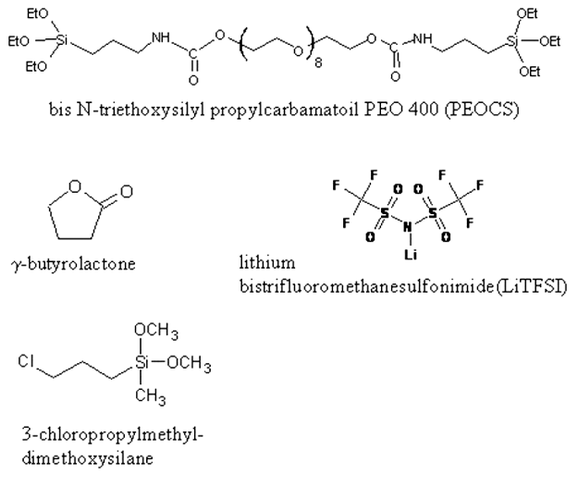

Figure 1: Precursors used for the preparation of the electrolytes for EC devices

Slika 1: Prekurzorji za pripravo elektrolitov za EC-sklope

An analogous di-urethanesil compound, bis end-capped sol-gel precursor bis N-triethoxysilyl propyl-carbamoil poly(ethylene oxide) 400 (PEOCS, for short), was synthesised. This compound is characterised by a urethane -NH-C(=O)-O- covalent bond that forms between the isocyanato group of the 3-isocianatopropyl-triethoxysilane and the terminal hydroxyl group of a poly(ethylene glycol) (PEG). Glacial acetic acid ($AcOH_{gl}$) was chosen as the catalyst for the initiation of sol-gel processes, which inevitably leads to the polycondensation of a bis end-capped alkoxysilane PEOCS precursor through a non-hydrolytic solvolysis route, liberating ester molecules[26]. In order to improve the conductivity values, γ-butyrolactone (γ-BL in **Figure 1**) was included in the sol-gel PEOCS network as a co-solvent, because it has already been successfully tested as an additive for lithium ion batteries[27]. The PEOCS hybrid and co-solvent were fully compatible and no segregation of the phases was noted. The final electrolytes were obtained after the dissolution of the LiTFSI (**Figure 1**) salt and were applied in EC devices between electrochromically active poly(3,4-ethylenedioxythiophene) (PEDOT) and V_2O_5 counter-electrode films. The performance of the EC devices was evaluated by *in-situ* UV-visible spectroelectrochemical measurements.

2 EXPERIMENTAL

The PEOCS was prepared by the reaction of 3-isocyanatopropyl-triehoxysilane with an equimolar amount of polyethylene glycol 400 (PEO 400) in tetrahydrofuran (THF). The reaction mixture was stirred together under reflux for 10 h. The THF was evaporated and the final product PEOCS was obtained. The electrolytes were made by mixing PEOCS : γ-BL : LiTFSI in molar ratios of 1 : 1 : 0.5, 1 : 15 : 0.5 and 1 : 20 : 3, with n values (where n is the molar ratio of ethyleneoxide moieties per Li^+ ion) of 18, 18 and 3, respectively. The solutions were stirred for several hours until the lithium salt dissolved and then glacial $AcOH_{gl}$ in a molar ratio of PEOCS : $AcOH_{gl}$ = 1 : 6 was added to initiate the sol-gel processes of the alkoxy groups. The fourth electrolyte was prepared with a molar ratio PEOCS : γ-BL : LiTFSI of 1 : 15 : 0.5, but before the addition of LiTFSI and glacial $AcOH_{gl}$, 0.5 mmol of 3-chloropropylmethyldimethoxysilane (CPMDMS in **Figure 1**) was added.

The specific conductivity was measured on an Autolab PGSTAT302N potentiostat-galvanostat with an FRA module in a Teflon cell between two Pt electrodes. The frequency range used for the electrochemical

impedance spectroscopy (EIS) was 10^5 to 0.01 Hz. The conductivity (σ/(S/cm)) was calculated according to the equation $\sigma = d/RA$, where R is the measured resistance obtained from the impedance plots, while d and A are the thickness and the area of the sample between the Pt electrodes.

All the types of ormolytes were used for the preparation of the EC devices, with a composition ITO-PET / PEDOT / various electrolytes / V_2O_5 (dip-coated) / FTO glass. The optically active PEDOT films[28] were deposited on sputtered ITO-PET substrates (CPFilms, Inc.; 125 μm, 60 Ω) using a roll-to-roll deposition technique (ISC Fraunhofer). The V_2O_5 films were prepared by the sol-gel route from vanadium (V) oxoisopropoxide[29], deposited by dip-coating on FTO glass (Pilkington) and thermally treated at 150 °C for 1 h. Prior to the EC device assembly, both film electrodes were stabilised in 1-M $LiClO_4$/propylene carbonate (PC) and the assembly was performed with reduced PEDOT and oxidized V_2O_5 films. The devices were designated according to the electrolyte composition, i.e., D(1–1–0.5), D(1–15–0.5), D(1–20–3) and the one with CPMDMS additive D(CPMDMS).

The *in-situ* UV-visible absorbance spectroelectrochemical characterisation of the EC devices was performed using a HP8453 diode array spectrophotometer and an Autolab PGSTAT30 potentiostat-galvanostat. The UV-visible spectra were recorded relative to an empty holder during chronocoulometric (CC; –2 V, 100 s and 2 V, 100 s) measurements every 4 s.

3 RESULTS AND DISCUSSION

Conductivity measurements. Conductivity measurements revealed that pure PEOCS is characterised by a conductivity value of $4 \cdot 10^{-8}$ S/cm, which is far too low for applications in any electrochemical device. The electrolytes for EC devices were therefore made by mixing of organic-inorganic hybrid PEOCS with γ-BL as the co-solvent and then the LiTFSI salt was added. Glacial $AcOH_{gl}$ was used as the catalyst for initiation of the sol-gel processes and the progress of the condensation of the sol-gel network could be evaluated from the conductivity values of the electrolytes, as shown in **Figure 2**. The decrease in conductivity up to the 8th day was most evident for the electrolyte prepared with the molar ratio PEOCS : γ-BL : LiTFSI = 1 : 1 : 0.5 (n = 18), with the lowest content of co-solvent. The value of n was, in this case, close to the values reported as the most optimal for achieving the highest conductivities, i.e., 15–25 depending on the electrolyte composition. When the amount of co-solvent was increased to PEOCS : γ-BL : LiTFSI = 1 : 15 : 0.5 (n = 18), a gradual drop in the conductivity up to the 14th day was still observed, but it was smaller. A simultaneous increase in the content of co-solvent and lithium salt, however, had a beneficial influence on the conductivity value, which did not change significantly with time, but the large amount of lithium salt induced the haziness of the electrolyte. Another approach was, therefore, used to improve the stability of the conductivity response with time. Namely, with the addition of various dialkoxysilanes, which can contribute to condensation reactions in only two directions, it is possible to prevent shrinkage of the sol-gel network. Therefore, 3-chloropropylmethyldimethoxysilane (CPMDMS in **Figure 1**) was added to the electrolyte with a molar ratio of PEOCS : γ-BL : LiTFSI = 1 : 15 : 0.5 and the conductivity did not change with time up to the 18th day (**Figure 2**).

Glass-transition temperature measurements. The T_g value is an important characteristic of ormolytes, since it controls the lower temperature limit of conduction in these materials and should therefore be kept as low as possible. Korwin and Masui[30] found that an increase in Li^+ and tetraethoxysilane content raises the T_g of the incorporated polyether, due to a restriction of the polymer's segmental motion by dipole-dipole and ion-dipole interactions and also by the cohesive contraction of the material. DSC measurements revealed that the T_g value of our PEOCS was –71.0 °C. Interestingly, de Zea Bermudez et al. [25] observed two T_g values, at –110 °C (T_{g1}) and –30 °C (T_{g2}) for undoped urethanepropyltriethoxysilane; however, their uretanesil compound was single end-capped and characterised by 7 repeating ethyleneoxide units. They tentatively associated T_{g2} with the mobility of the short side pendant oligopoly(ethyleneoxide) chains, but the origin of T_{g1} remained unassigned. The addition of a co-solvent to the PEOCS : γ-BL : LiTFSI = 1 : 1 : 0.5 electrolyte increased the T_g value to –39.0 °C, which is usually correlated with a decrease in the flexibility of the host polymer chain segments[19]. However, the concurrent increase in the conductivity values can be ascribed to the different constitution of the electrolyte, due to the presence of a

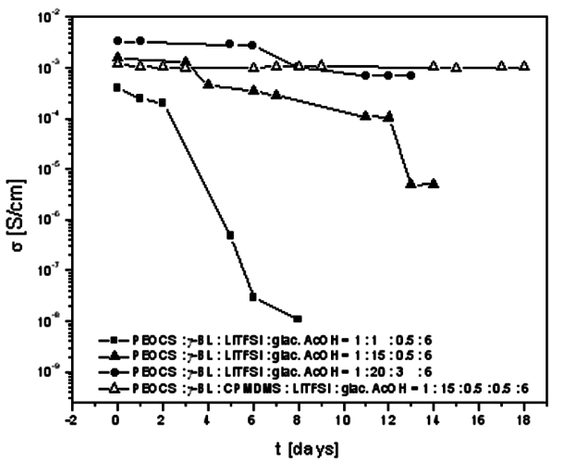

Figure 2: Time-dependent conductivity measurements of various PEOCS-based electrolytes

Slika 2: Časovno odvisne meritve prevodnosti različnih elektrolitov na osnovi PEOCS

liquid phase, which enabled ion transport to occur, not only by the segmentional motion of the polymer chains but also by diffusion through the liquid phase. Electrolytes with a higher content of γ-butyrolactone no longer showed T_g values.

Electrochromic devices. The described PEOCS-based electrolytes were also tested in EC devices with an optically active PEDOT layer and a V_2O_5 counter-electrode film. The first electrolyte tested was PEOCS : γ-BL : LiTFSI = 1 : 15 : 0.5 (EC device D(1–15–0.5) in **Figure 3**). As is evident from **Figure 3A**, the transmittance of the device D(1–15–0.5) in the bleached state was low, i.e., below 33 % *T*, and the optical modulation at 634 nm was about 20 %. This is a consequence of the large thickness of the roll-to-roll deposited PEDOT films (800 nm) and, for comparison, the *in-situ* UV-visible measurement of a PEDOT film in a three-electrode electrochemical cell filled with 1-M $LiClO_4$/PC electrolyte is shown (**Figure 3A**), revealing the optical modulation $\Delta T_{634\ nm} \approx 34$ %. The *in-situ* UV-visible measurements of the EC device D(1–15–0.5) showed that this device coloured in approximately 12 s and bleached in 8 s when exposed to potentials ±2 V vs. a counter electrode (**Figure 3B**).

When equivalent EC devices D(1–1–0.5) and D(1–20–0.5) were made, the recorded optical changes between the coloured and bleached states (Figure 4) were even smaller than in the case of device D(1–15–0.5) (**Figure 3**). The reason for the lower mobility of ions in D(1–1–0.5) in **Figure 4** is probably the smaller content of solvent, while for D(1–20–3), the amount of solvent was large (1 : 20). However, this electrolyte also contained a much larger amount of LiTFSI salt, which negatively influenced the performance of this EC device.

The performance of the EC device D(CPMDMS), which was prepared from electrolyte PEOCS : γ-BL : CPMDMS : LiTFSI = 1 : 15 : 0.5 : 0.5 and which had the most stable conductivity response (**Figure 2**), is shown in **Figure 3** (grey lines). Its optical response is quite similar to that of device D(1–15–0.5), composed of the same electrolyte, but without the addition of CPMDMS. Namely, the change in photopic transmittance (**Table 1**) reached ΔT_{ph} = 26.0 for D(1–15–0.5) and 22.5 for (D(CPMDMS). The switching characteristics also remained similar; colouring was achieved in 12 s, while bleaching became slightly more sluggish. Nevertheless,

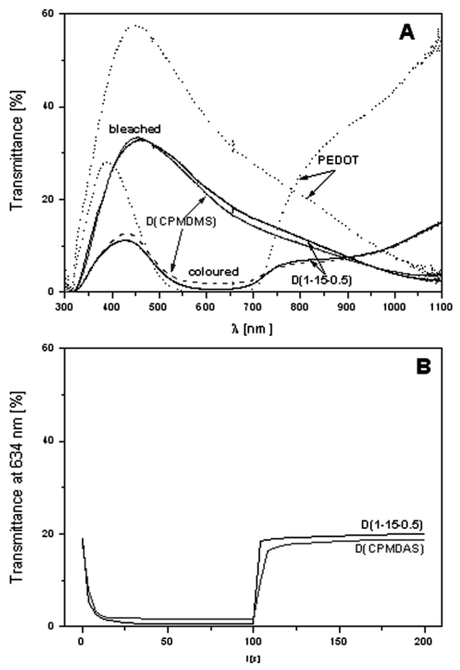

Figure 3: *In-situ* UV-visible spectroelectrochemical measurements of EC devices D(1–15–0.5) and D(CPMDMS): A) spectra obtained during chronocoulometric colouring at –2 V and bleaching at 2 V and B) monochromatic spectral response at 634 nm. A) UV-visible spectra of PEDOT film on ITO-PET measured in electrolyte 1 M $LiClO_4$/PC (coloured at –1 V vs. Ag/AgCl, bleached at 1 V vs. Ag/AgCl) are shown for comparison.

Slika 3: In-situ UV-vidne spektroelektrokemijske meritve EC-sklopov D(1–15–0,5) in D(CPMDMS): A) spektri, dobljeni pri kronokulometričnem obarvanju pri –2 V in razbarvanju pri 2 V in B) monokromatski spektralni odziv pri 634 nm. A) UV-vidni spektri PEDOT plasti na ITO-PET, izmerjeni v elektrolitu 1 M $LiClO_4$/PC (obarvan pri –1 V vs. Ag/AgCl, razbarvan pri 1 V vs. Ag/AgCl) so prikazani za primerjavo.

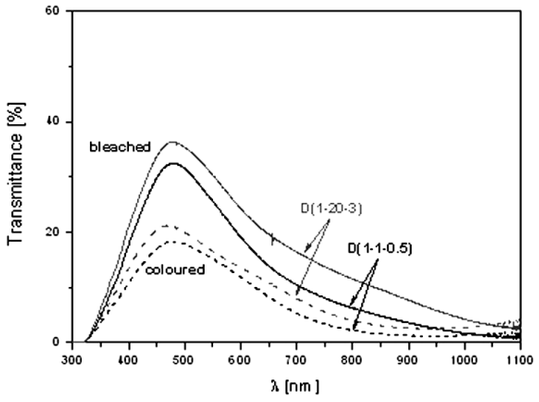

Figure 4: *In-situ* UV-visible spectroelectrochemical measurements of EC devices D(1–1–0.5) and D(1–20–3)

Slika 4: In-situ UV-vidne spektroelektrokemične meritve EC-sklopov D(1–1–0,5) in D(1–20–0,5)

Table 1: Lightness L^* and photopic transmittance T_{ph} of EC devices obtained from UV-visible spectra measured during chronocoulometric charging (–2 V, 100 s; 2 V, 100 s). For comparison, data for PEDOT film are also shown

Tabela 1: Svetlost L^* in fotopična transmisija T_{ph} EC-sklopov, izračunana na osnovi UV-vidnih spektrov, izmerjenih med kronokulometričnim obarvanjem (–2 V, 100 s) in razbarvanjem (2 V, 100 s). Za primerjavo je prikazana tudi svetlost PEDOT-plasti

EC device	L^*(col)	L^*(bl)	T_{ph}(col)	T_{ph}(bl)
PEDOT	13.2	72.5	1.6	44.4
D(1-1-0.5)	44.5	57.2	14.2	25.1
D(1-15-0.5)	11.1	59.2	1.3	27.3
D(1-20-3)	44.9	61.1	14.5	29.4
D(CPMDMS)	21.9	58.0	3.5	26.0

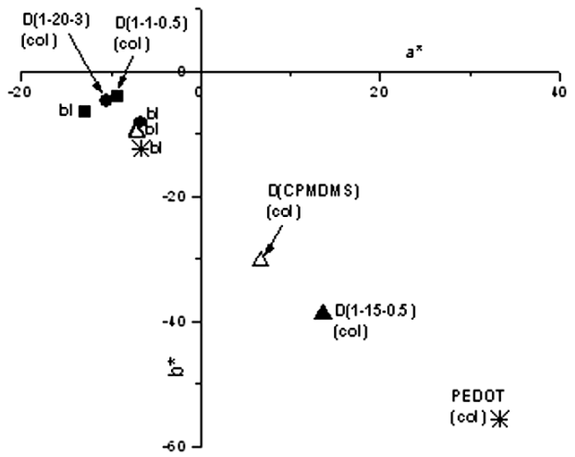

Figure 5: Colour coordinates of EC devices D(1–15–0.5), D(1–1–0.5), D(1–20–3) and D(CPMDMS) calculated in a $L^*a^*b^*$ CIE colour space

Slika 5: Barvne koordinate EC-sklopov D(1–15–0,5), D(1–1–0,5), D(1–20–3) in D(CPMDMS), izračunane v $L^*a^*b^*$ CIE barvnem prostoru

the stability of the conductivity response favours the application of an electrolyte with CPMDMS additive.

Colour coordinates. The colour coordinates that were calculated in the $L^*a^*b^*$ CIE colour space for EC devices and PEDOT film (**Figure 5**) showed that the PEDOT film moves from the region of dark-blue when coloured ($a^* = 33.4$, $b^* = -55.7$) to the region of light-blue when bleached ($a^* = -6.7$, $b^* = -12.3$) and similar behaviour was also characteristic of EC devices D(1–15–0.5) and D(CPMDMS), with the best optical performance. The colour coordinates of the other two EC devices, D(1–1–0.5) and D(1–20–3), could be found between $-6 < a^* < -13$ and $-4 < b^* < -8$ for the coloured and bleached states, indicating their lower colouration compared to the devices D(1–15–0.5) and D(CPMDMS). Similarly, the difference in the lightness L^* (Table 1) of the coloured state is also remarkable, being of the order of 11 to 22 for the PEDOT film and devices D(1–15–0.5) and D(CPMDMS), but much higher ($L^* \tilde{}\ 44$) for the EC devices D(1–1–0.5) and D(1–20–0.5).

4 CONCLUSIONS

It was shown in this work that di-urethanesil-based ormolytes incorporating lithium bis(trifluoromethane-sulfonyl)imide salt and co-solvent γ-butyrolactone can be sucessfully applied in EC devices with an optically active poly(3,4-ethylene-dioxythiophene) (PEDOT) film and a V_2O_5 counter electrode. The best EC devices were characterised by optical modulation above 30 % at 634 nm and fast-switching kinetics (colouring and bleaching in less than 12 s). The stability of the conductivity response over the course of an 18-day measurement was achieved by the addition of dialkoxysilane 3-chloro-propylmethyldimethoxysilane, which enables condensation reactions only in two directions, thus profoundly influencing the structural properties of the sol-gel network. Two major conclusions can be made on the basis of this work: (i) that the investigated organic-inorganic hybrid bis N-triethoxysilyl propylcarbamatoil poly(ethylene oxide) 400 is able to incorporate quite large amounts of co-solvent in its network and (ii) that dialkoxysilanes successfully stabilize the structure of the formed sol-gel network. Both conclusions open tremendous possibilities for improvements to existing ormolytes used in current EC devices, by the application of other co-solvents, lithium salts and dialkoxysilanes.

ACKNOWLEDGEMENT

The research leading to these results received funding from the European Community's Seventh Framework Programme (FP7) under grant agreement no. 200431 (INNOSHADE) and the Slovenian Research Agency (Programme P1-0030).

5 REFERENCES

[1] C. G. Granqvist, Handbook of electrochromic materials, Elsevier Science, Amsterdam, 1995
[2] C. G. Granqvist, E. Avendano, A. Azens, Thin Solid Films, 442 (**2003**), 201–211
[3] M. Deepa, A. Awadhia, S. Bhandari, S. L. Agrawal, Electrochim Acta, 53 (**2008**), 7266–7275
[4] G. Vaivars, A. Azens, C. G. Granqvist, Solid State Ionics, 119 (**1999**), 269–273
[5] L. Zhang, S. Xiong, J. Ma, X. Lu, Sol Energ Mat Sol C, 93 (**2009**), 625–629
[6] A. Brazier, B. B. Appetecchi, S. Passerini, A. Šurca Vuk, B. Orel, F. Donsanti, F. Decker, Electrochim Acta, 52 (**2007**), 4792–4797
[7] J. Livage, D. Ganguli, Sol Energ Mat Sol C, 68 (**2001**), 365–381
[8] S. Heusing, D. L. Sun, J. Otero-Anaya, M.A. Aegerter, Thin Solid Films, 502 (**2006**), 240–245
[9] P. Judeinstein, C. Sanchez, J Mater Chem, 6 (**1996**), 511–525
[10] M. M. Collinson, Handbook of advanced electronic and photonic materials and devices, in: H. S. Nalwa (Ed.) Chalcogenide glasses and sol-gel materials, Academic Press, 2001
[11] K. Dahmouche, M. Atik, N. C. Mello, T. J. Bonagamba, H. Panepucci, M. A. Aegerter, P. Judeinstein, Journal of Sol-Gel Science and Technology, 8 (**1997**), 711–715
[12] J. Chaker, K. Dahmouche, V. Briois, C. V. Santilli, S.H. Pulcinelli, P. Judeinstein, Journal of Sol-Gel Science and Technology, 26 (**2003**), 1075–1080
[13] U. Lavrenčič Štangar, B. Orel, J. Vince, V. Jovanovski, H. Spreizer, A. Šurca Vuk, S. Hočevar, J Solid State Electr, 9 (**2005**), 106–113
[14] E. Stathatos, P. Lianos, U. Lavrencic-Stangar, B. Orel, Adv Mater, 14 (**2002**), 354–357
[15] S. M. G. Correia, V. D. Bermudez, M. M. Silva, S. Barros, R. A. S. Ferreira, L. D. Carlos, A. P. P. de Almeida, M. J. Smith, Electrochim Acta, 47 (**2002**), 2421–2428
[16] S. C. Nunes, V. D. Bermudez, D. Ostrovskii, L. D. Carlos, J Mol Struct, 702 (**2004**), 39–48
[17] M. M. Silva, S. C. Nunes, P. C. Barbosa, A. Evans, V. de Zea Bermudez, M. J. Smith, D. Ostrovskii, Electrochim Acta, 52 (**2006**), 1542–1548

[18] S. C. Nunes, V. de Zea Bermudez, D. Ostrovskii, P. B. Tavares, P.C. Barbosa, M. M. Silva, M. J. Smith, Electrochim Acta, 53 (**2007**), 1466–1475

[19] P. Barbosa, L. C. Rodrigues, M. M. Silva, M. J. Smith, J Power Sources, 180 (**2008**), 607-611

[20] S. C. Nunes, V. D. Bermudez, D. Ostrovskii, P. C. Barbosa, M. M. Silva, M. J. Smith, Chem Phys, 345 (**2008**), 32–40

[21] P. C. Barbosa, M. M. Silva, M. J. Smith, A. Goncalves, E. Fortunato, S. C. Nunes, V. D. Bermudez, Electrochim Acta, 54 (**2009**), 1002–1009

[22] J. Syzdek, M. Armand, M. Marcinek, A. Zalewska, G. Zukowska, W. Wieczorek, Electrochim Acta, 55 (**2010**), 1314–1322

[23] P. C. Barbosa, M. M. Silva, M. J. Smith, A. Goncalves, E. Fortunato, Electrochim Acta, 52 (**2007**), 2938–2943

[24] L. C. Rodrigues, P. C. Barbosa, M. M. Silva, M. J. Smith, A. Goncalves, E. Fortunato, Opt Mater, 31 (**2009**), 1467–1471

[25] V. D. Bermudez, L. Alcacer, J. L. Acosta, E. Morales, Solid State Ionics, 116 (**1999**), 197–209

[26] B. Orel, R. Ješe, A. Vilčnik, U. Lavrenčič Štangar, Journal of Sol-Gel Science and Technology, 34 (**2005**), 251–265

[27] Y. Matsuo, K. Fumita, T. Fukutsuka, Y. Sugie, H. Koyama, K. Inoue, J Power Sources, 119 (**2003**), 373–377

[28] R. Ruffo, A. Celik-Cochet, U. Posset, C.M. Mari, G. Schouner, Sol Energ Mat Sol C, 92 (**2008**), 140–145

[29] A. Šurca Vuk, S. Benčič, B. Orel, F. Decker, Journal of Sol-Gel Science and Technology, 23 (**2002**) 53–66

[30] R. S. Korwin, H. Masui, Thermochimica Acta, 433 (**2005**), 157–162

UDK 546.3/.9
Original scientific article/Izvirni znanstveni članek

ISSN 1580-2949
MTAEC9, 45(5)439(2011)

COMBUSTIBLE PRECURSOR BEHAVIOUR IN THE LANTHANUM CHROMITE FORMATION PROCESS

TERMIČNE LASTNOSTI REAKCIJSKEGA GELA ZA PRIPRAVO LANTANOVEGA KROMITA

Klementina Zupan, Marjan Marinšek, Barbara Novosel

Faculty of Chemistry and Chemical Technology, University of Ljubljana, Aškerčeva 5, 1000 Ljubljana, Slovenia
klementina.zupan@fkkt.uni-lj.si

Prejem rokopisa – received: 2011-01-16; sprejem za objavo – accepted for publication: 2011-05-07

Combustion-derived lanthanum chromite (LC) powders were prepared with combustion synthesis from citrate-nitrate precursor gels. The transformation process of reactive citrate-nitrate gel to the cubic perovskite modification of (LC) was investigated. The influence of the fuel/oxidant molar ratio in the precursor gel on the combustion propagation and thermal characteristics of the combustion system was studied with simultaneous thermal analysis (TG, DTG and DTA), evolved gas analysis (MS) and gas chromatography (GC). The main (MS) responses detected were attributed to H_2, H_2O and CO_2 generation. It was found that the citrate-nitrate reaction proceeds through several separate consecutive steps and the precursor thermal decomposition characteristics depended strongly on the citrate/nitrate ratio prior to the combustion. The first two steps of the thermal decomposition at approximately 150 °C and 250 °C are strongly related to the citrate-nitrate reaction, while at around 400 °C the combustion of citric acid residuals occurs. The last step of the thermal decomposition is caused by transformation of $LaCrO_4$ to $LaCrO_3$. Intermediate precursors and final powder ashes were also analyzed with X-ray diffraction.

Keywords: combustion synthesis; lanthanum chromite; citrate- nitrate, thermal characteristics

Prahove lantanovega kromita (LC) smo pripravili s samovzdrževalno reakcijo iz citratno- nitratnih gelov. Preučevali smo pretvorbo reaktivnega citratno-nitratnega gela v perovskitno modifikacijo lantanovega kromita. Vpliv razmerja gorivo/oksidant v izhodnem prekurzorju na hitrost gorenja in termične karakteristike smo spremljali s simultano termično analizo (TG, DTG in DTA), EGA analizo ter plinsko kromatografijo (GC). Pomembnejše odzive na masnem spektrometru smo pripisali nastanku H_2, H_2O in CO_2. Termični razpad gela je močno odvisen od citratno-nitratnega razmerja v gelu pred sežigom, pri njegovem gorenju pa potekajo reakcije v več zaporednih med seboj ločenih stopnjah. Prvi dve stopnji termičnega razpada pri okoli 150 °C in 250 °C sta povezani z reakcijo med citronsko kislino in nitratom. Stopnja nad 400 °C kaže na razkroj ostanka citronske kisline, zadnja stopnja termičnega razpada pa je povezana s pretvorbo $LaCrO_4$ v $LaCrO_3$. Vmesne in končne produkte gorenja smo karakterizirali z rentgensko praškovno analizo.

Ključne besede: zgorevalna sinteza, lantanov kromit, citrat-nitrat, termične lastnosti

1 INTRODUCTION

Several synthetic techniques are available for the preparation of multi-component oxides including the solid-solution-precursor method,[1] sol-gel synthesis,[2] co-precipitation,[3] and spray drying.[4] The solution combustion synthesis of complex metal oxides has several advantages over other conventional preparation techniques. Because it starts in a solution, it has control over the homogeneity and stoichiometry of the products. With a judicious choice of starting precursors for the combustion synthesis, particle size reduction (nano-sized) and the high degree of conversion to reactive powders may also be achieved.[5]

Combustion synthesis utilizes different redox systems, each with its own characteristics. In the precursor formation process in which an oxidant (i.e. nitrate) and fuels (i.e. glycine, urea, carbohydrazide, citric acid) are mixed in appropriate molar ratios, the fuels also serve as complexing agents limiting the precipitation of individual precursor components prior to ignition.[8] The exothermic reaction between fuel and oxidant is accompanied by the release of a relatively large volume of gases leaving behind fine particulate solid residue. Generally, combustion synthesis can be performed in slow reaction mode, in thermal explosion mode, or self-propagating mode.[9] The first mode is characterised by a relatively slow, almost flameless reaction, and by the formation of an amorphous ash as a solid product. The second type of reaction occurs almost simultaneously throughout the mixture. In the self-propagating mode, the reaction is initiated at one end of the reaction mixture and propagates through the volume in the form of a combustion wave.[9,10] The combustion reaction mode depends on the fuel/oxidant ratio[10] and the reaction mixture packing prior to ignition.[11]

The thermal transformation behaviour of citrate-based gel precursors has attracted the attention of many authors.[12–17] Because of its less severe exothermic nature, the citrate-nitrate gel combustion reactions are the most widely used. Considering that citrate oxidation and nitrate reduction is complete, the reaction gas products (i.e. CO_2, N_2 and H_2O) are formed, although the oxidation state of product species is not restricted to one value but may vary. For instance, the oxidation state of nitrogen in the reaction product may vary from 0 (N_2) to 4+ (NO_2), meaning that there is no uniform chemical

description of the citrate-nitrate combustion. Although metal ions may affect the oxidation state and thus the appearance of volatile products, the citrate-nitrate redox/decomposition reaction is normally explained with a simplified reaction:[16]

$$C_6H_8O_7 + 6NO_3^- \rightarrow 6CO_2 + H_2O + 6OH^- + 6NO \quad (1)$$

Lanthanum chromite (LC) is one of the representative perovskites that has attracted much attention in recent years. It potential is based on its refractory properties (melting point >2400 °C), relatively high electrical conductivity and high temperature corrosion resistance.[18] The combustion synthesis of lanthanum chromite has been successfully applied by some authors.[6,7,8] Different combustion systems for LC synthesis for stoichiometric fuel/nitrate ratios are shown in **Table 1**.

The main objective of this paper is an attempt to clarify how the citrate-nitrate gel transformation process including the combustion reaction and end LC product properties are affected by experimental conditions owing to different citrate/nitrate initial ratios.

2 EXPERIMENTAL PROCEDURES

The lanthanum chromite powders were prepared with the modified citrate nitrate combustion synthesis. The starting substances (analytical reagent grade) for reactive gel preparation were aqueous solutions of $La(NO_3)_3 \cdot 6H_2O$, $Cr(NO_3)_3 \cdot 9H_2O$, and citric acid. All three precursors were mixed to prepare solution which was kept over a water bath at 60 °C under vacuum (p = 5–7 mbar) until it transformed into a dark violet gel (at least 3 h). The initial citrate/nitrate molar ratios in the starting solution were altered from c/n 0.13 to 0.33, as indicated in **Table 2**. The corresponding citrate nitrate gel was then crushed and pressed into pellets (Φ = 12 mm, h = 30 mm, p = 17 MPa. The pellets were ignited at the top to start an auto-ignition reaction with the flame of a very small gas burner. The reaction period and maximum temperature (Pyrometer Omega Engineering OS3722 type, 900–3000 °C temperature range) were measured.

The amounts of chromium in the samples were determined with atomic absorption spectrometry. The amount of water in the reactive gels was determined with Karl-Fisher titration, while spectrophotometry was used for determination of the nitrate (after its reduction to nitrite). The thermal behaviour (TG, DTG, DTA) of the reactive gels was studied with thermogravimetric analysis (Netzsch STA 409 apparatus and TG-50 Thermobalance) at a heating rate of 10 K/min supported by mass spectrometry (Evolved gas analysis, with a Pfeiffer mass spectrometer); Agilent Micro GC 3000A, Gas Chromatograph. Differential Scanning Calorimetry analyses (DSC) were performed on Mettler standard cell DSC 20 at a heating rate of 10 K/min). The products of synthesis were determined by the X-ray powder diffraction technique using a Philips PW-1710 apparatus. A Micromeritics Gemini II 2370 was used to determine specific surface areas by the BET method. The crystallite size was determined with the Scherer method. The width of peaks at half size was automatically determined according to the program algorithm.

Table 1: An overview of LC preparation using combustion synthesis route and characteristic synthesis conditions
Tabela 1: Pregled načinov priprave LC z zgorevalno sintezo s pogoji priprave

Reducing agent	Molar ratio fuel/nitrate	Combustion temperature (°C)	*SSA*/(m²/g)	Reference
TFTA-$C_4H_{16}N_6O_2$	0.19	1100 ± 100	8.7	6
urea	0.28	1000–1050	8.2–8.1*	7
glicine	0.55	1750	17	8
$(NH_4)_2Cr_2O_7$ + glycine	0.55	1250	29	8
apdefaultCitric acid	0.18	1230	14.8	19

* calculated from the particle size

Table 2: Sample preparation conditions
Tabela 2: Pogoji priprave vzorcev

Sample	Initial ratio c/n**	Combustion temperature [°C]	Combustion velocity [g/s]	*SSA****/(m²/g)	d_{110}/nm
A0.13	0.13		No self-sustaining reaction	19.1	24
B0.15	0.15		No self-sustaining reaction	23.0	18.7
C0.16	0.16		0.05	24.3	16.4
D0.18	0.18	1174	0.11	19.8	17.9
E0.23	0.23	1380	0.18	10.4	30.0
F0.28	0.28	1329	0.07	16.6	18.4
G0.33	0.33	1198	0.04	13.9	17.0

** citrate/nitrate
*** specific surface area

3 RESULTS AND DISCUSSION

The influence of the citrate/nitrate molar ratio on the reaction dynamic was determined by following the chemical composition of the various precursors and intermediates. The amounts of metal ions, water and nitrate were determined as described in the experimental procedure. To calculate the amount of citrate in the reactive gels, we performed an EGA analysis of the gases emitted by the gels during drying over a water bath. This analysis showed that under drying conditions there were no carbon oxides released from the gels, indicating that the citrate did not undergo decomposition during the gel formation. From the spectrophotometric-volumetric-water content analysis and by assuming that citrate when treated over a water bath did not decompose, the chemical formulae of the reactive citrate-nitrate gel can be calculated for the reactive gels (**Table 3**).

According to the results summarized in **Table 3**, dehydration of the starting reaction solution was accompanied by the loss of some nitrates, increasing the *c/n* molar ratio. It is also clear that gels lose water more easily when the *c/n* ratio is high; e.g. the water content in the dried gel is lower. It was also observed that pellets prepared from mixtures with a relatively high *c/n* ratio were less hydroscopic than those with a relatively low *c/n* ratio. The final *c/n* ratio also influences the combustion temperature and velocity (**Table 2**). Both were highest in the case of sample E0.23 with a final *c/n* ratio of 0.27 (i.e. 0.18 g/s was the combustion velocity and 1380 °C was the combustion peak temperature) and

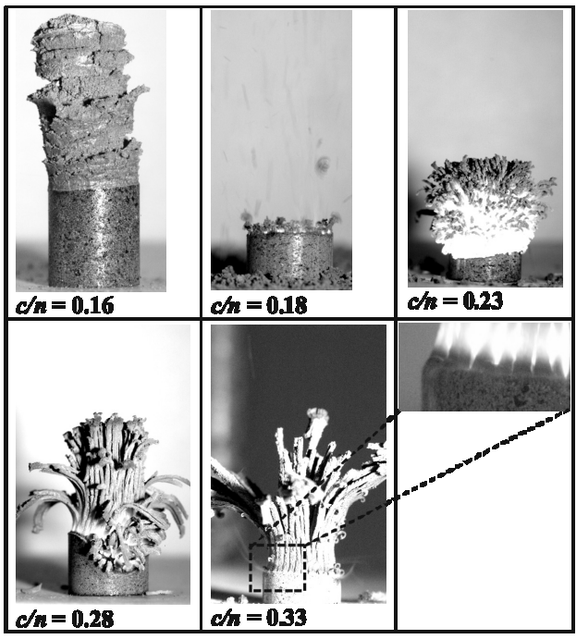

Figure 1: Photographs of gel combustion for different citrate-nitrate ratios

Slika 1: Fotografije gorenja gelov z različnimi citratno nitratnimi razmerji

Table 3: Chemical composition of the dried gels

Tabela 3: Kemijska sestava sušenih gelov

Sample	Proposed chemical formula of the reactive gel	*c/n* ratio in the reactive gel	Intermediate preparation temperature /°C	Amount of nitrate %
A0.13	$LaCr(NO_3^-)_{4.11}(C_6H_8O_7)_{0.78}(H_2O)_{5.80}$	0.19	180 380	15.58 8.03* 0.05**
B0.15	$LaCr(NO_3^-)_{4.51}(C_6H_8O_7)_{0.90}(H_2O)_{5.18}$	0.20	180 380	15.73 7.98* 0.04**
C0.16	$LaCr(NO_3^-)_{4.56}(C_6H_8O_7)_{0.96}(H_2O)_{5.16}$	0.21	180 320	15.44 7.98* 0.06**
D0.18	$LaCr(NO_3^-)_{4.69}(C_6H_8O_7)_{1.08}(H_2O)_{4.93}$	0.23	180 310	14.45 7.87* 0.05**
E0.23	$LaCr(NO_3^-)_{5.10}(C_6H_8O_7)_{1.38}(H_2O)_{4.84}$	0.27	170 300	14.12 7.69* 0,05**
F0.28	$LaCr(NO_3^-)_{5.25}(C_6H_8O_7)_{1.68}(H_2O)_{3.99}$	0.32	170 290	15,83 0,3* 0,04**
G0.33	$LaCr(NO_3^-)_{5.35}(C_6H_8O_7)_{1.98}(H_2O)_{3.91}$	0.37	160 240	15,86 0,2* 0,04**

* first stage intermediates, ** second stage intermediates

decreased mutually with higher or lower *c/n* ratios. In the case of samples A0.13 and A0.15, the final *c/n* ratio did not allow a self-sustaining reaction. The critical *c/n* ratio for this particular combustion system is between 0.19 and 0.20.

For better understanding of gel transformation behaviour during dried gel decomposition, a series of thermo-analytical tests were performed. DSC and TG in combination with EGA were used to examine the thermal stabilities of the gels and for the determination of the gases exiting the reaction mixture. These tests are probably not an ideal model of the combustion process, because the initial masses and reaction periods for complete burning are not equivalent in the two cases. Nevertheless, thermal analysis provides good insight into the combustion reaction, especially if we compare the combustion behaviour of gels with different *c/n* molar ratios, as indicated in **Figure 1**.

The DSC curves of the dried gels performed in air atmosphere are presented in **Figure 2**, indicating that the combustion process proceeds during several steps. The first, more pronounced step is an endothermic effect at approximately 110–130 °C. This endothermic peak is attributed to liquid phase formation (as indicated in Figure 1 for sample G0.33) prior to the combustion reaction itself. Similar results were also reported for other combustion systems.[17]

The first exothermic peak took place in the temperature range between 130 °C and 170 °C, depending on the gel composition (*c/n* ratio). The exothermicity of this step increased with the increasing *c/n* molar ratio; however, for samples A0.13 and B0.15 this exothermic peak was hardly noticeable. Contrary to the first exothermic effect, the second step occurred over a broader temperature range, from 180 °C to 300 °C, and was more pronounced if the *c/n* ratio was small. This step could be represented by two successive peaks (samples A0.13 and B0.15) or was only slightly detectable if the *c/n* ratio was high (sample G0.33). The third exotherimic peak was proceeding in the temperature range between 250 °C and 400 °C; the intensity of this reaction step increased with increasing *c/n* molar ratio. According to the literature data describing reactions in similar citrate- nitrate reaction systems,[19,20] the third step is not related to the citrate-nitrate combustion reaction, but is rather a consequence of residual fuel burning with air.

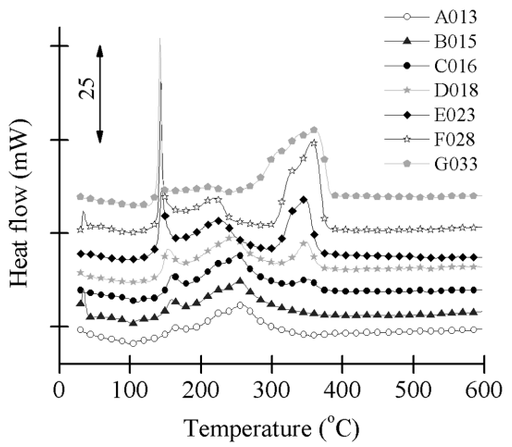

Figure 2: DSC thermal analysis plots of different citrate-nitrate gels taken in air

Slika 2: DSC analize gelov z različnimi citratno nitratnimi razmerji v zraku

Heat effects during citrate- nitrate combustion were usually accompanied by losses of mass of the reactive gel. Mass changes were measured with TG-DTG analysis and are presented in **Figure 3**. TG analysis confirmed that the *c/n* molar ratio in the gel prior to combustion has a major influence on the thermal decomposition behaviour of the citrate-nitrate precursors. The TG-DTG curves revealed several consecutive steps in mass loss if the *c/n* ratio was between 0.13 and 0.23 and was in accordance with DSC curves; i.e. every heat effect had its response in an equivalent mass loss. The first temperature range of higher rate mass loss occurred between 120 °C and 160 °C. This step was followed by the second stage of mass loss between 180 °C and 300 °C. The final mass loss was achieved in the temperature range between 300 and 400 °C. With an increasing *c/n* ratio, the DTG peaks in the temperature ranges of 120–160 °C and 300–400 °C rose, while those between 180 °C and 300 °C became less evident. Finally, if the *c/n* ratio was as high as 0.28 (samples F0.28 and G0.33), only two stages of rapid mass loss were detected at approximately 120 °C and in the range from 300 °C to 350 °C. Final mass losses for all samples were found to be between 64.9 % and 70.1 %.

Previous work by Couty et al.[12] proposed the existence of two types of citrate-nitrate combustion reactions. Type I occurs with reaction mixtures containing catalytically active metal ions, such as Fe, Ni, Ag, Cu, and Co, and is characterized by continuous dynamic reaction. Type II proceeds over several stages, in which an intermediate semi-decomposed precursor occurs. According to this classification, our reaction system is related to Type I reactions. Nevertheless, the thermal analysis data given in **Figures 2 and 3** show that our reaction system can correspond to both reaction types, depending on the *c/n* ratio. If the last step of mass loss or heat effect between 300 °C and 400 °C is a consequence of the removal of the citric acid residual step rather than citrate-nitrate combustion reaction, higher *c/n* ratios favour single-step combustion, while lower *c/n* ratios favour a several stage process.

The EGA data during thermal decomposition of various citrate- nitrate gels in a synthetic air atmosphere are shown in **Figure 4**. Synthetic air (Ar/O_2) was used instead of air (N_2/O_2) since N_2 is one of the gaseous products of the reactive gel thermal decomposition. The main mass spectrometry (MS) responses detected were at mass/charge ratio (*m*/e) 2, 18, 28, 30 and 44

(expressed in atomic mass units). Signals at *m/e* 2, 18 and 44 were attributed to H_2, H_2O and CO_2 evolution, respectively. We excluded any NO_2 formation during combustion gel transformation because no fragmental signal at *m/e* 46 was detected, meaning that the signal at *m/e* 30 can be related to NO evolution. An indication of CO evolution was indicated by the analysis of fragmental peak at *m/e* 12 caused by CO_2 and the CO fragmental response. Even if the corresponding CO_2 fragmental response was subtracted from the signal at *m/e* 12, there was some residual peak showing the CO evolution pattern. Further, the EGA signal at *m/e* 28 could be caused by CO and /or N_2 evolution and partially due to CO_2 fragmental response. However, if the N_2 fragmental peak is examined carefully, and the fragmental contributions of CO and NO are subtracted from the signal, there was some residual peak contributed to N_2 generation. Therefore, it is apparent that the peak at *m/e* 28 follows both CO and N_2 evolution.

According to the EGA results, the gaseous products during citrate-nitrate gel decomposition were H_2O, CO, CO_2, NO, N_2 and H_2. In all cases, NO and N_2 were detected during the first stage of thermal decomposition in the temperature range between 160 °C and 200 °C. Some NO and N_2 were also evolved in the second temperature range, while in the third temperature range above 350 °C no NO and N_2 were detected. This confirms the assumption made on the basis of DSC and TG data that the mass loss between 300 °C and 400 °C is not a consequence of citrate-nitrate combustion itself but rather of pyrolysis of the residual citrate. The EGA results were in good agreement with the GC analysis that was performed simultaneously with the EGA analysis.

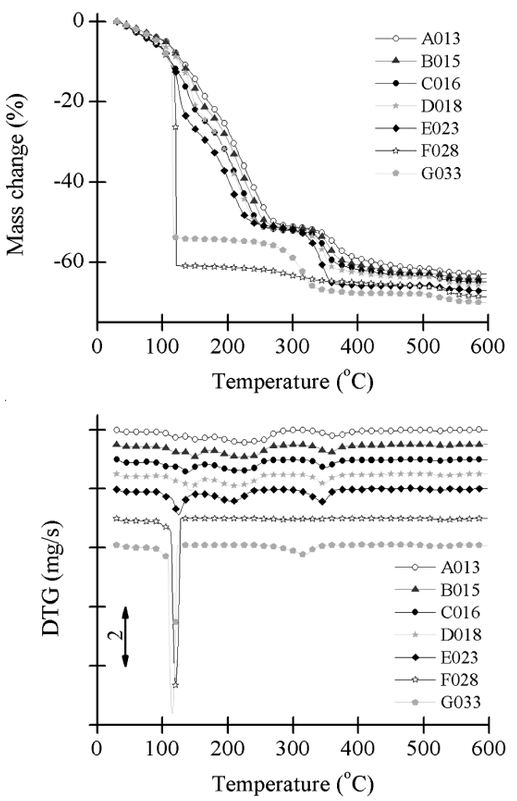

Figure 3: Mass changes of different citrate- nitrate gels taken in an air atmosphere followed by TG-DTG analysis

Slika 3: Spremembe mase gelov za različna citratno nitratna razmerja v zraku posnete z TG-DTG analizo

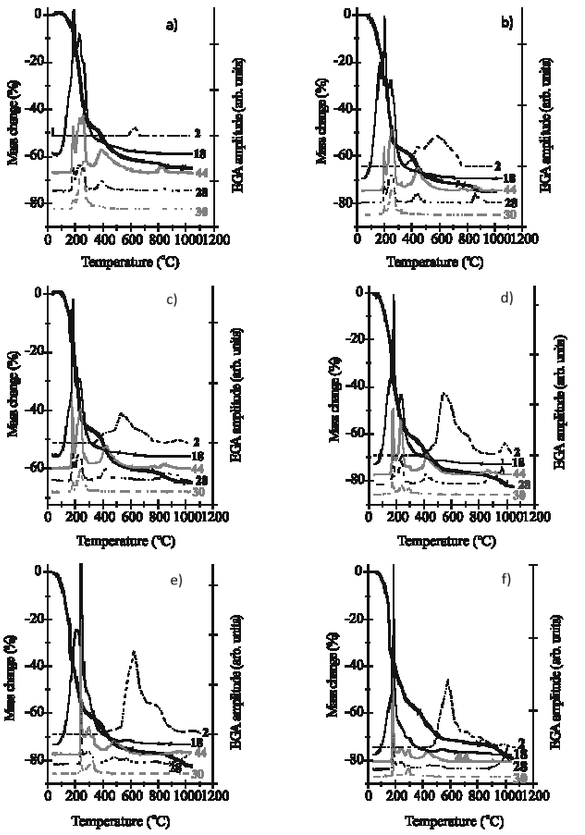

Figure 4: Evolved gas analysis by mass spectrometry for various precursors taken in synthetic air ($\varphi(O_2)$ = 20 %$_2$, φ(Ar) = 80 %). (a) Sample A0.13, (b) Sample C0.16, (c) Sample D0.18, (d) Sample E0.23, (e) Sample F0.28, (f) Sample G0.33

Slika 4: Analiza EGA različnih prekurzorjev v sintetičnem zraku (20 vol.% O_2, 80 vol.% Ar) (a) Vzorec A0.13, (b) Vzorec C0.16, (c) Vzorec D0.18, (d) Vzorec E0.23, (e) Vzorec F0.28, (f) Vzorec G0.33

During the late stages of combustion, some H_2 was detected. H_2 evolution was not caused by citrate decomposition but was probably generated by the water gas shift (WGS) reaction. Some H_2 evolves due to the water gas shift reaction as a possible catalytic effect of lanthanum chromium oxide. At this late stage, the combustion of CO, H_2O and CO_2 products together with lanthanum chromium oxide in the reaction system leads to the WGS reaction.[21, 22]

An insight into the course of the citrate-nitrate combustion can also be obtained by following the nitrate amount in the reactive precursors. The results of nitrate

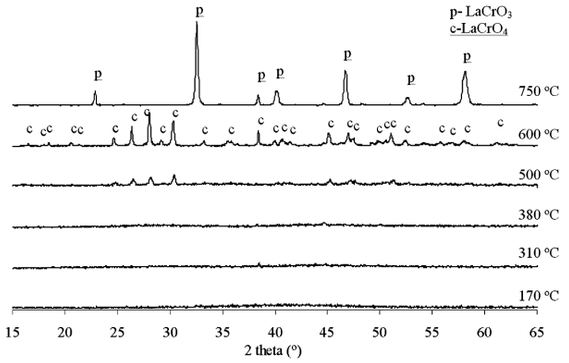

Figure 5: Phase development in E0.23 precursor during thermal treatment in air

Slika 5: Nastanek kristalnih faz v prekurzorju E0.23 pri termični obdelavi v zraku

content in different precursors together with the precursors' characteristics are summarized in **Table 3**. The intermediate preparation temperature was chosen on the basis of thermal analysis results, e.g. at a temperature that a step of TG-DTG analysis was completed. As the combustion proceeds, citrate and nitrate are consumed, resulting in their diminishing content in the precursor. It is evident that the amount of nitrates in the precursors is negligible before the third stage of mass loss occurs (between 300 °C and 400 °C).

The sequence of crystalline phases formed during the course of thermal treatment of the precursor E0.23 was followed by XRD analysis (**Figure 5**). It is apparent that the intermediate precursors were amorphous at temperatures below 500 °C . The first crystalline phase found in intermediates treated above 500 °C corresponded to $LaCrO_4$, and was completely crystallized at 600 °C. Lanthanum chromite in a perovskite form was identified after intermediate precursors were heated to 750 °C.

The degree of crystallization of combustion reaction products is a consequence of the reaction temperature and time. The highest combustion velocity and reaction temperature for sample E0.23 causes the highest degree of sample crystallization. From X-ray broadening of the peaks, average crystallite sizes in as-synthesized samples were calculated to be (24, 19, 16, 19, 30, 18 and 17) nm [plane perovskite (110)] for samples A0.13, D0.18, E0.23, F0.28 and G0.33, respectively.

A simplified reaction between nitrate and citrate proposed by Courty et al.[12] Eq. (1) implies a complete oxidation of the citrate without any residual carbon. However, if the citrate oxidation is performed under conditions where the stoichiometry of Eq. (1) does not apply, a part of residual organic fuel may be left in the product. An indication of residual carbon presence after the reaction is the formation of CO, H_2O and CO_2 at relatively high temperatures (1000 °C). By analogy with the reaction scheme proposed by Wang et al.[17] for the nitrate-EDTA precursor and with the respect to our data obtained by the thermal analysis, the general reaction between nitrate and citrate may be represented by Eq. (2).

$$a\mathrm{C_6H_8O_7} + b\mathrm{NO_3^-} \rightarrow c\mathrm{C} + d\mathrm{CO} + e\mathrm{CO_2} + f\mathrm{H_2O} + g\mathrm{OH^-} + h\mathrm{NO} + i\mathrm{N_2} \quad (2)$$

Stoichiometric factors *a-I* depend on the conditions during the reaction. The above reaction between nitrate and citrate may be solved in various stoichiometries. However, kinetically preferred models should be based on smallest possible number of reacting molecules. By solving the above equation, the amount of the residual mass when citrate and nitrate are decomposed can be calculated. Such prediction can also be applied to the reactive gels, which (in addition to citrate and nitrate) contain metal ions and water as well. With respect to the calculated *c/n* ratio, the stoichiometric factors *a-i* in the case of sample E0.23 are 1, 4, 1, 1, 4, 2, 4, 2 and 2, respectively; the *c/n* ratio in the case of sample E0.23 is the closest to the stoichimometric ratio.

4 CONCLUSIONS

The citrate-nitrate combustion is very sensitive to the fuel/oxidant molar ratio prior to the reaction. The highest combustion velocity and highest combustion temperature were achieved in the case of sample E0.23 with *c/n* molar ratio 0.27. If the *c/n* ratio differs from this ratio, either up or down, the combustion rate and temperature decrease. The critical *c/n* ratio that still enables the self-sustaining citrate-nitrate combustion is between 0.21 and 0.23. The citrate-nitrate reaction proceeds through several separate steps. Prior to combustion, the reactive precursor melts. During thermal treatment, the citrate-nitrate decomposition takes place in the temperature range between 150 °C and 300 °C. In the temperature range between 300 °C and 400 °C, the residual citrate or its decomposition products are eliminated. According to the EGA results, the CO_2 evolution during combustion is always accompanied by CO evolution. Nitrogen leaves the reaction system partly as NO and also as N_2. During the late stages of combustion, some H_2 evolves due to the water gas shift reaction as a possible catalytic effect of lanthanum chromium oxide. The two main crystalline phases formed in samples during the combustion process were $LaCrO_4$ at 500 °C and $LaCrO_3$ at 750 °C.

Acknowledgements

This investigation was supported by Centre of Excellence Low-Carbon Technologies and Slovenian Research Agency.

5 REFERENCES

[1] K. Vidyasagar, J. Gopalakrishnan, R. Rao, A convenient route for the synthesis of complex metal oxides employing solid- solutions precursors, Inorg. Chem., 23 (**1984**), 1206–1210

[2] S. Bilger, G. Blass, R. Forthmann, Sol-gel synthesis of lanthanum chromite powder, J. Eur. Ceram. Soc., 17 (**1997**), 1027–1031

[3] M. R. De.Guire, S. E. Dorris, R. B. Poeppel, S. Morissette, U. Balacandran, Coprecipitation synthesis of doped lanthanum chromite, J. Mater. Res., 8 (**1993**), 2327–2335

[4] K. Masters, Spray Drying Handbook, 4th ed. Wiley, New York, 1985

[5] Self-propagating high-temperature synthesis of materials, Editors A. A. Borisov, L. De Luca, A. Merzhanov, Taylor & Francis, 2002, New York, 189–196

[6] S. S. Manoharan, K. C. Patil, Combustion rute to fine particle perovskite oxides, Journal of Solid State Chemistry, 102 (**1993**), 267–276

[7] M. R. Morelli, R. J. Brook, Combustion synthesis of $LaCrO_3$ powders, Ceramic Transactions, 51 (**1995**), 81–85

[8] J. J. Kingsley, L. R. Pederson, Combustion synthesis of perovskite $LnCrO_3$ powders using ammonium dichromate, Mater. Lett., 18 (**1993**), 89–96

[9] A. Varma, J. P. Lebrat, Combustion Synthesis of advanced materials, Chemical Engineering Science, 47 (**1992**), 2179–2194

[10] A. S. Mukasyan, C. Costello, K. P. Sherlock, D. Lafarga, A. Varma, Perovskite membranes by aqueous combustion synthesis and properties, Separation and Purification Technology, 25 (**2001**), 117–126

[11] K. Zupan, M. Marinšek, S. Pejovnik, J. Maček, K. Zore, Combustion synthesis and the influence of precursor packing on the sintering properties of LCC nanopowders, J. Eur. Ceram. Soc, 24 (**2004**), 1935–1939

[12] Courty, H. Ajot, Ch. Marcilly, B. Delmon, Oxydes mixtes ou en solution solide sous forme très divisée obtenus par décomposition thermique de précurseurs amorphes, Powder Technology, 7 (**1973**), 21–38

[13] D. J. Anderton, F. R. Sale, Production of strontium- doped lanthanum cobaltite conducting oxide powder by freeze-drying technique, Powder Metallurgy, 22 (**1979**), 9–13

[14] M. S. G. Baythoun, F. R. Sale, Production of strontium-substituted lanthanum manganite perovskite powder by the amorphous citrate process, J. Mater. Sci., 17 (**1982**), 2757–69

[15] F. R. Sale, F. Mahloojchi, Citrate gel processing of oxide superconductors, Ceramic International, 14 (**1988**), 229–237

[16] H.-W. Wang, D. A. Hall, F. R. Sale, A thermoanalytical study of the metal nitrate- edta precursors for lead zirconate titanate ceramic powders, Journal of Thermal Analysis, 41 (**1994**), 605–620

[17] Wang, H. W., Hall, D. A., Sale, F. R., Effects of metal salts on the thermal decomposition of EDTA-gel precursors for ferroelectric ceramic powders, Journal of Thermal Analysis, 42 (**1994**), 823–838

[18] Nguyen Q. Minh, Ceramic Fuel Cells, J. Am. Ceram. Soc., 76 (**1993**) 3, 563–588

[19] K. Zupan, D. Kolar, Study of citrate-nitrate gels for $LaCrO_3$ based ceramics preparation. Kovine zlit. tehnol., 32 (**1998**), 355–358

[20] M. Marinšek, K. Zupan, J. Maček, Citrate- nitrate gel transformation behaviour during the synthesis of combustion-derived NiO-yttria-stabilized zirconia composite, J. Mater. Res., 18 (**2003**), 1551–1560

[21] A.–L. Sauvet, J. Fouletier, Catalytic properties of new anode materials for solid oxide fuel cells operated under methane at intermediary temperature, J. Power. Sources, 101 (**2001**), 259–266

[22] S. Georges, G. Parraour, M. Henault, J. Fouletier, Gradual internal reforming of methane: A demonstration, Solid State Ionics, 177 (**2006**), 2109–2112

UDK 621.89:620.18
Original scientific article/Izvirni znanstveni članek

ISSN 1580-2949
MTAEC9, 45(5)447(2011)

NANOSCALE MODIFICATION OF HARD COATINGS WITH ION IMPLANTATION

NANOVELIKOSTNA MODIFIKACIJA TRDNIH PREKRITIJ Z IONSKO IMPLANTACIJO

Branko Škorić, Damir Kakaš, Marin Gostimirović, Aleksandar Miletić

University of Novi Sad, Faculty of Technical Sciences, Trg D. Obradovića 6, 21000 Novi Sad, Serbia
skoricb@uns.ac.rs

Prejem rokopisa – received: 2010-11-06; sprejem za objavo – accepted for publication: 2011-03-31

The mechanical properties of new hard coatings based on a multilayer structure have been investigated at the nanometre scale. The multilayer structure consists of a nitrided layer on a steel substrate and a hard coating deposited by Physical Vapor Deposition and Ion Beam Assisted Deposition. In the present investigation the subsequent ion implantation was provided by $N2^+$ ions. This paper describes the use of the nano-indentation technique for a determination of the hardness and elastic modulus. The results are analyzed in terms of load-displacement curves, hardness, Young's modulus, unloading stiffness and elastic recovery. The analysis of the indents was performed with an Atomic Force Microscope. The analyzed AE signal was obtained by a scratch test designed for adherence evaluation. The coating is often in tensile stress with greater microhardness. The stress determination follows the conventional $\sin^2 \psi$ method, using an X-ray diffractometer. A variety of analytic techniques were used for the characterization, such as a scratch test, calo test, SEM, AFM, XRD and EDAX for engineering applications. The experimental results indicated that the mechanical hardness is elevated by the penetration of nitrogen, whereas the Young's modulus is significantly elevated.

Keywords: coatings, ion implantation, microstructure, adhesion, nanohardness

Mehanske lastnosti novih prekritij na podlagi večplastne strukture so bile raziskane v merilu nanometra. Večplastna struktura sestoji iz nitridne plasti na podlagi iz jekla, trdo prekritje pa je naneseno s fizikalnim nanosom par in nanosom z ionskim curkom. Uporabljena je tudi ionska implantacija z N_2-ioni. Opisana je uporaba nanoindentacije za določitev trdote in elestičnega modula. Rezultati so analizirani z upoštevanjem odvisnosti obremenitev – deformacija, trdote, Youngovega modula, razbremenitvene togosti in elastične poprave. Analiza indentacij je bila izvršena z mikroskopom na atomsko silo. Analizirani AE-signal je bil dobljen s preizkusom razenja, namenjen za določanje oprijetosti. V prekritju so pogosto natezne napetosti,,ima pa tudi veliko mikrotrdoto. Določitev napetosti je bila izvršena z metodo $\sin^2 \psi$ in uporabo rentgenskega difraktometra. Za karakerizacijo je bila uporabljana vrsta analitičnih tehnik, kot so preizkus razenja, calo-preizkus, SEM, AFM, XRD in EDAX za inženirsko uporabo. Eksperimentalni rezultati kažejo, da se mehanska trdota povečuje s penetracijo dušika, pri čemer je Youngov modul pomembno povečan.

Ključne besede: prekritje, ionska implantacija, mikrostruktura, oprijetost, nanotrdota

1 INTRODUCTION

The film-deposition process exerts a number of effects such as crystallographic orientation, morphology, topography, densification of the films. The optimization procedure for coated parts could be more effective, knowing more about the fundamental physical and mechanical properties of a coating. In this research we present the results of a study of the relationship between the process, composition, microstructure and nanohardness.

A duplex surface treatment involves the sequential application of two surface technologies to produce a surface composition with combined properties.[1] A typical duplex process involves plasma nitriding and a coating treatment of materials. In the paper we present the characteristics of hard coatings deposited by PVD (physical vapour deposition) and IBAD (ion beam assisted deposition). The synthesis of the TiN film by IBAD has been performed by the irradiation of Ar ions. Subsequent ion implantation was provided with N^{5+} ions. Ion implantation has the the capabilities of producing new compositions and structures unattainable by conventional means. Implantation may result in changes in the surface properties of a material.

Thin hard coatings deposited by physical vapour deposition (PVD), e.g., titanium nitride (TiN), are frequently used to improve tribological performance in many engineering applications.[2,3] In many cases a single coating cannot solve the wear problems.[4]

Conventional TiN and correspondingly alloyed systems show high hardness and good adhesion strength. However, these coatings have poor cracking resistance, especially in high-speed machining. The duplex surface treatment was used to enhance the adhesion strength and hardness of hard coatings.

In the nano-indentation technique, hardness and Young's modulus can be determined by the Oliver and Pharr method, where hardness (H) can be defined as: $H = P_{max}/A$, where P_{max} is the maximum applied load, and A is the contact area at maximum load.

In nano-indentation, the Young's Modulus, E, can be obtained from:

$$\frac{1}{E_r} = \frac{1-\nu^2}{E} + \frac{1-\nu_i^2}{E_i}$$

where ν_i = Poisson ratio of the diamond indenter (0.07) and E_i = Young's modulus of the diamond indenter.

This paper describes the use of the nano-indentation technique for a determination of the hardness and elastic modulus. The depth of nanopenetration provides an indirect measure of the area of contact at full load and thus the hardness is obtained by dividing the maximum applied load with the contact area.[5]

2 EXPERIMENTAL

The substrate material used was high-speed steel type M2. Prior to deposition the substrate was mechanically polished to a surface roughness of 0.12 μm (R_a). The specimens were first austenized, quenched and then tempered to the final hardness of 850 HV. In order to produce good adhesion of the coating, the substrates were plasma nitrided at low pressure (1×10^{-3} Pa), prior to deposition of the coating. The PVD treatment was performed in a Balzers Sputron installation with a rotating specimen. The deposition parameters were as follows: Base pressure in the chamber was 1×10^{-5} mbar. During etching, the bias voltage was $U_b = 1$ kV and the current was $I_d = 50$ mA. During deposition the substrate temperature was $T_s = 200$ °C, the partial pressure of Ar was $P_{Ar} = 1 \times 10^{-3}$ mbar and the partial pressure of N_2 was $P_{N2} = 3 \times 10^{-4}$ mbar. Prior to entering the deposition chamber the substrates were cleaned.

The IBAD system consists of an e-beam evaporation source for evaporating Ti metal and 5-cm-diameter Kaufman ion source for providing argon ion beam. The base pressure in the IBAD chamber was 1×10^{-6} mbar. The partial pressure of Ar during deposition was $(3.1–6.6) \times 10^{-6}$ mbar and partial pressure of N_2 was $6.0 \times 10^{-6}–1.1 \times 10^{-5}$ mbar. The ion energy ($E_{Ar} = 1.5–2$ keV), ion beam incident angle (15°), and substrate temperature $T_s = 200$ °C, were chosen as the processing variables. The deposition rate was $a_D = 0.05–0.25$ nm/s. A quartz crystal monitor was used to gauge the approximate thickness of the film. After deposition, the samples were irradiated with 120 keV, N^{5+} ions at room temperature (RT). The Ion Source is a multiply charged heavy-ion injector, based on the electron cyclotron resonance effect (ECR). The implanted fluencies (ions) were in the range from 0.6×10^{17} to 1×10^{17} cm^{-2}.

A pure titanium intermediate layer with a thickness of about 50 nm was deposited first for all the coatings to enhance the interfacial adhesion to the substrates.

The mechanical properties on the coated samples were characterized using a Nanohardness Tester (NHT) developed by CSM Instruments. Nano-indentation testing was carried out with applied loads in the range of 10 mN to 20 mN. A Berkovich diamond indenter was used for all the measurements. The data was processed using proprietary software to produce load–displacement curves and the mechanical properties were calculated using the Oliver and Pharr method.

The scratch adhesion testing was performed using commercially available equipment (REVETEST CSEM) fitted with a Rockwell C diamond stylus (cone apex angle of 120 °C, tip radius 200 μm). Acoustic Emission (AE) is an important tool for the detection and characterization of failures in the framework of non-destructive testing. The analyzed AE signal was obtained by a scratching test designed for adherence evaluation. The detection of elastic waves generated as a result of the formation and propagation of micro-cracks.

X-ray diffraction studies were undertaken in an attempt to determine the phases present, and perhaps an estimate of the grain size from line broadening. The determination of phases was realized by X-ray diffraction using a PHILIPS APD 1700 X-ray diffractometer. The X-ray sources were from CuKα with a wavelength of 15.443 nm (40 kV, 40 mA) at a speed of 0.9°/min. The surface roughness was measured using stylus-type (Talysurf Taylor Hobson) instruments. The most popular experimental XRD approach to the evaluation of residual stresses in polycrystalline materials is the $\sin^2 \psi$ method. The method requires a θ–2θ scan for every ψ angle around the selected diffraction peak, in order to emphasize the peak shifts.

3 RESULTS

The nitrogen-to-metal ratio (EDX) is stoichiometric for the IBAD technology and something smaller from the PVD (0.98). For the sample with additional ion implan-

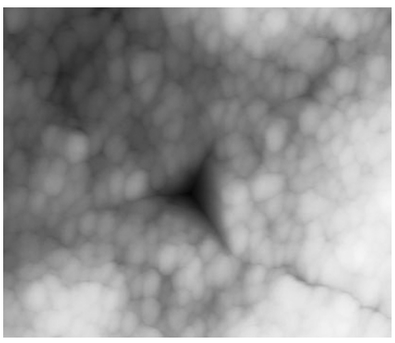

Figure 1: AFM image of crack paths from nano-indentation
Slika 1: AFM-posnetek smeri razpok pri nanoindentaciji

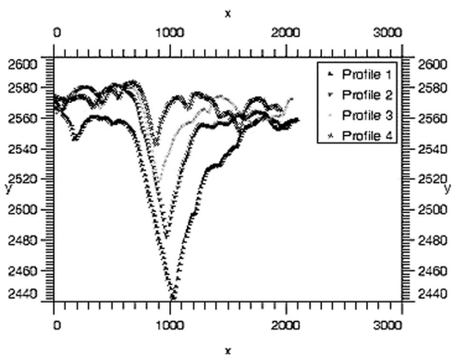

Figure 2: Cross-section of the indentation
Slika 2: Prerez nanoindentacije

tation, the value is significantly smaller (0.89). It is possibly diffused from the layer of the TiN to the interface.

All the results of the nanohardness are obtained with the Oliver & Pharr method and using a supposed sample Poisson's ratio of 0.3 for the modulus calculation The analysis of the indents was performed with an Atomic Force Microscope (**Figure 1**).

It can be seen, from the cross-section of an indent during indentation, that the indents are regularly shaped with slightly concave edges tipically seen where there is a significant degree of elastic recovery (**Figure 2**).

The nanohardness values and the microhardness are shown in **Table 1**.

Table 1: Surface nanohardness (load-10mN)
Tabela 1: Nanotrdota površine (breme 10 mN)

Unit	pn/IBAD	PVD	pn/PVD/II
GPa	21.6	32.6	42.6

For each adhesion measurement, the penetration (P_d), the residual penetration (R_d), the acoustic emission (AE) and the frictional force are recorded versus the normal load. The breakdown of the coatings was determined both by AE signal analysis and scanning electron microscopy. AE permits an earlier detection, because the shear stress is a maximum at a certain depth beneath the surface, where a subsurface crack starts. The critical loads are presented in **Table 2**.

Table 2: Critical loads for different type of coatings.
Tabela 2: Kritično breme za prekritja različne vrste

	pn/TiN(IBAD)	pn/TiN(PVD)
L_{c1}	–	23
L_{c2}	100	54
L_{c3}	138	108

The critical load L_{c1} corresponds to the load inducing the first crack on the coating. No cracks were observed on sample 1. The critical load L_{c2} corresponds to the load

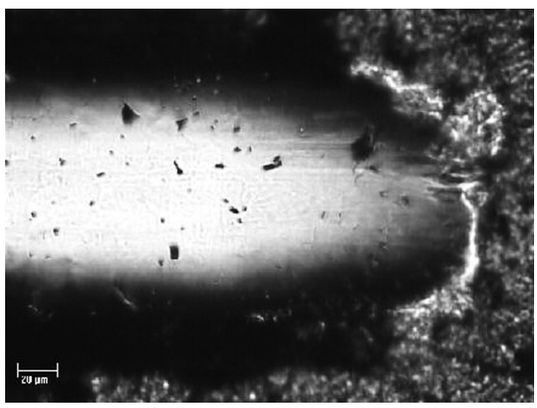

Figure 3: Delamination of coating
Slika 3: Luščenje prekritja

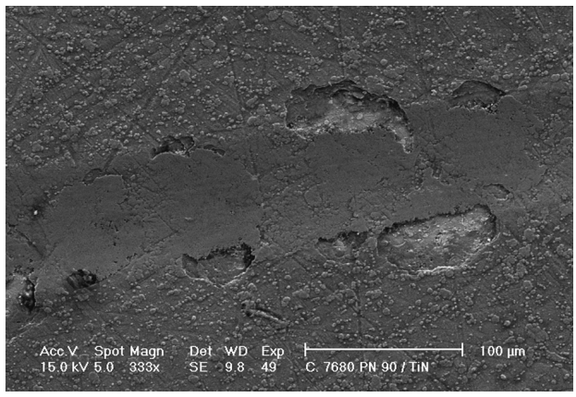

Figure 4: SEM morphology of scratch test pn/TiN(PVD).
Slika 4: SEM-morfologija preizkusa razenja pri pn/TiN (PVD)

inducing the partial delamination of the coating. The critical load L_{c3} corresponds to the load inducing the full delamination of the coating. In some places of hard coatings the cohesive failure of the coating and the delamination of the coating were observed (**Figure 3**).

It was found that the plasma-nitriding process enhanced the coating-to-substrate adhesion. In some places of the hard coatings cohesive failure of the coating and the delamination of the coating were observed (**Figure 4**).

The width of the column, for plane (422) is derived from the width of the diffraction peaks (Scherrer formula: $t = 0.9\ \lambda/(\beta \cos\theta/\lambda \cos\theta)$) of TiN, ($\beta = 0.154$ nm, $\theta = 62.5°$ and $\beta = 0.056$ rad), and it is 70 nm. Because of the low deposition temperature, it is possible that other planes also have a small width of the columns.

The stress determination follows the conventional $\sin^2\psi$ method. The stress determination was performed using a PHILIPS XPert diffractometer. The (422) diffraction peak was recorded in a 2θ interval between 118° and 130°, with tilting angle: $\psi_o^1 = 0°$, $\psi_o^2 = 18.75°$, $\psi_o^3 = 27.03°$, $\psi_o^4 = 33.83°$, $\psi_o^5 = 40°$. A typical result for the compact film, with residual stresses $\sigma = -4.28$ GPa, was TiN(PVD).

4 DISCUSSION

A hardness increase is observed for implanted samples. This can be attributed to iron nitride formation in the near-surface regions. The standard deviation of the results is relatively important due to the surface roughness of the samples. Because the thickness of the TiN coatings presented here is sufficiently large, which for all coatings is about 2900 nm (TiN-PVD), the hardness measurements will not be affected by the substrate, as in the three-times thinner (900 nm TiN-IBAD).

The individual values of E are different for all the measurements. The errors related to the measurements and estimations were different and for duplex coating with ion implantation they are less than 4 %. Good

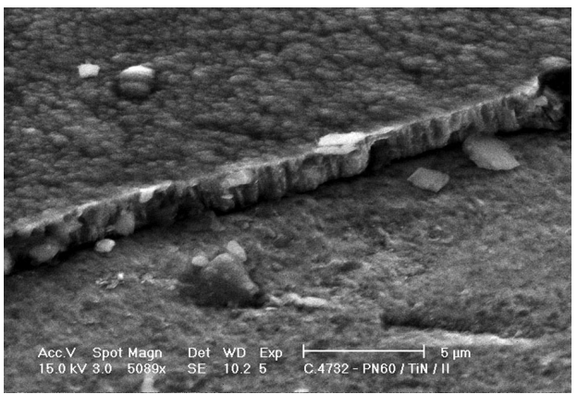

Figure 5: Surface morphology of duplex coating with ion implantation
Slika 5: Morfologija površine dupleksnega prekritja z ionsko implantacijo

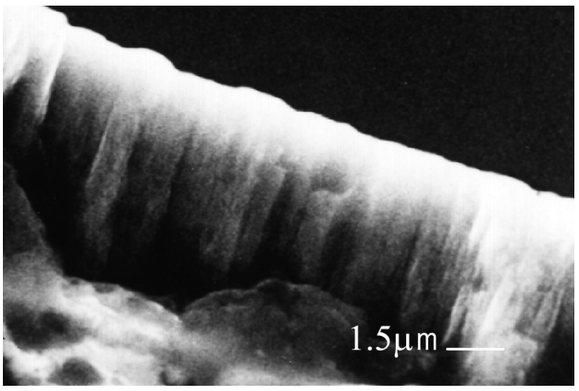

Figure 6: SEM of coating cross-section TiN (PVD)
Slika 6: SEM-prereza prekritja TiN (PVD)

agreement could be achieved between the E_c values and the nanohardness.

The topography of the TiN coatings was investigated using SEM (**Figure 5**).

The PVD coating process did not significantly change the roughness. For practical applications of IBAD coatings it is important to know that the roughness of the surface decreased slightly after the deposition (from R_a = 0.19 µm to R_a = 0.12 µm).

The formation of TiN by IBAD has its origin in a kinetically controlled growth. The nitrogen atoms occupy the octahedral sites in varying numbers according to the energy that these atoms possess to cross the potential barriers created by the surrounding titanium anions. The ion bombardment is believed to enhance the mobility of the atoms on the sample surface. The XRD analysis revealed the presence of only one phase, δ-TiN, and no evidence for other phases, such as Ti_2N, could be found. The ε-Ti_2N does not lead to an improvement in the tribological behavior.

The coating morphology was evaluated using the well-known structure zone model of Thornton. All the observed morphologies, **Figure 6**, are believed to be from a region of zone I (PVD) and from the border of region zone T (IBAD).

It has been suggested[5] that the transition from an open porous coatings with a low microhardness and rough surface, often in tensile stress to dense coating films with a greater microhardness, a smooth surface occurs at a well defined critical energy delivered to the growing film.

5 CONCLUSIONS

The experimental results indicated that the mechanical hardness is elevated by the penetration of nitrogen, whereas the Young's modulus is significantly elevated. Nitrogen-ion implantation leads to the formation of a highly wear resistant and hard surface layer.

Nitrogen implantation into hard TiN coatings increases the surface hardness and significantly reduces the tendency of the coatings to form microcracks when subjected to loads or stresses.

The above findings show that the deposition process and the resulting coating properties depend strongly on the additional ion bombardment.

6 REFERENCES

[1] S. Zheng Y. Sun, T. Bell, J. M. Smith, Mechanical properties microprobing of TiN coatings deposited by different techniques, The Fourth European Conference on Advanced Materials, 1995, 177–184

[2] V. Nelea, C. Ristoscu, C. Ghica, I. Mihailescu, P. Mille, 2000, Hydroxyapatite thin films growth by pulsed laser deposition: effects of the Ti alloys substrate passivation on the film properties by the insertion of a TiN buffer layer, *Sixth Conference on Optics 2000*, Bucharest, Romania, 247–252

[3] J. A. Batista, C. Godoy, A. Matthews, A. Leyland, Process developments towards producing well adherent duplex PAPVD coatings, Surface Engineering, 9 (**2003**), 37

[4] W. Ensinger, Ion bombardment effects during deposition of nitride and metal films, Surface and Coatings Technology, 99 (**1998**), 1–13

[5] M. Pharr, D. S. Harding, W. C. Oliver, in: M. Nastasi et al. Mechanical properties and deformation behavior of materials having ultra-fine microstructures, Kluwer, Dordrecht, 1993, 449

[6] M. Griepentrog, at al., Properties of TiN hard coatings prepared by unbalanced magnetron sputtering and cathodic arc deposition using a uni- and bipolar pulsed bias voltage, Surface and Coatings Technology, 74–75 (**1995**), 326–332

UDK 621.74:622.362
Original scientific article/Izvirni znanstveni članek

ISSN 1580-2949
MTAEC9, 45(5)451(2011)

INFLUENCE OF THE GRANULATION AND GRAIN SHAPE OF QUARTZ SANDS ON THE QUALITY OF FOUNDRY CORES

VPLIV GRANULACIJE IN OBLIKE ZRN KREMENOVEGA PESKA NA KAKOVOST LIVARSKIH JEDER

Marjan Marinšek, Klementina Zupan

University of Ljubljana, Faculty of Chemistry and Chemical Technology, Aškerčeva 5, 1000 Ljubljana, Slovenia
marjan.marinsek@fkkt.uni-lj.si

Prejem rokopisa – received: 2011-01-16; sprejem za objavo – accepted for publication: 2011-08-23

Several quartz moulding sands were used for the preparation of foundry models. All the moulding sands were similar with respect to their sieving parameters, yet different in terms of some morphological characteristics. Foundry models were analysed with regards to their mechanical properties. It was shown that the flexural strength of the prepared foundry models varied substantially, despite the fact that the grain size distributions obtained by sieving analyses of the moulding sands were very similar. The observed dissimilarities were explained pertaining to some differences in the micro-morphological characteristics of the sands, i.e., the particle shape and the grain statistical parameters. A quantitative morphological analysis of the sands was made on photographs taken with optical and electron microscopy using Zeiss KS 300 software. Crucial morphological parameters were defined by treating the moulding sands in laboratory-scale homogenization equipment and subsequent flexural strength measurements.

Key words: quartz moulding sands, foundry cores, mechanical properties, morphological analysis

Različni kremenovi peski so bili uporabljeni za pripravo livarskih jeder. Pred določitvijo mehanskih lastnosti livarskih modelov so bili vsi peski analizirani s sejalno analizo. Kljub podobnim osnovnim morfološkim lastnostim različnih kremenovih peskov so bile razlike v upogibni trdnosti livarskih modelov relativno velike. Razlike v mehanskih lastnostih livarskih modelov smo razložili z mikromorfološko karakterizacijo peskov. Karakterizacijo mikrostrukture smo izvedli z optičnim ter vrstičnim elektronskim mikroskopom ter kvantitativno analizirali rezultate z uporabo programa Zeiss KS 300. Z medsebojno primerjavo rezultatov se je izkazalo, da se ključni morfološki parametri, kot so oblika ter površina zrn, ter statistični parametri velikosti zrn pri različnih peskih spreminjajo. Izvedli smo tudi obedavo peska na vrtečih se valjih, s čimer smo na preprost način simulirali obdelavo peska na večjih industrijskih napravah, ki se uporabljajo v te namene. S tem je bil demonstriran način obdelave peska z namenom spreminjanja njegovih morfoloških parametrov ter posledično mehanskih lastnosti pripravljenih livarskih jeder.

Ključne besede: kremenov pesek, livarska jedra, mehanske lastnosti, morfološka analiza

1 INTRODUCTION

In foundry practice, sand cores are very extensively used to form various complicated casting cavities. The main ingredients of the moulding sand cores are base sand (i.e., a high-quality silica sand or lake sand), binder (clay binders, organic binders or inorganic binders) and moisture, if clays such as kaolinite are used as binders[1,2]. The ceramic moulding cores should have sufficient mechanical strength, resistance to erosive wear and chemical corrosion of the liquid metal, high refractoriness, low expansion coefficient and superior thermal stability. At the same time, no chemical reactions of the foundry core with liquid metal at high temperatures are allowed[3].

The mechanical strength of the moulding cores prior to pouring the molten metal into the mould is termed "green strength". The key to obtaining optimal sand cores with a high green strength and the desired performance during moulding is a feasible core binder. Therefore, producers and researchers have paid great attention to selecting and developing optimum binders, which can correspond well with the various required properties of the sand cores[4–8]. Such chemically bonded sand cast systems are often used for the moulds in ferrous (iron and steel) and nonferrous (copper, aluminium, brass) castings processes.

When producing cores and moulds, the so-called cold-box method has become increasingly widely used. This method does not require any heating of the moulding sand for hardening. In short, the method is based on the preparation of a mixture of particle-formed material (base sand) and a bonding agent (i.e., a polyisocyanate compound and a polyhydroxy compound), then the mixture is given the form desired and, finally, it is hardened by means of a catalyst. The cold-box method enables accelerated machining of the moulds in large quantities. The raw strength of the moulds, i.e., the strength directly after machining, is high enough to minimize the risks involved in handling the cores and moulds, so they can be used in the casting process shortly after preparation. Moulds and cores prepared by the cold-box method are also characterized by excellent disintegration after the casting of the metal[9].

The mechanical properties of moulds are determined on the basis of strength moduli. The flexural modulus

determination is often chosen as the strength parameter, because it can be easily determined experimentally in a practical way[10–12]. However, the mechanical properties of the moulding cores are strongly influenced by the binding mechanism in the moulds' machining process and also by the morphological properties of the sand being used.

The aim of this paper was to demonstrate the relationship between the morphological characteristics of the mould sand and the flexural strength of the prepared moulds. For the first time, crucial morphological parameters were defined and subsequently tested through the tailoring of moulding sands.

2 EXPERIMENTAL PROCEDURE

Six types of silica moulding sands (silica content > 98 %), similar with respect to their sieving parameters, were used in the experimental work. The particle size analysis was carried out on dry samples (110 °C, 2 h) of about 1 kg reduced to a mass of about 100 g using a Jones splitter and a +GP+ mechanical sieve shaker equipped with 12 sieves from 3.000 mm to 0.063 mm. The sieves were shaken continuously for a period of 12 min. After shaking, the sieves were taken apart and the sand left over on each of the sieves was carefully weighed and expressed as a percentage of the total mass.

Prior to the testing of the mechanical properties, mixtures of various sands (5 kg) and bonding agents (50 g of di-isocyanate and benzyl-ether polyole) were prepared, shaped in a sand rammer into bar specimens (18 × 3 × 3) cm and hardened according to the cold-box method with the ethyl-di-methyl-amine catalyst (T = 105 °C, t = 15 s). The flexural strength of the specimens was measured one day after their preparation using +GF+ apparatus and was expressed as an average flexural strength of 11 measurements for each sample.

For the morphological analysis, the sands were first embedded into Technovit resin and polished. After polishing, the samples were analyzed with a Leitz optical microscope (Leitz Wetzlar). The quantitative morphological analysis of the sands was performed on digital images and expressed as the parameters FERET X, FERET Y, FERET MIN and FERET MAX (intercept lengths in the x or y directions and the minimum or maximum intercept lengths, respectively), FERET RATIO as a ratio of the min and max ferrets, PERIM F (perimeter of the filled analysed region), PERIM C (perimeter of the convex shell of the analysed region), D CIRCLE (diameter of the circle with equivalent area as analysed region), F CIRCLE (form factor of the analysed region – sphericity) and AREA (area of the analysed region). The images were digitized into pixels with 255 different gray values using Zeiss KS300 3.0 image-analysis software. To obtain statistically reliable data, 7–10 different images were analysed in each case.

In order to tailor the morphological characteristics of the selected powder, ≈1.5 kg of sand was put into a ball mill's grinding bottle and rotated (≈0.2 r/s) for an extended time (no grinding balls were used).

3 RESULTS AND DISCUSSION

The results of the sieving analysis of the six different silica moulding sands are summarized in **Figure 1** and **Table 1**. It appears that the basic morphological characteristics of all six sands, including the granulometric interval, the mean diameter value $\bar{x}$ and the standard deviation d_s, are very similar and within the range of the morphological requests of silica sands used in a foundry. However, one of the crucial parameters for distinguishing silica sands in the foundry industry is the mechanical strength of the prepared casting model. From this point of view, the six silica sands differ substantially, as indicated in **Table 1**. The highest values of flexural strength were measured in the case of the samples Sand 1 and Sand 2 (777 and 679, respectively), while the lowest values were obtained for the samples Sand 4 and Sand 5 (369 and 317, respectively). Since the basic morphological parameters for the sample pairs Sand 1 and Sand 5, and Sand 2 and Sand 4 are very close, and cannot explain the big difference in the measured flexural strength of the prepared models, a more in-depth morphological analysis of the sands was performed. The optical micrographs and the results of the quantitative morphological analysis are summarized in **Figure 2** and in **Table 2**.

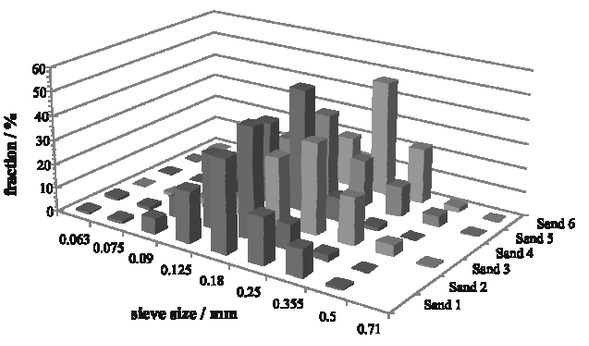

Figure 1: Granulometric histograms of the moulding sands
Slika 1: Histogrami različnih livarskih peskov

Table 1: Basic morphological characteristics of the silica sands and the flexural strengths of the prepared foundry models
Tabela 1: Osnovne morfološke karakteristike kremenovih peskov in upogibna trdnost pripravljenih livarskih jeder

Sample	$\bar{x}$/mm	d_s/mm	σ_{flex}/ (N cm^{-2})
Sand 1	0.196	0.079	777
Sand 2	0.164	0.054	679
Sand 3	0.250	0.095	567
Sand 4	0.167	0.050	369
Sand 5	0.210	0.099	317
Sand 6	0.254	0.081	382

Table 2: Morphological parameters of silica sands
Tabela 2: Morfološki parametri kremenovih peskov

Parameter	Sand sample					
	Sand 1	Sand 2	Sand 3	Sand 4	Sand 5	Sand 6
FERET X / μm	100.785	102.899	143.911	120.273	74.796	123.465
FERET Y / μm	100.221	103.729	140.119	119.183	77.62	122.288
FERET MIN / μm	78.271	80.627	106.389	89.137	56.567	91.705
FERET MAX / μm	117.792	121.547	168.389	143.656	93.003	146.425
FERET RATIO /	0.6645	0.6633	0.6318	0.6205	0.6082	0.6263
PERIM F / μm	368.745	379.89	569.329	467.135	340.922	485.994
PERIM C / μm	314.482	322.784	443.152	375.305	241.109	385.725
D CIRCLE / μm	90.636	92.619	122.214	102.79	63.158	105.489
F CIRCLE /	0.6915	0.6836	0.5402	0.5577	0.4585	0.5531
AREA / μm^2	8799.479	8703.74	15228.13	9298.84	4614.615	10431.86

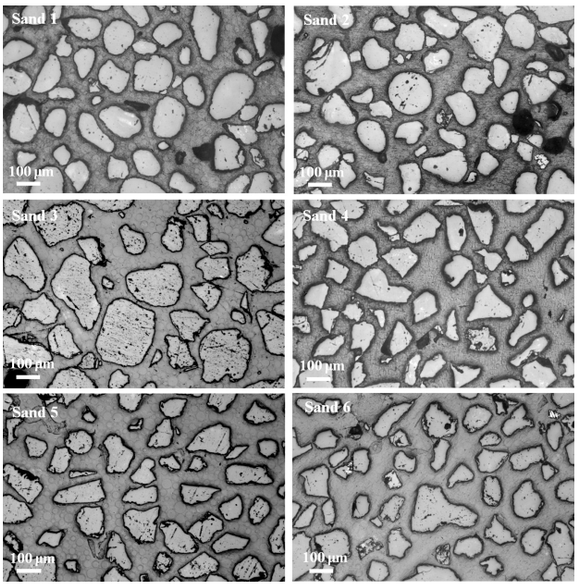

Figure 2: Optical micrographs of silica moulding sands (silica particles were embedded into polymer resin and polished)
Slika 2: Morfološka analiza kremenovih peskov z optičnim mikroskopom (kremenovi peski so bili zaliti v polimerno rezino in polirani)

According to the results summarized in **Table 2**, the FERET X and FERET Y values are very close for each analysed sample. Some differences among the samples can be seen if the values of the minimum or maximum intercept lengths and their ratios (FERET MIN, FERET MAX and FERET RATIO) are compared. The highest FERET RATIO values (close to 0.665) were calculated for the samples Sand 1 and Sand 2. These three values together somehow also indicate the origin of the silica sands. If the silica sands are treated with mechanical processing in crushers, the grains of the finally prepared sands are normally irregularly shaped, meaning that such sands should have fairly different values of FERET MIN and FERET MAX and consequently relatively low FERET RATIO values. A similar deduction may also be used when the parameters PERIM F (perimeter of the filled analysed region) and PERIM C (perimeter of the convex shell of the analysed region) are compared. Both parameters should be dissimilar if the grains are irregularly shaped. Again, by calculating the ratio of PERIM C/PERIM F, a single number is obtained, which indicates in some way the grain shape. The closer the calculated PERIM C to PERIM F ratio is to 1, the more spherical and full (without cavities or large pores) are the silica grains. The highest PERIM C to PERIM F ratios were calculated for the samples Sand 1 and Sand 2 (0.85 in both cases) and the lowest perimeter ratio in the case of the sample Sand 5 (0.71). The parameters D CIRCLE and AREA are not indicative when the morphological characteristics of the sands are compared with the flexural strength of the casting models. These two values describe the size class of an average sand grain. In contrast, the F CIRCLE (sphericity) value is significant for the final mechanical strength of the prepared models. When comparing the values of the measured flexural strength and sphericity, it can be concluded that higher F CIRCLE values also result in a higher flexural strength of the foundry models. More precisely, the highest F CIRCLE values (0.69 and 0.68) were determined for the samples Sand 1 and Sand 2, respectively, which also exhibited the highest flexural strength, while a relatively low flexural strength was characteristic for the prepared foundry model from the Sand 5 sample with the lowest F CIRCLE value of 0.46.

Such a relationship, in which more spherically shaped (less irregular) silica particles also resulted in a higher flexural strength of the prepared foundry models, is in accordance with the principles of the dispersion strengthening of composite materials. Foundry models can be understood as a composite of hard silica particles and softer, more ductile polyurethane, which is formed by the reaction between the di-isocyanate and the benzyl-ether polyole. In such a composite material, any sharp-edged particles locally act as stress intensifiers, reducing the critical stress needed for the mechanical degradation of the tested model.

To confirm that silica particle shape is one of the crucial parameters for controlling the flexural strength of

Table 3: Change of morphological parameters and flexural strength during sand treatment
Tabela 3: Sprememba morfoloških parametrov in upogibne trdnosti med obdelavo peskov

Parameter	Time of sand treatment				
	t = 0	t = 3 d	t = 6 d	t = 10 d	t = 14 d
FERET X / μm	120.273	118.963	111.461	101.811	100.969
FERET Y / μm	119.183	125.086	112.723	103.674	105.883
FERET MIN / μm	89.137	91.304	85.124	79.106	80.856
FERET MAX / μm	143.656	146.075	133.087	123.079	123.951
FERET RATIO /	0.6205	0.6292	0.6396	0.6427	0.6523
PERIM F / μm	467.135	466.154	424.539	382.031	380.529
PERIM C / μm	375.305	381.347	352.102	320.762	323.869
D CIRCLE / μm	102.79	103.319	95.852	85.997	88.268
F CIRCLE /	0.5577	0.5757	0.5897	0.6297	0.6488
AREA / μm^2	9298.84	10462.27	9542.703	7058.766	7416.08
σ_{flex} / N·cm^{-2}	330	/	/	/	

foundry models, silica sand (Sand 4) was rotated in a grinding bottle for several days. Such a treatment of the silica sand should not change its mean particle size considerably; however, it should tailor the shape of the sand grains. The results of the quantitative morphological analysis of the treated silica sand and the flexural strength of the prepared foundry models are summarized in **Table 3**.

The main characteristic of silica-sand treatment is the substantial increase in the flexural strength value if foundry models machined from non-treated and maximally treated sands are compared. However, sand treatment tailors not only the flexural strength of the foundry models but also alters the morphological characteristics of the sand. The parameters that describe the size class of an average sand grain (FERET X, FERET Y, FERET MIN, FERET MAX and D CIRCLE) diminish over time. In this respect, the diameter of the average sand grain (D CIRCLE) was reduced by 14 %. However, strictly from the aspect of grain size, silica sand (Sand 4) is within the range of morphological requirements to be used in the foundry.

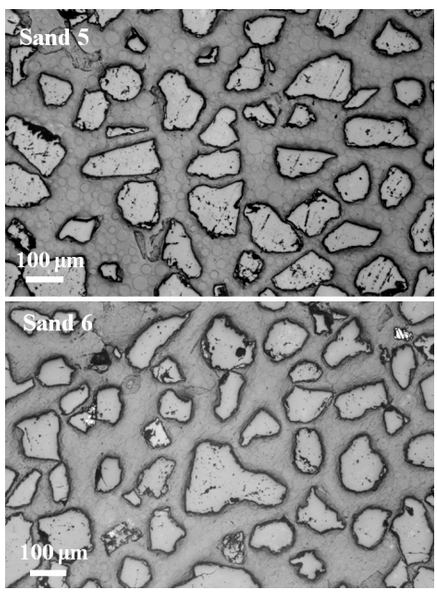

Figure 3: Optical micrographs of the silica sand (Sand 4) before (left image) and after (right image) the sand treatment
Slika 3: Slike optičnega mikroskopa vzorca kremenovega peska (Sand 4) pred obdelavo (levo) in po njej (desno)

In view of the fact that the parameters determining morphological size (if silica grain size is within the range of requests) are not decisive for the foundry model flexural strength, as discussed previously, the increased flexural strength of the foundry model was ascribed to the shape change of the average sand grain. The sand treatment increased the ratio PERIM C to PERIM F from 0.80 to the final value of 0.85. Simultaneously, the F CIRCLE value also increased from 0.56 to 0.65, meaning that the sand grains became increasingly spherical. This change in the sphericity of the particles is also evident from the optical micrographs of the non-treated and treated silica sand (**Figure 3**).

4 CONCLUSION

Foundry models prepared from various silica sands may express quite different values of flexural strength. These differences may be interpreted by the morphological characteristics of silica sands. It was shown that the basic morphological parameters, i.e., the mean particle diameter and the standard deviation, were not sufficient to explain the measured differences in flexural strength. Instead, an in-depth morphological analysis revealed that when the silica grain size is within the range of requests, particle shape is one of the crucial parameters for controlling the flexural strength of the foundry models. More spherically shaped silica particles also resulted in a higher flexural strength of the prepared foundry models. The crucial morphological parameters of the silica sands to predict the flexural strength of prepared foundry models are F CIRCLE (sphericity), the PERIM C to PERIM F ratios (ratio between the perimeters of the convex shell of the analysed region and the filled

analysed region, respectively) and the FERET RATIO as a ratio of the ferret min to ferret max.

5 REFERENCES

[1] D. M. Gilson, The role of different core binder systems in iron casting production: Effect of porosity defects and casting properties, AFS Trans., 101 (**1993**), 491–496

[2] M. Stancliffe, J. Kroker, X. Wang, Focusing core binder needs, Modern Casting, 97 (**2007**), 40–48

[3] F. Jorge Lino, T. Pereira Duarte, Ceramic components for foundry industry, Journal of Materials Processing Technology, (**2003**), 628–633

[4] A. Ferrero, M. Badiali, R. Schreck, J. Siak, W. Whited, New binder for casting cores: An industrial application to safety suspension parts, J. Mater. Manufact., 107 (**1998**), 894–899

[5] Y. Kato, T. Zenpo, N. Asano, New core binder system for aluminium casting based on polysaccharide, AFS Trans., 113 (**2005**), 327–332

[6] Z. P. Xie, J. L. Yang, Y. Huang, The effect of silane contents on fluidity and green strength for ceramic injection moulding, Journal of Materials Science Letters, 16 (**1997**), 1286–1287

[7] W. Yu, H. He, N. Cheng, B. Gan, X. Li, Preparation and experiments for a novel kind of foundry core binder made from modified potato starch, Materials and Design, 30 (**2009**), 210–213

[8] N. A. Ademoh, A. T. Abdullahi, Assessment of foundry properties of steel casting sand moulds bonded with the grade 4 Nigerian acacia species (gum arabic), International Journal of Physical Sciences, 4 (**2009**), 238–241

[9] J. Jakubski, S. M. Dobosz, The thermal deformation of core and moulding sands according to the hot distortion parameter investigations, Arch. Metall. Mater., 52 (**2007**), 421–428

[10] J. O. Aweda, Y. A. Jimoh, Assessment of Properties of Natural Moulding Sands in Ilorin and Ilesha, Nigeria, Journal of Research Information in Civil Engineering, 6 (**2009**), 68–77

[11] J. Petrík, P. Gengeľ, The capability of green sand mould strength and mould permeability measurement process, Acta Metallurgica Slovaca, 15 (**2009**), 86–92

[12] F. Peters, R. Voigt, S. Z. Ou, C. Beckermann, Effect of mould expansion on pattern allowances in sand casting of steel, International Journal of Cast Metals Research, 20 (**2007**), 275–287

UDK 537.5:621.3
Original scientific article/Izvirni znanstveni članek

ISSN 1580-2949
MTAEC9, 45(5)457(2011)

CHARACTERIZATION OF EXTREMELY WEAKLY IONIZED HYDROGEN PLASMA WITH A DOUBLE LANGMUIR PROBE

KARAKTERIZACIJA ŠIBKO IONIZIRANE VODIKOVE PLAZME Z DVOJNO LANGMUIRJEVO SONDO

Miran Mozetič

Center of Excellence for Polymer Materials and Technologies, Tehnološki park 24, 1000 Ljubljana, Slovenia
miran.mozetic@guest.arnes.si

Prejem rokopisa – received: 2010-11-04; sprejem za objavo – accepted for publication: 2011-06-23

Basic parameters of hydrogen plasma created in a large discharge chamber were determined using a double Langmuir probe. Plasma was created in a Pyrex cylinder with the diameter of 25 cm and the height of 80 cm by an antenna connected to a RF generator operating at the frequency of 27.12 MHz and the power of about 200 W. The antenna was a copper coil of 4 turns. The discharge chamber was pumped with an oil diffusion pump with the nominal pumping speed of 600 L/s backed by a two stage rotary pump with the pumping speed of 4.4×10^{-3} m^3 s^{-1}. The ultimate pressure of about 2×10^{-3} Pa was obtained in the vacuum system after pumping for few hours. A double Langmuir probe was galvanic separated from the mains and placed into the centre of the discharge chamber. The probe was made from 2 tungsten rods with a diameter of 1.2 mm and separated for 2 cm. The length of un-insulated part of the rods was 17.5 mm. Plasma parameters were measured at different pressures between 0.4 and 7.2 Pa. The electron temperature reached the maximum of about kT_e = 3.5 eV at the pressure of 1 Pa. The plasma density was slowly decreasing with increasing pressure and was of the order of 10^{15} m^{-3}, and the Debye length was rather constant at about 2×10^{-4} m. The results were explained by characteristics of an electrode less RF discharge in the E mode.

Keywords: plasma, hydrogen, double Langmuir probe, electron temperature, plasma density, Debye length

Z Langmuirjevo sondo smo določali parametre vodikove plazme, ustvarjene v velikem plazemskem reaktorju. Ta je bil narejen iz cilindrične cevi iz stekla pyrex premera 25 cm in višine 80 cm. Plazmo smo vzbujali z anteno, povezano z RF-generatorjem s frekvenco 27,12 MHz in močjo 200 W. Antena je bila narejena iz bakrene tuljave s 4 ovoji. Razelektritveno komoro smo črpali z difuzijsko črpalko z nazivno črpalno hitrostjo 600 L/s in povezano z dvostopenjsko rotacijsko predčrpalko s črpalno hitrostjo 4,4 $\times 10^{-3}$ m^3 s^{-1}. Po nekajurnem črpanju smo dosegli končni tlak 2×10^{-3} Pa. Dvojna Langmuirjeva sonda je bila galvansko ločena od omrežja in vstavljena v sredino razelektritvene komore. Sonda je bila narejena iz dveh volframovih palic premera 1,2 mm, ki sta bili med seboj oddaljeni 2 cm. Dolžina neizoliranega dela palic je bila 17,5 mm. Parametre plazme smo merili pri tlakih med 0,4 Pa in 7,2 Pa. Temperatura elektronov je dosegla maksimum okoli kT_e = 3,5 eV pri tlaku 1 Pa. Gostota plazme je počasi padala z naraščajočim tlakom in je bila reda 10^{15} m^{-3}. Debyeva dolžina je bila dokaj konstantna okoli 2×10^{-4} m. Rezultate smo razložili z značilnostmi brezelektrodne RF-razelektritve v E-načinu.

Ključne besede: plazma, vodik, dvojna Langmuirjeva sonda, temperatura elektronov, gostota plazme, Debyeva dolžina

1 INTRODUCTION

Low pressure non-equilibrium plasma is nowadays widely used for treatment of solid materials on both laboratory and industrial scales. Interaction of plasma radicals with solid materials allows for modification of the surface free energy of different materials,[1–3] selective removal of particular compounds from the surface of composite materials,[4–7] modification of the surface roughness,[3,8–9] controlled destruction of organic materials[10–13] or surface functionalization,[14–24] and formation of non-equilibrium nanostructures on several materials.[25–38] Plasma is created in a suitable electrical discharge. Both magnetized and non-magnetized discharges are created using DC, AC, RF and MW power supplies. Depending on particular requirements, plasma is created in discharge chambers with different dimensions. Rather small chambers are usually applied for laboratory experiments. Namely, small systems are easy to control, almost free from electromagnetic interferences and cheap to build. A disadvantage of a small system is that plasma sustaining requires a certain density of charged particles. According to Paschen rules, the gas breakdown cannot occur in a small system at low pressure and low power. In some applications, however, very weak plasma is required. Since the Paschen rules prevent sustaining of such plasma in a small volume, one should either create plasma in a large system or use a flowing afterglow instead of plasma itself. Flowing afterglows are popular, but have an important disadvantage: since the reactive particles enter an afterglow chamber from a remote source, their density is very sensitive to properties of samples placed into the afterglow chamber. This effect is avoided by creation of plasma in a large chamber. In such a case, plasma can be created and easily sustained at pretty small discharge power and any particles that are lost at the surface of a sample are replaced by production in the chamber itself.

In order to understand interaction between plasma particles and solid materials, plasma should be characterized. A variety of methods have appeared for plasma characterization including titration,[39–41] optical emission and absorption spectroscopy,[42–46] mass spectrometry,[47–49]

catalytic probes[50–60] and electrical probes (often called Langmuir probes).[61–64] Basic plasma parameters are the density of charged particles, the electron temperature, the Debye length, plasma potential and floating potential. They can be all determined using electrical probes. A simple electrical probe is just a piece of metal immersed into plasma and connected to a DC power supply. The current against voltage characteristic is measured and the plasma parameters are calculated using an appropriate model. The probes perform well in stable discharges, but often fail in RF discharges due to stray effects. A piece of metal acts as a receiver and is self biased against surrounding plasma causing misleading results. An effective way to avoid such effects is application of a double electrical probe. In this configuration the probe is kept floating according to local space potential so the system is pretty unaffected by any stray effects as long as the entire probe circuit is galvanic separated from mains or any other metallic component. Such a probe was used at present experiments.

2 EXPERIMENTAL

A high vacuum experimental system was built to create very weak plasma. Schematic of the system is shown in **Figure 1**. The discharge chamber is a Pyrex cylinder with the diameter of 25 cm and the height of 80 cm. Plasma is created by an antenna connected to a RF generator operating at the frequency of 27.12 MHz and the power of about 200 W. The antenna is a copper coil of 4 turns. The discharge chamber is pumped with an oil diffusion pump with the nominal pumping speed on 0.6 m^3 s^{-1} backed by a two stage rotary pump with the pumping speed of 4.4 × 10^{-3} m^3 s^{-1}. Pressure is measured with a Pirani gauge that has been previously calibrated for hydrogen. The ultimate pressure of about 2 × 10^{-3} Pa was obtained in the vacuum system after pumping for few hours. After receiving a constant (ultimate) pressure the discharge vessel was filled with hydrogen to the desired pressure. Experiments were performed at different pressures between 0.4 and 7.6 Pa.

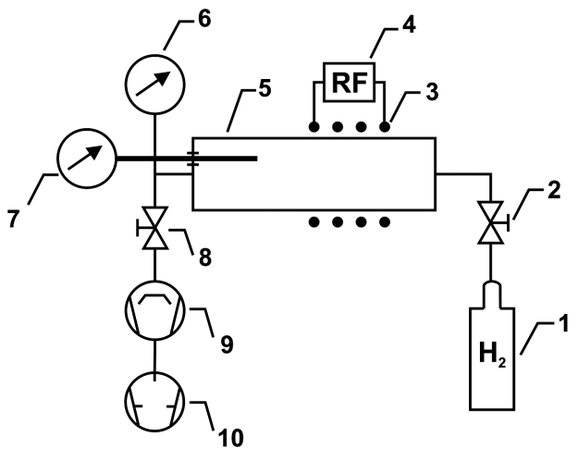

Figure 1: Schematic of the experimental setup. 1 – hydrogen flask, 2 – leak valve, 3 – copper coil, 4 – RF generator, 5 – discharge chamber, 6 – Pirani gauge, 7 – Langmuir probe, 8 – high vacuum valve, 9 – diffusion pump, 10 – mechanical pump

Slika 1: Shema eksperimentalnega sistema. 1 – jeklenka vodika, 2 – vpustni ventil, 3 – bakrena tuljava, 4 – RF-generator, 5 – razelektritvena posoda, 6 – Piranijev vakuummeter, 7 – Langmuirjeva sonda, 8 – visokovakuumski ventil, 9 – difuzijska črpalka, 10 – mehanska črpalka

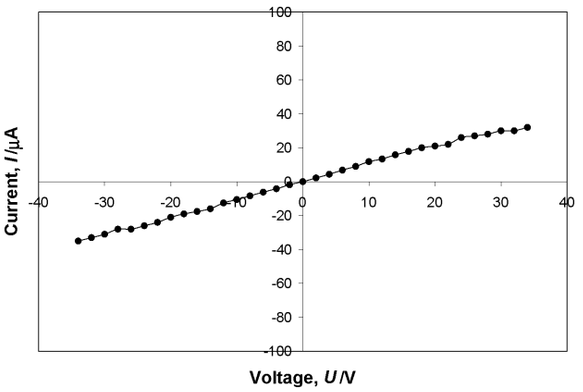

Figure 2: A typical characteristic of the small Langmuir probe
Slika 2: Značilna karakteristika majhne Langmuirjeve sonde

A double Langmuir probe was galvanic separated from the mains and placed into the centre of the discharge chamber. Two sets of probes were made: a small one with the length of 10 mm and the diameter of 30 μm and a much larger probe. The large probe was made from 2 tungsten rods with a diameter of 1.2 mm and separated for 2 cm. The length of un-insulated part of the rods was 17.5 mm. A typical characteristic of the small probe is plotted in **Figure 2**. The probe characteristic is rather linear instead of being similar to hyperbolical tangen as it should be according to literature. Obviously the small probe fails to operate properly and the reasons for this will be discussed later in the paper. Large probes were used for plasma characterization instead.

3 RESULTS

The probe characteristic was measured manually at different pressure. The voltage between the electrodes of the double probe was varied from –34 V to +34 V in steps of 2 V. The resulting current was measured by an ampermeter at each step. Some typical characteristics of the probe measured at different pressures are presented in **Figures 3 – 7**. Plasma parameters were then determined following the procedure suggested by Chen in his classical work.[65] The electron temperature was determined as[65]

$$kT_e = \frac{e_0 I_1 I_2}{\frac{dI}{dU}(I_1 + I_2)} \quad (1)$$

Here, k is the Boltzmann constant, T_e the electron temperature, e_0 the elementary charge, I_1 the saturated ion current on the first electrode extrapolated to zero net current, I_2 the saturated ion current on the second electrode extrapolated to zero net current, and dI/dU the first derivative of the curve at the inflection point. The values of I_1, I_2 and dI/dU are determined graphically as shown in **Figure 7** as for example. Once the electron temperature is known, the density of charged particles is calculated using the following equation:

$$N = \frac{I_1 + I_2}{e_0 A \sqrt{\frac{kT_e}{m_+}}} \quad (2)$$

Here, N is the density of charged particles in the vicinity of the probe, A the probe area, and m_+ is the positive ion mass (for H_2^+ ions it is 3.32×10^{-27} kg). The electron temperature and plasma density versus pressure calculated using Equations 1 and 2 are presented in **Figure 8**.

The Debye length is calculated as

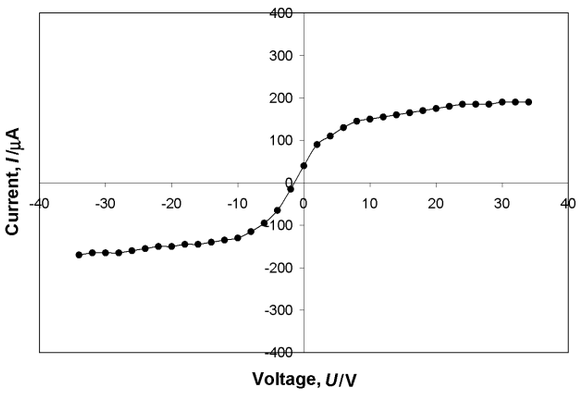

Figure 3: A characteristic of the large Langmuir probe measured at the pressure of 0.4 Pa

Slika 3: Karakteristika velike Langmuirjeve sonde, izmerjena pri tlaku 0,4 Pa

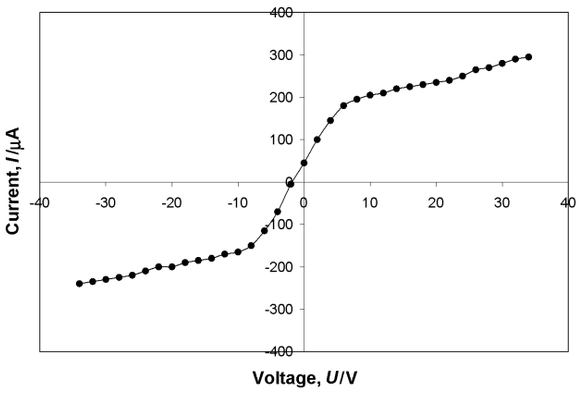

Figure 4: A characteristic of the large Langmuir probe measured at the pressure of 0.8 Pa

Slika 4: Karakteristika velike Langmuirjeve sonde, izmerjena pri tlaku 0,8 Pa

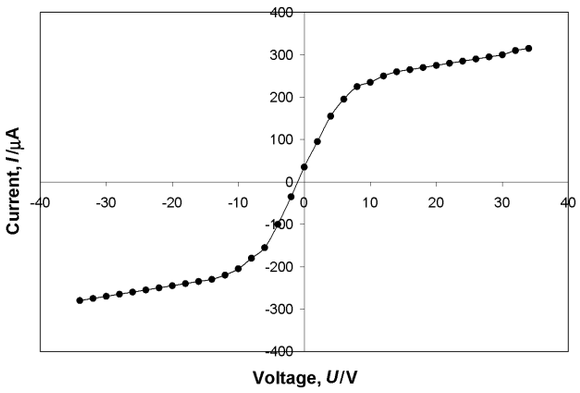

Figure 5: A characteristic of the large Langmuir probe measured at the pressure of 2.4 Pa

Slika 5: Karakteristika velike Langmuirjeve sonde, izmerjena pri tlaku 2,4 Pa

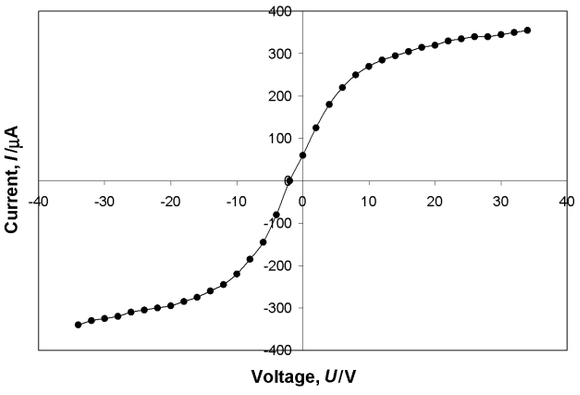

Figure 6: A characteristic of the large Langmuir probe measured at the pressure of 4.8 Pa

Slika 6: Karakteristika velike Langmuirjeve sonde, izmerjena pri tlaku 4,8 Pa

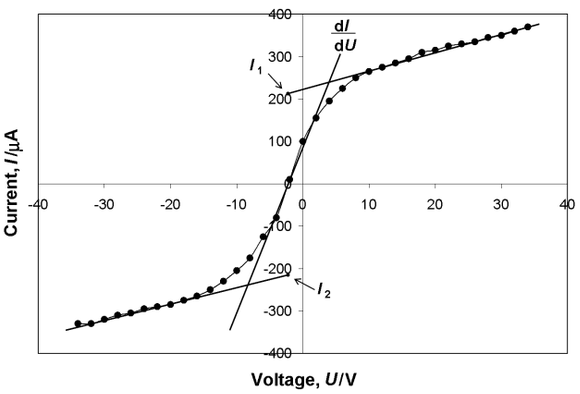

Figure 7: A characteristic of the large Langmuir probe measured at the pressure of 7.2 Pa

Slika 7: Karakteristika velike Langmuirjeve sonde, izmerjena pri tlaku 7,2 Pa

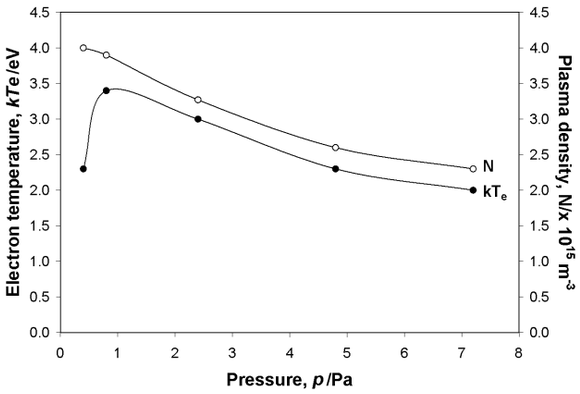

Figure 8: Variation of electron temperature and plasma density versus pressure

Slika 8: Spreminjanje elektronske temperature in gostote plazme v odvisnosti od tlaka

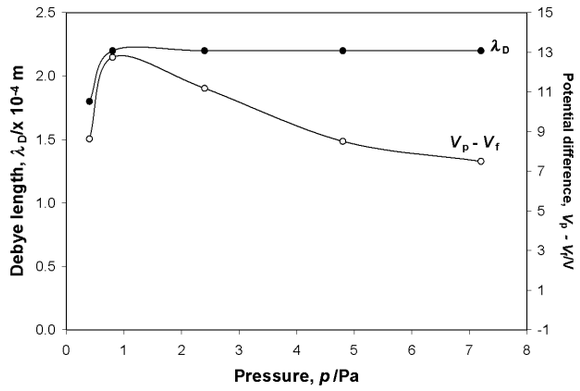

Figure 9: Variation of Debye length and variation of the difference between the plasma potential and the floating potential versus pressure

Slika 9: Spreminjanje Debyjeve dolžine ter spreminjanje razlike plazemskega in plavajočega potenciala v odvisnosti od tlaka

$$\lambda_{\mathrm{D}} = \sqrt{\frac{e_0 kT_{\mathrm{e}}}{N_{\mathrm{e}} e_0^2}} \tag{3}$$

Here, λ_{D} is the Debye length, and ε_0 the vacuum permittivity. Finally, the difference between the plasma and floating potentials is calculated from (4):

$$V_{\mathrm{p}} - V_{\mathrm{f}} = \frac{kT_{\mathrm{e}}}{2e_0} \ln\left(\frac{m_+}{2m_{\mathrm{e}}}\right) \tag{4}$$

Here, V_{p} is plasma potential, V_{f} floating potential, k Boltzmann constant, m_+ ion mass and m_{e} electron mass. The plots of the Debye length and difference between plasma and floating potentials versus pressure are presented in **Figure 9**.

4 DISCUSSION

Electrical probes usually fail in RF fields due to stray effects caused by electromagnetic interferences. Namely, any metal placed into the RF field acts as a receiver. This practical problem was minimized effectively by galvanic separation of the probe from any metallic part including the mains.

According to any literature, the probes should be made as small as possible in order to avoid drain of charged particles. While this criterion is particularly sever in the case of single probes that are biased also above the plasma potential to make proper reading of the electron temperature, it is less important in the case of a double probe. Namely, both electrodes of the double probe are kept well below the space potential so the drain of electrons is minimized. Still, an attempt was made to measure plasma parameters with a small probe with the electrode diameter of 30 μm. As clearly demonstrated in **Figure 2**, the small probe does not perform well in our case – the probe characteristic is rather linear instead of hyperbolical tangens. The strange behavior of the small probe is explained by taking into account the measured value of the Debye length (**Figure 10**). The Debye length is an order of magnitude larger than the small probe diameter. According to classical literature any object placed into plasma is surrounded by a sheath, i.e. an intermediate layer rich in positive charge between unperturbed plasma and an object. The sheath thickness is of the order of a Debye length and it increases with increasing bias of an electrode versus unperturbed plasma. The positive ions are well thermallized in unperturbed plasma and move randomly in unperturbed plasma. As they reach the sheath boundary they are accelerated towards the electrode and are finally collected by the electrode. The area from where the ions are collected is thus not the geometric area of the electrode but rather the sheath area. The sheath area increases rather linearly with increasing bias and so does the ion current. In the case when the electrode diameter is much smaller than the sheath thickness, the ion current therefore does not depend much on the electrode area but rather on the sheath area. Taking into account this consideration the observed characteristic of the small probe (**Figure 2**) is not surprising: the ion current is almost linear since the probe diameter is an order of magnitude smaller than the Debye length which is, as mentioned above, a measure of the sheath thickness. This is why the small probe fails in our plasma.

The situation is reversed in the case of the large probe (**Figures 3–7**). In this case, the Debye length is an order of magnitude smaller than the electrode diameter. The sheath thickness is thus much smaller than the electrode diameter so the characteristics are satisfactory. Still, a (rather linear) increase of the probe characteristics is observed in the ion saturation regime (at large biasing). This is due to the fact that the sheath thickness increases with increasing bias. Happily, the increase is not dramatic and can be taken into account following the suggestions of Chen.

Taking into account the upper considerations the value of the ion saturation currents used for determination of the plasma density (Equation 2) is somehow arbitrary since, strictly, the values should have been obtained at plasma potential. Happily enough, the slope of the characteristics in the saturated regime is much smaller than at the inflection point so the uncertainty in the plasma density is not big. Still, it is worth mentioning that the values of plasma density should be only taken as the first approximation.

5 CONCLUSION

The basic plasma parameters were measured in a rather large discharge chamber. The discharge power was kept pretty low at about 200 W. Pretty weak plasma was created at such experimental conditions. The plasma density was found to be of the order of 10^{15} m^{-3}. Such plasma is suitable for mild treatment of delicate materials that do not stand aggressive treatments. The plasma density slowly decreases with increasing pressure. Since the Debye length is much lower than the mean free path of hydrogen molecules at pressures applied, the sheath that forms around any object is collision less, so ions bombard the surface with the kinetic energy gained across the sheath. This energy depends on the voltage across the sheath and, according to **Figure 9**, on pressure, and is around 10 eV. The bombardment is thus really weak and should not cause any damage of samples immersed into the plasma due to kinetic effects.

ACKNOWLEDGEMENT

The author acknowledges the financial support from the Ministry of Higher Education, Science and Technology of the Republic of Slovenia through the contract No. 3211-10-000057 (Center of Excellence Polymer Materials and Technologies).

6 REFERENCES

[1] A. Asadinezhad, I. Novak I, M. Lehocky, V. Sedlarik, A. Vesel, I. Junkar, P. Saha, I. Chodak, Plasma Processes Polym., 7 (**2010**), 6, 504–514

[2] S. Marais, M. Metayer, M. Labbe, J. M. Valleton, S. Alexandre, J. M. Saiter, F. Poncin - Epaillard, Surf. Coat. Technol., 122 (**1999**) 2–3, 247–259

[3] A. Vesel, I. Junkar, U. Cvelbar, J. Kovac, M. Mozetic, Surf. Interface Anal., 40 (**2008**) 11, 1444–1453

[4] R. Kulcar, M. Friskovec, N. Hauptman, A. Vesel, M. Klanjsek - Gunde, Dyes Pigm., 86 (**2010**) 3, 271–277

[5] A. Vesel, M. Mozetic, P. Panjan, N. Hauptman, M. Klanjsek - Gunde, M. Balat - Pichelin, Surf. Coat. Technol., 204 (**2010**), 9/10, 1503–1508

[6] T. Belmonte, J. M. Thiebaut, D. Mezerette, J. Phys. D: Appl. Phys., 35 (**2002**), 16, 9–1926

[7] F. Gaboriau, G. Cartry, M. C. Peignon, C. Cardinaud, J. Vac. Sci. Technol. B, 20 (**2002**) 4, 1514–1521

[8] A. Vesel, M. Mozetic, A. Drenik, N. Hauptman, M. Balat - Pichelin, Appl. Surf. Sci., 255 (**2008**) 5, 1759–1765

[9] I. Junkar, U. Cvelbar, A. Vesel, N. Hauptman, M. Mozetic, Plasma Processes Polym., 6 (**2009**) 10, 667–675

[10] A. Vesel, M. Mozetic, A. Hladnik, J. Dolenc, J. Zule, S. Milosevic, N. Krstulovic, M. Klanjsek-Gunde, N. Hauptman, J. Phys. D: Appl. Phys., 40 (**2007**) 12, 3689–3696

[11] N. Krstulovic, I. Labazan, S. Milosevic, U. Cvelbar, A. Vesel, M. Mozetic, J. Phys. D: Appl. Phys., 39 (**2006**) 17, 3799–3804

[12] D. Vujosevic, Z. Vranica, A. Vesel, U. Cvelbar, M. Mozetic, A. Drenik, T. Mozetic, M. Klanjsek-Gunde, N. Hauptman, Mater. Tehnol., 40 (**2006**) 6, 227–232

[13] K. Elersic, I. Junkar, A. Spes, N. Hauptman, M. Klanjsek-Gunde, A. Vesel, Mater. Tehnol., 44 (**2010**), 3, 153–156

[14] U. Cvelbar, M. Mozetic, I. Junkar, A. Vesel, J. Kovac, A. Drenik, T. Vrlinic, N. Hauptman, M. Klanjsek-Gunde, B. Markoli, N. Krstulovic, S. Milosevic, F. Gaboriau, T. Belmonte, Appl. Surf. Sci., 253 (**2007**), 21, 8669–8673

[15] T. Vrlinic, A. Vesel, U. Cvelbar, M. Krajnc, M. Mozetic, Surf. Interface Anal., 39 (**2007**), 6, 476–481

[16] A. Vesel, M. Mozetic, A. Zalar, Surf. Interface Anal., 40 (**2008**), 3–4, 661–663

[17] A. Vesel, M. Mozetic, A. Zalar, Vacuum, 82 (**2008**) 2, 248–251

[18] M. Sowe, I. Novak, A. Vesel, I. Junkar, M. Lehocky, P. Saha, I. Chodak, Int. J. Polym. Anal. Ch., 14 (**2009**) 7, 641–651

[19] A. Vesel, Inf. MIDEM, 38 (**2009**), 257–265

[20] M. Gorjanc, V. Bukosek, M. Gorensek, A. Vesel, Tex. Res. J., 80 (**2010**) 6, 557–567

[21] A. Vesel, M. Mozetic, S. Strnad, K. Stana-Kleinschek, N. Hauptman, Z. Persin, Vacuum, 84 (**2010**) 1, 79–82

[22] I. Junkar, A. Vesel, U. Cvelbar, M. Mozetic, S. Strnad, Vacuum, 84 (**2010**) 1, 83–85

[23] A. Asadinezhad, I. Novak, M. Lehocky, F. Bilek, A. Vesel, I. Junkar, P. Saha, A. Popelka, Molecules, 15 (**2010**) 2, 1007–1027

[24] A. Vesel, K. Elersic, I. Junkar, B. Malic, Mater. Tehnol., 43 (**2009**) 6, 323–326

[25] M. Mozetic, U. Cvelbar, M. K. Sunkara, S. Vaddiraju, Adv. Mater., 17 (**2005**) 17, 2138–2142

[26] U. Cvelbar, M. Mozetic, J. Phys. D: Appl. Phys., 40 (**2007**) 8, 2300–2303

[27] U. Cvelbar, K. Ostrikov, I. Levchenko, M. Mozetic, M. K. Sunkara, Appl. Phys. Lett., 94 (**2009**) 21, 211502-1–211502-3

[28] U. Cvelbar, K. Ostrikov, A. Drenik, M. Mozetic, Appl. Phys. Lett., 92 (**2008**) 13, 133505-1–133505-3

[29] Z. Chen, U. Cvelbar, M. Mozetic, J. He, M. K Sunkara, Chem. Mater., 20 (**2008**) 9, 3224–3228

[30] K. Ostrikov, Plasma Nanoscience, Wiley, New York 2008

[31] A. Drenik, U. Cvelbar, K. Ostrikov, M. Mozetic, J. Phys. D: Appl. Phys., 41 (**2008**) 11, 115201-1–115201-7

[32] U. Cvelbar, K. Ostrikov, M. Mozetic, Nanotechnology, 19 (**2008**) 40, 405605-1–405605-7

[33] U. Cvelbar, Z. Chen, M. K. Sunkara, M. Mozetic, Small, 4 (**2008**) 10, 1610–1614

[34] M. Mozetic, A. Vesel, U. Cvelbar, A. Ricard, Plasma Chem. Plasma Process., 26 (**2006**) 2, 103–117

[35] M. Mozetic, U. Cvelbar, Plasma Sources Sci. Technol., 18 (**2009**) 3, 034002-1–034002-5

[36] D. Mariotti, K. Ostrikov, J. Phys. D: Appl. Phys., 42 (**2009**) 9, 092002-1–092002-4

[37] I. Levchenko, U. Cvelbar, K. Ostrikov, Appl. Phys. Lett., 95 (**2009**), 2, 021502-1–021502-3

[38] I. Levchenko, K. Ostrikov, K. Diwan, K. Winkler, D. Mariotti, Appl. Phys. Lett., 93 (**2008**), 18, 183102-1–183102-3

[39] T. Czerwiec, J. Gavillet, T. Belmonte, H. Michel, A. Ricard, Surf. Coat. Technol., 98 (**1998**), 1–3, 1411–1415

[40] A. Ricard, M. Gaillard, V. Monna, A. Vesel, M. Mozetic, Surf. Coat. Tech., 142–144 (**2001**), 333–336

[41] C. Jaoul, T. Czerwiec, T. Belmonte, A. Ricard, H. Michel, Eur. Phys. J. Appl. Phys., 26 (**2004**) 3, 227–234
[42] N. Krstulovic, U. Cvelbar, A. Vesel, S. Milosevic, M. Mozetic, Mater. Tehnol., 43 (**2009**) 5, 245-249
[43] F. Gaboriau, G. Cartry, M. C. Peignon, C. Cardinaud, J. Phys. D: Appl. Phys. 39 (**2006**) 9, 1830–1845
[44] N. Krstulovic, I. Labazan, S. Milosevic, U. Cvelbar, A. Vesel, M. Mozetic, Mater. Tehnol., 38 (**2004**) 1, 51–54
[45] M. Balat-Pichelin, M. Passarelli, A. Vesel, Mat. Chem. Phys., 123 (**2010**) 1, 40–46
[46] M. Balat-Pichelin, J. M. Badie, R. Berjoan, P. Boubert, Chem. Phys., 291 (**2003**) 2, 181–194
[47] J. A. Ferreira, F. L. Tabares, Plasma Sour. Sci. Technol., 18 (**2009**) 3, 034019
[48] J. A. Ferreira, F. L. Tabares, J. Vac. Sci. Technol. A, 25 (**2007**) 2, 246–251
[49] F. L. Tabares, D. Tafalla, I. Tanarro, V. J. Herrero, A. M. Islyaikin, Vacuum, 73 (**2004**) 2, 161–167
[50] M. Balat-Pichelin, A. Vesel, Chem. Phys., 327 (**2006**) 1, 112–118
[51] A. Vesel, A. Drenik, M. Mozetic, M. Balat-Pichelin, Vacuum, 84 (**2010**) 7, 969–974
[52] A. Vesel, M. Mozetic, M. Balat-Pichelin, Vacuum, 81 (**2007**) 9, 1088–1093
[53] A. Drenik, A. Tomeljak, M. Mozetic, A. Vesel, D. Babic, M. Balat-Pichelin, Vacuum, 84 (**2010**) 1, 90–93
[54] M. Mozetic, U. Cvelbar, A. Vesel, A. Ricard, D. Babic, I. Poberaj, J. Appl. Phys., 97 (**2005**) 10, 103308-1–103308-7
[55] M. Mozetic, A. Vesel, U. Cvelbar, A. Ricard, Plasma Chem. Plasma Process., 26 (**2006**) 2, 103-117
[56] M. Mozetic, A. Vesel, A. Drenik, I. Poberaj, D. Babic, J. Nucl. Mater., 363-365 (**2007**), 1457–1460
[57] M. Mozetic, A. Vesel, V. Monna, A. Ricard, Vacuum, 71 (**2003**) 1–2, 201–205
[58] A. Vesel, M. Mozetic, Vacuum, 61 (**2001**) 2–4, 373–377
[59] A. Drenik, U. Cvelbar, A. Vesel, M. Mozetic, Inf. MIDEM, 35 (**2005**), 85–91
[60] A. Drenik, U. Cvelbar, A. Vesel, M. Mozetic, Strojarstvo, 48 (**2006**) 1/2, 17–22
[61] T. Gyergyek, B. Jurcic-Zlobec, M. Cercek, J. Kovacic, Plasma Sources Sci. Technol., 18 (**2009**), 3, 035001-1 - 035001-19
[62] T. Gyergyek, M. Cercek, B. Jurcic-Zlobec, Contrib. Plasma Phys., 48 (**2008**), 5–7, 440–445
[63] T. Gyergyek, J. Kovacic, M. Cercek, Phys. Plasmas, 17 (**2010**), 8, 083504-1– 083504-16
[64] T. Gyergyek, J. Kovacic, M. Cercek, Contrib. Plasma Phys., 50 (**2010**), 2, 121–134
[65] F. F. Chen, Electric probes, in Plasma diagnostic techniques, Eds. Huddlestone and Leonard, Academic Press, New York, 1970, 113–200
[66] J. D. Swift, M. J. R. Schwar, Electrical probes for plasma diagnostics, Iliffe Books Co., London 1969

UDK 669.3:620.17
Original scientific article/Izvirni znanstveni članek

ISSN 1580-2949
MTAEC9, 45(5)463(2011)

OPTICAL PROPERTIES OF PLASTICALLY DEFORMED COPPER: AN ELLIPSOMETRIC STUDY

OPTIČNE LASTNOSTI PLASTIČNO DERFORMIRANEGA BAKRA: ŠTUDIJ ELIPSOMETRIJE

Nebojša Romčević,[1,2] Rebeka Rudolf,[3,4] Jelena Trajić,[1] Maja Romčević,[1] Branka Hadžić,[1] Dana Vasiljević – Radović,[5] Ivan Anžel[3]

[1]Institute of Physics, University of Belgrade, 11080 Belgrade, Serbia
[2]Kristal infiz, d. o. o., 11080 Belgrade, Serbia
[3]Faculty of Mechanical Engineering, University of Maribor, 2000 Maribor, Slovenia
[4]Zlatarna Celje, d. d., Kersnikova 19, 3000 Celje, Slovenia
[5]IHTM – Institute of Microelectronic Technologies and Single Crystals, 11000 Belgrade, Serbia
romcevi@ipb.ac.rs

Prejem rokopisa – received: 2011-01-15; sprejem za objavo – accepted for publication: 2011-03-18

In this paper the results of optical properties investigations on plastically deformed copper are presented. The optical properties of the plastically deformed copper were studied using spectroscopic ellipsometry in the ultraviolet-visible (UV-VIS) range. Chemically pure copper was deformed by applying the Equal Channel Angular Pressing (ECAP) technique. During the last decade, equal-channel angular pressing procedure was used for the fabrication of ultrafine-grained metals and alloys. The plastic deformation of metallic materials leads to the production of bulk nano-scale structures with ultrafine grains and cross-sections, which remain about equal before and after deformation. The parameters of the sample were calculated using a two-film model together with the Bruggeman effective medium approximation.

Key words: ellipsometric spectroscopy, atomic force microscopy, copper, amorphisation

V članku so predstavljeni rezultati raziskav optičnih lastnosti plastično deformiranega bakra. Te so bile raziskane s spektralno elipsometrijo v območju vidne UV-svetlobe. Kemijsko čist baker je bil deformiran z uporabo ECAP-metode (enakokotno koničasto stiskanje). V zadnjem času se ECAP-postopek uporablja za izdelavo ultra udrobnjenih kovin in zlitin. Takšna plastična deformacija kovinskih materialov vodi k izdelavi masivnih nanostruktur z ultra drobnimi zrni in prečnim prerezom, kar omogoča približno enakost pred deformacijo in po njej. Parametri preiskanih vzorcev so bili izračunani na osnovi uporabe dvojne plasti – filma skupaj s Bruggemanovo srednjo efektivno aproksimacijo.

Ključne besede: elipsometrična spektroskopija, atomska mikroskopija, baker, amorfizacija

1 INTRODUCTION

Modern life has a number of applications for copper, ranging from coins to pigments, and demand for copper remains high, especially in industrialized nations. Many consumers interact with copper in various forms on a daily basis. Copper is used in a vast variety of products in the domestic and industrial domains as thermal and electrical conductors and as a constituent of various metal alloys, in building construction, power generation and transmission, manufacturing of electronic products, and the production of industrial machinery and transportation vehicles.[1] Copper wiring and plumbing are integral to appliances, heating and cooling systems, and telecommunications links used every day in homes and businesses.

Copper is easily worked, being both ductile and malleable. It is easily stretched, molded, and shaped; it is resistant to corrosion; and conducts heat and electricity efficiently. As a result, copper was important to early humans and continues to be a material of choice for a variety of domestic, industrial, and high-technology applications today.

The most important use of copper is in electrical wiring; it is an excellent conductor of electricity (second only to silver), it can be made extremely pure, it corrodes very slowly, and it can be formed easily into thin wires – it is also very ductile. Due to this property, copper has been widely used as an electrode in electrochemical studies.[2]

Copper can be machined, although it is usually necessary to use an alloy for intricate parts, such as threaded components, to get really good mach inability characteristics. Good thermal conduction makes it useful for heat sinks and in heat exchangers. It has excellent brazing and soldering properties and can also be welded, although the best results are obtained with gas metal arc welding.[3]

Copper has a reddish, orange, or brownish color because a thin layer of tarnish (including oxides) gradually forms on its surface when gases (especially oxygen) in the air react with it. But pure copper, when fresh, is actually a pinkish or peachy metal. Copper, cesium and gold are the only three elemental metals with a natural color other than gray or silver.[4] Copper has its characteristic color because of its unique band structure.

The aim of this paper is to examine the gradient in the microstructure and texture that develops during Equal Channel Angular Pressing (ECAP).

2 EXPERIMENTAL

A chemically pure copper sample (99.99), prepared as a specimen of square cross-sections (10 mm ×10 mm) and about 50 mm long, was extremely plastically deformed with the repeated application of the Equal Channel Angular Pressing (ECAP).[5] ECAP is a novel technique for producing an ultra-fine-grain structure at the submicron level by introducing a large amount of shear strain into the material without changing the built shape or dimensions.

The deformations were performed in our experimental hydraulic press (VEB WEMA 250 MP), equipped with a tool for ECAP. The tool consists of two intersecting channels with the same cross-section (10 mm × 10 mm) that meet at an angle $2\Phi = 90°$. The geometry of the tool ensures that the material is deformed by a simple shear in ideal, frictionless conditions. The cross-section of the specimen remains almost equal before and after each step of the process, thus it is possible to subject one specimen several times to ECAP in order to reach a high degree of plastic deformation. In our case, the sample of chemically pure copper was subjected to the ECAP process eight times at room temperature (20 °C).

An atomic force microscope (AFM) was used to determine the general cell wall structure together with the assembly of particular components into the wall structure as a whole.

Ellipsometric measurements were a versatile and powerful optical technique for the investigation of the dielectric properties, used to characterize surface changes, optical constants of bulk or layered materials, overlayer thicknesses, multilayer structures, and surface or interface roughness.[6] The variable-angle spectroscopic ellipsometer (VASE) SOPRA GES5–IR in the rotating polarizer configuration was used for the ellipsometric measurements. The data were collected over the range from 1.5 eV to 4.2 eV with a step of 0.05 eV for three different angles of incidence 65°, 70° and 75°. The 70° angle was chosen as the apparatus has the maximum sensitivity for the ellipsometric data. All the calculations were made using Winelli_II Version 2.0.0.0. The fitting of the model to the experimental data was done using the Levenberg-Marquardt algorithm.[6–7]

3 RESULTS AND DISCUSSION

During our research, two copper samples were deformed and analyzed: Cu 1 – cross-section surface and Cu 2 – longitudinal section surface.

The typical appearance of the initial, undeformed Cu sample is present in **Figure 1a**. The topological morphology in two directions, longitudinal and transverse, is shown in **Figures 1b** and **1c**. As one can see from the figures, on the longitudinal surface there are essentially less phases than on the transverse surface. These phases

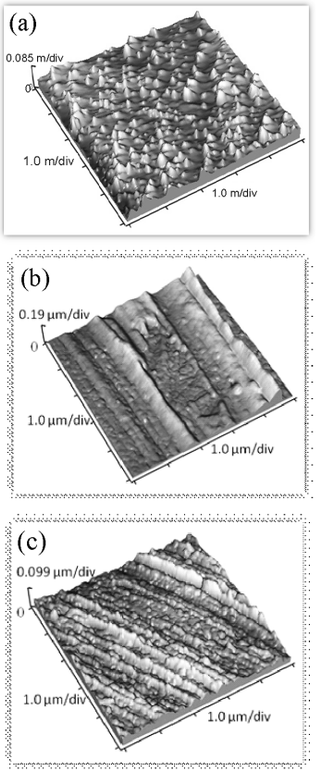

Figure 1: AFM image of surface of the pure Cu (a), Cu 2 (b) and Cu 1 (c) samples
Slika 1: AFM-slika površine čistega Cu (a), Cu 2 (b) in Cu 1 vzorcev

(particles contour) probably corresponds to nano-sized crystalline phases.

Ellipsometry is an optical measurement technique that characterizes light reflection (or transmission) from samples.[8] The key feature of ellipsometry is that it measures the change in polarized light upon light reflection from a sample (or light transmission by a sample). The ellipsometry measures the two values: the amplitude ratio ψ and phase difference Δ between the light waves. These parameters are defined by:

$$\rho = r_p / r_s = \tan(\psi)\, e^{i\Delta} \quad (1)$$

where ρ is the complex reflectance ratio, r_p and r_s are the complex reflectance coefficients of light polarized parallel (p) and perpendicular (s) to the plane of incidence, respectively.

The ellipsometric quantities ψ and Δ are sensitive to changes of different parameters, such as surface conditions, over layer structure, dielectric function of the material and others.

The real and imaginary parts of the pseudo-dielectric function for the bulk copper and samples Cu 1 and Cu 2 are presented in **Figure 2**. When it is exposed to oxygen, copper naturally oxidizes to copper(I) oxide (Cu_2O), therefore the ellipsometric spectra ($\tan(\psi)$, $\cos(\Delta)$) of the two samples Cu 1 and Cu 2 were fitted using a two-film

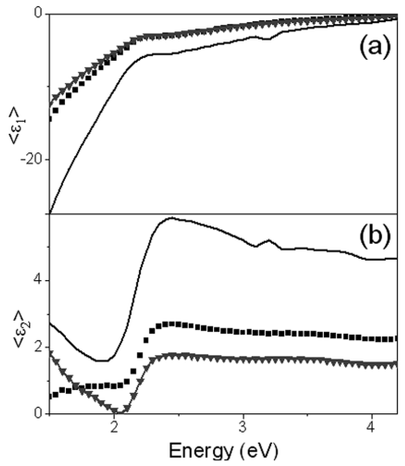

Figure 2: Real (a) and imaginary (b) parts of the pseudo–dielectric function for Cu 1 (squares), Cu 2 (triangles) and bulk copper (solid line)

Slika 2: Realni (a) in imaginarni (b) del pseudo-dialekrične funkcije za Cu 1 (kvadrat), Cu 2 (trikotnik) in masivni baker (polna črta)

model: Cu as a substrate, an over layer of Cu_2O and a surface-roughness layer (**Figure 3a**). The influence of the surface roughness also has to be taken into account. Namely, the surface over layer roughness is composed of the bulk copper oxide and an ambient. We calculated the volume fraction of the constituents. [6]

The experimental and the best-fitting data of the sample Cu 1 are presented in **Figure 3b**. The experimental data are represented by circles, while the solid lines represent the fitted data. The thickness of the Cu_2O was about 1.5 nm, and the roughness of the over layer with 80 % of Cu_2O and 20 % of void was about 25.6 nm. For the energies above 2 eV this fit is better than for the energies around and below this value. This is a consequence of plastic deformation, because the dielectric function of the sample substrate differs from the one of the bulk copper.[9]

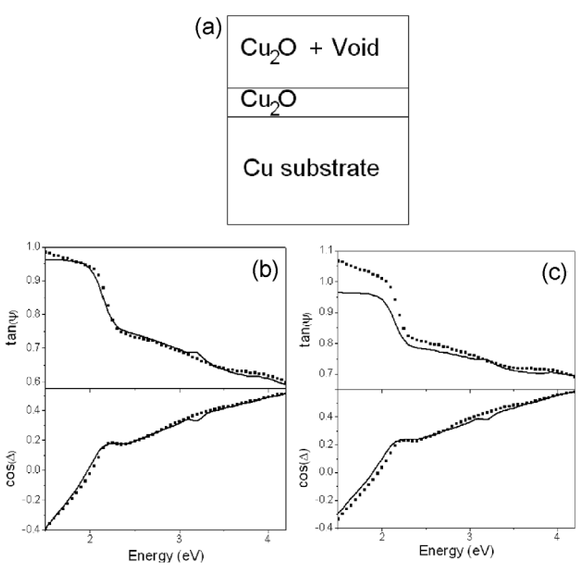

Figure 3: Sketch of a two-film model (a), experimental data (dots) and fitted data (solid line) of the ellipsometric spectra of samples Cu 1 (b) and Cu 2 (c)

Slika 3: Skica dvoplastnega modela: (a) eksperimentalni podatki (pikice) in dobljeni podatki (polna črta) elipsoidnega spektra za vzorca Cu 1 (b) in Cu 2 (c)

The experimental and the best-fitting data of the sample Cu 2 are presented in **Figure 3c**. The thickness of the copper oxide was about 1.7 nm, and the roughness over layer, with 81 % of oxide and 19 % of voids, was about 35 nm. Comparing these two fits, it is obvious that the model with Cu_2O and surface roughness is more appropriate for the case of the Cu 1 sample, than for the case of the Cu 2 sample.

4 CONCLUSION

Ellipsometric measurements were used to determine the optical properties of plastically deformed copper. The thickness of the spontaneously formed copper oxide and the surface roughness was calculated by applying a two-layer model. We showed that this model is better suited for the microstructure investigation of the sample Cu 1 – cross-section surface than for the Cu 2 – longitudinal section surface. The obtained results indicated that the plastic deformation of the sample did not lead to total amorphization of the specimen.

ACKNOWLEDGMENTS

This work is supported under the Programme of Scientific and Technological Cooperation between the Republic of Slovenia and the Republic of Serbia. The work in Serbia is supported by the Serbian Ministry of Science and Technological Development (Project III 45003). This paper is part of the Slovenian MNT ERA-NET Project No. 3211-07-000023: Nano Structured Metal Ceramic Composites.

5 REFERENCES

[1] N. Habbache, N. Alane, S. Djerad, L. Tifouti, Chemical Engineering Journal, 152 (**2009**) 2–3, 503–508

[2] G. Karim–Nezhad, R. Jafarloo, P. Seyed Dorraji, ElectrohimicaActa, 54 (**2009**) 24, 5721–5726

[3] W. F. Smith, J. Hashemi, Foundations of Materials Science and Engineering, 3rd ed., McGraw – Hill Edducation New York, 2003, 223

[4] W. Chambers, R. Chambers, , 5th ed., W. & R. Chambers. 1884, 312

[5] R. Z. Valiev, T. G. Langdon, Progress in Materials Science, 51 (**2006**), 881–981

[6] R. M. A. Azzam, N. M. Bashara, Ellipsometry and Polarized Light, North-Holland, Amsterdam, 1977, 371

[7] M. Losurdo, Thin Solid Films, 455–456 (**2004**), 301–312

[8] H. Fujiwara, Spectroscopic Ellipsometry, Principles and Applications, John Wiley & Sons, Chichester, England, 2007

[9] E. D. Palik, Handbook of Optical Constants of Solids, Academic Press, USA 1985

UDK 621.771:621.778
Original scientific article/Izvirni znanstveni članek

ISSN 1580-2949
MTAEC9, 45(5)467(2011)

RELAXATION OF THE RESIDUAL STRESSES PRODUCED BY PLASTIC DEFORMATION

RELAKSACIJA ZAOSTALIH NAPETOSTI ZARADI PLASTIČNE DEFORMACIJE

Nebojša Tadić[1], Miloš Jelić[2], Duško Lučić[3], Mitar Mišović[1]

[1]University of Montenegro, Faculty of Metallurgy and Technology, Džordža Vašingtona, b. b., 20000 Podgorica, Montenegro
[2]Kirilo Savić Institute, Vojvode Stepe 51, 162705 Belgrade, Serbia
[3]University of Montenegro, Faculty of Civil Engineering, Džordža Vašingtona, b .b., 20000 Podgorica, Montenegro
nebojsa@ac.me

Prejem rokopisa – received: 2010-12-01; sprejem za objavo – accepted for publication: 2011-03-14

The relaxation of residual stresses in cold-rolled strips of the alloy AA5083 and drawn bars of the steels 1.1141 and 1.7015 depending on the important parameters of the thermal and mechanical relaxation process were investigated. The measurement of residual stresses and the control of their complete or partial removal were performed using the deflection method and *x-ray* diffraction. The residual stresses are very unstable and intensely affect the changes of shape and dimensions when their balance is disturbed. This instability serves to their relaxation. The performed analyses and dependences enable the efficient planning and control of the relaxation processes.

Key words: cold rolling, drawing, residual stresses, thermal relaxation, mechanical relaxation

Raziskana je bila relaksacija notranjih napetosti v hladno valjanem traku iz zlitine AA5083 in v vlečenih palicah iz jekla 1.1141, ki je odvisna od pomembnih termičnih in mehanskih značilnosti. Notranje napetosti in kontrola njihove delne ali popolne odprave so bile izmerjene z metodama defleksije in uklona rentgenskih žarkov. Notranje napetosti so zelo nestabilne in močno vplivajo na spremembo oblike in dimenzij, ko je spremenjeno njihovo ravnotežje, kar je podlaga za relaksacijo Izvršeni preizkusi in njihova analiza omogoča učinkovito načrtovanje in kontrolo procesa relaksacije.

Ključne besede: hladno valjanje, vlečenje, notranje napetosti, termična relaksacija, mehanična relaksacija

1 INTRODUCTION

The technological processes of plastic deformation are characterized by the presence of different non-homogeneities that cause non-homogeneous deformation. The consequence of non-homogeneous deformation is the inevitable occurrence of residual stresses, which are permanently retained in metal products [1–3]. The residual stresses are spatially balanced, but they are also latently unstable. In case of an uncontrolled disturbance of their balance in further treatments and exploitation, permanent changes of the shape and dimensions of metal elements are possible. The typical examples are the bending and distortion of cold-rolled strips and pressed profiles, bending, distortion and changes in diameter of drawn bars and wires, etc. [2,4–7]. Furthermore, the total stress of the elements exposed to an external load, due to the superposition of the residual stresses, can reach the limit value and cause damage or reduce the reliability of the structural elements [8]. Therefore, the residual stresses need to be relaxed, i.e., completely removed or transformed to a more appropriate form that cannot cause permanent consequences. For the performance and control of the relaxation process it is necessary to know the values of the stress, their distribution within the element and the changes in the relaxation processes.

The values of the residual stresses were obtained by a measurement that had to be adapted to the shape of the element, the stress condition and the material condition. The typical methods for the determination of residual stresses are destructive (mechanical) and non-destructive. The mechanical methods are based on the destruction of the stress balance and the measurement of the elastic effects. In rolled plates and strips the procedure consists of the removal of metal layers from one side, while in bars it consists of longitudinal cutting. Both procedures are based on the deflection method, i.e., on the determination of the residual stresses on the basis of measurements of an elastic bend.

The model of stress distribution in the cross-section can also be performed on the basis of a deflection using the equivalent moment load for balanced residual stresses [7,10–15]. Typical non-destructive methods are based on the measurements of physical constants of the material in the presence of residual stresses, such as measurement of the changes of diffraction properties of the waves in the presence of residual stresses (e.g., x-ray) [7,9].

The most important processes that cause complete or partial relaxation of the residual stresses can be thermal or mechanical. The thermal processes consist of heating at the temperatures necessary for active thermal processes for the relaxation of residual stresses (e.g., low-temperature tempering), the kinetics of which is described by the known *Zener-Wert-Avrami*'s function [10,17,18]. The mechanical processes imply a limited plastic

deformation for the relaxation of residual stresses, mostly by axial stress acting or bending (cyclic bending) [8,16].

In this paper the investigation results of the relaxation of residual stressess in cold-rolled and drawn products by thermal and mechanical processes is presented. The stress relaxation curves were determined depending on the parameters of the thermal and mechanical process, and the models of comparative analogy which can contribute to the prediction of the process of total or partial relaxation were derived.

2 EXPERIMENTAL

2.1 Materials and preparation

For the investigation of cold-rolled strips the commercial aluminum alloy AA5083 was chosen, while for the investigation of drawn bars the construction steels 1.1141 and 1.7015 were chosen. Their chemical composition and mechanical properties in the initial state are shown in **Table 1**.

The thickness of the initial strips was 1.28 mm in the soft-annealed condition. For cold drawing the initial hot-rolled bars with a diameter of 16 mm were pickled in a hot dilute solution of H_2SO_4 according to the usual technological process for surface cleaning. The bars were then machined by milling to half of the diameter, and then the two parts were connected by a rivet joint. This kind of bar is an initial sample for the drawing process.

2.2 Deformation processes

The cold rolling was performed on a laboratory duo-rolling stand, using rolls with a diameter of 125 mm and a speed of 0.17 m/s. The dimensions of the strips (width and thickness) and the reduction ratio were chosen in order to provide conditions of plane strain [2]. The cold drawing was performed on an industrial drawing machine with the reductions of diameter normally used in production for calibration drawing. The lubrication was made using oil, the drawing speed was 0.35 m/s, and the matrix angle was 0.314 rad. The dimensions of the samples and the reduction ratio (ε) are shown in **Table 2**.

2.3 Measurement of the residual stresses

The residual stresses arising from the rolling of thin strips and the bar drawing are in accordance with the stress state of the processes [2,3], and the two-dimensional residual stresses state is formed in rolled strips, while the axisymmetric residual stresses state is formed in drawn bars. All the components of the stress include the whole cross-section, they are balanced and they have maximum values on the surface and/or in the centre [3,5,7]. The longitudinal residual stresses have a dominant influence on the properties and shape of the elements, so the experimental process was adapted to their measurement.

The measurement of the longitudinal residual stresses was performed using the deflection method, based on the stress balance disruption and the measurement of the formed elastic lines (bends). The stress balance disruption in flat-rolled strips was performed by the removal of metal layers on one side by etching in a 20 % NaOH solution at room temperature, while the remaining part of the sample was protected. Due to the stress balance disruption the strip is elastically bent, symmetrically with respect to the transverse axis. The strip after rolling and after layer removal is in **Figure 1**.

In drawn bars the stress balance change was performed by the rivet joint removal at one end of the connected halves. After the removal of the joint, the halves were bent in the form presented in **Figure 2a**. In

Table 1: Chemical composition and mechanical properties of the investigated alloys in the initial state
Tabela 1: Kemična analiza in mehanske lastnosti raziskanih zlitin v začetnem stanju

Alloy	Chemical composition, *w*/%						Mechanical properties			
	Mn	Mg	Cu	Si	Fe	Zn	$R_{p0.2}$/MPa	R_m/MPa	*A*/%	*E*/MPa
AA5083	0.42	4.23	0.015	0.13	0.26	0.02	134.7	289.7	22.86	70000
	C	Si	Mn	P	S	Cr				
1.1141*	0.15	0.40	0.3-0.6	0.035	0.035	–	275	434.2	–	191400
1.7015*	0.18	0.40	0.60	0.035	0.035	0.80	328	479.6	–	203400

* En 10027-2

Table 2: Dimensions of the samples and the parameters of the processes
Tabela 2: Dimenzije vzorcev in parametri procesa

Process	Alloy	*B*/mm	H_0/mm	H_1/mm	/%	Measuring length, *l*/mm
Rolling	AA5083	20	1.28	1.088–0.512	15–60	80
Drawing		(D_0/mm)/(D_1/mm)				
	1.1141	16/15; 16/14.5; 16/14			12.11–23.44	225
	1.7015					

B – width of strip; H_0, H_1 – thickness of initial and rolled strip; D_0, D_1 – diameter of initial and drawn bar

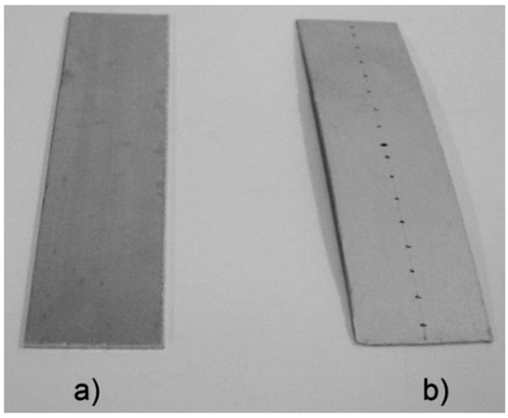

Figure 1: Rolled strip: initial state (a) and after the removal of metal layer (b)
Slika 1: Valjan trak: začetno stanje (a) in po odstranitvi plasti kovine (b)

both cases the measured elastic line follows the form of the bent sample after balance disruption. The elastic line model is the initial data for the calculation of residual stresses and it is derived by the measurement of the bending along the length of the rolled strip, i.e., along the length of bent halves of the bar. In order to derive the final relation for the calculation of residual stresses, the model of their distribution along the cross-section, i.e., the equivalent exterior load corresponding to the presented elastic line model as well as to the balance of residual stresses, must be known. The detailed investigation showed that the measured elastic lines can be described with high precision by the elastic line of the cantilever bend. It also defined the model of the equivalent exterior load. The complete procedure for these measurements and the calculation of residual stresses in cold-rolled strips and drawn bars were presented in [12,14]. The derived final relations for the elastic line, the distribution model and the value of longitudinal residual stresses are shown in **Table 3**.

If the metal layers from the strip surface are removed successively (Δ is changed from 0 up to half the thickness), the elastic lines retain exactly the same properties. This means that the residual stresses can be precisely described by the model equation presented in **Table 3**.

In the measurement of residual stresses in drawn bars after cyclic bending it is not possible to use the previously described measurement procedure because the cyclic bending demands a compact bar (made of one piece). Therefore, the measurement of residual stresses was performed by the x-ray ($\sin^2 \psi$) method using apparatus of the DRON-2 type.

2.4 Processes of relaxation of residual stresses

The thermal stress relaxation in AA5083 strips was performed by annealing at a temperature of 140 °C for 1 min to 10 min. The process was conducted in original samples after the cold rolling and removal of the layer from one side. These elastically bent strips were placed on a 3-mm-thick metal plate, afterwards attached and aligned, and thermally treated. In drawn bars the annealing regime of 370 °C/h was used. The experiment consisted of the connection of the bar halves at the separated end and annealing. In both cases after annealing the connection of the samples was removed again and the elastic line was measured. If annealing continues the procedure is repeated in the same way.

The mechanical relaxation of the residual stresses with axial tension was performed with a permanent

Table 3: Schemes and equations for elastic line and residual stresses
Tabela 3: Shema in enačbe za elastično linijo in notranje napetosti

	Cold rolled strips	Drawn bars
Scheme of stress distribution through the thickness / cross-section	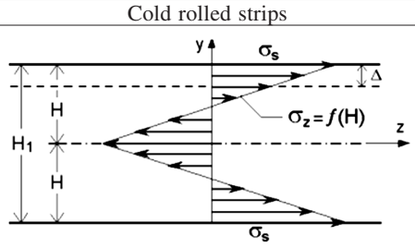	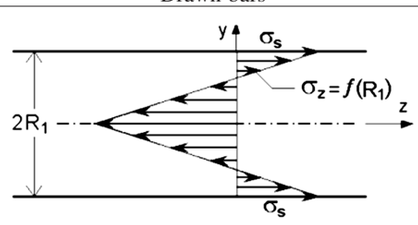
Equation for stress distribution	$\sigma_z = \sigma_s \left[2\frac{h}{H} - 1 \right]$	$\sigma_z = \sigma_s \left[3\frac{r}{R_1} - 2 \right]$
Equation for elastic line	$y = a \cdot (z/L)^2$	$y = a \cdot (z/L)^2$
Equation for surface stress	$\sigma_s = \frac{8E(H - \Delta/2)^3}{\left[6\Delta H - 6\Delta^2 + \Delta^3/H\right]} \frac{f}{L^2}$	$\sigma_s = 12\left(\frac{\pi}{8} - \frac{8}{9\pi}\right)\frac{f}{L^2}$

where:
y – strip bend, in bars the half of distance between the separated halves; a – coefficient; z – coordinate in the length direction; L – half of measuring length of the strip, measuring length of the bar; σ_z, σ_s – longitudinal stress along the cross-section and surface respectively; H – half the thickness of rolled strip ($H_1/2$); Δ – thickness of the removed layer; R_1 – radius of the drawn bar; E – modulus of elasticity; f – maximum bend

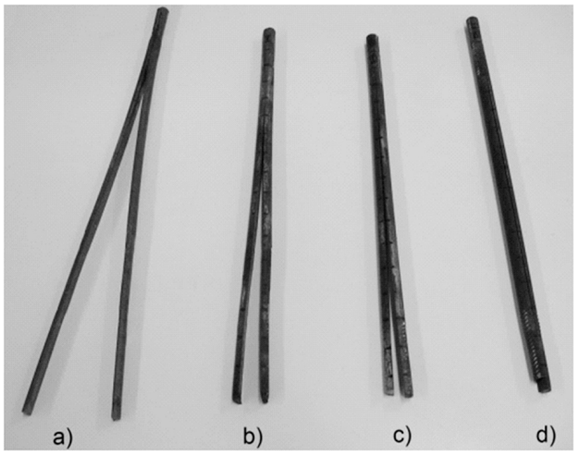

Figure 2: Appearance of drawn bar after the removal of joint rivet (a) and after mechanical relaxation by the tension with a deformation degree of 0.5 % (b), 0.7 % (c) and 1.65 % (d)

Slika 2: Videz vlečenih palic po odstranitvi vezne zakovice (a) in po mehanski relaksaciji z nategom s stopnjo deformacije 0.5 % (b), 0.7 % (c) in 1,65 % (d)

deformation degree of 0.5–1.65 %. The cold-rolled strips after tension were chemically etched in order to remove the metal layer from one side and measure the elastic line. The drawn bars were connected at the separate end and deformed by tension, afterwards the connection was removed again and the elastic line was measured (**Figures 2b, c, d**).

The mechanical relaxation of the residual stresses by the removal of surface layers was performed by the treatment of the bars drawn on a lathe. The connected halves of the bars were machined through the projected number of feeds with the constant thickness of the removed layer. After each operation the connection was removed and the elastic line was measured.

The mechanical relaxation of the residual stresses with cyclic bending was investigated on compact bars which were drawn under the same conditions as the connected ones. The experiment was performed in industrial strike with hyperbolic rollers with parallel bending and bar rotation. The measurement of the residual stresses in this case was done using the x-ray method.

3 RESULTS AND ANALYSIS

3.1 Thermal relaxation of residual stresses

The thermal relaxation of the residual stresses is based on the initiation of thermally active processes for relaxation of the accumulated elastic energy. The parameters of the processes (temperature, time) are coordinated with the material state, the stress state and the dominant mechanism of the process. The mechanism of the processes that led to the relaxation of the residual stresses can be performed on the basis of *Zener-Wert-Avrami*'s function (equation 1), where numerous values of coefficients, together with the temperature (T) and time (t), can indicate known structural changes. The reactions that take place during the relaxation of elastic energy are: vacancy creep, dislocation creep and dislocation climb, and they are based on the diffusion in metal lattice. At a low tempering temperature the limiting process is thermal dislocation climb with the activation energy equal to the energy of self-diffusion. However, the determination of activation energy of thermally active processes does not always enable a precise separation of the dominant mechanism [17,18]. Therefore, in this section the investigation was focused on the choice of temperature and time with the decrease of the projected values of residual stresses, according to the equation:

$$\sigma_{t,T} / \sigma_0 = \exp[-(A \cdot t)^m] \quad (1)$$

where:

σ_0, $\sigma_{t,T}$ – the value of the residual stresses for the initial state and the after-annealing state in t-T conditions;

m – the numerical value that indicates the dominant mechanism;

A – the parameter that depends on the temperature, the activation energy and *Boltzmann*'s constant.

In cold rolled strips of the alloy AA5083 the temperature of 140 °C was chosen, within the area of the lower limit of the temperature interval of recovery. The annealing time varied within the interval 1 min to 10 min. The investigations were performed with the samples shown in **Table 4**, and they included the variation of strip thickness, i.e., the reduction ratio, the thickness of the removed layer and the annealing time.

Table 4: Parameters of the processes and effects of the relaxation of residual stresses for the cold rolled strips

Tabela 4: Parametri procesa in vpliv relaksacije notranjih napetosti v valjanem traku

Sample	H_1/mm	ε/%	Δ/mm	f_0/mm	σ_0/MPa	t/min	$f_{t,T}$/mm	$\sigma_{t,T}$/MPa	$\sigma_{t,T}/\sigma_0$
1	0.512	60.0	0.240	4.664	53.30	1	4.580	52.34	0.982
2	0.886	30.8	0.323	2.475	62.61	2	2.405	60.84	0.972
3	0.826	35.5	0.383	2.555	47.41	3	2.175	40.36	0.851
4	1.081	15.5	0.327	1.64	63.60	3	1.325	51.39	0.808
5	0.512	60.0	0.189	4.426	63.76	5	1.142	16.45	0.258
6	1.005	21.5	0.331	1.813	58.84	5	0.810	26.29	0.447
7	0.576	55.0	0.270	5.167	66.43	5	1.224	15.74	0.238
8	0.63	50.8	0.310	4.865	67.18	8	0.973	13.44	0.200
9	0.704	45.0	0.340	3.986	61.78	10	0.696	10.79	0.175

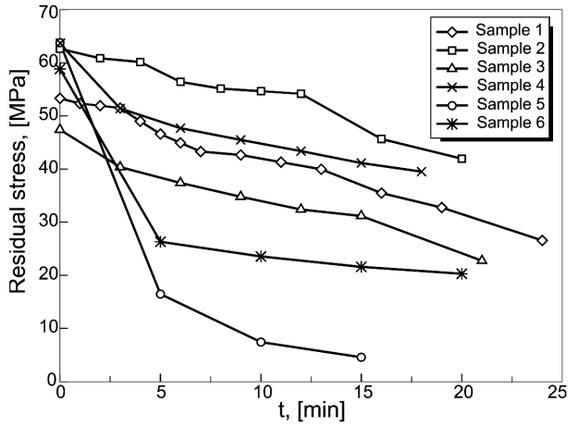

Figure 3: Change of residual stresses depending on the annealing time in multilevel relaxation
Slika 3: Sprememba notranjih napetosti pri večstopenjski relaksaciji v odvisnosti od časa žarjenja

For samples 1 to 5 the multilevel annealing was performed, and the time interval was constant with the value presented in **Table 4**.

After each annealing, the elastic line was measured. The values of the residual stresses are presented in **Figure 3**.

The results presented in **Table 4** and **Figure 3** show that the relaxation of residual stresses begins even at the shortest annealing time and it continues without interruption with its prolongation. This shows the high stress instability under the conditions of thermal treatment. However, within the area of small annealing times (1 min to 3 min), the stress relaxation is partial, with not very excessive changes, typical for the initial nucleation period. The results of multiple heating indicate that each new phase starts with the initial nucleation period, therefore the changes are small, and the shape of the curves is approximately linear. The intensive stress changes start at an annealing time of 5 min, when the stresses decrease even to 75 %, and in further annealing cycles this change has a lower intensity, similar to the shorter heating times. The different intensity of relaxation at the same annealing times is the consequence of the different thickness of samples, and therefore the consequence of through heating conditions. Obviously, the relaxation of the stress is sensitive to the important factors presented by the *Zener-Wert-Avrami*'s function, on the one hand, and the stress values (factors presented by the equation for the calculation of residual stresses: H_1, Δ and f) on the other hand.

The basic shape of the curve of the stress change with the annealing time is shown in **Figure 4** and it corresponds to the literature data in [10,17,18].

In the area of small annealing times the initial nucleation period is present, which continues with the intensive relaxation (middle part of the curve), and ends with a repeated slowed relaxation until the end of the annealing time. Therefore, the relaxation of residual stresses demands a relatively short time, which needs to be adapted to the properties of heating devices and the dimensions of the piece, i.e., to the conditions of reliable recovery temperature and reliable time of through heating of the piece.

In drawn steel bars the possibility of a precise prediction of the conditions of thermal treatment was checked, where the residual stresses can relax at half of the initial value. Therefore, a temperature of 370 °C and an annealing time of 1 hour were chosen. The procedure was conducted on two bars made of chosen steels, and drawn with a D_0/D_1 = 16/15 ratio. The results of the change of the residual stresses along the elastic line for the drawn and thermally relaxed state are presented in **Figure 5**.

In the obtained diagrams the influence of thermal treatment on the continuous relaxation of the residual stresses within the interval 36 % to 46 % can be identified. The present differences were influenced by

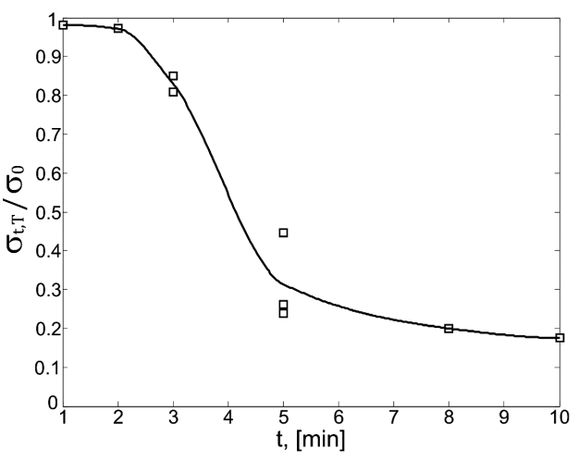

Figure 4: Change of $\sigma_{t,T}/\sigma_0$ ratio depending on the annealing time
Slika 4: Sprememba razmerja $\sigma_{t,T}/\sigma_0$ v odvisnosti od časa žarjenja

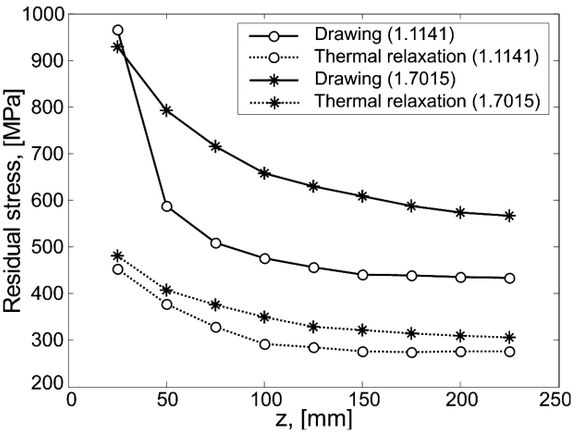

Figure 5: Distribution of residual stresses along the elastic line for the drawn and thermally relaxed state for the steel bars 1.1141 and 1.7015
Slika 5: Porazdelitev notranjih napetosti vzdolž elastične linije za vlečene in termično relaksirane palice jekel 1.1141 in 1.7015

the different modules of elasticity, stress level as well as the different activation energies for relaxation in accordance with the *Zener-Wert-Avrami*'s function. The obtained results are acceptable enough and they are in accordance with the results obtained for strips. They also show that for accurate planning of complete relaxation, the properties of the furnace for thermal treatment and the conditions of reliable recovery temperature as well as reliable time of the heating of the piece must be known.

3.2 Mechanical relaxation of residual stresses by axial tension

The relaxation of residual stresses by axial tension is possible only with the elements of simple shape, such as strips and bars. In order to examine the conditions for the relaxation of stress the model of their distribution presented in **Table 3** and stress-strain diagram for the chosen materials (**Figure 6**) are analyzed.

The analysis of the influence of external axial tension on the removal of residual stresses starts from the balance of the forces:

$$F_e + F_s + F_c = F_r \tag{2}$$

where: F_e – external tension force; F_s – the force of the residual stresses in surface layer; F_c – the force of the residual stresses in the core; and F_r – resultant force.

The transfer from the balance of the force to the stress equation is possible if the surfaces of the cross-sections with the stresses of the same sign are known. Starting from the equation:

$$A_s + A_c = A_t \quad \text{i.e.} \quad \frac{A_s}{A_t} + \frac{A_c}{A_t} = 1 \tag{3}$$

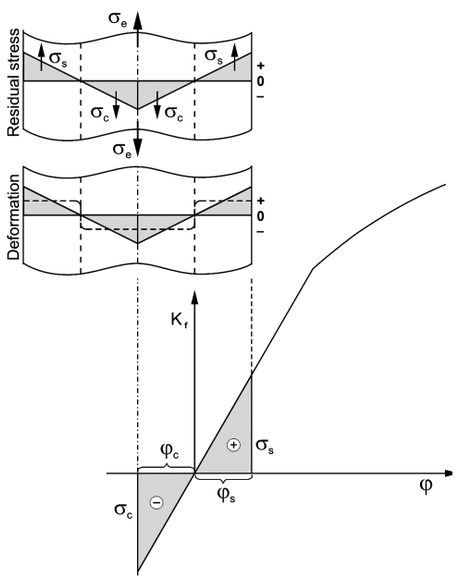

Figure 6: Scheme of the conditions for the relaxation of residual stresses by uniaxial tension

Slika 6: Shema pogojev relaksacije notranjih napetosti pri enoosnem nategu

and combining equations (2) and (3) the stress equation is obtained:

$$\sigma_e = \sigma_r - \left[\sigma_c \left(1 - \frac{A_s}{A_t} \right) + \sigma_s \frac{A_s}{A_t} \right] \tag{4}$$

where: σ_e – external stress on the total surface A_t; σ_s – resultant residual stress in the surface layer of the surface A_s; σ_c – resultant residual stress in the core of the surface A_c; and σ_r – resultant stress on the total surface A_t.

The resultant stress σ_r causes plastic deformation along the whole cross-section and it changes according to the curve stress-strain presented in Figure 6. If we replace σ_r in equation (4) with the equation of the curve of the strain hardening of the material, the final form of the equation for external stress which causes permanent plastic deformation for the relaxation of residual stresses is obtained:

$$\sigma_e = (K_0 + K\varphi^n) - \left[\sigma_c \left(1 - \frac{A_s}{A_t} \right) + \sigma_s \frac{A_s}{A_t} \right] \tag{5}$$

where: K_0 – yield stress, K – strength coefficient, n – strain hardening index, and φ – deformation degree.

When the residual stresses in the surface layer and in the core are symmetrically balanced ($-\sigma_c = \sigma_s = \sigma$ i $A_s = A_c$), as in the case of rolled strips, their effects are canceled, on the right-hand side of the equation (5) the member in the brackets is equal to zero. In that case the external stress is equal to the deformation resistance of the metal. This means that in these cases the beginning of the relaxations of residual stresses immediately after the beginning of plastic flow, as well as intense flow and ending with the limited degree of deformation, can be expected.

In the case of the asymmetrical balance of residual stresses, as in the case of rolled bars ($-\sigma_c = 2\sigma_s = \sigma$ and $4A_s = 5A_c$), the resultant residual stress is different from zero, and equation (5) is transformed into the form:

$$\sigma_e = (K_0 + K\varphi^n) + \frac{\sigma}{6} \tag{6}$$

The presence of resultant residual stress in equation (6) indicates that their intensity and direction affect the value of the external residual stress, which causes the relaxation of the residual stresses. Accordingly, in drawn bars, slightly higher permanent deformations, which cause complete relaxation of residual stresses in relation to the rolled strips, should be expected.

The experimental control of this approach in cold-rolled strips was conducted on a series of samples rolled with reduction ratios of 15 % to 50 %, and the values of residual stresses within the interval of 40 MPa to 70 MPa. These samples were then deformed by axial tension with the plastic deformation degrees of (0.5, 0.7 and 1)%. With the further application of the deflection method, the residual stresses were not identified in any of the three deformation degrees. This confirmed the

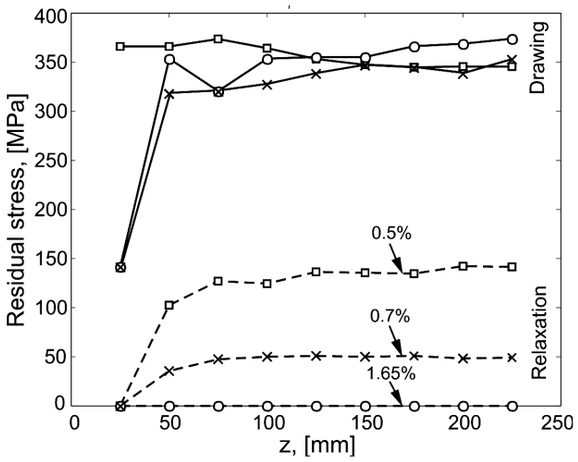

Figure 7: Distribution of the residual stresses along the elastic line for drawn and mechanically relaxed states

Slika 7: Porazdelitev notranjih napetosti vzdolž elastične linije za vlečeno in mehansko relaksirano stanje

expected complete relaxation of the residual stresses immediately at the beginning of the interval of plastic flow. The obtained results are in accordance with the results presented in [16].

In the bars the experiment was conducted with the original samples of steel 1.1141 drawn with a D_0/D_1 = 16/14 ratio and residual stresses within the interval 345 MPa to 375 MPa. The axial tension of these samples was conducted with the degrees of plastic deformation of (0.5, 0.7 and 1.65)% (**Figure 2b, c, d**). The change of the values of the residual stresses along the elastic line before and after the relaxation is presented in **Figure 7**.

The relaxation effects are very pronounced and at the first two degrees of deformation they are 60 % and 88 %, respectively. At the deformation degree of 1.65 % the connected halves of the bar were not bent after the removal of the connection, which indicated the total relaxation of the stress (**Figure 7**). The obtained values of the plastic deformation for the relaxation of residual stresses in drawn bars with respect to the drawn strips are in accordance with equation (6). In both cases, the experimental values of the deformation are within the interval of recommended deformations up to 2 to 3 %[8,16].

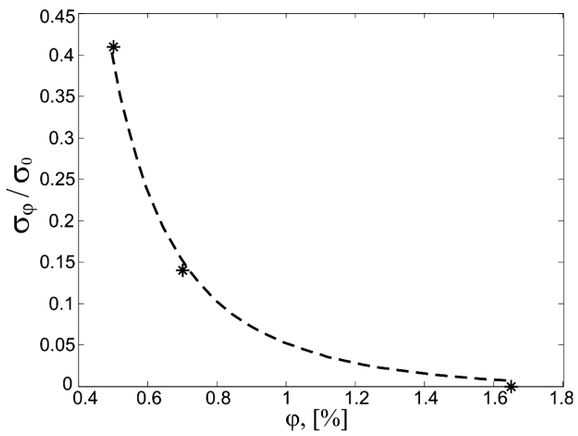

Figure 8: The stress ratio after (σ_φ) and before (σ_0) the relaxation in dependence on the deformation degree by axial tension

Slika 8: Razmerje napetosti po (σ_φ)-relaksaciji in pred (σ_0)-relaksacijo v odvisnosti od stopnje deformacije pri aksialnem nategu

The curve of the stress change with the degree of permanent deformation shown in **Figure 8** can be described by the equation:

$$\frac{\sigma_\varphi}{\sigma_0} = A \cdot \varphi^{-b} \tag{7}$$

where: A, b – coefficients. The shape of the curve is close to the shape at the thermal relaxation, and the most important differences start from general regulations of the thermal processes described by exponential functions, and the deformation processes, which are predominantly described by the degree functions.

3.3 Machining and relaxation of residual stresses

The physical disturbance of the continuum in the presence of residual stresses causes their change. Therefore, it is very important to predict the state and possible consequences within these actions. Precisely, with the even removal of the metal layers the accumulated elastic energy in the complete element is removed also, which brings also the relaxation and inevitable redistribution of residual stresses. This is particularly important for the final operations performed by machining.

The investigations of the relaxation in machining by scraping were conducted on drawn bars made of two halves. In order to use this procedure, the residual state should not be disturbed by the cyclic separation and connection of the halves of the bars between two operations on the lathe. The basic presumption was that the stress change was performed according to the initial model of the distribution and thickness of the removed layer. In this manner the change of the elastic line as a function of the sample diameter after machining was obtained.

The bars of steel 1.1141 drawn with the D_0/D_1 = 16/15 ratio were investigated. During seven operations on the lathe the bar diameter was reduced from 15 mm to 11.7 mm, with the same thickness of the removed layer of 0.2 mm in one operation. The change of the axial residual stress as a function of the reduced diameter shown in **Figure 9** indicates the clear effects of relaxation – the values of stress are reduced from 446.7 MPa to 159.6 MPa.

The relaxation process was followed by the redistribution of the residual stresses. In order to predict the behavior it was necessary to provide a physically acceptable model for the reduction of the diameter and the redistribution of stress. It is real to assume that in machining together with the layer the elastic energy which belonged to that layer is also removed in one

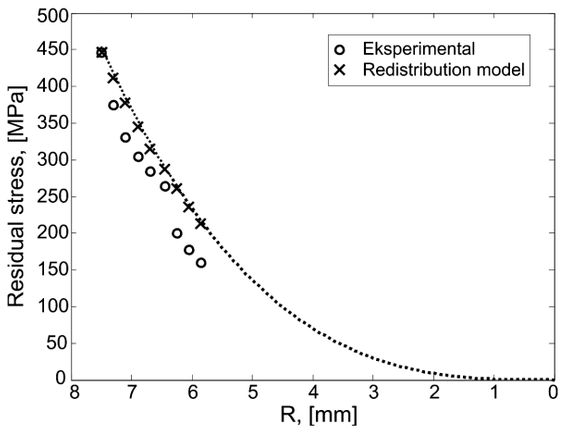

Figure 9: Residual stresses obtained experimentally and according to the model of redistribution as a function of reduced radius
Slika 9: Notranje napetosti, izmerjene eksperimentalno in po modelu porazdelitve v odvisnosti od zmanjšanega polmera

operation. In this way the stress at the new surface retains the value that corresponds to the presented position in the initial drawn state. The formation of the new surface with the given stress has as a consequence the establishment of the new balance of the stress which retains the initial distribution model along the cross-section. After each machining operation the same conditions are used. The presented model for the stress change depending on the removed layer has the form presented by the following equation [13]:

$$\frac{\sigma_{s,n}}{\sigma_s} = \prod_{i=1}^{n} \left[\frac{R_1 - (i+2)\Delta}{R_1 - (i-1)\Delta} \right] \quad (8)$$

The equation (8) contains all the relevant parameters of the redistribution model: the initial value of the stress on the surface (σ_s), the stress values on the surface after n-th operation ($\sigma_{s,n}$), the initial radius (R_1), the thickness of the removed layer (Δ) and the number of operations (n). The confirmation of the equation is evident for the condition $\sigma_{s,n} = 0$, i.e., it is completely compatible with the thickness of the removed layer, the initial radius and the number of operations.

The redistribution curve obtained with equation (8) as a function of the reduced radius is shown in parallel with the experimental values in **Figure 9**. The values of the stress obtained by the model of redistribution are extrapolated to the values of the reduced radius when the total relaxation of the residual stresses is expected. The obtained curve form is also similar to the form in the described thermal and mechanical relaxation of the residual stresses.

In **Figure 9** the good correlation of the results obtained experimentally and using equation (8) is evident, as well as physically realistic behavior in the case of extrapolation, i.e., the stress values that corresponds to the less-reduced radius: $\sigma_{s,n} = 0$ for $R = 0$.

3.4 Mechanical relaxation of residual stresses by cyclic bending

The experiment was conducted on three bars of steel 1.1141 drawn with different ratios D_0/D_1. The measurement results of the residual stresses after drawing and cyclic bending on the strike with hyperbolic rollers are presented in **Table 5**.

Table 5: Parameters of the drawing process and measurement results of the residual stresses using the diffraction method
Tabela 5: Parametri procesa vlečenja in notranje napetosti, izmerjene po metodi difrakcije

D_0/D_1	State	σ/MPa
16/15	Drawing	520
	Straightening	> −150
16/14.5	Drawing	360
	Straightening	−280
16/14	Drawing	640
	Straightening	−420

Straightening enables little plastic deformation by cyclic bending with a very small percentage, which is enough to relax the residual stresses. Since the straightening process brings too limited compression of the bar surface, the residual stresses on the surface are transformed from tensile stresses to compression stresses, which was also confirmed in ref. [19]. This process is adequate for the increase of the properties within the elements which demand higher mechanical properties on the surface.

4 CONCLUSIONS

The investigations of the relaxation of the residual stresses by thermal and mechanical processes in cold-rolled strips and drawn bars showed:

– the high instability of the residual stresses in thermal and mechanical processes with similar effects and shape of the change curve;
– the projected level of relaxation of residual stresses can be achieved with sufficient precision in thermal process by optimum temperature choice and annealing time in accordance with the function which describes the kinetics of thermal processes;
– in mechanical process by axial tension, the complete relaxation of the stress appears at low values of the plastic deformation, and the differences that occur in cold-rolled strips and drawn bars appear as a consequence of the model of the balance of residual stresses;
– the machine scraping of drawn bars was followed by the relaxation and redistribution of residual stresses. The suggested model of redistribution gives a real picture of made changes;
– the mechanical process by cyclic bending of the drawn bars was followed by the reduction of tensile

residual stresses and their transformation into the compression stresses.

5 REFERENCES

[1] E. G. Thomsen, C. T. Yang, S. Kobayashi, Mechnaics of Plastic Deformation in Metal Processing, Macmillan Co., New York, 1968

[2] Walter A. Backofe, Deformation processing, Addison-Wesley Publishing Company, 1975

[3] G. E. Dieter, H. A. Kuhn, S. L.Semiatin, Handbook Workability Process Design, ASM International, 2003

[4] Davies W. E., Sivilotti O. G., Tulett M. W., Production and Control of strip flatness in cold rolling, Metals Technology, (**1975**), Oct., 494–498

[5] W. L. Roberts, Cold Rollinf of Steel, Marcel Dekker, INC, New York and Basel, 1978

[6] V. B. Ginzburg, R. Ballas, Cold Rolling Fundamentals, Marcel Dekker, INC, New York and Basel, 2000

[7] A. Peiter, Nandbuch Spannungs Messpraxis – experimentelle ermittlung mechanischer spannungen, Viewing, Braunschweig/Wisbaden, 1992

[8] O. Vöhringer, H. Wohlfahrt, Eigenspannungen und Lastspanungen, C. Hanser Verlag, München, 1982

[9] V. Hauk, Eigenspnnunge, Entstehung-Messung-Bewertung, Vortragstexte eines Symposium, Deutsche Gesellschaft fur Metallkunde e. v., Band 1 (**1983**), 2–36

[10] G. Totten, M. Howes, T. Inoue, Handbook of Residual Stress and Deformation of Steel, ASM International, 2002

[11] N. Tadić, Master thesis, Faculty of Metallurgy and Technology, University of Montenegro, Podgorica, 2000

[12] N. Tadić, M. Mišović, Residual Stresses in Cold Rolled Narrow Strips: Exsperimental Measurement – FEM Simulation, Metalurgija, 13 (**2007**) 4, 251–258

[13] M. Jelić, Ph.D Thesis, University of Montenegro, Podgorica, 1998

[14] M. Jelić, M. Mišović, M. Jaćimović, The Flow Characteristics and Residual Stresses in Drawn Steel Bars, ICRS-5, Linköping, (**1997**), 269–275

[15] M. Jelić, M. Mišović, N. Tadić, Model of Generation and Values of Axial Residual Stresses in Drawn Bars, FME Transactions, 32 (**2004**), 2

[16] R. S. Barker, J. G. Sutton, Aluminium, Vol. III, ASM, Metals Park Ohio, 1967

[17] U. Wolfsteig, E. Macherauch, In Eigenspannungen, DGM, Oberursel, 1980, 345

[18] W. C. Leslie, The Physical Metallurgy of Steels, McGraw-Hill Book Comp., New York, 1981

[19] E. Doege, F. Weber, The Effect of Production Conditions on Residual Stresses in Bars, Stahl und Eisen, 111 (**1991**), 85–88

UDK 620.193:621.89:669.14.018
Original scientific article/Izvirni znanstveni članek

ISSN 1580-2949
MTAEC9, 45(5)477(2011)

ACCELERATED CORROSION BEHAVIORS OF Zn, Al AND Zn/15Al COATINGS ON A STEEL SURFACE

POSPEŠENO KOROZIJSKO OBNAŠANJE Zn, Al IN Zn/15Al PREKRITIJ NA POVRŠINI JEKLA

Ahmet Gulec[1], Ozgur Cevher[2], Ahmet Turk[2], Fatih Ustel[2], Fevzi Yilmaz[3]

[1]Istanbul Water and Sewerage Administration-İSKİ, Subscription Department For European 1st Side, Nurtepe 34406, Istanbul/Turkey
[2]Sakarya University, Faculty of Engineering, Metallurgical and Materials Engineering, Esentepe Campus, 54187 Sakarya/Turkey
[3]Fatih Sultan Mehmet University, The Faculty of Engineering And Architecture, Fatih, 34093, Istanbul/Turkey
agulec@iski.gov.tr

Prejem rokopisa – received: 2010-11-29; sprejem za objavo – accepted for publication: 2011-03-30

Zn, Al and Zn/15Al coatings can be produced in optimum conditions by the twin wire arc (TWEA) spraying technique. The coatings are used for corrosion protection in a variety of industrial applications. In this study, the accelerated corrosion behavior of Zn, Al and Zn/15Al coatings on a steel surface during the salt-spray testing period was investigated. The surfaces of steel coupons were coated with Zn, Al and Zn/15Al using the TWEA spray-deposition system. The corrosion test was performed in a chloride atmosphere in a salt-spray test for over 2000 h. The corrosion of samples is assessed as the ratio of the corroded area of the specimens. The salt-spray test results showed that Al and Zn/15Al coatings have a better corrosion resistance than Zn coatings.

Keywords: salt spray, corrosion, coating, Zn, Al, Zn/15Al

Zn, Al in Zn/15Al prekritja lahko pripravimo v optimalnih pogojih s tehniko dvožičnega ločnega brizganja (RWEA). Prekritja se uporablja za zaščito proti koroziji pri različnih industrijskih uporabah. V tem delu smo raziskali pospešeno korozijsko obnašanje Zn, Al in Z/Al prekritij na površini jekla z metodo slanega naprševvanje. Površina vzorcev jekla je bila prekrita z Zn, Al ali Zn/Al prekritjem s TWEA sistemom depozicije. Preizkus v kloridni atmosferi in naprševanjem je trajal 2000 ur. Korozija je bila ocenjena kot delež korodirane površine vtorcev. Preizkusi so pokazali da imata večjo korozijsko obstojnost pri slanem naprševanju prekritji A in Zn/15Al kot prekritje Zn.

Ključne besede: naprševanje s slanico, korozija, prekritja Zn, Al, Zn/15Al

1 INTRODUCTION

Corrosion is one of the main causes of the degradation of metallic materials. Corrosion is the most widespread form of metal deterioration, because most metallic structures and equipment installations are exposed to natural corrosive environments. The generation of zinc (Zn) and zinc alloy coatings on steel is one of the commercially most important processing techniques used to protect steel components exposed to corrosive environments [1].

In recent decades, aluminum (Al) and zinc-aluminum (Zn-Al) alloy coatings have been used instead of zinc in certain atmospheric applications. Although these coatings have some advantages over zinc, they are not able to cathodically protect steel substrates in all types of natural atmospheres [2]. Aluminum, which can passivate both in air and when immersed in a solution, has good corrosion-resistance properties, whilst Zn can provide mainly galvanic protection for most metal substrates. A Zn–Al alloy possesses the advantages of both Al and Zn, making it a good coating material for corrosion protection [3].

The corrosion protection of Zn-coated steels arises from the barrier action of the zinc layer, the secondary barrier action of the zinc corrosion products and the cathodic protection of zinc on an unintentionally exposed part of the steel, with the coating acting as a sacrificial anode. If the exposure conditions are such that there is either depletion of air, but a high humidity or a medium containing, strongly aggressive species like chloride or sulphate ions, the Zn dissolves, forming soluble, less dense and scarcely protective corrosion products, which sometimes lead to localized corrosion. Aluminum coatings have overcome these two problems. Nevertheless, as they cannot provide cathodic protection to exposed steel in most environments, early rusting occurs at the coating defects and cut edges. In addition, these coatings are also subjected to crevice corrosion in marine environments. For years, many attempts to improve the corrosion resistance of zinc and aluminum coatings through alloying such as Zn/Al 85/15 were carried out [4,5].

Thermal spray coatings have been used for over 50 years in industries for a variety of applications. The TWEA spraying process is a very suitable method for metallic coatings. Aluminum and zinc aluminum coatings are extensively used for the corrosion protection of iron and steel in a wide range of environments and have been shown to provide long-term protection (over 20 years) for both marine and industrial service [6].

Several methods have been developed for the deposition of zinc coatings, one of which is zinc thermal spray metallizing using the TWEAS process. In this case, me-

tallic zinc in the form of wire is fed to a torch, with which it is heated to its melting point. The resulting molten or nearly molten droplets are accelerated in a gas stream and projected against the surface to be coated (i.e., the substrate). On impact, the droplets flow into thin lamellar particles adhering to the surface, overlapping and interlocking as they solidify. The total coating thickness is usually generated in multiple passes of the coating device. Heat for melting is provided either by a combustion of an oxygen-fuel gas flame or an electric arc. In any case this method produces thick coatings composed of large sized grains. The intrinsic characteristics of these coatings are a high porosity and a very rough surface. Furthermore, due to the fast cooling procedure of the liquid droplets, diffusion at the Fe–Zn interface is inhibited and as a result, the coating adherence mechanism is mostly mechanical, depending on the kinetic energy of the sprayed particles, while no Fe–Zn alloy layers are present, as in the case of hot-dip galvanizing. A common phenomenon in the process industries is the oxidation of the exterior surface of steel pipes used in superheated steam or industries for anticorrosion applications. Thermally sprayed zinc, aluminum and zinc/aluminum alloy coatings that are produced by the TWEA spraying process find widespread applications in distribution and transmission pipes and electrical lines, bridges etc.

The aim of the present study is to compare the corrosion performance of Zn, Al and Zn/15Al coatings produced by the TWEA spraying process on steel surfaces in salt-spray environments.

2 EXPERIMENTAL

In this study, Zn-, Al- and Zn/15Al-coated mild-steel coupons were used. A Sulzer Metco Smartarc TWEA system and wires (pure zinc, pure Al and Zn/15Al, commercially) were used for the production of the coatings. The surface-coating types and the coating parameters of the coupons are given in **Table 1**. They are coated with the arc-spray deposition method by using different currents of (100, 200, and 300) A. These Zn-, Al- and Zn/15Al-coated steel coupons, which have nominal dimensions of (150 × 100 × 2) mm, were used for the structural examination and the corrosion testing.

After the surface coatings of the samples are completed, they are scribed with an Erichsen 463 scratch stylus. This hand-operated instrument complete with a carbide cutting tip provides a convenient means of scoring a 1-mm-wide rectangular track on the surface of the coating for the corrosion tests. A neutral (5 % NaCI) salt-spray corrosion that is frequently used in international applications, such as the automotive industry and military investigations, is applied to the prepared samples according to the ASTM B 117, D 1654 and D 1193 standards [7–14]. The surface is scribed up to the steel substrate according to ASTM D 1654 [16]. The samples were placed in an Angelantoni DCTC 600 P salt-spray test cabinet with an angle of 15–30° according to ASTM B 117 [15]. The structural analysis was carried out using a high-resolution camera in order to evaluate the surface characterization. A Deflesko positector 6000 FNS is used for measuring the thicknesses of the coatings. A cross-sectional examination using optical and scanning electron microscopy (SEM) was carried out after the surface polishing.

3 RESULTS AND DISCUSSION

3.1 Microstructural Investigation

The general structures of the Zn, Zn/15Al and Al coating are presented **Figure 1**. The Zn and Zn/15Al coating structures contain oxides, which are gray areas and less porosity in microstructure, but the coatings are relatively dense. There is little porosity but no oxide formation in the Al coating. The wavy surface of the Al coatings is due to the high melting temperature as well as the formation of a thin surface oxide film around the droplets. The EDS analyses results are shown in **Figure 2**. Although Zn and Zn/15Al have high oxygen peaks, the Al coating has a weak indication of an oxygen peak in the EDS analyses results. All the structures were revealed under the same coating conditions as shown in **Figure 1**.

The spray current value deals with the wire feed rate directly in the TWEAS process. When the arc current is

Table 1: Surface coating types and coating parameters of the steel coupons
Tabela 1: Vrste prekritij površine in parametri naprševanja vzprcev jekla

Number of sample	Zn Coating	Al Coating	Zn/15Al Coating	Wire Voltage /V	Current /A	Compressive Air bar	Spray Distance /mm
1	Applied	None	None	24	100	3	150
2	Applied	None	None	24	200	3	150
3	Applied	None	None	24	300	3	150
4	None	Applied	None	23	100	3	150
5	None	Applied	None	23	200	3	150
6	None	Applied	None	23	300	3	150
7	None	None	Applied	26	100	3	150
8	None	None	Applied	26	200	3	150
9	None	None	Applied	26	300	3	150

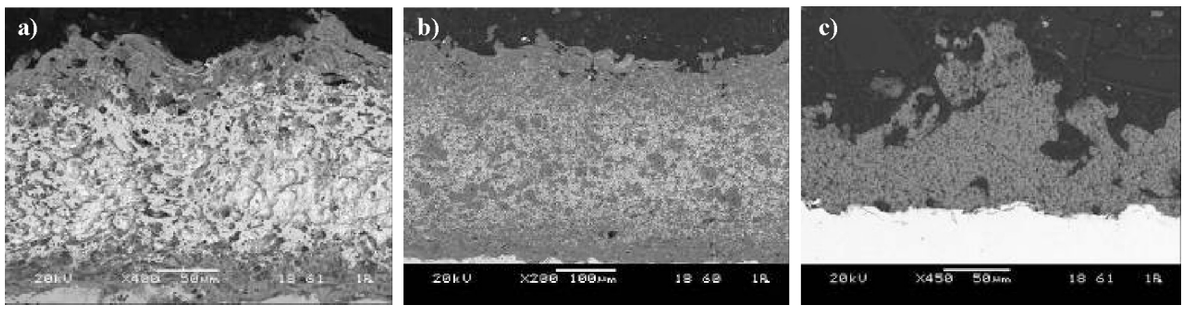

Figure 1: SEM microstructure of cross-section of coatings: a) Zn coating, b) Zn/15Al coating and c) Al coating
Slika 1: SEM mikrostrukture preseka prekritij: a) Zn plast, b) ZN/15 Al plast in c) Al plast

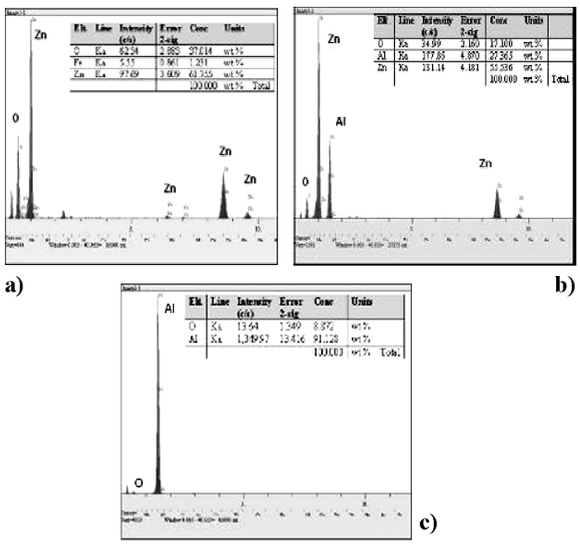

Figure 2: EDS analysis results of a) Zn coating, b) Zn/15Al coating and c) Al coating
Slika 2: EDS analiza a) Zn plasti, b) Zn/15Al plasti in c) Al plasti

increased, the wire feeding accelerates during the spray process. In this study, Zn, Al and Zn/15Al coatings were produced with different spray-current values of (100, 200, 300) A, a constant air pressure of 3 bar and 7 passes. The coating thickness changed with a different spray current. **Figure 3** shows that the coating thickness increases with a high spray current because of the low melting point of the Zn due to a high temperature with a high spray current because the high spray current composes the high wire feeding during the coating application. On the other hand, a high spray current of 300 A leads to overmelting of Zn, which spreads on the substrate surface. For Zn/15Al and Al the thickness of the coatings increased at a high spray current of 300 A due to high wire feeding onto the substrate, as can be seen in **Figure 4** and **Figure 5**.

When the coating process was carried out with a high arc current, the wire feed speed was increased. As a result the thickness of the coating increased. Furthermore, the Zn coating thickness was higher than for Zn/15Al because the melting point of the Zn is lower than for Zn/15Al. For comparison, it is clear that the thicknesses of Zn and Zn/15Al at a given current value are 200 µm and 170 µm, respectively. Nevertheless, all the coating thicknesses increased with high spray-current values. The variation of the coating thicknesses with the different spray currents and a constant air pressure (3 bar) is given in **Figure 6**.

3.2 Salt-spray corrosion test

The corrosion performance of Zn, Al, and Zn/15Al coatings produced with different currents of (100 A, 200 A, and 300) A are given in **Figure 7, Figure 8, and Figure 9**. It is clear that the corrosion performances of the Zn coatings produced with 100 A and 200 A were lower

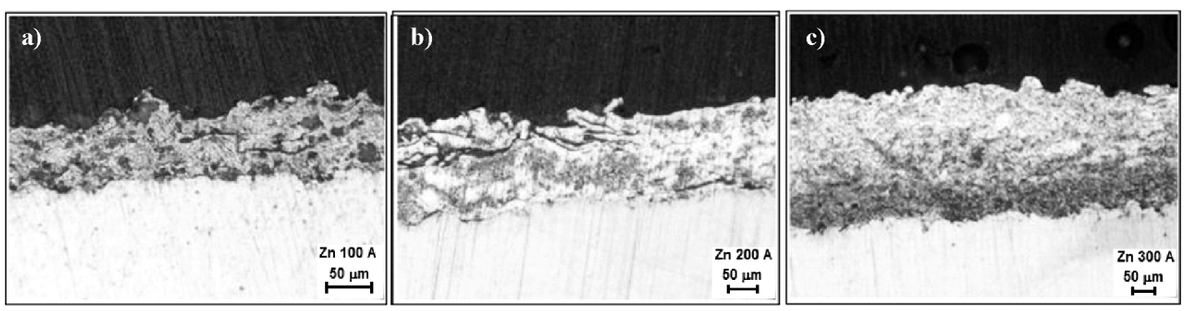

Figure 3: Zn coating with a different arc current; a) 100 A, b) 200 A, c) 300 A
Slika 3: Zn plast napršena z različnim tokom loka; a) 100 A, b) 200 A, c) 300 A

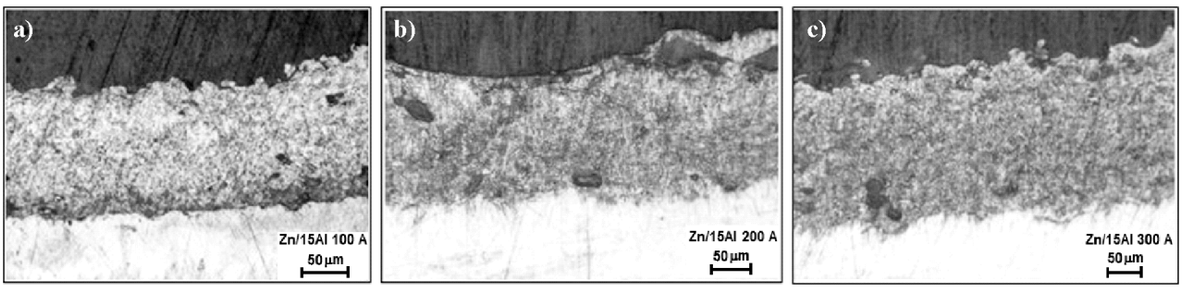

Figure 4: Zn/15Al coatings with different arc current; a) 100 A, b) 200 A, c) 300 A
Slika 4: Zn/15Al plast napršena z različnim tokom loka; a)100 A, b) 200 A, c) 300 A

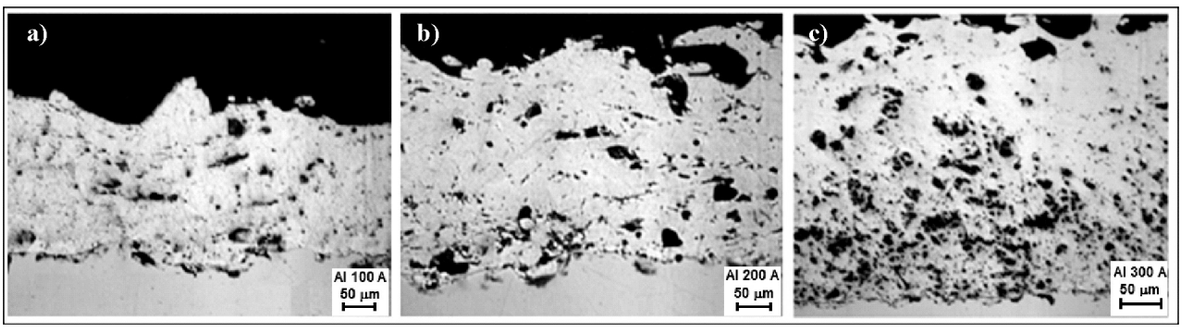

Figure 5: Al coatings with different arc current; a) 100 A, b) 200 A, c) 300 A
Slika 5: Al plast napršena z različnim tokom loka; a)100 A, b) 200 A, c) 300 A

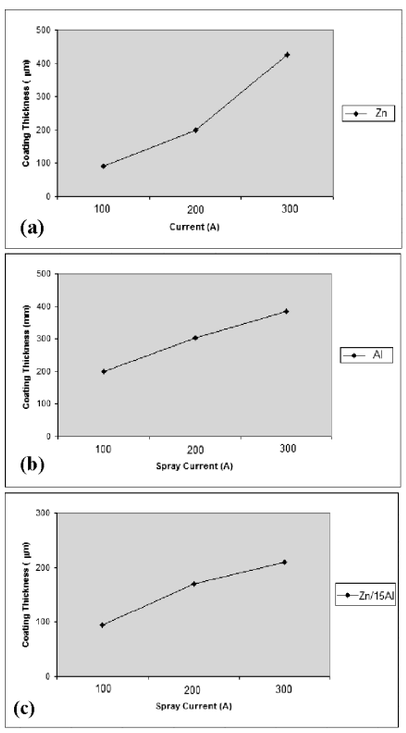

Figure 6: Influence of the arc current on the coating thickness at a constant pressure of 3 bar; a) Zn, b) Zn/Al 85/15, and c) Al (air pressure 3 bar)
Slika 6: Vpliv toka lokana debelino plasti pri konstantnem pritisku 3 bare; a) Zn, b) Zn/Al 85/15 in c) Al

than the Zn/15Al and Al coatings. Red rust initiation showed in these samples' coating surface, first after 500 hours. But no blistering, delamination and faults were found in the scribed area (R_s) for all of the samples. Zinc corrosion products (white rust) were found on the Zn and Zn/15Al coating surface and the white rust covered the scribed areas of this samples. There was no white rust on the Al-coated sample surfaces. No red rust was determined after 1000 h in the scribed area of the samples Zn and Al coatings produced with 300 A and all the

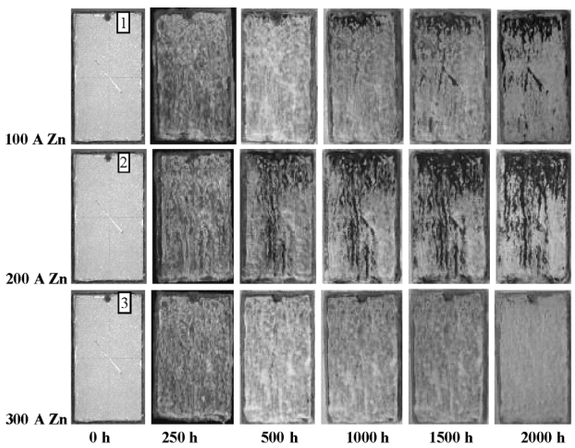

Figure 7: Images of the corrosion behaviors of Zn-coated samples during the salt-spray corrosion test
Slika 7: Posnetki korodiranih vzorcev z Zn plastjo med preizkusom slanega naprševanja

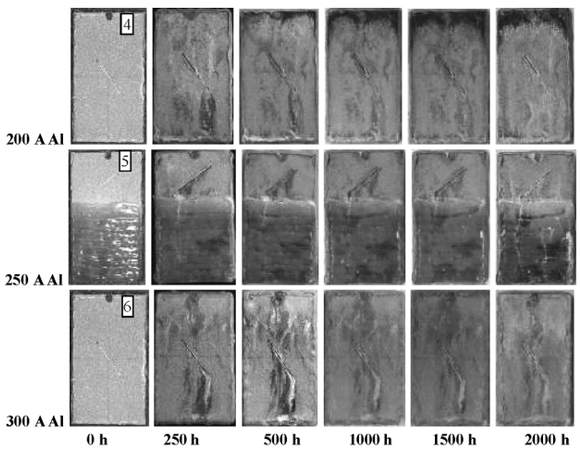

Figure 8: Images of the corrosion behaviors of Al-coated samples during the salt-spray corrosion test

Slika 8: Posnetki korodiranih vzorcev z Al Zn plastjo med preizkusom slanega naprševanja

Zn/15Al coatings. In the Al coatings, red rust occurred in the corners of the sample surfaces because of the lower coating thickness in the corners than in the middle of the coating surface. According to manual spraying application, a non-homogeneous coating thicknesses consists of Al coatings. In addition, the Al coating that was produced with 300 A has no red rust on the coating surface. Hamdy [18], has pointed out that no sign of corrosion was observed even after 2000 h of exposure in the salt-spray chamber on Al substrates. The Zn and Al coating produced with a high current value (300 A) showed the best corrosion resistance performance among the Zn- and Al-coated group, respectively. When the blistering and fallen coatings were evaluated for samples 2, the unscratched area (R_{us}) was found to be 0 and this result showed that the corrosion resistance of this sample is low according to ASTM D 1654 [16].

Zn and Al coatings produced at a high current showed a high corrosion-protection performance due to the increasing coating thickness during the salt-spray corrosion test period. It is revealed that the anti-corrosion performances of the Zn and Al coatings increased directly when the coating thickness of the Zn and Al coatings increased. In unscribed area R_{us} is determined as 0 as a result of taking the faulty regions (>75 %) on the surface of the sample into account in the evaluation. As a conclusion, Zn/15Al coatings showed a higher corrosion performance than other samples. In particular, all the Zn/15Al of the surfaces and the scribed area were covered with white rust.

As shown in **Figure 9**, the blistering is visible, after the corrosive solution reaches substrate 9 by going through the coating layer. Initially, as result of the corrosion on the surface of sample 9, the formation of the outer circle of the blister was observed. It was shown that the corrosion products blistered the coating layer by a volume expansion and peeled at the end of the corrosion test. It was observed that the Al (samples 4–6) and Zn/15Al (samples 7–9) coatings have a higher corrosion resistance than the Zn coating (samples 1–3) after 2000 h of salt-spray testing. The samples with numbers 8 gave the best result when it was evaluated for the scratched and the unscratched area. The salt-spray corrosion test results can explain that the Zn/15Al coating produced at 200 A showed a higher corrosion performance than the other coatings.

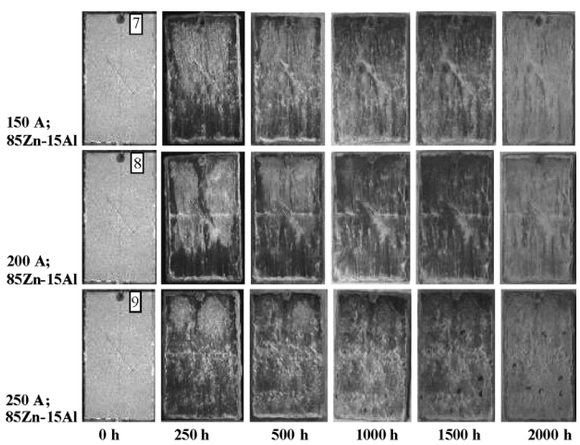

Figure 9: Images of the corrosion behaviors of Zn/15Al-coated samples during the salt-spray corrosion test

Slika 9: Posnetki korodiranih vzorcev z Zn/15Al plastjo med preizkusom slanega naprševanja

4 CONCLUSIONS

After the accelerated corrosion test (the salt-spray test), it is obvious that the corrosion resistances on the Al- and Zn/15Al-coated surfaces are better than the Zn-coated surfaces. As a result, it was found that the Al-coated surfaces were not affected very much by an aggressive chloride environment. For all of the Zn- and Zn/15Al-coated surfaces, the pitting and corrosion products (white rust) occurred during the salt-spray test. By comparing the different pre-treatments of the Al, Zn and Zn/15Al, it was found that the Zn/15Al coatings have a higher corrosion resistance than the Zn and Al coatings. According to the occurrence of the Zn corrosion products (white rust), the Zn- and Zn/15Al-coated steel substrates were protected against corrosion because of the sacrificial anode protection mechanisms of the Zn. Al creates a stable oxide on the coating surface and it protects from oxygen diffusion through the steel substrate as a known barrier effect. The Zn/15Al coating has two protection mechanisms together. The salt-spray measurements indicate that the Al and Zn/15Al systems are more suitable than the Zn system as far as protection against a chloride environment is concerned.

Acknowledgements

The authors would like to thank the Istanbul Water and Sewerage Administration (İSKİ) and TUBITAK (The Scientific and Technological Research Council of Turkey) for research project number 105M061.

5 REFERENCES

[1] A. R. Marder, The metallurgy of zinc-coated steel, Progress in Materials Science, 45 (**2000**), 191–271

[2] H. C. Shih, J. W. Hsu, C. N. Sun, S. C. Chung, The lifetime assessment of hot-dip 5 % Al–Zn coatings in chloride environments, Surface and Coatings Technology, 150 (**2002**), 70–75

[3] B. Wang, Z. W. Lai, C. B. Jiang, Study of the corrosion protection properties of Al–Zn films synthesized by IBAD, Journal of Materials Processing Technology, 74 (**1998**), 122–125

[4] Panossian, Z., Mariaca, L., Morcillo, M., Flores, S., Rocha, J., Pena, J. J., Herrera, F., Corvo, F., Sanchezi, M., Rincon, O. T., Pridybailo, G., Simancas, J., Steel cathodic protection afforded by zinc, aluminum and zinc/aluminum alloy coatings in the atmosphere, Surface & Coatings Technology, 190 (**2005**), 244– 248

[5] M. A. Baker, W. Gissler, S. Klose, M. Trampert, F. Weber Morphologies and corrosion properties of PVD Zn–Al coatings, Surface and Coatings Technology, 125 (**2000**), 207–211

[6] D. J. Varacalle, D. P. Guillen, D. M. Deason, W Rhodaberger, E. Sampson, Effect of Grit-Blasting on Substrate Roughness and Coating Adhesion, Journal of Thermal Spray Technology, 15 (**2006**), 3, 348–355

[7] G. Vourlias, N. Pistofidis, D. Chaliambalias, K. Chrissafis, El. Pavlidou, G. Stergioudis, Resistance of Zinc Thermal Sprayed Coatings on Different Corrosive Environments, Journal of Thermal Analysis and Calorimetry, 87 (**2007**), 2, 401–409

[8] Varacalle D. J., Zeek D. P., Zanchunck V., Sampson E., Couch K. W., Benson D., Cox G. S., Experimental studies of twin-wire electric arc sprayed zinc/aluminum alloy coatings, Journal of Thermal Spray Technology, 7 (**1988**), 513–520

[9] G. Vourlias, N. Pistofidis, E. Pavlidou, K. Chrissafis, Zinc Coatings for Oxidation Protection of Ferrous Substrates Part II. Microscopic and oxidation mechanism examination, Journal of Thermal Analysis and Calorimetry, 90 (**2007**) 3, 777–782

[10] A. Gulec, A. Turk, F. Ustel, F. Yilmaz, The effect of process parameters on the microstructure and mechanical properties of arc sprayed Zn, Zn/Al 85/15 coatings, International Thermal Spray Conference, (June 2–4, **2008**), 1159–1164

[11] O. Cevher, A. Gulec, A. Turk, F. Ustel, F. Yilmaz, Study on corrosion resistance behaviors of Zn, Al, Zn/Al 85/15 coatings that produced by twin wire arc spray technique on steel, International Thermal Spray Conference, (June 2–4, **2008**), 1156–1158

[12] A. Gulec, A. Turk, O. Cevher, F. Ustel, F. Yilmaz, Comparation of performance of TWEA sprayed zinc and zinc/aluminum 85/15 coatings for ductile iron pipe protection against corrosion, International Thermal Spray Conference, (June 2–4, **2008**), 288–293

[13] A. Akinci, Evaluation methods of the coatings with accelerated corrosion experiments, Surface Treatment, 56 (**2007**), 15–24

[14] A. Akinci, Natural salt spray (fog) corrosion of protective aimed coatings, Surface Treatment, 55 (**2007**), 64–74

[15] ASTM B117 - 09 Standard practice for operating salt spray (Fog) apparatus

[16] ASTM D1654 - 08 Standard test method for evaluation of painted or coated specimens subjected to corrosive environments

[17] ASTM D1193 - 06 Standard specification for reagent water

[18] S. Hamdy, Enhancing corrosion resistance of aluminum composites in 3.5 % NaCl using pigmented epoxy fluoropolymer, Progress in Organic Coatings, 55 (**2006**), 218–224

UDK 669.14.018
Professional article/Strokovni članek

ISSN 1580-2949
MTAEC9, 45(5)483(2011)

ALLOYS WITH MODIFIED CHARACTERISTICS

ZLITINE Z MODIFICIRANIMI LASTNOSTMI

Mirsada Oruč[1], Milenko Rimac[1], Omer Beganović[1], Sulejman Muhamedagić[2]

[1]University of Zenica, Instutute of metallurgy "Kemal Kapetanović" Travnička cesta 7, Zenica, BiH
[2]University of Zenica, Faculty of Metallurgy and Materials Science, Travnička cesta 1, Zenica, BiH
miz@miz.ba

Prejem rokopisa – received: 2011-02-01; sprejem za objavo – accepted for publication: 2011-05-20

Industry has a permanent need for new materials to improve the performance of constructions. However, the development of new materials is a complicated and costly process, and in many cases the existing materials with modified characteristics are used. By the use of certain technological processes of producing liquid metals, deformation processes, thermal and surface treatments, the mechanical and exploitation characteristics of existing materials can be improved. In this paper is an overview of several research activities at the Institute in Zenica with the goal to improve the characteristics of some materials in use in the air and car industries. With semi-industrial facilities and in laboratories of the institute some researches where conducted on stainless steels and maraging steels as well as on superalloys based on nickel and iron.

Key words: new materials, new technologies, stainless steels, maraging steels, super alloys

Industrija potrebuje nove materiale, če želi izboljšati lastnosti konstrukcij. Razvoj novih materialov je zapleten in drag proces in so zato mnogokrat uporabljeni materiali s spremenjenimi lastnostmi. Z spremembami v tehnologiji obdelave taline, procesov predelave, toplotne in površinske obdelave je mogoče izboljšati mehanske in uporabne lastnosti materialov. V tem delu je kratek pregled raziskav na Inštitutu v Zenici, ki so bile izvršene s ciljem izboljšanja materialov, ki so v uporabi v industriji vozil in letal. Na polindustrijskih in laboratorijskih napravah na inštitutu so bile opravljene raziskave na nerjavnih in maraging jeklih in na superzlitinah niklja in železa.

Ključne beside: novi materiali, nove tehnologije, nerjavno jeklo, maraging jeklo, superzlitine

1 INTRODUCTION

Modern industry has a permanent need for new materials to improve the performance of their constructions. The introduction and application of new materials for the improvement of existing structures with a higher level of exploitation properties is related to new material development and the mastering of these materials. In some cases designers, in cooperation with research and development institutions, use simple and economically reasonable solutions. One possibility is a modification (improvement) of some of the properties of existing materials with the aim to increase the exploitation and mechanical properties at room and elevated temperatures or improve the corrosion, heat and wear resistance. The term modification used here includes specific changes in chemical composition and microstructure, achieved with changes of technology during the production of liquid metal, hot, warm and cold processing and heat treatment.

This paper reviews several studies conducted on experimental equipment and in laboratories of the Institute of Metallurgy "Kemal Kapetanović", University of Zenica, aimed at improving the properties of some special steels and superalloys used in the automotive industry: austenitic stainless steel, maraging steel and some nickel- and iron-based superalloys. Application of the remelting process in the case of maraging steel, the optimization of the chemical composition of austenitic stainless steel, and the application of modified rolling technology of the superalloy Nimonic 80A, lead to an improvement of some properties. The application of metallic coatings on iron-based superalloy A286 also leads to a significant improvement of the exploitation properties.

2 APPLICATION OF REMELTING TECHNOLOGY IN MARAGING STEEL MAKING

High-strength maraging steels are strengthened to a high level with the coherent precipitation of the intermetallic phase Ni_3(Mo,Ti,Al) in a carbon-free, nickel-martensite matrix by aging at temperatures of 480 °C. They are intended to provide high values of tensile strength and typically have a high content of nickel, cobalt and molybdenum, but a very low carbon content. In fact, carbon and nitrogen are impurities limited to very low levels.

The high strength of maraging steel is achieved by the strengthening of the soft and ductile low-carbon nickel martensite with aging and the forming of a high density of very fine coherent intermetallic precipitates Ni_3 (Mo, Ti, Al). The basic martensitic matrix with a high density of disoriented dislocations interacting with fine, uniformly distributed precipitates, forms a structure particularly resistant to local slip and premature breaking by stretching. The primary goal in making liquid maraging metal is to achieve a high-purity microstructure with a low content of non-metallic inclusions and parti-

cularly low levels of harmful elements such as carbon, nitrogen, sulfur and phosphorus. Carbon, nitrogen and sulfur tend to form brittle carbides, carbonitrides, sulfides and carbosulfides that could strongly reduce the absorbed impact energy. For this reason, the technology of liquid metal production is a process of fundamental importance for further processing and the achieving of the optimal mechanical and exploitation properties.

The elaboration of several maraging steel types (18Ni 200, 18Ni 250, 18Ni 300 and 18Ni 350) was developed in semi-industrial facilities and laboratories of the Institute and special attention was given to the manufacturing technology of 18Ni250 maraging steel. Respecting the highly complex final processing by means of cold flow turning, it was necessary to achieve the maximum purity and an extremely low content of carbon, nitrogen and sulfur and high levels of strength and ductility. These properties were achieved with remelting, especially electron-beam remelting [1].

The elaboration of the steel consists of three technologically related stages:

- Melting the charge in open induction furnaces (OIP);
- Remelting in vacuum induction furnaces (VIP);
- Remelting under inert-gas-protected electric conductive slag (ETP) and under electron beam remelting (ESP);

Here, only the final results for remelted melts during ETP and ESP are presented.

Electrolytic iron, pure metals and the standard technology of liquid metal manufacturing in the OIP were used to obtain the basic charge. A high steel purity and a low content of undesirable elements were obtained by remelting of the basic charge in induction vacuum furnaces. The remelting on ETP led to a further reduction of the sulfur content and electron beam remelting to a further purity increase and a gas content reduction. In addition, both methods (ETP and ESP) achieve solidification grains very suitable for deformation. The maraging steel manufacturing and processing scheme, with basic reactions during molten metal processing is shown in **Figure 1**, and the chemical composition and mechanical properties are shown in **Table 1**.

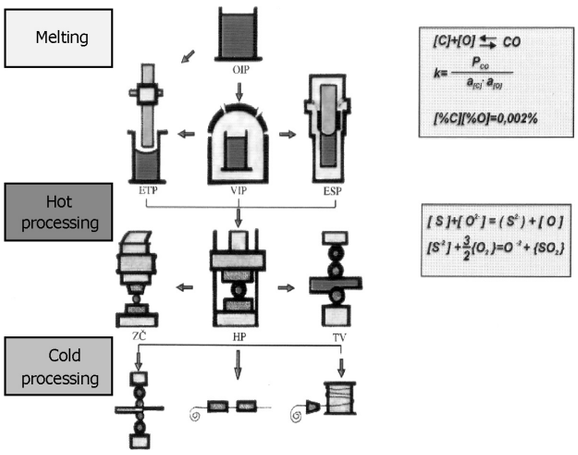

Figure 1: Technological scheme of production with variations in the processes of melting (remelting) and deformation

Slika 1: Tehnološka shema proizvodnje s spremembami v procesih taljenja (pretaljevanja) in predelave

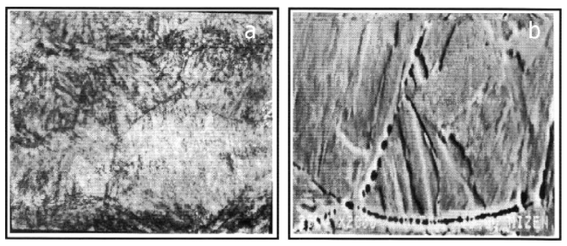

Figure 2: Microstructure of maraging steel: a) optical microscopy (500-times), b) SEM microscopy (2000-times)

Slika 2: Mikrostruktura maraging jekla: a) optični posnetek (povečava 500-kratna), b) SEM posnetek (povečava 2000-kratna)

The mechanical properties, especially the impact energy and fracture toughness K_{1C}, clearly show the effects of remelting that allow very good further processing with cold working. In **Figure 2** the maraging steel microstructure is shown. The examination in the optical and scanning electron microscopes showed that the microstructure consisted of a lath nickel martensitic matrix.

Table 1: Chemical composition and mechanical properties of maraging steel X2NiCoMo 18 9 5 (18Ni 250) according to WL 1.6354 (AMS 6514) in heat treated condition*

Tabela 1: Kemična sestava in mehanske lastnosti maraging jekla X2NiCoMo 18 9 5 (18Ni 2 50) po WL 1. 63 54 (AMS 6514) v toplotno obdelanem stanju*

Making	Content of elements, *w*/%										Mechanical properties				
	Ni	Co	Mo	Ti	Al	C	S	P	B	N	$R_{p0.2}$/ MPa	R_m/ MPa	A_5/%	*K*V/J	K_{1c}/ (MPa m$^{0.5}$)
Prescribed WL1.6354	17–19	8.0–9.5	4.6–5.2	0.6–0.9	0.05–0.15	max 0.03	max 0.010	max 0.010	max 0.03	0.001–0.15	1910	1960	4.5	12	
VIP+ETP	18.4	8.3	5.2	0.55	0.16	0.01	0.001	0.009	0.002	0.004	1905	1940	8.5	21.5	76
VIP+ESP	18.4	8.4	5.0	0.72	0.12	0.01	0.006	0.008	0.002	0.003	1893	1970	10.0	29.4	80.5

*Heat treatment: Triple quench from temperature 920 °C/water and aged at 480 °C/ 34 h/air

3 INFLUENCE OF NITROGEN ALLOYING ON THE MECHANICAL AND EXPLOITATION PROPERTIES OF AUSTENITIC STAINLESS-STEEL AISI 316

Austenitic stainless steel type AISI 316 has a very wide range of applications due to its good technological and exploitation properties. The possibilities of a variation of the chemical composition and the regime of technical processing for maintaining the austenitic structure and constant demands for cleanliness and corrosion resistance, have initiated an active research activity on this type of steel.

A significant role in these studies was played by the possibility of alloying with nitrogen for the replacement of part of the nickel content for the stabilization of the austenitic structure and the affect of nitrogen on the increase of the strength properties. A reduction of the nickel content has its economic justification and the increase in the yield and tensile strength is necessary for the production of structural components operating in aggressive media under high loads.

For the purposes of this research six experimental melts were produced in a vacuum induction furnace with three different variations of nitrogen content, i.e., (0.03, 0.06 and 0.12) %. For each variation of alloying with nitrogen, two melts were made with nickel contents of approx. 10.5 % and 13.5 %. This experiment enabled the simultaneous testing of the effect of alloying with nitrogen and to evaluate the possibility of reducing the nickel content within the limits prescribed for the steel AISI 316. The content of the basic elements and the achieved mechanical properties in the wrought and quenched conditions are given in **Table 2** and in **Figure 3 and 4**. The obtained results show that alloying with nitrogen in amounts up to 0.12 % has a favorable effect on the strength properties of the steel AISI 316 [2].

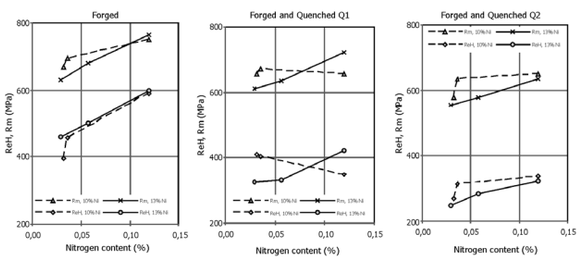

Figure 3: Yield and tensile strength of experimental melts depending on the nitrogen content and the heat-treatment condition (Q1 – 950 °C, Q2 – 1100 °C)

Slika 3: Meja plastičnosti in raztržna trdnost eksperimentalnih talin v odvisnosti od vsebnosti dušika in pogojev toplotne obdelave (QI – 950 °C, Q2 – 1100 °C

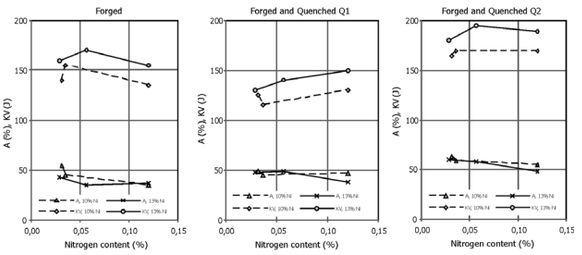

Figure 4: Elongation and absorbed energy of experimental melts depending on the nitrogen content and heat-treatment condition (Q1 – 950 °C, Q2 – 1100 °C)

Slika 4: Raztezek in absorbirana energija eksperimentalnih talin v odvisnosti od vsebnosti dušika in toplotne obdelave (QI – 950 °C, Q2 – 1100 °C)

4 METALLIC ALLOYS FOR WORK AT ELEVATED TEMPERATURES

4.1 Austenitic stainless steel Nitronic 60

In recent years, based on conventional austenitic stainless steel 18/8, steels under the commercial name Nitronic, with the addition of manganese, nitrogen and silicon, have been developed. These steels are intended to operate at elevated temperatures and extended the exploitation area of austenitic stainless steel. In addition, it is significant that the austenitic structure is achieved with less-expensive stabilizing alloying elements, manganese and nitrogen.

Research results show that the occurrence of δ-ferrite in steel Nitronic 60 can be prevented with elements that stabilize austenite, nickel, and especially nitrogen, closer to the upper permitted limits, while the content of ferrite stabilizing elements is maintained in the middle of the allowed range. If the content of a ferrite stabilizing

Table 2: Content of the basic elements and mechanical properties in the forged and quenched condition of the experimental melts
Tabela 2: Vsebnost baznih elementov in mehanske lastnosti eksperimentalnih talin po kovanju in gašenju

Melts	Content of elements*, *w*/%				Mechanical properties											
					Forged (F)				Quenched 950 °C (F+Q1)				Quenched 1100 °C (F+Q2)			
	C	Cr	Ni	N	R_{eH}/ MPa	R_m/ MPa	A_5/ %	*KV*/ J	R_{eH}/ MPa	R_m/ MPa	A_5/ %	*KV*/ J	R_{eH}/ MPa	R_m/ MPa	A_5/%	*KV*/ J
1	0.07	16.5	10.5	0.032	395	670	55	140	410	655	49	125	270	580	63	165
2	0.07	15.8	13.2	0.029	460	630	43	160	325	610	48	130	250	555	60	180
3	0.08	16.4	10.1	0.036	475	695	45	155	405	670	45	115	315	635	59	170
4	0.07	15.9	13.1	0.057	500	680	35	170	330	635	49	140	285	580	58	195
5	0.08	17.5	10.6	0.120	590	750	35	135	350	655	47	130	340	650	55	170
6	0.07	16.7	13.7	0.120	600	765	37	155	420	720	38	150	325	635	48	190

* The contents of other elements Mo, Mn, Si, S i P is approximately equal in all melts

Table 3: Chemical composition of the experimental melts of steel S 218 00 (Nitronic 60)
Tabela 3: Kemična sestava eksperimentalnih jekel S 218000 (Nitronic 60)

Making	Content of elements, *w*/%								Cr_{ekv}[1]	Ni_{ekv}[2]	δ-ferrite[3]
	C	Mn	Si	P	S	Cr	Ni	N			
Prescribed ASTM A 276	max. 0.10	7.0–9.0	3.5–4.5	max 0.06	max. 0.03	16.0–18.0	8.0–9,0	0.08–0.18	–	–	–
Melt 1	0.06	7.0	3.6	0.002	0.015	16.5	8.1	0.113	21.9	16.8	3
Melt 2	0.07	7.8	4.2	0.002	0.012	18.0	9.0	0.109	24.3	18.3	8
Melt 3	0,08	7.8	3.6	0.001	0.012	16.8	9.0	0.178	22.2	20.6	0

NOTE:
1. $w(Cr_{ekv}) = w(Cr) + 1{,}5\ w(Si)$
2. $w(Ni_{ekv}) = w(Ni) + 30\ w(C) + 30\ w(N) + 0{,}5\ w(Mn)$
3. According to revised Schaeffler constitution diagram[3]

Table 4: Chemical composition of experimental melts of superalloy Nimonic 80A
Tabela 4: Kemična sestava eksperimentalnih talin superzlitine Nimonic 80 A

Variant	Content of elements, w/%										
	C	Cr	Si	Mn	Fe	Co	S	P	Ti	Al	Ni
Variant I	0.05	19.7	0.25	0.03	2.10	1.25	0,007	0.005	2.52	1.32	Balance
Variant II	0.04	20.8	0.23	0.16	1.48	1.30	0,006	0.005	2.68	1.44	Balance

element would be close to the upper limit to achieve the specific use characteristics, the content of the other ferrite stabilizing elements should be lower. Otherwise, the purely austenitic structure cannot be achieved, regardless of the content of the austenite stabilizing elements. The revised Schaeffler diagram [3] can be used to optimize the chemical composition at which the formation of δ-ferrite will be prevented [4].

4.2 Nickel-based superalloy Nimonic 80A

The superalloy Nimonic 80A is a nickel-base alloy intended for use at elevated and high temperatures where significant creep may occur. The primary strengthening mechanism of this superalloy is based on the precipitation of fine and coherent particles of intermetallic γ' phase $Ni_3(Al,Ti)$ that increase the creep resistance. This strengthening mechanism for such a superalloy is more favorable than other strengthening mechanisms [5]. The effect of hardening that can be achieved by the γ' phase depends on the amount, dispersion, and size of the γ' phase and it is controlled by heat treatment. The standard heat treatment includes a solution annealing at 1080 °C 8 h and precipitation aging at 700 °C 16 h. The maximal hardness of the superalloy Nimonic 80A achieved after this treatment is around 360 HV, but certain applications in the automotive industry require higher hardness. Since by long-lasting solution annealing at high temperature coarsening of grains occur, it is not possible to increase the hardness (additional strengthening) significantly with a reduction of the grain size. The increase of the dislocation density after solution annealing and before precipitation aging, with cold or warm deformation, increases the strength, but the ductile properties are reduced significantly. A partial recrystallization after such a deformation results in a significant increase in the ductile properties and retains a high level of strength properties.

For additional strengthening of the superalloy Nimonic 80A the application of warm deformation is considerably more favorable than cold deformation, because the warm deformation can be done on a hot-rolling mill. In addition, the dislocation substructure obtained after the warm deformation is more favorable than that obtained after cold deformation, because the

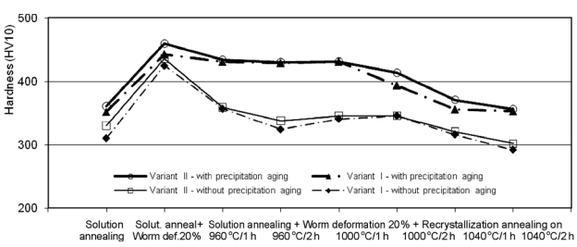

Figure 5: Hardness (HV10) after corresponding treatment
Slika 5: Trdota (HV10) po označeni toplotni obdelavi

Table 5: Chemical composition and structure of the base material A286 and NiCrAlY metal powders
Tabela 5: Kemična sestava in struktura osnovnega materiala A286 in prhov NiCrAlY

Material	Content of elements, *w*/%							Structure
	C	Ni	Cr	Mo	Al	Ti	Y	
A 286	0.05	26.0	15.5	1.3	0.2	2.1		$\gamma' + \gamma + K$
NiCrAlY	–	67	22.0	–	10.0	–	1.0	$\gamma'+\gamma+Al_2O_3+Y_3O_3+\beta$

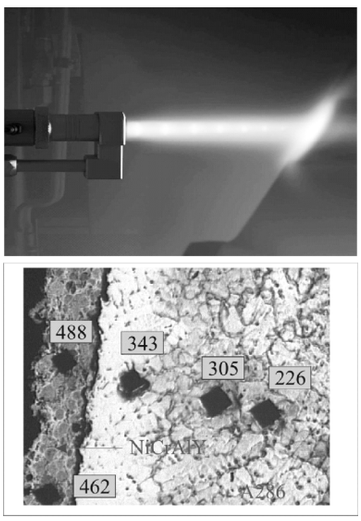

Figure 6: Applying metallic coatings with the HVOF process and the microstructure of superalloy A286 and coatings after the thermal treatment (solution annealing at 1080 °C and hardening at 740 °C for 8 h)

Slika 6: Nanašanje metalnih prekritij z HVOF-procesom in mikrostruktura superzlitine A286 in prekritja po toplotni obdelavi (topilno žarjenje pri 1080 °C in utrditev pri 740 °C 8 h)

structure after cold deformation is characterized by chaotically distributed dislocations.

A change of the hardness of the two experimental melts (**Table 4**), subjected to solution annealing (1080 °C 8 h) after hot rolling, and then to 20 % warm deformation and recrystallisation annealing at different temperatures (960 °C, 1000 °C and 1040 °C in duration of one or two hours) and finally to precipitation aging (700 °C 16 h) is shown in **Figure 5**. The hardness of the alloy can be significantly increased through warm deformation after solution annealing. With the subsequent partial recrystallization the values of the hardness and the ductile properties can be controlled [5].

5 IMPROVEMENT OF THE CHARACTERISTICS OF IRON-BASED SUPERALLOYS WITH METALLIC COATINGS

A surface-enhanced structural element can be obtained with the application of surface-engineering technologies [6]. The coated element combines the good properties of the base material and of the applied metallic layer. The combined properties could not be achieved using only one type of coating material. The selection of the base material and the metal coating is based on the requirements from manufacturers in the automotive industry that needed a cold-deformed iron-based superalloy A286 for some structural parts. However, the idea of rationalization with use of this as cast did not give satisfactory results, primarily because the required strength properties (hardness at the surface) could not achieved. The required surface hardness with improved resistance to high-temperature corrosion was achieved by applying HVOF technology (High velocity oxyfuel) for forming metallic coatings (**Figure 6**). The process of applying the metallic powder NiCrAlY on the superalloy A286 was carried out by using a Diamond Jet technology in cooperation with the Development Department of "ORAO" Bijeljina.

The microstructural constituents of the base material A286 and the NiCrAlY coatings are given in **Table 5**. Aluminum and yttrium oxides improve the resistance to high-temperature corrosion and yttrium oxide particles act as a strengthening phase. The percentage of 40% of γ' phase in the coating increases the surface hardness to values that exceed the hardness that can be achieved with the superalloy A286 [7].

6 CONCLUSION

The producer's requirements ensured that particular structural elements satisfy the exploitation conditions were the starting base for this work. The concept of research included a preliminary analysis of the content and the interaction of the alloying elements, the structure analysis and the analysis of the relationship between the microstructure and the properties. Depending on the properties to be modified, the corresponding chemical composition and microstructure of the alloy, and then corresponding manufacturing technology, were designed. Well-known methods of designing (modeling) technologies were tested experimentally. In this article an overview of the modification of the properties of some materials suited for structural parts with improved performance is presented.

7 REFERENCES

[1] Rimac M., Jurić D.: Osvajanje tehnologije izrade martenzitno starenog čelika OZ N18K9M5, Metalurški institut Hasan Brkić Zenica, 1988

[2] Rimac M.: Uticaj legiranja azotom na tehnološke i eksploatacione osobine austenitnog nehrđajućeg čelika AISI 316, Magistarski rad, Metalurški fakultet Zenica, Zenica, 1996

[3] Metals Handbook: Properties and Selection: Irons, Steels and High-Performance Alloys, 10th ed., Vol.1, ASM American Society for Metals, 1990

[4] Beganović O., Muminović B.: Optimizacija hemijskog sastava austenitnog nehrđajućeg čelika Nitronic 60 u cilju sprečavanja nastanka δ-ferita, VII Naučno/stručni simpozij sa međunarodnim učešćem METALNI I NEMETALNI MATERIJALI Zenica, BiH, 22–23. maj 2008

[5] Beganović O., Oruč M., Rimac M., Uzunović F.: Additional strengthening of superalloy Nimonic 80A, 14th International Research/ Expert Conference Trends in the Development of Machinery and Associated Technology TMT 2010, Mediterranean Cruise, 11–18 September 2010

[6] Hocking M. G., Vasantasree V., Siolky P. S.: Metallic and Ceramic Coatings, High Temperature Properties and Applications, John Willy and sons, INC., New York, 2000

[7] Oruč M., Rimac M., Beganović O., Delić A.: New materials as the base for development of modern industrial technologies, 13th International Research/Expert Conference Trends in the Development of Machinery and Associated Technology TMT 2009, Tunisia, 2009

UDK 669.14.018.252:621.785
Professional article/Strokovni članek

ISSN 1580-2949
MTAEC9, 45(5)489(2011)

EVALUATION OF THE MICROSTRUCTURAL CHANGES IN Cr-V LEDEBURITIC TOOL STEELS DEPENDING ON THE AUSTENITIZATION TEMPERATURE

OCENA SPREMEMB MIKROSTRUKTURE V LEDEBURITNEMN ORODNEM JEKLU Cr-V V ODVISNOSTI OD TEMPERATURE AVSTENITIZACIJE

Pavel Bílek, Jana Sobotová, Peter Jurči

Czech Technical University in Prague, Faculty of Mechanical Engineering, Karlovo nám. 13, Prague 2, CZ 121 35, Czech Republic
pavel.bilek@fs.cvut.cz

Prejem rokopisa – received: 2010-11-29; sprejem za objavo – accepted for publication: 2011-04-14

Samples of Vanadis 6 PM Cr-V ledeburitic steel were austenitized at temperatures in the range 1000–1200 °C and oil-quenched. The structural changes were investigated by scanning electron microscope and evaluated using NIS Elements software. The obtained results indicated that the M_7C_3-carbides underwent intensive dissolution in austenite and were not detected above a temperature of 1100 °C. On the other hand, the MC-carbides remained almost completely unaffected and symptoms of dissolution were found only at a temperature of 1200 °C. The saturation of austenite by carbon, chromium and partly vanadium increased the hardness of the as-quenched material, with the maximum at an austenitizing temperature of 1025 °C.

Key words: Cr-V ledeburitic steels, Vanadis 6, MC carbides, M_7C_3 carbides, temperature of austenitization.

Vzorci ledeburitnega jekla Cr-V Vanadis 6 PM so bili avstenitizirani v temperaturnem območju 1000–1200 °C in kaljeni v olju. Spremembe mikrostrukture so bile raziskane z vrstičnim elektronskim mikroskopom in ocenjene z uporabo NIS-elementnega softvera. Rezultati kažejo, da so se karbidni M7C3 hitro raztapljali v avstenitu in jih ni bilo opaziti nad temperaturo 1100 °C. Po drugi strani so VC-karbidi ostali nespremenjeni, a simptome raztapljanja smo opazili le pri temperaturi 1200 °C. Nasičenje avstenita z ogljikom, kromom in delno vanadijem je povečalo trdoto kaljenega materiala z maksimumom pri temperaturi 1025 °C.

Ključne besede: ledeburitno jeklo Cr-V, Vanadis 6, MC-karbidi, M7C3-karbidi, temperatura avstenitizacije

1 INTRODUCTION

The group of Cr-V ledeburitic steels is widely used in various industrial processes and operations. To meet the industrial requirements for high production stability and reliability, they have to withstand wear and plastic deformation. On the other hand, the steels should be resistant to micro- and macro-cracking, e.g., their toughness and fracture toughness must be as high as possible.[1,2]

The main alloying element of Cr-V ledeburitic steel is chromium. It forms various types of more or less stable carbides. These carbides are well soluble in austenite, which saturates the solid solution with carbon and the alloying elements. A large amount of alloying elements in austenite makes good though-hardenability of the material.[3]

Vanadium is the second typical element of Cr-V ledeburitic steel. Vanadium has a high affinity for the carbon and forms very stable MC-carbides.[4] Vanadium deteriorates the machinability (as a result of very hard carbides) and the grindability of steels. In tool steels, vanadium is used for the following reasons: improvements of hardenability, formation of very hard carbides, increase of the wear resistance and hot hardness. Due to the small size of the carbide particles and their high thermal stability, the steels containing vanadium are resistant to grain coarsening during austenitizing. It preserves the relatively favourable mechanical properties after the heat treatment.[3]

The structure and properties of ledeburitic steels are determined by the character of the matrix and the type, quantity, size and distribution of the carbides. The properties of tool steels are given by the superposition of the matrix and the carbides. The hardness in the soft-annealed state, for instance, is closely related to the quality and amount of carbides. The matrix composition is not as important, since it consists in any case of ferrite. On the other hand, after austenitizing and quenching, the matrix hardness is the most important factor influencing the hardness of the steels. But, it is impossible to get a sufficient as-quenched matrix hardness without the presence of carbides in the material. During austenitizing, as is well known, some of them undergo dissolution in the austenite, which results in a high hardness of the material after heat treatment. The other part of the carbides, which does not undergo the dissolution, hinders the austenite grains coarsening and makes the steels wear resistant.[1]

Carbide phases have different thermal stability and, while some of them are dissolved during austenitizing in the solid solution at relatively low temperatures, others remain stable up to the solidus temperature.[3]

The standard heat treatment of Cr-V ledeburitic steels consists of the following steps: austenitizing, holding at temperature to dissolve a certain amount of carbides and to homogenize the austenite, quenching to room (or sub-zero) temperature and several times tempering, usually to the secondary hardness peak. After these procedures, the hardness reaches more than 60 HRC.[5]

The paper is focused on an investigation of what happens with the carbides and the matrix of the Cr-V ledeburitic steels, when heated up to different austenitizing temperatures. The PM made Vanadis 6 steel is used as an example.

2 EXPERIMENTAL

2.1 Material and processing

The experimental substrate material was the ledeburitic steel Vanadis 6 with nominally 2.1 % C, 1.0 % Si, 0.4 % Mn, 6.8 % Cr, 1.5 % Mo, 5.4 % V and Fe as balance, made by PM.[6]

Round-shaped samples from the steel were austenitized at the temperatures (1000, 1025, 1050, 1075, 1100, 1150 and 1200) °C and oil-quenched. From the heat-processed material, metallographic specimens were prepared, ground, polished and etched with 2 % Nital solution.

2.2 Characterization

The microstructure was investigated using SEM. EDS mapping was done on the same device at an accelerating voltage of 15 kV and a standard working distance of 15 mm. For the quantification of the structural changes, for each specimen 10 micrographs were taken at a standard magnification of 5000-times.

To quantify the amount of M_7C_3- and MC-carbides, each carbide particle was identified using the corresponding EDS mapping of chromium and vanadium. Afterwards, the volume fraction, size and density (number of particles per mm^2 on a metallographic sample) of particles were determined for the specimens processed at all the austenitizing temperatures, as well as for the as-delivered material, using the NIS-elements® software. From the obtained results, the mean value and the standard deviation were calculated. The size of the carbides, as a function of austenitizing temperature, was evaluated as follows: the size classes of the particles were chosen first. Then, the particles were classified according to their dimensions.

The hardness was measured using the Rockwell C method (HRC). Five measurements were made on each specimen and the mean value was calculated.

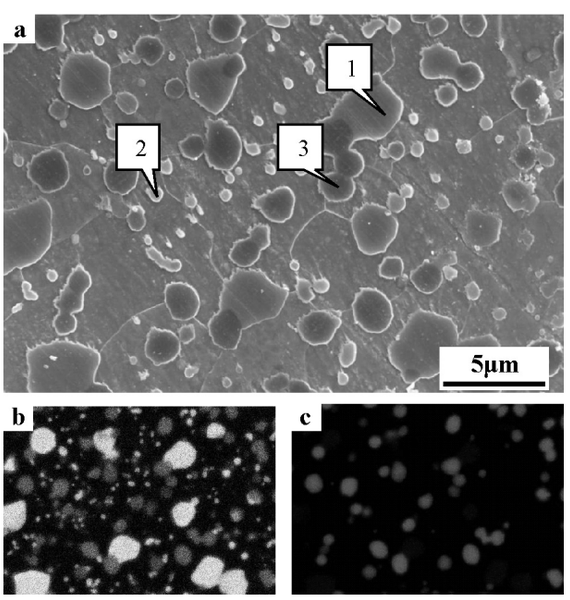

Figure 1: Microstructure of PM ledeburitic steel Vanadis 6 in soft-annealed state: a – overview (SEM), b – EDS-map of chromium from the Figure 1a, c – EDS-map of vanadium from the Figure 1a

Slika 1: Mikrostruktura PM-ledeburitnega jekla Vanadis 6 v mehko žarjenem stanju: a – pregled (SEM), b – EDS-posnetek kroma s slike 1a, c – EDS-posnetek vanadija s slike 1a

3 RESULTS AND DISCUSSION

The as-received Vanadis 6 steel contains a matrix together with fine and uniformly distributed carbides (**Figure 1a**). The particles are of two types. Large particles (1) as well as those of sub-micron size (2) are chromium-based carbides (**Figure 1b**). Smaller particles (3) are the vanadium-rich phases (**Figure 1c**). A previous investigation has shown that the chromium-based particles are M_7C_3 and the vanadium-rich particles are MC.[7]

The hardness of the as-received material was 21.3 HRC.

The as-quenched structure consists of martensite, retained austenite and two types of undissolved carbides (**Figure 2**). In previous investigations, the larger and

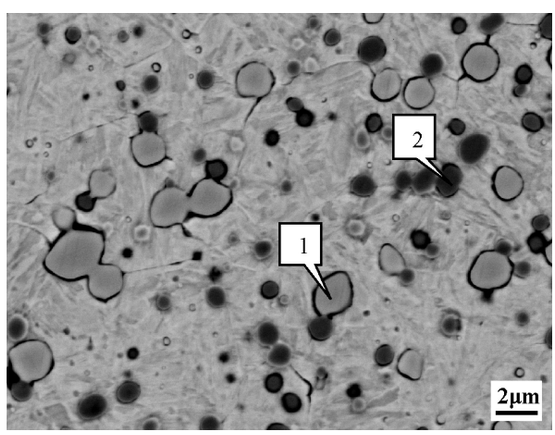

Figure 2: Microstructure of PM ledeburitic steel Vanadis 6 after heat treatment (SEM)

Slika 2: Mikrostruktura PM-ledeburitnega jekla Vanadis 6 po toplotni obdelavi (SEM)

brighter particles were identified as being the M_7C_3 type (1) and the smaller and darker particles as being the MC type (2).

The volume fractions of the MC- and M_7C_3-particles, as well as the total amount of carbides, as a function of the austenitizing temperature, are shown in **Figure 3**. In the soft-annealed (SA) state, the material contains 29.5 % of carbides. The volume fraction of M_7C_3 carbides was 15.6 % and the volume fraction of MC carbides was 13.9 %.

During austenitizing, the dissolution of carbides occurs. This is particularly so for the M_7C_3 particles. After austenitizing at a temperature of 1000 °C, their volume fraction was 7.3 % and it decreased further with increasing austenitizing temperature. Above 1100 °C, no M_7C_3 particles were found.

The amount of MC particles decreased only slightly with the austenitizing temperature up to 1150 °C. Beyond that, the decrease in the amount of the MC particles became more significant.

These results indicate that while the M_7C_3 particles dissolved completely in the austenite during heating to the austenitizing temperature, the MC phase remained very stable up to high temperature. Only at temperatures of about 1200 °C does it undergo dissolution to a limited extent.

Figure 4 shows the density of both the MC- and M_7C_3-particles as a function of austenitizing temperature. As shown, the density of M_7C_3 particles decreases with increasing austenitizing temperature. After austenitizing at a temperature of 1000 °C, the density was about 5000 M_7C_3 particles per square millimeter. After austenitizing at a temperature of 1100 °C, the density was lowered to about 1000 /mm^2. The austenitizing at temperatures above 1100 °C leads to complete dissolution of the M_7C_3 particles. The density of the MC particles, on the other hand, decreased only weakly up to a temperature of 1150 °C, and only above did it decrease more markedly. At a temperature of austenitizing of 1000 °C, the density was about 21 000 MC carbide particles per square millimeter. At a temperature of 1150 °C, the density was lowered to about 17 500 /mm^2 and more significant lowering, to a mean value of 12 500 /mm^2 was fixed when the material was austenitized at the temperature of 1200 °C.

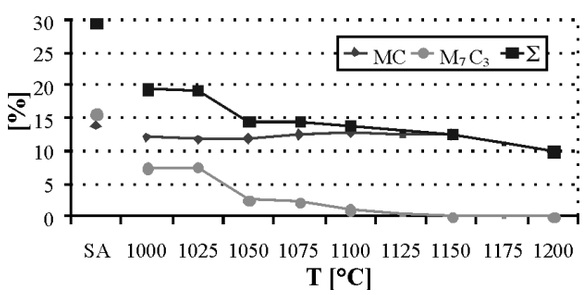

Figure 3: The amounts of carbides for samples of Vanadis 6 ledeburitic steel depending on the austenitizing temperature.

Slika 3: Količina karbidov za vzorce jekla Vanadis 6 v odvisnosti od temperature avstenitizacije

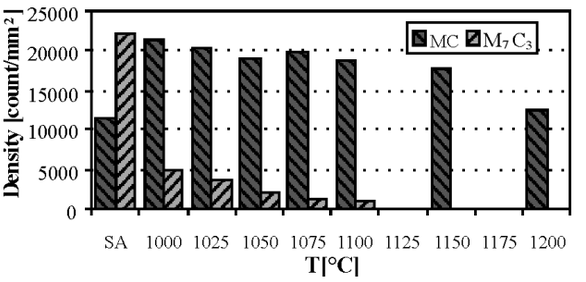

Figure 4: The density of carbides as a function of the austenitizing temperature

Slika 4: Gostota karbidov v odvisnosti od temperature avstenitizacije

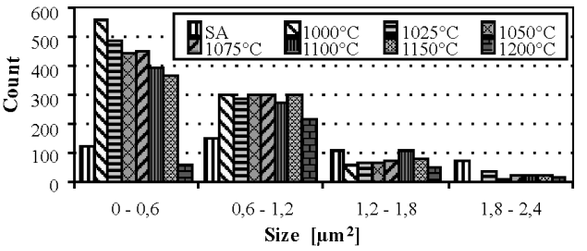

Figure 5: The size distribution of MC particles as a function of the austenitizing temperature

Slika 5: Velikostna porazdelitev MC-karbidov v odvisnosti od temperature avstenitizacije

Figure 5 documents the size distribution of the MC particles. Two phenomena are visible from the diagram. The first one is that finer particles have a tendency to dissolve in austenite in some, but a relatively limited extent. On the other hand, it seems that the larger MC particles remain practically unaffected.

Figure 6 shows the size distribution of the M_7C_3 particles. It can be seen that with an increased austenitizing temperature, the number of carbide particles of all size classes decreases rapidly. This confirms that the M_7C_3 phase is less stable than the MC phase and undergoes much more easily the dissolution in austenite.

Figure 7 shows SEM micrographs from samples austenitized at various temperatures (left column) and

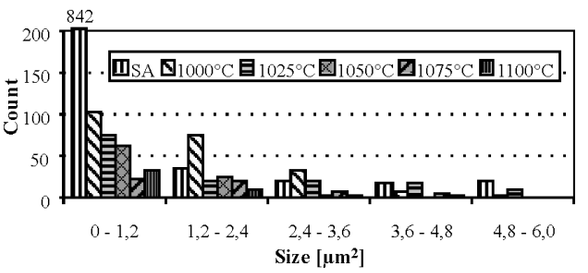

Figure 6: The size distribution of M_7C_3 particles as a function of the austenitizing temperature

Slika 6: Velikostna porazdelitev M_7C_3-karbidov v odvisnosti od temperature avstenitizacije

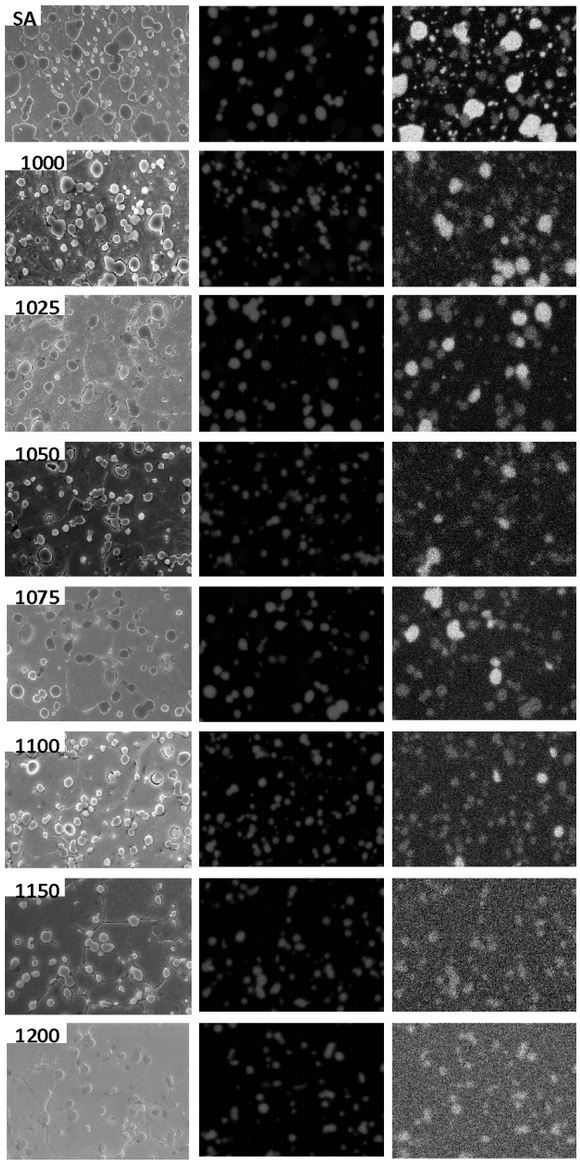

Figure 7: SEM micrographs and corresponding EDS-maps of the samples processed at various austenitizing temperatures

Slika 7: SEM-posnetki in ustrezni EDS-posnetki vzorcev, ki so bili procesirani pri različni temperaturi avstenitizacije

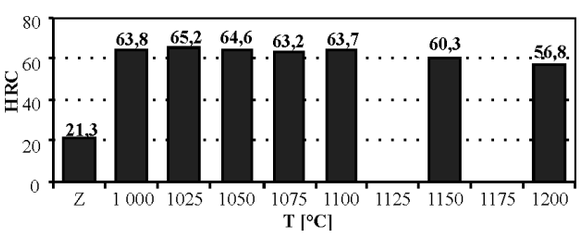

Figure 8: Hardness of the samples made from the Vanadis 6 steel depending on the austenitizing temperature

Slika 8: Trdota vzorcev jekla Vanadis 6 v odvisnosti od temperature avstenitizacije

the corresponding EDS-maps of the vanadium (central column) and chromium (right column). The micrographs and EDS-maps are in good agreement with the above-presented and discussed results of the investigations. It means that the total volume fraction of carbides decreases with the increasing austenitizing temperature. The phase that is more sensitive to dissolution in austenite is the M_7C_3.

Figure 8 shows the results of the hardness measurements of HRC. The heat treatment induced a rapid increase in the hardness.

After the maximum hardness peak, the hardness decreases slightly and for the steel austenitized above 1100 °C more rapidly. The hardness behavior can be explained as follows. Due to the dissolution of carbides, the austenite becomes saturated with carbon and the alloying elements. The saturation is higher when a higher austenitizing temperature was applied. The increased content of carbon and alloying elements increased the hardness of the martensite. But they also induce a decrease of the temperatures of M_S and M_F, respectively, which tends to increase the amount of retained austenite.[8] The final steel hardness is then a result of the competition between the martensite supersaturation (hardness increase) and the retained austenite amount (hardness decrease), with an optimum at the austenitizing temperature of 1025 °C.

4 CONCLUSIONS

We found that the microstructure of the material in the soft-annealed state consisted of a ferritic matrix and two types of carbides. The volume fraction of the MC particles was 13.9 % and the volume fraction of the M_7C_3 particles was 15.6 %.

After the heat treatment, the microstructure of the steel consists of martensite, retained austenite and both carbide phases or only MC particles. With an increasing temperature of austenitizing, the M_7C_3 carbides underwent dissolution, which reduced their density and size. The M_7C_3 particles were not detected above 1100 °C. The MC particles are stable up to a temperature of 1150 °C. Above this, the MC particles also began to dissolve in the matrix to a limited extent. The density of the MC particles decreased slightly with the increasing temperature of austenitizing.

Furthermore, it was found that the highest hardness of 65.2 HRC was for the steel austenitized at a temperature of 1025 °C. Any further increase of the austenitizing temperature induced a decrease of the hardness of the samples.

The obtained results confirmed that the M_7C_3 particles easily undergo the dissolution in austenite. The MC particles are stable and can effectively hinder the grain coarsening up to high temperatures.

5 REFERENCES

[1] Macek, K, Janovec, J., Jurči, P., Zuna, P.: Kovové materiály, ČVUT, Praha, 2006

[2] Jurči, P., Šuštaršič, B., Leskovšek, V.: Freacture charakteristics of the Cr-V ledeburitic steel Vanadis 6. Mater. Tehnol., 44 (**2010**), 77–84, ISSN 1580-2949

[3] Jurči, P.: *Nástrojové oceli ledeburitického typu,* ČVUT, Praha, 2009

[4] Fremunt, P., Krejčík, J., Podrabský.: Nástrojové oceli, Dům techniky Brno, 1994

[5] Jurči, P. Structural changes in Cr-V ledeburitic steel during austenitizing and quenching. *Materials Engineering*, 17 (**2010**) 1, 1–10

[6] Materiálový list firmy Uddeholm, Vanadis 6 – Super Clean High performance powder metallurgical cold work tool steel [online]. 2009 [cit. 2010-3-8]. WWW: http://www.bucorp.com/files/van_6_ds.pdf.

[7] Jurči, P., Hnilica, F., Suchánek, J., Stolař, P.: Microstructual features of Cr-V ledeburitic steel saturated with nitrogen, Mater. Tehnol., 38 (**2004**), 1–2

[8] Kraus, V. Tepelné zpracování a slinování : Přednášky [online]. Plzeň : ZČU, 2000 [cit. 2010-06-17]. WWW: http://tzs.kmm.zcu.cz/TZSprcelk.pdf

IN MEMORIAM
HANS JÜRGEN GRABKE

Prof. Hans Jürgen Grabke, dr. rer. nat., dr. h.c. in mednarodni pridruženi član uredniškega odbora revije Materiali in Tehnologije – Materials and Technology.

Rojen je bil v Hamburgu, Nemčija, kjer je tudi maturiral. Kemijo je študiral na Univerzah v Göttingenu, Hamburgu in Münstru, kjer je tudi doktoriral. Leta 1971 je bil na Univerzi v Stuttgartu habilitiran za docenta in leta 1977 za profesorja za fizikalno kemijo na Univerzi v Dortmundu. V letih 1962–1966 je bil podoktorski raziskovalec na Max-Planck-Institut für Physikalische Chemie v Göttingenu, kjer je bil pod vodstvom prof. C. Wagnerja vključen v raziskave temeljnih mehanizmov in kinetike heterogenih reakcij z opredelitvijo parcialnih reakcijskih korakov, ravnotežnih aktivnosti, sestavo vmesnih produktov in izračunom termodinamičnih in kinetičnih zakonitosti reakcij.V letu 1966 se je zaposlil na Max-Planck-Institut für Metallforschung v Stuttgartu in delal kot vodja skupine, ki je nadaljevala raziskovanje heterogenih reakcij. Leta 1972 je prešel na Max-Planck-Institut für Eisenforshung (MPIE) v Düsseldorfu, kjer je postal vodja oddelka za fizikalno kemijo. Na tem mestu se je njegovo raziskovalno delo postopoma močno razširilo z vključevanjem študentov diplomantov, doktorantov, podoktorskih in gostujočih raziskovalcev.

H. J. Grabke je vrhunski znanstvenik s področja fizikalne kemije trdnega stanja. Njegova odkritja so bila temelj za znanstveno interpretacijo zelo pomembnih izkustvenih spoznanj, za termokemično in termodinamično opredelitev novih reakcij in pojavov ter za razvoj novih in izboljšanje obstoječih zlitin in postopkov. Odkril je, kako so pojavi povezani z aktivnostjo v reakciji

Prof. dr. rer nat. And dr.h.c. Hans Jürgen Grabke

Born in Hamburg, Germany, where he graduated in secondary school. He studied chemistry at the universities of Göttingen, Hamburg and Münster, where he attained also the of rer. nat. doctorate In the years 1962–1966 he worked with C. Wagner in MPI for physical chemistry in Göttingen as part of the group working on mechanisms and kinetics of heterogeneus reactions with accent on partial steps of reactions, equilibrium activity, intermediate products, and thermodinamic and kinetic calculations. In 1966 He joined at Max Planck Institut for Metallforschung in Stutgart as leader of the group working in heterogeneus reactions and in 1972 He joined the Max Planck Institut für Eisenforschung as chief of the Dpt. of physical chemistry. At this place, his research work increased gradually with involvement of candidated for university degree, doctorate, postdoc work and guest scientists and mentored several tens of doctorate and diploma works

H. J. Grabke was a highest level scientist in field of physical chemistry of solid state with discoveries that became the foundation for scientific interpretation of significant earlier empirical findings, of thermochemical and thermodynamical undestatanding of new reactions and phenomena, as well as development of new alloys and processes. He explained the connection of phenomena with the actvity in reacions involved elements in alloys and atmosphreres with temperature and difffusivity. His articles on own findings and reviews were published in a number of scientific periodicals and

sodelujočih elementov in spojin, ki so v kovini in atmosferi, odvisni od temperature in difuzivnosti. Nad 500 del, ki predstavljajo lastne znanstvene izsledke in pregledna dela je objavil v številnih znanstvenih revijah v vseh raziskovalno pomembnih državah, tudi v Sloveniji, in v teh državah tudi predaval o svojem znanstvenem delu.

Bil je ned pionirji raziskovanja ravnotežne površinske segregacije atomov nekovinskih elementov, ki so v α-železu raztopljeni v zelo majhni količini (pod 0,01 %). Za nekatere elemente je izmeril kinetiko segregacije, opredelil je vpliv različnih elementov in njihove koncentracije na geometrijsko porazdelitev atomov matične kovine in segreganta na površini ter v globino segregirane plasti. Interakcijo različnih segregiranih elementov je razložil s pojavom, ki ga je opredelil kot "site competition", ker je na površini kovine omejeno število mest, v katera se lahko vgnezdijo atomi segregantov. Podobne segregacije je odkril tudi na kristalnih mejah v mikrostrukturi kovin in zlitin in tako postavil znanstveno podlago za razumevanje nekaterih pojavov degradacije kovin in zlitin. Opredelil je spremembo proste energije in entropije površine zaradi segregacije in odkril, da je gonilna sila za segregacijo prosta energija površine, ki je najmanjša pri neki specifični geometrični porazdelitvi atomov matične kovine in segreganta, pri kateri so najmanjše površinske elastične napetosti in površinska energija. Pri raziskavah je uporabljal tudi eksperimentalne metode, ki so se tedaj šele uvajale, npr. spektroskopijo Augerjevih elektronov (AES), rentgensko foto elektronskospektroskopijo (XPS) in difrakcijo maloenergijskih elektronov (LEED). Temeljnega pomena so njegova odkritja v zvezi z mehanizmom in kinetiko naogljičenja železa, ki so znanstvena podlaga za razlago, zakaj se pri nekaterih jeklih ne dosegajo pričakovane lastnosti po utrditvi površine z naogljičenjem in kaljenjem; raziskal je kompleksne reakcije naogljičenje-oksidacija, oksidacija-sulfidizacija in oksidacija-kloriranje na površini zlitin zaradi problemov pri sežigu odpadkov in v petrokemijskih napravah. Odkril je, da zlitine železa v močno reduktivni atmosferi in temperaturi nad 800 °C razpadejo v prah, če aktivnost ogljika v atmosferi presega tisto v železovem karbidu in da neprepustna plast kromovega oksida zlitino zavaruje proti upraševanju. Njegovo delo je postalo podlaga za razvoj novih zlitin za naprave, ki obratujejo v močno reduktivnih atmosferah.

H. J. Grabke je dosegel pomembne znanstvene uspehe tudi pri raziskovanju drugih pojavov in reakcij, vse od vpliva elektrodnih potencialov na mehanizem korozijskih reakcij v različnih medijih, adsorpcije tujih atomov in adhezivnost kovinskih površin; prenosa ogljika skozi oksidne sloje; detekcije vodika v oksidnih slojih na površini kovin in pojasnil še druge pojave povezane z reaktivnostjo zlitin v različnih atmosferah.

Dosežki pri raziskovanju so ga uvrstili med najbolj prodorne in produktivne raziskovalce reakcij in interakcij

lectures delivered in a number of countries, in Slovenia, also.

He pionered the investigations ob equilibrium surface segregation of atoms of low content elements in solid solution in α iron and determined for some elements the kinetics of segregation, it influence on the geometrical distribution of segregated atoms on the mother metal surface and the thickness of the segregated layer. He explained the interaction of different segregating elements as site competition due to the limited sites on disposition for the segregant atom on the mother metal surface. A similar intergranular segregation was the base of scientific interpretaion of some degradation processes. Based on the determination of change of free energy and entropy of segregation, He found that the segregation driwing force was the free surface energy depending on the distribution of atoms of segregant and mother metal that governs the surface elastical stresses.

In His investigations new experimental methods wrere used, f.i. Auger spectroscopy, x-rays spectroscopy in low energy electrons spectroscopy. Of basic signficance are the discoveries related to the mechanism and kinetics of carbonisation of iron that are the scientific base for understanding the causes of low effect of case hardening for some steels. Investigating the complex reactions carburisation-oxydation, oxydation-sulphidisation and oxydation-clorinisation on the surface of alloys in petro-chemistry and wastes burning installations, He discovered that iron alloys decomposed in powder if carbon activity in atmosphere exceeded that in iron carbide and that the process was arrested by a layer of chromium oxide on alloys surface. These findings helped to improve the resistance of allloys used in part of installaions working at high temperature and complex atmosphere.

H. J. Grabke achievements are significanst for other phenomena and reactions, also, f.i.: influence of electrode potentials on the mechanims of corrosion reactions in different media, adsorption of foreign atoms and adhesivty of metals surfaces diffusion of carbon and detection of hydrocen in oxide layers on metal surface and explanation of other phenomena and processes connected with the reactivity of metal surface in different atmospheres.

For orriginal scientific discoveries He received several high recognitions, f.i. the Nernst-Haber Bodenstein award of the German Bunsen Society for Physical Chemistry, the Reamur Medaille of the Société Française de Métallurgie, the Tamman Medail of Germain Society for Materials Science and others and was elected to memberships of the Polish Acadamy of Sciences.

He cooperated with and helped slovenian scientists active in iron solid state processes and reactions and continued the tradition started with prof. dr. h.c. C. Rekar, nestor od slovenian research in metallurgy. With his cooperations international conferences were organised in joined effort of MPI, Düsseldorf, IRSID, St

med površino kovin in različnimi atmosferami. Bil je tudi mentor več deset doktorantov in diplomantov, organiziral je učne delavnice na temo reakcij med površino kovin in atmosferami, predsedoval je in bil član znanstvenega odbora mednarodnih konferenc na temo znanosti o površinah ter o mejnih površinah in pripravil tudi številna uvodna in pregledna predavanja.

Njegova biliografija obsega nad 500 del, ki so bili objavljena v Nemčiji in v številnih drugih državah, tudi v Sloveniji. Nekatera so bila izbrana za najboljši članek leta v več znanstvenih revijah. Za izvirna znanstvena odkritja je prejel številne nagrade, npr. Nernst-Haber Bodenstein nagrado nemške Bunsen Society for Physical Chemistry, Reaumur medaljo Société Française de Métallurgie, Tamman medaljo Germain Society for Materials Science in druge in bil izvoljen za častnega člana Poljske akademije znanosti.

H. J. Grabke je intenzivno sodeloval z raziskovalci v Sloveniji že od leta 1980 in nadaljujeval tradicijo sodelovanja, ki ga je vzpostavil desetletja prej prof. dr.h.c. C. Rekar, nestor raziskovanja o kovinah v Sloveniji. S prof. H. J. Grabkejem se je sodelovanje okrepilo tudi z oživitvijo organizacije mednarodnih konferenc, ki so jih skupno organizirali inštituti: IRSID iz Francije, MPIE iz Nemčije in takratni Metalurški inštitut, sedaj Inštitut za kovinske materiale in tehnologije Ljubljana. Prav nekaj let prej se je začel hiter razvoj znanosti o površinah z uporabo novih analitskih tehnik, ki so omogočale kvantitativne raziskave zelo tankih plasti na površini kovin, tudi, površinske segregacije in segregacije po mejah kristalnih zrn ter razlago fizikalno-kemijskih pojavov na površini kovin. Prof. Grabke je omogočil slovenskim raziskovalcem usposabljanje v svojem oddelku za fizikalno kemijo na MPIE, delo na tej opremi in preskrbel zanje štipendije nemških inštitucij. Za dosežke svojega znanstvenega dela in za sodelovanje z raziskovalci iz Slovenije mu je Univerza v Ljubljani podelila častni doktorat.

Mnogi ga bomo ohranili v spominu kot vrhunskega znastvenika in dobrega človeka, ki je bil vedno pripravljena na odprt pogovor, sodelovanje in pomoč in pri tem nikdar ni dal občutiti, da je iz prostora, ki je večji in bolj razvit kot je slovenski prostor.

Franc Vodopivec
Glavni urednik
Materiali in Tehnologije –
Materials and Technology

Germain- en- Laye and MIL, later IMT Ljubljana. When a rapid growth of science of metals surfaces was started with use of new analytical instruments that enabled quantitative investigations of surface and interface segregations of residuals in metals, H-J Grabke opened his dpt. at MPI for work slovenian scientists providing germain research grants, also. As recognition for scientific discoveries and cooperation with slovenian scientists H. J. Grabke was aknowledged with the h.c. doctorate of the Unversity of Ljubljana.

A number of scientists, in Slovenia also, will conserve the memory of H. J. Grabke as great scientists and a good man always ready to open talk, cooperation and assistance and without traces of provenience from a more developped and greater country.

Franc Vodopivec,
Chief Editor
Materiali in Tehnologije –
Materials and Technology